

# Studying dusty star-forming galaxies with *Herschel*-SPIRE

by

Viktoria Asboth

A THESIS SUBMITTED IN PARTIAL FULFILLMENT OF  
THE REQUIREMENTS FOR THE DEGREE OF

**Doctor of Philosophy**

in

The Faculty of Graduate and Postdoctoral Studies

(Astronomy)

THE UNIVERSITY OF BRITISH COLUMBIA

(Vancouver)

October 2015

© Viktoria Asboth, 2015

# Abstract

Observations suggest that almost half of the total light emitted by stars in the Universe is absorbed by dust, and the emission is re-radiated at far-infrared and submillimeter wavelengths. Dusty star-forming galaxies play a significant role in the stellar mass build-up at high redshift, but their contribution to the cosmic star formation rate density at  $z > 4$  is still unknown, due to the currently limited availability of statistically significant high-redshift dusty galaxy samples.

In this thesis we analyze data from two large area surveys, the HerMES Large Mode Survey (HeLMS) and the *Herschel* Stripe 82 Survey (HerS), observed with the *Herschel*-SPIRE instrument at far-infrared wavelengths of 250, 350 and 500  $\mu\text{m}$ . We describe the process of constructing maps from detector data that provide an unbiased estimate of the sky signal, then we use a map-based detection method to assemble a large catalog of candidate  $z > 4$  dusty star-forming galaxies detected in HeLMS. The large area of the survey allows us to detect a significant number of sources and we are able to determine the differential number counts of these galaxies at 500  $\mu\text{m}$ . We find an excess of such high-redshift galaxies compared to model predictions, and our counts suggest strong evolution in their properties.

We examine the properties of our sources at different wavelengths. Follow-up observations with ALMA, SCUBA-2 and ACT strengthen our initial assumption that the detected population consists of high- $z$  dusty galaxies with their spectrum dominated by thermal dust emission, best fitted with an optically thick modified blackbody. These follow-up observations also allow us to examine the biasing effects in our number counts due to blending of nearby sources.

We also investigate the mean dusty star formation activity in moderate redshift massive galaxy clusters detected by the Atacama Cosmology Telescope. We find that, on average, there is an excess of far-infrared emission in the line of sight of these clusters. Finding dusty star-forming galaxies in massive clusters implies that the environment can affect the star formation activity in galaxies.

# Preface

During my doctoral studies I contributed to research done by the HerMES (*Herschel* Multi-tiered Extragalactic Survey) collaboration and I was also part of the SCUBA-2 commissioning team, the HerS (*Herschel* Stripe 82 Survey) team and I was involved in projects in the HerMES-ACT (Atacama Cosmology Telescope) joint collaboration. Throughout this thesis I summarize work done by others in these collaborations, and I describe in detail the analysis carried out by me.

My contribution to the map-making project described in Chapter 2 was the adaptation of the SANEPIC map-maker software to work with pre-processed SPIRE data. I carried out tests to determine the additional pre-processing steps that need to be applied to the SPIRE detector timestreams before map-making with SANEPIC (Sec. 2.4.2). I created SANEPIC maps from the HeLMS and HerS datasets (Sec. 2.4.3) that will be part of the next public HerMES data release. I compared the performance of the SANEPIC and the SHIM map-makers through various tests (Sec. 2.4.4–2.4.6). Part of this work was published in the article Viero et al.: "The *Herschel* Stripe 82 Survey (HerS): Maps and Early Catalog." *ApJS*, 210:22 (2014). Any similarities of the text in Chapter 2 with the text in this paper are due to the fact that the map-making sections of this article were written by me. Fig. 2.9 and 2.11 of this thesis are taken from this article, but these plots were also created by me.

I contributed to the high-redshift source search project described in Dowell et al. (2014), and I lead a similar project based on the new HeLMS field, this project is described in Chapter 3. The HeLMS high-redshift source catalog and my results will be published in a paper lead by me, this publication is currently under internal review. The final publication will be a shorter version of Chapter 3, so the text and figures in this paper will show similarities with Chapter 3. Most of the data analysis in Chapter 3 was done by me. The ALMA spectroscopy analysis in Sec. 3.4 was carried out by Alex Conley, but the text of this section was written by me. The ACT maps used in Sec. 3.5 were processed by the ACT collaboration, I used the final data products in my analysis.

The SCUBA-2 telescope-time proposal that our data in Chapter 4 are based upon

was written by Rob Ivison, and I was a Co-Principal Investigator of this project. I helped in the sample selection, in the preparation of the observations and I was at the telescope supervising part of the observing run. All data analysis presented in Chapter 4 was carried out by me. In the analysis described in Chapter 5 I used the public ACT-selected cluster catalog and the HeLMS and HerS maps created by me with SANEPIC. All text in this thesis was written by me and all plots except for Fig 1.2 were created by me.

# Table of Contents

<b>Abstract</b> . . . . .	<b>ii</b>
<b>Preface</b> . . . . .	<b>iii</b>
<b>Table of Contents</b> . . . . .	<b>v</b>
<b>List of Tables</b> . . . . .	<b>viii</b>
<b>List of Figures</b> . . . . .	<b>ix</b>
<b>List of Acronyms and Symbols</b> . . . . .	<b>xi</b>
<b>Acknowledgements</b> . . . . .	<b>xiii</b>
<b>1 Introduction</b> . . . . .	<b>1</b>
1.1 Structure formation and stellar mass assembly . . . . .	1
1.2 The role of dusty star-forming galaxies . . . . .	4
1.3 Thermal emission from dust . . . . .	5
1.4 Observing the far-infrared/submillimeter sky . . . . .	7
1.4.1 Number counts . . . . .	9
1.4.1.1 Effects of gravitational lensing on the number counts . . . . .	10
1.4.1.2 Confusion noise . . . . .	11
1.5 The evolution of the luminosity function and the star formation rate density . . . . .	12
1.6 Modelling the evolution of dusty star-forming galaxies . . . . .	16
1.7 Outline of this thesis . . . . .	17
<b>2 Making large maps from <i>Herschel</i>-SPIRE data</b> . . . . .	<b>19</b>
2.1 The <i>Herschel</i> -SPIRE instrument . . . . .	20
2.2 Initial data processing . . . . .	22
2.2.1 Deglitching . . . . .	22
2.2.2 Electrical filter response correction . . . . .	23

2.2.3	Flux Calibration . . . . .	24
2.3	Map-makers . . . . .	25
2.3.1	SANEPIC . . . . .	26
2.3.2	SHIM . . . . .	29
2.4	Using SANEPIC with SPIRE data . . . . .	31
2.4.1	The HeLMS and HerS surveys . . . . .	31
2.4.2	Additional timeline processing . . . . .	34
2.4.3	SANEPIC maps . . . . .	36
2.4.4	Comparison of SANEPIC and SHIM maps . . . . .	37
2.4.5	Noise properties . . . . .	39
2.4.6	Transfer function . . . . .	40
2.4.7	Applications . . . . .	43
<b>3</b>	<b>A search for high redshift dusty galaxies in the HerMES Large Mode Survey . . . . .</b>	<b>45</b>
3.1	Catalog creation . . . . .	46
3.1.1	Maps . . . . .	47
3.1.2	Matched filter . . . . .	47
3.1.3	Difference map . . . . .	51
3.1.4	Source extraction . . . . .	52
3.1.5	Final catalog . . . . .	54
3.2	Number counts . . . . .	56
3.2.1	Intrinsic number counts . . . . .	57
3.2.1.1	Blending . . . . .	58
3.2.1.2	Detection efficiency . . . . .	60
3.2.1.3	False detections and Eddington bias . . . . .	61
3.2.1.4	Simulations . . . . .	62
3.2.2	Comparison to models . . . . .	65
3.3	Colors and SED fits . . . . .	67
3.4	ALMA spectroscopy . . . . .	72
3.5	Red sources in the ACT maps . . . . .	75
3.6	Summary . . . . .	78
<b>4</b>	<b>Observing SPIRE-selected “red” sources with SCUBA-2 . . . . .</b>	<b>80</b>
4.1	Sample selection . . . . .	81
4.2	Observations . . . . .	82
4.3	Data reduction . . . . .	85

4.4	Results and discussion . . . . .	86
4.4.1	Daisy observations . . . . .	86
4.4.2	Pong observations . . . . .	98
4.5	Summary . . . . .	102
<b>5</b>	<b>Average dusty star-formation activity in Sunyaev-Zel'dovich-selected galaxy clusters . . . . .</b>	<b>104</b>
5.1	The ACT equatorial cluster sample . . . . .	107
5.2	Data analysis . . . . .	107
5.3	Results and discussion . . . . .	110
<b>6</b>	<b>Conclusions . . . . .</b>	<b>115</b>
	<b>Bibliography . . . . .</b>	<b>119</b>

# List of Tables

3.1	Noise levels in the smoothed maps . . . . .	52
3.2	Raw $500\ \mu\text{m}$ number counts of the detected red sources. . . . .	57
3.3	Average flux densities of sources in each $500\ \mu\text{m}$ flux density bin. . . . .	76
4.1	HerMES fields used for red source sample selection . . . . .	82
4.2	JCMT observing weather grades . . . . .	84
4.3	Measured 250, 350, 500 and $850\ \mu\text{m}$ flux densities . . . . .	88
4.4	$S_{850} > 3.75\sigma$ sources detected around the central red galaxy . . . . .	100
5.1	ACT clusters in HeLMS . . . . .	108
5.2	ACT clusters in HerS . . . . .	108

# List of Figures

1.1	Negative k-correction . . . . .	7
1.2	Star formation rate density evolution . . . . .	15
2.1	Auto- and cross-power spectra of bolometer timestreams . . . . .	29
2.2	HeLMS coverage map . . . . .	33
2.3	HerS coverage map . . . . .	33
2.4	Temperature drift . . . . .	35
2.5	Cooler-burp . . . . .	36
2.6	2D power spectra of HeLMS maps made with SHIM and SANEPIC . . . . .	38
2.7	Azimuthally averaged power spectra of HeLMS maps made with SHIM and SANEPIC . . . . .	38
2.8	Comparison of large scale structures recovered in SHIM and SANEPIC maps	39
2.9	Pixel flux histogram of the HerS maps . . . . .	41
2.10	Azimuthally averaged power spectra of the sky signal, the noise and the full maps . . . . .	42
2.11	Transfer function . . . . .	43
3.1	Grayscale image of the HeLMS field with the applied mask . . . . .	48
3.2	Matched filter . . . . .	49
3.3	Comparison of the final resolution of the maps using different filters . . . . .	50
3.4	Cirrus background removal in the maps . . . . .	51
3.5	Flux density recovery bias . . . . .	54
3.6	Failed glitch flagging in the time ordered data . . . . .	55
3.7	Image of a cosmic ray hit in the maps . . . . .	56
3.8	Raw 500 $\mu\text{m}$ differential number counts of our sample of “red” sources. . . . .	58
3.9	Postage-stamp images of isolated sources and blends . . . . .	59
3.10	Detection efficiency . . . . .	61
3.11	Measured completeness . . . . .	62
3.12	SPIRE colors of red sources as a function of the 500 $\mu\text{m}$ flux density . . . . .	66
3.13	Color-color plot of red sources detected in HeLMS . . . . .	69

3.14	MCMC contours of modified blackbody fit . . . . .	71
3.15	MCMC parameter distribution without applied priors . . . . .	72
3.16	Observed temperature and peak wavelength distribution of the HeLMS red sources . . . . .	73
3.17	ALMA spectra of HELMS34 and HELMS65 . . . . .	74
3.18	(a.) ACT stacks (Bin 1-3) . . . . .	76
3.18	(b.) ACT stacks (Bin 4-6) . . . . .	77
3.19	Average SED of stacked sources . . . . .	78
4.1	Coverage of “daisy” and “pong-900” maps . . . . .	83
4.2	(a.) SPIRE and SCUBA-2 postage-stamp images of observations . . . . .	89
4.2	(b.) SPIRE and SCUBA-2 postage-stamp images of observations . . . . .	90
4.2	(c.) SPIRE and SCUBA-2 postage-stamp images of observations . . . . .	91
4.2	(d.) SPIRE and SCUBA-2 postage-stamp images of observations . . . . .	92
4.3	(a.) Modified blackbody SED fits . . . . .	93
4.3	(b.) Modified blackbody SED fits . . . . .	94
4.3	(c.) Modified blackbody SED fits . . . . .	95
4.3	(d.) Modified blackbody SED fits . . . . .	96
4.3	(e.) Modified blackbody SED fits . . . . .	97
4.4	Maps of LSW28, LSW102, XMM26, XMM30 . . . . .	99
4.5	Cumulative 850 $\mu$ m number counts around red sources . . . . .	101
4.6	Cumulative number of sources within different radii of the central red source	102
5.1	Cluster image re-binning . . . . .	110
5.2	Stacked SPIRE images of ACT SZ clusters . . . . .	111
5.3	Radial average of SPIRE images stacked at ACT cluster positions . . . . .	112
5.4	Radial average of SPIRE images stacked at random positions . . . . .	113

# List of Acronyms and Symbols

<b>ACT</b>	Atacama Cosmology Telescope
<b>ALMA</b>	Atacama Large Millimeter/submillimeter Array
<b>AGN</b>	Active galactic nucleus
<b>BCG</b>	Brightest cluster galaxy
<b>BLAST</b>	Balloon-borne Large Aperture Submillimeter Telescope
<b>CIB</b>	Cosmic Infrared Background
<b>CMB</b>	Cosmic Microwave Background
<b><math>D_A</math></b>	angular diameter distance
<b><math>D_L</math></b>	luminosity distance
<b>dex</b>	“decimal exponent”, a logarithmic unit being used in astronomy. 1 dex equals a factor of 10.
<b>FIR</b>	far-infrared
<b>FWHM</b>	full-width at half-maximum
<b>HeLMS</b>	HerMES Large Mode Survey
<b>HerMES</b>	Herschel Multi-tiered Extragalactic Survey
<b>HerS</b>	Herschel Stripe 82 Survey
<b>HIPE</b>	Herschel Interactive Processing Environment
<b>JCMT</b>	James Clerk Maxwell Telescope
<b>Jy</b>	Jansky ( $1\text{Jy} = 10^{-26}\text{W m}^{-2}\text{ Hz}^{-1}$ )
<b><math>L_\odot</math></b>	solar luminosity ( $L_\odot = 3.846 \times 10^{26}\text{W}$ )
<b><math>L_{\text{IR}}</math></b>	infrared bolometric ( $8 - 1000\mu\text{m}$ ) luminosity
<b>LIRG</b>	luminous infrared galaxy
<b><math>M_\odot</math></b>	solar mass ( $M_\odot = 1.99 \times 10^{30}\text{kg}$ )
<b><math>M_*</math></b>	stellar mass of a galaxy
<b>Mpc</b>	megaparsec ( $1\text{ pc} = 3.26\text{ light-years} = 3.0857 \times 10^{16}\text{ m}$ )
<b>MS</b>	main sequence mode of star formation
<b>PSF</b>	point spread function

<b>PWV</b>	precipitable water vapor
<b>SANEPIC</b>	Signal And Noise Estimation Procedure Including Correlations
<b>SB</b>	starburst mode of star formation
<b>SCUBA-2</b>	Submillimetre Common-User Bolometer Array-2
<b>SDSS</b>	Sloan Digital Sky Survey
<b>SED</b>	spectral energy distribution
<b>SFR</b>	star formation rate
<b>SHIM</b>	SPIRE-HerMES Iterative Mapper
<b>SNR</b>	signal-to-noise ratio
<b>SPIRE</b>	Spectral and Photometric Imaging Receiver
<b>sSFR</b>	specific star formation rate ( $\text{sSFR} = \text{SFR} / M_*$ )
<b>SZ</b>	Sunyaev-Zel'dovich effect
<b><math>T_d</math></b>	dust temperature
<b><math>T_{\text{obs}}</math></b>	observed dust temperature ( $T_{\text{obs}} = T_d / (1 + z)$ )
<b>TOD</b>	time-ordered data
<b>ULIRG</b>	ultraluminous infrared galaxy
<b>z</b>	redshift

# Acknowledgements

I thank my supervisor Mark Halpern for his guidance, patience and support throughout my graduate studies. I thank members of my supervisory committee, Sarah Burke, Gary Hinshaw and Douglas Scott for their support. I thank my collaborators in the HerMES/HerS and SCUBA-2 teams, and I thank my fellow lab-mates. In particular, thanks to Gaelen Marsden and Alex Conley for all their help and encouragement during my research. I thank my family and friends for always encouraging me and for believing in me even at times when I did not believe in myself. A special thank you goes to my sister, Timea Asboth, your support is invaluable, I could not have done this without you.

# Chapter 1

## Introduction

One of the key goals of astronomy is to understand how the structure of the Universe evolved from primordial density fluctuations into the galaxies and galaxy clusters we see today. The visible building blocks of these structures are the stars, made of luminous baryons. Although baryons only represent a small fraction of the total mass of the Universe, they trace the underlying dark matter distribution, and thus it is important to understand the process of the stellar mass assembly in galaxies in order to study the structure formation in the Universe.

Stars emit most of their light in the optical and ultraviolet wavelength range, but observations show that almost half of the total light emitted by stars is absorbed by dust, and this radiation is re-emitted by the heated dust grains at far-infrared and submillimeter wavelengths. Optical surveys miss a whole population of optically faint but infrared-luminous distant dusty star-forming galaxies at the epoch when the bulk of the stellar mass in the Universe formed. Thus it is crucial to study the far-infrared/submillimeter sky to gain a comprehensive view of the cosmic star formation history.

In this chapter we give a broad overview of our current knowledge of the history of star formation, emphasizing the role of dusty star-forming galaxies, and we describe what we can learn from dedicated surveys of the far-infrared/submillimeter sky.

### 1.1 Structure formation and stellar mass assembly

According to the current cosmological models (e.g. Bennett et al., 2013; Planck Collaboration et al., 2014a) the Universe began  $\sim 13.8$  billion years ago with the Big Bang as a hot and dense plasma of baryons, electrons, and photons. As the Universe expanded, the plasma started to cool down, and eventually protons and electrons combined to form hydrogen atoms, while the photons decoupled from the matter and radiated away freely.

This recombination occurred  $\sim 378,000$  years after the Big Bang, corresponding to a redshift of  $z \sim 1100$  (The wavelength  $\lambda_e$  of the light a distant object emits increases as the Universe expands, and it is observed at  $\lambda_o = (1+z)\lambda_e$ . The redshift  $z$  is often used to describe cosmological distances). In the “dark ages” following the recombination, small initial density fluctuations in the molecular gas started to grow as the gas fell into the gravitational potential well of dark matter halos. When these over-densities became massive enough to overcome the internal pressure of the gas, they collapsed, nuclear fusion began and the first stars were born at perhaps  $z \sim 30$  (Barkana and Loeb, 2001). Today the stars are a part of large structures, spiral, elliptical or irregularly shaped galaxies, and these galaxies form even larger structures, galaxy groups, clusters and superclusters. The most accepted theory describing the evolution of galaxies from the first light in the Universe to these large structures is the hierarchical structure-formation model (Press and Schechter, 1974; White and Rees, 1978). This theory describes a “bottom-up” formation scenario, where small dark matter halos form first and larger structures are created by merging and accretion of these smaller halos. Large N-body simulations of the evolution of the dark matter distribution have been carried out that support this model (e.g. Springel et al., 2005). However, to include the star-forming processes in these simulations, additional complex, and often non-linear physical effects must be included, and the results of the simulations will also strongly depend on the wide range of initial conditions.

There are several theories about processes that can trigger and quench star formation activity in galaxies. The fuel of star formation is the cold molecular gas. Star formation at a moderate rate can be maintained for an extended period of time by cold gas accretion from the intergalactic medium and by minor mergers with gas rich dwarf galaxies (e.g. Dekel et al., 2009). Additionally, major mergers of gas rich galaxies (e.g. Li et al., 2007; Tacconi et al., 2008; Genzel et al., 2010) can trigger intense short-lived bursts of star formation. These “starburst” galaxies can form stars at a rate hundreds to thousands times larger than normal star-forming galaxies, but this starburst phase is expected to be relatively short, since intense star formation uses up all of the cold gas on a short timescale. There is also evidence that early galaxies contained more cold gas, than galaxies in the local Universe; thus they could form more stars even without the high star formation efficiency of a starburst (e.g. Daddi et al., 2008, 2010; Geach et al., 2011).

Many local galaxies have old, passively evolving stellar populations and do not show significant current star formation activity, suggesting that the star formation was stopped (“quenched”) by some process. Star formation stops if there is not enough cool gas left in the system. The environment in which galaxies reside is suspected to play a

role in quenching star formation. In the local Universe elliptical and lenticular galaxies with evolved stellar populations and very little star formation activity tend to reside in dense environments in the cores of galaxy clusters, while star-forming spiral galaxies are more common in the outskirts of clusters or in the field (Dressler, 1980; Gómez et al., 2003). Observations suggest that this trend might change at higher redshifts, as more distant star-forming galaxies are found in dense environments (Butcher and Oemler, 1978; Ellingson et al., 2001; Saintonge et al., 2008; Haines et al., 2009). This evidence suggests that the environmental effects arising as galaxies fall into clusters can stop the star formation activity. Interactions between galaxies in dense environments can remove cold gas, for example, through tidal effects (“strangulation”, Larson et al., 1980), disturbance by close high-speed passes between galaxies (“galaxy harassment”, Moore et al., 1996) or ram-pressure stripping as galaxies move through the intra-cluster medium (Gunn and Gott, 1972).

Apart from environmental quenching, there are intrinsic processes that can remove cold gas from the star-forming regions. In merging galaxies the gas can be accreted by the central black hole, creating an active galactic nucleus (AGN), which then emits radiation that can blow away or heat up the remaining gas, thus stopping star formation activity (Hopkins et al., 2008). To a lesser degree, feedback from stellar winds and supernova explosions in intense starburst regions can have a similar effect. There is also some evidence that the quenching can depend on the stellar mass of the galaxy (Peng et al., 2010) such that more massive galaxies experience quenching earlier than low mass galaxies. This is also similar to the observational trend called “downsizing” (Cowie et al., 1996; Collins et al., 2009), that suggests that more massive galaxies formed their stars earlier than smaller galaxies. The most massive local elliptical galaxies have evolved stellar populations that must have formed much earlier than the hierarchical models predict. This seemingly anti-hierarchical evolution for the largest galaxies also supports the mass quenching scenario.

Current observations cannot determine unambiguously which one of these wide range of processes is the most dominant in affecting the star formation history. The stellar mass build-up in merging dark matter halos can depend on many complex, non-linear effects that are hard to simulate, and more observational constraints from star formation activity at different epochs are needed to fine-tune these models and to properly determine the initial conditions.

## 1.2 The role of dusty star-forming galaxies

While the dominant component of the interstellar medium is gas, it also contains dust particles. This dust consists of irregularly shaped, sub-micron sized grains made typically of graphites and silicates. These dust particles can scatter and absorb the optical/UV light emitted by stars; thus the measured intensity of the radiation is reduced. It has been known for a long time that optical studies need to apply a correction factor when measuring the brightness of stars to account for the dust extinction in the interstellar medium (e.g. Trumpler, 1930). These studies, however, assume that the dust is not very optically thick, and the light is only partially blocked out. While the optical light of stars is dimmed, the absorbed power of the radiation also causes the dust to warm up to typically 10s or 100s of Kelvin; thus the light is re-radiated at infrared wavelengths. The real importance of studying the dust emission was only discovered when the first space-based infrared telescopes were launched.

The first survey to detect a large number of galaxies based on their infrared radiation was carried out by the *InfraRed Astronomy Satellite* (IRAS, Neugebauer et al., 1984). The highlight of this mission was the discovery of a 60- $\mu\text{m}$ -selected population of luminous infrared galaxies (LIRGs, Soifer et al., 1984; Sanders and Mirabel, 1996) with infrared bolometric luminosities  $L_{\text{IR}} > 10^{11}L_{\odot}$  ( $L_{\odot} = 3.846 \times 10^{26} \text{ W}$  is the solar luminosity), and ultraluminous infrared galaxies (ULIRGs, Houck et al., 1985) with  $L_{\text{IR}} > 10^{12}L_{\odot}$ . These galaxies turned out to be very faint or undetected at optical wavelengths. The extreme IR luminosity of these sources was attributed to emission from dust heated by intense starburst regions or active galactic nuclei, while the optical emission of the young massive stars is completely blocked out by the dust. Most of these local ( $z \lesssim 0.3$ ) LIRGs and ULIRGs were identified as major mergers between gas rich galaxies, or as galaxies with irregular morphologies, where interaction probably triggers the very active dusty star formation phase (e.g. Murphy et al., 1996; Clements et al., 1996).

Although the discovery of these LIRGs and ULIRGs showed that optical surveys potentially miss the most active star-forming galaxies that are heavily obscured by dust, these galaxies turned out to be very rare locally compared to normal galaxies, and they were shown to only contribute  $\sim 30\%$  to the total local infrared luminosity (Soifer and Neugebauer, 1991). However, the discovery of the cosmic infrared background (CIB) suggested, that dusty star-forming galaxies should be more common at higher redshifts. The extragalactic background light is the integrated radiation from galaxies at all distances in the Universe. It was long predicted that the integrated background light should contain a contribution from the infrared emission of galaxies (Partridge and Peebles, 1967). The

CIB was first detected by the *Cosmic Background Explorer* (COBE) satellite with the FIRAS instrument (Far Infrared Absolute Spectrophotometer, Puget et al., 1996; Fixsen et al., 1998) and later with the DIRBE instrument (Diffuse Infrared Background Experiment, Hauser et al., 1998). Surprisingly, the contribution from the infrared background light was measured to be comparable to the total integrated optical light, suggesting that almost half of the light emitted by stars in the Universe must be absorbed by dust and re-emitted at far-IR wavelengths (Dwek et al., 1998). Since the contribution of local LIRGs and ULIRGs cannot explain this emission, it was expected that most of the infrared light comes from the redshifted emission of more distant dusty star-forming galaxies.

A high redshift population of dusty star-forming galaxies was first discovered at submillimeter wavelengths with the SCUBA instrument (Submillimetre Common-User Bolometer Array, Holland et al., 1999) at the James Clerk Maxwell Telescope (Smail et al., 1997; Hughes et al., 1998; Barger et al., 1998). These 850- $\mu\text{m}$ -selected galaxies looked like distant ULIRGs with luminosities  $L_{\text{IR}} > 10^{12}L_{\odot}$ , forming hundreds to thousands of stars per year. It was shown that almost all of these sources are at redshifts  $z > 1$ , with a median at  $z \sim 2.3$  (Smail et al., 2000; Chapman et al., 2005; Pope et al., 2005), and based on their observed number counts their emission can account for most of the 850  $\mu\text{m}$  background light (Blain et al., 1999; Barger et al., 1999).

Since the discovery of the first submillimeter galaxies, further surveys at different far-infrared and submillimeter wavelengths were able to successfully resolve most of the CIB, proving that the background is really made up of individual galaxies mostly at high- $z$  (e.g. Dole et al., 2006; Knudsen et al., 2008; Devlin et al., 2009; Marsden et al., 2009). It was shown that dust-obscured star formation dominates the total star formation activity at redshifts  $z \gtrsim 1$  (Le Floch et al., 2005); thus star formation studies based on optical and UV data alone are expected to significantly under-predict the star formation rate at these epochs.

### 1.3 Thermal emission from dust

The source of the far-infrared and submillimeter emission of galaxies is thermal radiation from dust heated by star-forming regions or an AGN. The dominant emission comes from dust grains in thermal equilibrium with the local radiation field. In equilibrium the total power absorbed by the dust is equal to the total radiated power, and the dust temperature is determined by this balance. Typical equilibrium temperatures of local LIRGs and ULIRGs range between  $T_{\text{d}} \sim 20\text{ K}$  and  $60\text{ K}$  (Sanders and Mirabel, 1996). The amount of radiation these galaxies emit at different frequencies depends on the dust

properties. The dust grains can differ in size, geometry, composition and emissivity properties, and their spatial distribution also affects the resulting functional form of the radiation. Assuming an optically thin dust cloud, the featureless continuum emission from dust grains in equilibrium can be modelled as a modified blackbody radiation, and the spectral energy distribution (SED) can be expressed as

$$S_\nu \propto \nu^\beta B_\nu(T_d). \quad (1.1)$$

Here

$$B_\nu(T_d) = \frac{2h}{c^2} \frac{\nu^3}{e^{h\nu/kT_d} - 1} \quad (1.2)$$

is the Planck function, describing the blackbody radiation,  $c$  is the speed of light,  $h$  is the Planck constant,  $k$  is the Boltzmann constant, and  $\beta$  is the dust grain spectral emissivity index ( $\beta \sim 1-2$ , e.g. Hildebrand, 1983). The quantity

$$S_\nu = \frac{L_{\nu'}}{4\pi D_L(z)^2} \quad (1.3)$$

is the observed spectral flux density of a source of luminosity  $L$  at redshift  $z$ . Here the spectral luminosity  $L_{\nu'}$  is the total power per unit frequency interval radiated by the source at the rest frame frequency  $\nu' = (1+z)\nu$ , and  $D_L(z)$  is the model-dependent luminosity distance (see e.g. Hogg, 1999). Note, that in submillimeter astronomy the flux density is usually expressed in units of Jansky, with  $1 \text{ Jy} = 10^{-26} \text{ W m}^{-2} \text{ Hz}^{-1}$  (hence the notation in terms of frequency), but it is common to plot these flux density values as a function of wavelength as  $S_\nu(\lambda)$ , where  $\lambda = c/\nu$ .

Small dust grains can be heated transiently above their equilibrium temperatures by absorbing single photons near star-forming regions. Emission from these grains dominates the mid-infrared part of the spectrum. Narrow emission and absorption line features from silicates and Polycyclic Aromatic Hydrocarbons (PAHs) also contribute at these wavelengths. The spectrum of dusty star-forming galaxies also contains emission lines from atomic and molecular transitions, (e.g. the CO ladder, C+, HCN and HCO+) that can be excited in high density regions. Spectroscopic redshift measurements are based on the detection of such spectral lines.

Apart from the fact that a significant fraction of the star formation activity at high redshift is obscured by dust, and thus it is invisible at optical wavelengths, observing sources at submillimeter wavelengths has another unique advantage. The shape of the dust emission spectrum allows us to easily observe objects in a significantly larger redshift range than is possible at optical or radio wavelengths. The observed flux densities

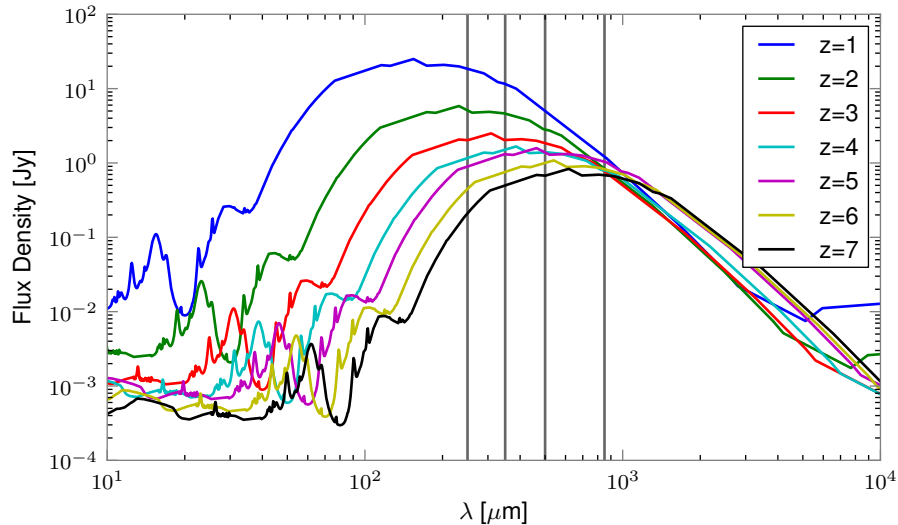


Figure 1.1: The so-called “negative k-correction” at submillimeter wavelengths illustrated with the redshifted spectral energy distribution of a local ULIRG, Arp220. The vertical lines correspond to the wavelengths we discuss in this thesis, the *Herschel*-SPIRE bands at  $250 \mu\text{m}$ ,  $350 \mu\text{m}$  and  $500 \mu\text{m}$ , together with the  $850 \mu\text{m}$  SCUBA-2 band. At far-infrared and submillimeter wavelengths the measured flux densities are not decreasing as fast with redshift as they do in the optical range, and they remain approximately constant at  $850 \mu\text{m}$ .

of a source with a fixed luminosity normally decrease with the square of the distance (Eq. 1.3). In the rest frame the dusty SED typically peaks around  $100 \mu\text{m}$ , and this peak is redshifted to  $\lambda \gtrsim 200 \mu\text{m}$  at  $z \gtrsim 1$ . Thus FIR/submillimeter wavelengths sample the SED closer to its peak at higher redshift, and this effect can counteract the decrease of flux density. On the long wavelength side of the SED peak, where the flux densities are a steeply decreasing function of  $\lambda$ , this can mean that the observed flux densities remain approximately constant at a large redshift range ( $z \sim 1-10$ ). This effect is also called a “negative k-correction” (Franceschini et al., 1991; Blain and Longair, 1993), and is illustrated on Figure 1.1. At  $\lambda \sim 200-500 \mu\text{m}$  the FIR/submillimeter flux densities still decrease with increasing redshift, but not at the same rate as they do at optical or radio wavelengths, so even in this range we can observe higher redshift sources more easily.

## 1.4 Observing the far-infrared/submillimeter sky

Since the discovery of the first submillimeter galaxies with SCUBA, a large range of experiments have been designed to observe the far-infrared/submillimeter sky at different

wavelengths in an attempt to resolve the cosmic infrared background into individual sources, and to investigate the properties of these dusty star-forming galaxy populations. The two biggest limiting factors when observing at these wavelengths are the opacity of the atmosphere, and the relatively large beamsizes of single dish telescopes at the observed wavelengths. Water vapour in the atmosphere absorbs most of the infrared radiation; thus ground-based telescopes can only observe the FIR/submillimeter part of the electromagnetic spectrum through specific atmospheric windows. To overcome this effect, balloon-borne or space-based telescopes have been built, but the resolution of these experiments is typically limited due to the small diameters of their mirrors. Ground-based interferometric instruments can achieve much better resolution, but due to their small fields of view they are usually better suited to carry out targeted follow-up observations of individual sources rather than performing large area surveys.

Although the physical properties of individual galaxies can be very different from one another, it is useful to investigate the average properties of a galaxy population as a whole. Selecting sources at different wavelengths usually selects different populations. Notable instruments that have mapped large areas of the FIR/submillimeter sky include *Spitzer*-MIPS (24, 70, 160  $\mu\text{m}$ , Rieke et al., 2004), *Herschel*-PACS (70, 100, 160  $\mu\text{m}$ , Poglitsch et al., 2010), BLAST (250, 350, 500  $\mu\text{m}$ , Devlin et al., 2004), *Herschel*-SPIRE (250, 350, 500  $\mu\text{m}$ , Griffin et al., 2010), SCUBA and SCUBA-2 (450 and 850  $\mu\text{m}$ , Holland et al., 1999, 2013), LABOCA (870  $\mu\text{m}$ , Siringo et al., 2009), and AzTEC (1.1 mm, Wilson et al., 2008), among others.

It needs to be noted, that an important wavelength-dependent selection effect arises due to the different dust temperatures. For example, it was shown that 850- $\mu\text{m}$ -selected SCUBA samples were biased against warmer dust galaxies and preferentially select colder dust ( $T \sim 40\text{K}$ ) objects (Eales et al., 2000; Blain et al., 2004; Kovács et al., 2006). BLAST and SPIRE sample the spectral energy distribution closer to the peak, and they are less biased against warmer dust objects. Also, since the k-correction becomes very negative above 500  $\mu\text{m}$  wavelengths, galaxy samples selected at longer wavelengths are more likely to detect higher redshift galaxy populations. In the following subsections we describe what we can learn about populations of galaxies from large dedicated surveys, emphasizing the results from *Herschel*-SPIRE, the instrument used to obtain the majority of the data analyzed in this thesis.

### 1.4.1 Number counts

Measurements of the number of galaxies detected in a survey per unit area in different flux density bins can provide an insight into the evolution of the selected population of sources. Number counts are usually expressed in a differential form as  $dN/dS$ , describing the number of objects falling into a flux density bin, or in an integral form,  $N(> S)$ , corresponding to the total number of objects with flux densities above  $S$ . The observed differential counts are usually best fitted by either a Schechter-type function,

$$\frac{dN}{dS} = \frac{N_0}{S_0} \left( \frac{S}{S_0} \right)^{-\alpha} \exp \left( -\frac{S}{S_0} \right), \quad (1.4)$$

or a double power law,

$$\begin{aligned} \frac{dN}{dS} &= \frac{N_0}{S_0} \left( \frac{S}{S_0} \right)^{-\alpha} ; S \leq S_0, \\ \frac{dN}{dS} &= \frac{N_0}{S_0} \left( \frac{S}{S_0} \right)^{-\beta} ; S > S_0, \end{aligned} \quad (1.5)$$

where  $N_0$ ,  $S_0$ ,  $\alpha$ , and  $\beta$  are parameters of the fit.

Assuming a flat Euclidean universe, the expected shape of the number counts for a non-evolving population can be easily derived. No evolution means that all sources have luminosity  $L$  and their number density  $\rho$  is constant. For such a distribution the number of sources in a radial shell with radius  $r$  and thickness  $dr$  can be determined as

$$dN = \rho 4\pi r^2 dr \propto r^2. \quad (1.6)$$

The flux at distance  $r$  from a luminosity  $L$  object is  $S = L/(4\pi r^2)$ , and from this we can derive

$$\frac{dS}{dr} = -\frac{L}{2\pi r^3} \propto r^{-3}, \quad (1.7)$$

and

$$r = \left( \frac{L}{4\pi S} \right)^{\frac{1}{2}} \propto S^{-\frac{1}{2}}. \quad (1.8)$$

Combining equations 1.6, 1.7 and 1.8 we get

$$\frac{dN}{dS} = \rho 4\pi r^2 \frac{dr}{dS} \propto r^5 \propto S^{-\frac{5}{2}}. \quad (1.9)$$

Thus in a flat Euclidean universe, which contains uniformly distributed sources, the counts are expected to vary as  $dN/dS \propto S^{-5/2}$ , or in integral form as  $N(> S) \propto S^{-3/2}$ .

If the population of sources is evolving (e.g. their luminosity or number density changes with redshift), then the slope of the observed counts will deviate from the Euclidean value. Note however, that number counts at submillimeter wavelengths are expected to appear steeper than the Euclidean counts, even without an evolving population, due to the increasing negative k-correction and the larger volume sampled at higher  $z$ , but the expected number counts for a non-evolving population can be modelled. Steep number counts can suggest that the number of luminous sources decreases over time. Submillimeter number counts are known to be much steeper than predictions based on non-evolving models, suggesting that the properties of these populations are strongly evolving with redshift (e.g. Borys et al., 2003; Coppin et al., 2006; Perera et al., 2008; Patanchon et al., 2009; Austermann et al., 2010; Glenn et al., 2010; Oliver et al., 2010; Béthermin et al., 2012b; Geach et al., 2013).

#### 1.4.1.1 Effects of gravitational lensing on the number counts

Massive objects between a distant source and the observer can act as lenses, bending the light coming from the background source. This effect is called gravitational lensing, and it can magnify and distort the image of the distant object. The magnification of faint sources by foreground galaxies and galaxy clusters has been widely exploited in submillimeter astronomy, since it allows the investigation of objects that would be otherwise too faint to be detected based on the typical survey flux density limits. Surface brightness (the flux density per unit solid angle) is conserved by gravitational lensing, so if an object is magnified by a factor of  $\mu$  (meaning that the observed solid angle of the source becomes  $d\Omega_{\text{obs}} = \mu d\Omega$ ), then its observed flux will also increase as  $S_{\text{obs}} = \mu S$ . This magnification effect can change the observed number counts (e.g. Paciga et al., 2009; Jain and Lima, 2011). Due to the magnification of the solid angle, the observed volume decreases, so the number of sources in the same area decreases to  $N_{\text{obs}} = N/\mu$ , thus the differential number counts will change as

$$\frac{dN_{\text{obs}}}{dS_{\text{obs}}}(S_{\text{obs}}) = \frac{1}{\mu^2} \frac{dN}{dS}(S_{\text{obs}}/\mu). \quad (1.10)$$

As discussed before, the unlensed FIR/submillimeter number counts usually decrease very steeply at the bright end, and scale as  $dN/dS \propto S^{-\alpha}$ , so the observed lensed counts will be proportional to  $dN_{\text{obs}}/dS_{\text{obs}} \propto \mu^{\alpha-2} S_{\text{obs}}^{-\alpha}$ . Since  $\alpha \gg 2$  at the bright end of the counts, we see more bright sources than we would without lensing. Combining this effect with the negative k-correction at submillimeter wavelengths above about  $500 \mu\text{m}$  suggest that the bright end of the submillimeter counts could be dominated by high- $z$  lensed

objects (Blain, 1996; Negrello et al., 2007). This lensed population has already been detected with *Herschel*-SPIRE (Negrello et al., 2010; Busmann et al., 2013; Wardlow et al., 2013), where objects with  $500\ \mu\text{m}$  flux densities above  $\sim 100\ \text{mJy}$  are all expected to be magnified by lensing. Similarly, the majority of the bright galaxies selected at  $1.4\ \text{mm}$  wavelengths with the South Pole Telescope (SPT) are strongly lensed (Vieira et al., 2013; Weiß et al., 2013).

### 1.4.1.2 Confusion noise

One of the limitations of FIR/submillimeter astronomy that makes it difficult to resolve the faint sources contributing to the CIB is confusion noise (Condon, 1974; Dole et al., 2003). This noise arises due to the combination of the limited resolution of FIR-submillimeter telescopes and the steep source counts of the galaxy populations selected at these wavelengths. The smallest angular scale  $\theta$  that a telescope can resolve depends on the diameter ( $D$ ) of the optics and the observed wavelength  $\lambda$  as  $\theta \sim \lambda/D$ . Since the wavelengths we want to observe are relatively large compared to the diameter of single dish telescopes, the beam sizes of these instruments are fairly wide. Due to the steep source counts, faint objects on the sky become increasingly numerous, and below a flux density limit each beam-area in the sky will contain more than one source. These sources cannot be distinguished from each other anymore, and the sum of their flux densities creates an uncertainty in the maps. If the beam response function of the telescope is  $f(\theta, \phi)$ , then the fluctuation from sources below the confusion limit  $S_{\text{lim}}$  can be expressed as

$$\sigma_{\text{conf}}^2 = \int f(\theta, \phi)^2 d\theta d\phi \int_0^{S_{\text{lim}}} S^2 \frac{dN}{dS} dS. \quad (1.11)$$

Unlike the instrumental noise, confusion noise cannot be reduced by longer observing times, since it is fixed on the sky.

Although sources with flux densities below the confusion limit cannot be resolved, statistical methods can be used to investigate the properties of these faint galaxies. One of the commonly used methods is called probability of deflection analysis or  $P(D)$ , which is based on recovering the number counts based on pixel intensity histograms in FIR/submm maps (Patanchon et al., 2009; Glenn et al., 2010). Another often used method is based on determining the covariance between the confusion-limited maps and *Spitzer*-MIPS  $24\ \mu\text{m}$  selected source positions (“stacking”, Pascale et al., 2009; Marsden et al., 2009). It has been shown that  $24\text{-}\mu\text{m}$ -selected catalogs are able to resolve the majority of the CIB (Papovich et al., 2004; Dole et al., 2006), and it has been assumed that these objects are the same sources that create the confusion limit at longer wavelengths. There is a

good agreement between the  $P(D)$  and stacking results and the counts also agree well with the extrapolation of the resolved number counts (B  thermin et al., 2012b), showing that these statistical methods work well to determine the counts below the confusion limit.

Investigating the statistics of the unresolved emission in FIR/submillimeter maps can also be useful to study the clustering properties of the sources that constitute the cosmic infrared background. A strongly clustered population will create an excess in the angular power spectrum of the background intensity variations compared to the Poisson-term caused by unclustered sources. At small angular scales this excess power dominantly comes from clustering of galaxies within a single dark matter halo, while on large angular scales the extra power is the result of the clustering of galaxies residing in different halos (e.g. Cooray and Sheth, 2002; Amblard et al., 2011). The one-halo term starts to dominate above the unclustered signal at angular scales of a few arcminutes, while the transition to the two-halo term is detected at  $\sim 10$  arcminute angular scales (e.g. Viero et al., 2009, 2013). To detect this low spatial frequency correlated signal in the background anisotropies it is crucial to carry out large-area surveys and to create maps from the observed data that reconstruct these large-scale signal variations in an unbiased way. One of the main goals of the current work is to produce such maps from large-area *Herschel*-SPIRE observations.

## 1.5 The evolution of the luminosity function and the star formation rate density

As we discussed in Section 1.4.1, the observed functional form of the number counts provides a hint to the evolution of the source population. The number of objects we are able to observe on the sky above some flux density limit is the projected number of sources at different redshifts having different luminosities. If we know the redshift of a source then we can calculate its bolometric infrared luminosity by integrating the observed spectral energy distribution over the wavelength range 8–1000  $\mu\text{m}$  (this range being the conventional choice),

$$L_{\text{IR}} = \int_{8\mu\text{m}}^{1000\mu\text{m}} 4\pi D_L(z)^2 S_\nu(\lambda) d\lambda. \quad (1.12)$$

Thus if we know the redshift distribution of our sources, we can convert our number counts into a function  $\phi(L)$  describing the number of galaxies per unit luminosity and unit volume. In flux-limited samples, high luminosity galaxies can be detected to greater distances than faint sources, and the luminosity function is usually determined by the  $1/V_{\max}$  method (Schmidt, 1968). In this method the maximum redshift  $z_{\max}$  is found at which a source with luminosity  $L_{\text{IR}}$  would still be detectable based on the flux density limits of the survey. Then the comoving maximum volume corresponding to this redshift is calculated as

$$V_{\max} = \frac{4\pi}{3} \left( \frac{D_L(z_{\max})}{1+z_{\max}} \right)^3, \quad (1.13)$$

where the term  $D_L/(1+z)$  is called ‘‘comoving distance’’ (see e.g. Hogg, 1999). After we calculate the maximum available volume for each of our sources, the number of galaxies in  $\Delta L$  luminosity intervals can be determined as

$$\phi(L) = \frac{1}{\Delta L} \sum_i \frac{1}{V_{\max,i}}, \quad (1.14)$$

where the sum includes all  $i$  sources with luminosities falling into the given  $\Delta L$  bin,  $L \leq L_i < L + \Delta L$ . The quantity  $\phi(L)$  can often be parametrized as a Schechter function:

$$\phi(L)dL = \phi_* \left( \frac{L}{L_*} \right)^\alpha \exp \left( -\frac{L}{L_*} \right) d \left( \frac{L}{L_*} \right), \quad (1.15)$$

where the parameters of the fit are the faint end slope  $\alpha$ , the characteristic density  $\phi_*$ , and the break luminosity  $L_*$ , above which the number of bright sources decreases exponentially. For an evolving population  $L_* = L_*(z)$  and  $\phi_* = \phi_*(z)$ , thus the shape of the luminosity function changes with redshift. To investigate this evolution in an observed population, the luminosity function is usually determined separately in several different redshift bins, and  $L_*$  and  $\phi_*$  are obtained from fitting the luminosity distribution in the given  $z$  range. Studies of the FIR luminosity function all show strong evolution of these parameters, which implies that the contribution of dusty galaxies to the total luminosity density increases towards higher redshift (e.g. Le Floc’h et al., 2005; Gruppioni et al., 2013; Magnelli et al., 2013; Burgarella et al., 2013).

If we assume that the stellar light is fully reprocessed by dust, we can infer the star formation rate from  $L_{\text{IR}}$ , as discussed in Kennicutt (1998):

$$\text{SFR}_{\text{IR}} = \kappa_{\text{IR}} \times L_{\text{IR}}, \quad (1.16)$$

where the conversion factor  $\kappa_{\text{IR}} = 1.72 \times 10^{-10} \text{M}_{\odot} \text{yr}^{-1} \text{L}_{\odot}^{-1}$  proposed by Kennicutt (1998) is widely used in the literature. Although the infrared luminosity only traces star formation obscured by dust, observations show that in most of the massive dusty star-forming galaxies the obscured star formation activity dominates over the unobscured contribution (e.g. Buat et al., 2010) and so  $L_{\text{IR}}$  is a good tracer for the total star formation activity in dusty galaxies. With this relation the luminosity functions can be used to determine the evolution of the dust-obscured star formation rate density. The infrared comoving luminosity density is determined as

$$\rho_{L,\text{IR}}(z) = \int_{L_{\text{lim}}}^{\infty} L \phi(L, z) dL, \quad (1.17)$$

where  $L_{\text{lim}}$  is the limiting luminosity of the survey at the given redshift. Using Equation 1.16 we can obtain the star formation rate density as

$$\rho_{\text{SFR,IR}}(z) = \kappa_{\text{IR}} \times \rho_{L,\text{IR}}(z). \quad (1.18)$$

Based on the analysis of a large range of available of multi-wavelength (both infrared and ultraviolet) datasets, Madau and Dickinson (2014) showed that the star formation activity in the Universe peaked  $\sim 3.5$  Gyr after the Big Bang, corresponding to a redshift of  $z \sim 1.9$ , and the star formation rates declined towards both earlier and later epochs (see top of Figure 1.2). UV studies of star formation are very sensitive to reddening effects caused by dust extinction in the interstellar medium. The bottom panel of Figure 1.2 shows the contribution from the UV data uncorrected for the dust attenuation and also from infrared surveys that trace the obscured star formation. The limitations in the correct determination of the cosmic star formation history are clearly visible. While the infrared luminosity densities provide a calorimetric measure of the obscured star formation rate density, the UV data need substantial correction, and the exact values of this correction are quite uncertain, even in the local Universe. The IR values give a less biased result, but so far the available redshift range is limited. Currently *Herschel* surveys provide the highest redshift results, as Gruppioni et al. (2013) used PACS and SPIRE data to determine the luminosity evolution up to  $z \lesssim 4$ . While several examples of  $z > 4$  dusty star-forming galaxies are known (e.g. Daddi et al., 2009; Coppin et al., 2009; Capak et al., 2011; Riechers et al., 2013), due to the lack of statistically significant higher redshift samples there are no current estimates of the luminosity function at  $z > 4$  and the contribution of dusty star-forming galaxies to the high- $z$  star formation rate density is still unknown. One of the main goals of this thesis is to assemble a catalog

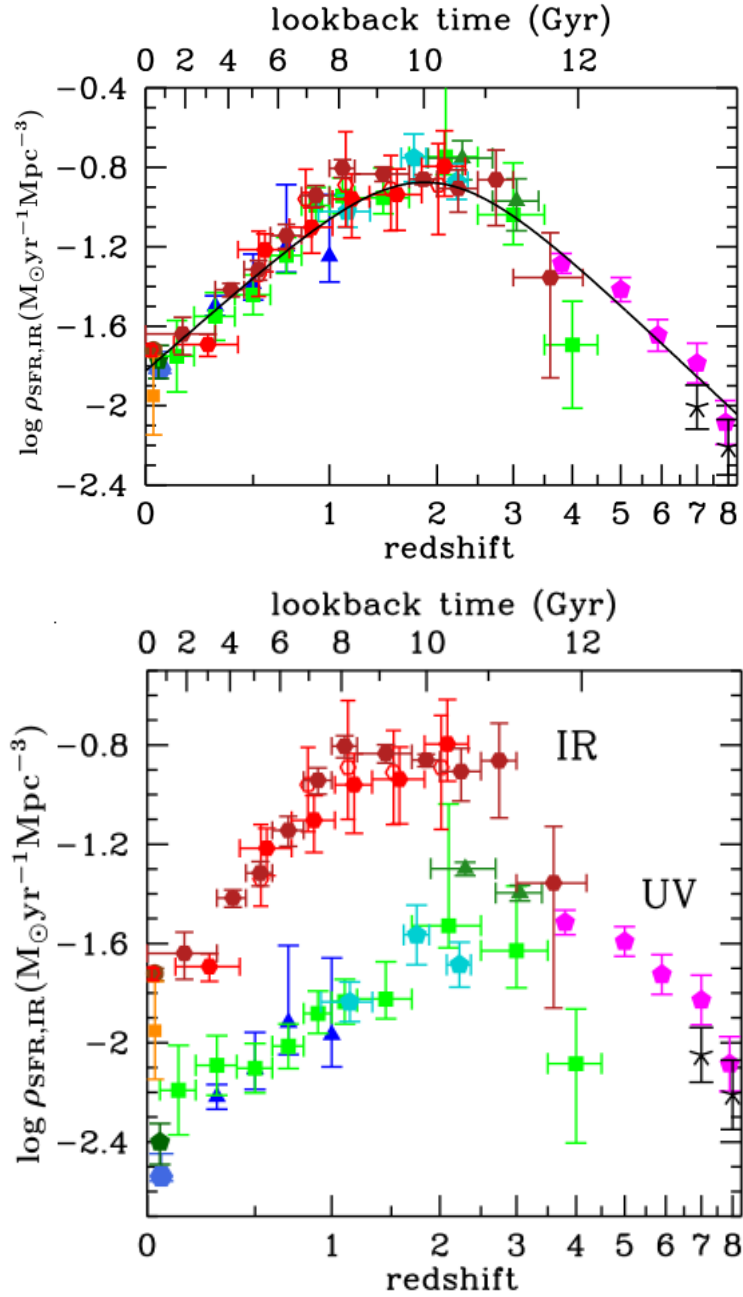


Figure 1.2: Star formation rate density of the Universe at different redshifts. The top figure shows the best fit to a range of datasets in the infrared, as well as ultraviolet data corrected for dust attenuation, while the lower figure shows the IR and the uncorrected UV values. Republished with permission of Annual Reviews, from Madau and Dickinson (2014); permission conveyed through Copyright Clearance Center, Inc.

of candidate  $z > 4$  galaxies detected in a large area survey observed by *Herschel*-SPIRE and to examine the number counts of these sources in order to infer their role in the stellar mass build-up in the early Universe.

## 1.6 Modelling the evolution of dusty star-forming galaxies

The steep slope of the observed far-infrared and submillimeter number counts and studies of the infrared luminosity function suggest that the properties of dusty star-forming galaxies are strongly evolving. There are many different ways to create models that describe this evolution, with the main constraint that they should be able to predict the observed number counts and redshift distribution of the dusty galaxy populations.

Backward evolution models are purely empirical. In these approaches the physical properties of individual sources are ignored, and instead the observed number counts are predicted by extrapolating locally observed correlations (e.g. luminosity functions or stellar mass functions) and spectral energy distributions, assuming an evolution in redshift (e.g. Valiante et al., 2009; Béthermin et al., 2011, 2012a). Forward semi-analytic models and hydrodynamical simulations are more physical. First the build-up of dark matter halos is reconstructed, then the physical processes are modelled that can drive the build-up of the baryonic component. These include feedback processes, star formation rates, gas cooling physics, chemical enrichment and dust radiative transfer models (e.g. Baugh et al., 2005; Davé et al., 2010; Hayward et al., 2013).

The widely accepted view is that dusty star-forming galaxies represent a relatively short phase in the evolution of local elliptical galaxies (Lilly et al., 1999; Swinbank et al., 2006). One of the popular theories of forming dusty starburst galaxies describes a merger driven picture, in which major mergers between gas rich galaxies trigger a short starburst period lasting  $\sim 100\text{--}200$  Myr (e.g. Smail et al., 2004; Greve et al., 2005; Tacconi et al., 2008), then gas depletion and feedback processes from the central AGN quench the star formation and an elliptical galaxy is formed with a passively evolving stellar population. Observations of individual submillimeter galaxies seem to support the merger-driven theory by showing disturbed morphologies (Conselice et al., 2003; Chapman et al., 2003; Kartaltepe et al., 2012); however other studies claim that there is no evidence that merging would be the dominant reason for the starburst activity (Swinbank et al., 2010a). Another possibility is that these galaxies are very massive, gas rich galaxies that simply contain more molecular gas than local galaxies, so they can form more stars even without

an increased star formation efficiency (Tacconi et al., 2010; Targett et al., 2013). Local star-forming galaxies show a tight correlation between their stellar mass and specific star formation rate (SFR per unit stellar mass). The majority of galaxies follow this star formation “main sequence” (Brinchmann et al., 2004; Noeske et al., 2007), while starbursts show an elevated specific star formation rate compared to similar mass main sequence galaxies. Some studies claim that the majority of the submillimeter bright galaxies might be massive star-forming galaxies on the main sequence instead of being starbursts (Rodighiero et al., 2011).

Since locally the most massive ellipticals can be found in the centres of large virialized clusters, it is reasonable to think that if dusty star-forming galaxies are indeed the progenitors of these ellipticals at high redshift, then they could reside in a proto-cluster environment consisting of galaxies falling into a cluster. Some massive galaxy clusters already contain an evolved sequence of quiescent galaxies at  $z > 1-2$  (Cimatti et al., 2004; Gobat et al., 2011) suggesting that they should have formed the bulk of their stars much earlier than the epoch when the cosmic star formation rates peaked. There are several examples in the literature of  $z > 3-5$  starburst galaxies that reside in proto-cluster environments (Chapman et al., 2001; Daddi et al., 2009; Capak et al., 2011), but as a counter example, the environment of the highest redshift dusty star-forming galaxy found to date (HFLS3; Riechers et al., 2013) does not show signs of an over-density of star-forming galaxies around it (Robson et al., 2014). In this thesis we will investigate the environments of several  $z > 4$  candidate galaxies. Finding an over-density of star-forming galaxies around these sources would strengthen the theory that distant starbursts can trace proto-clusters and indicate that the environmental effects of falling into the cluster can increase the star formation activity in galaxies. We will also investigate the dusty star-forming activity in moderate redshift massive virialized galaxy clusters. While these clusters mostly contain galaxies with passively evolving stellar populations, finding dusty star-forming galaxies in these clusters can provide additional constraints on evolution models.

## 1.7 Outline of this thesis

This thesis is organized as follows. In Chapter 2, we describe the process of making optimal large maps from *Herschel*-SPIRE data and we describe the two large area surveys used in this thesis. In Chapter 3, we describe a method to select  $z > 4$  galaxies based on their SPIRE colors, and we investigate the statistics of the catalog created. In Chapter 4, we describe a follow-up observing campaign of high- $z$  galaxy candidates using SCUBA-

2. In Chapter 5. we investigate the dusty star formation activity in the line of sight of moderate redshift galaxy clusters selected by the Atacama Cosmology Telescope. In Chapter 6. we discuss our main results and future directions and we conclude the thesis.

## Chapter 2

# Making large maps from *Herschel*-SPIRE data

With the advancement of techniques used to observe the far-infrared sky, the importance of designing large-area surveys will increase as well. The study of the cosmic infrared background, either through statistical analysis of the unresolved emission itself, or by the investigation of the properties of individual galaxies that constitute this background radiation, gives us a unique insight into the evolution of star formation and large-scale structure in the Universe. Mapping large areas on the sky helps us to create statistically significant samples of the resolved galaxy populations that contribute to the CIB and it increases our chances to find very rare objects that were not previously well studied. As we discussed in Section 1.4.1.2, we can also learn about the clustering properties and evolution of the different populations from cross-correlation studies of datasets at different wavelengths. A large area survey allows the reconstruction of the power spectrum down to very low angular frequencies. For these studies it is crucial to create maps from the raw detector data that contain an unbiased estimate of the brightness variations in the sky on all angular scales.

Far-infrared and submillimeter instruments generally contain incoherent detectors, that only measure the intensity of the incoming signal, and not the phase. In these detectors the power of the incoming radiation is converted into a change in voltage or current compared to the detector baselines. The detectors are also sensitive to variations in the conditions in the instrument; thus these baselines can change in time. Slow variations, like temperature drifts in the instrument, cause an  $1/f$ -type low frequency noise in the detector timestreams, but short noise spikes are also often present in the data. The main goal of map-making is to separate the observed sky signal from these components. The crucial step in recovering the large-scale variations in a field is the

correct handling of the  $1/f$ -type correlated noise in the observed data. To create maps that are optimal for point-source reconstruction, the easiest approach is to use a high-pass filter that removes frequencies below the noise knee-frequency where the correlated noise starts to dominate over the white noise level. However, this process removes any large-scale astronomical signal too, and it is not optimal to measure large-scale variations in the maps. The current far-infrared and submillimeter instruments often contain hundreds of individual detectors in their focal planes, and the observed data timestreams can contain significant correlated noise between different detectors, thus the map-makers need to be optimized to handle these noise components carefully.

The main goal of the map-making project described in this chapter is to create maps from observations of two wide area fields along the celestial equator carried out by the SPIRE instrument (Griffin et al., 2010) on the *Herschel Space Observatory* (Pilbratt et al., 2010). These two fields are the 280 deg<sup>2</sup> HeLMS field, which is part of the *Herschel* Multi-tiered Extragalactic Survey (HerMES, Oliver et al., 2012) and the adjacent 80 deg<sup>2</sup> field called the *Herschel* Stripe 82 Survey (HeRS, Viero et al., 2014). In this chapter we describe the *Herschel*-SPIRE instrument and the main data processing steps, then we discuss the SHIM and SANEPIC map-makers used in HerMES and HeRS to create maps. SANEPIC (Patanchon et al., 2008) was developed for the BLAST-telescope (Devlin et al., 2004), which was a technical and scientific prototype for SPIRE. This map-maker can handle correlated noise between detectors to better recover the large-scale sky signal. We discuss the adaptation of the SANEPIC map-maker to work with SPIRE data; we test the performance of recovering large structures by comparing the results to maps made with the SHIM map-maker; we investigate the noise properties of the final maps and discuss current and future science projects that are based on these datasets.

## 2.1 The *Herschel*-SPIRE instrument

The European Space Agency’s *Herschel Space Observatory* (Pilbratt et al., 2010) was operational between 2009 and 2013 and observed the sky at far-infrared/submillimeter wavelengths covering the peak of the thermal emission spectrum of cold dust. *Herschel* had a large aperture (3.5 m) mirror and a better sensitivity than the detectors operating at similar wavelengths before. The satellite had three instruments on board; HIFI (Heterodyne Instrument for the Far Infrared, de Graauw et al., 2010), PACS (Photodetector Array Camera and Spectrometer, Poglitsch et al., 2010) and SPIRE (Spectral and Photometric Imaging Receiver, Griffin et al., 2010), which contained a three-band imaging photometer and an imaging Fourier transform spectrometer.

The SPIRE photometer had a field of view of  $4' \times 8'$  and was capable of imaging the sky simultaneously at  $250 \mu\text{m}$ ,  $350 \mu\text{m}$  and  $500 \mu\text{m}$  wavelengths with beam sizes that can be approximated by Gaussian profiles with a full-width half-maximum of  $18''$ ,  $25''$  and  $36''$ , respectively. These beam sizes result in a confusion limit of  $5.8 \text{ mJy beam}^{-1}$ ,  $6.3 \text{ mJy beam}^{-1}$  and  $6.8 \text{ mJy beam}^{-1}$  at  $250 \mu\text{m}$ ,  $350 \mu\text{m}$  and  $500 \mu\text{m}$ , respectively, as calculated by Nguyen et al. (2010). The instrument consisted of arrays of 139 ( $250 \mu\text{m}$ ), 88 ( $350 \mu\text{m}$ ) and 43 ( $500 \mu\text{m}$ ) hexagonally packed feedhorn-coupled spider-web Neutron Transmutation Doped (NTD) germanium bolometers (Turner et al. 2001; Rownd et al. 2003).

Bolometers are common types of thermal detectors used in infrared astronomy. In SPIRE, the light is absorbed by a spider-web shaped mesh made of silicon nitride coated with a thin resistive metal layer, and the generated heat is conducted to the thermistor made of NTD germanium. As the absorbed power increases, the resistance of an NTD bolometer will decrease. Each bolometer has a biasing AC-current passing through it and the voltage on the bolometers is measured. The voltage change due to the change in resistance after photon absorption is registered by the readout electronics.

The SPIRE bolometers have a very low operating temperature of  $0.3 \text{ K}$ . To achieve this the arrays need to be cooled to reduce thermal fluctuation from the  $\sim 85 \text{ K}$  telescope mirror and the instrument electronics. The bolometer arrays are connected to a  $^3\text{He}$  cooler bath (Duband, 1997) in order to keep their temperature in the operating regime. At the beginning of the cooler-cycle all of the  $^3\text{He}$  is in liquid form. As the Helium starts to evaporate, a  $2 \text{ K}$  temperature cyro-pump reduces the vapour pressure and cools the liquid. The slowly evaporating gas keeps the temperature at  $\sim 300 \text{ mK}$ . When all of the Helium has evaporated, the refrigerator is recycled by recondensing the Helium into liquid form again. For this the pump first needs to be heated up to  $40 \text{ K}$  to release the absorbed gas, then the pump is cooled down to  $2 \text{ K}$  again and a new cooling cycle starts. The stable temperature phase usually lasts for more than 46 hours, and the recycling process lasts for 2 hours.

Fluctuations in temperature inside the instrument can change the resistivity of the bolometers; thus they can imitate the effect of absorbed emission from the sky. Variations in the cooler bath temperature will affect all bolometers in a similar way, creating a varying baseline for the detectors. The detector arrays can also be hit by charged high-energy particles. The detected power from these cosmic rays also has a similar effect on the measured voltage as absorbed photons. It is therefore crucial to understand these instrumental and external effects and to correctly disentangle them from the sky signal.

## 2.2 Initial data processing

The main operating mode of the telescope is scan-mapping. During this operation the field of view of the detectors is scanned back and forth across the sky with a speed of  $30 \text{ arcsec s}^{-1}$  (nominal mode) or  $60 \text{ arcsec s}^{-1}$  (fast-scan mode). During this process a large amount of data is recorded for each bolometer as a function of time, including the measured voltage, the pointing information, information about the telescope movements and the instrument conditions. The bolometers are sampled with a frequency of 18.6 Hz, corresponding to a 0.05 s sampling time-interval. These time-ordered data (TOD) are uncalibrated and uncorrected. Before any map-making step we need to correct the TODs for instrumental effects and convert the signal from Volts into flux density units in  $\text{Jy beam}^{-1}$  ( $1 \text{ Jy} = 10^{-26} \text{ W m}^{-2} \text{ Hz}^{-1}$ ). These initial processing steps are carried out using the *Herschel* Interactive Processing Environment (HIPE, Ott 2010) software package. The details of the pre-processing are described in Griffin (2009).

### 2.2.1 Deglitching

As a first step, glitches in the timestream caused by cosmic rays hitting the detector arrays need to be detected and removed. These cosmic rays can hit a bolometer directly, causing a large glitch in the timeline of that single detector, or they can hit the bolometer array frame and cause a change in the signal of multiple detectors simultaneously.

The pipeline first applies a concurrent deglitcher module, which finds and flags the simultaneously appearing cosmic ray hits. First the timestream for bolometer  $j$ ,  $d_j(t)$  is smoothed with a boxcar filter of width 15, then this smoothed timeline  $d_{j,\text{sm}}(t)$  is subtracted from the original timeline to find the residuals

$$r_j(t) = d_j(t) - d_{j,\text{sm}}(t). \quad (2.1)$$

This is repeated for all bolometers in the array, and the median of all bolometer values at each time index  $t$  is calculated as

$$m(t) = \text{median}_j\{r_j(t)\}. \quad (2.2)$$

The median absolute deviation from this value is determined as

$$\text{mad}(t) = \text{median}_j\{r_j(t) - m(t)\}. \quad (2.3)$$

Now calculating the median in time we get an average number for the whole array as

$$m_{\text{mad}} = \text{median}_t\{\text{mad}(t)\}. \quad (2.4)$$

Finally the algorithm flags time samples with

$$m(t) > \kappa m_{\text{mad}} \quad (2.5)$$

where  $\kappa$  is typically set to 4 during SPIRE map-making. To ensure that the tail of the glitch is removed too, the algorithm also flags an extra sample at the end of blocks of consecutive flagged samples.

The next step after concurrent deglitching is to identify and flag the individual cosmic ray hits that only affect a single detector. Two different methods are implemented in the reduction pipeline, a “sigma-kappa” deglitcher and a “wavelet” deglitcher. The sigma-kappa deglitcher works similarly to the concurrent deglitcher, except here we do not combine the residuals of different detectors, but calculate a standard deviation value for each TOD separately. The glitch detection is iterative, such that the glitches are flagged and excluded when recalculating the standard deviation. The process is repeated until no new glitches are flagged in the timeline.

A more complex deglitching method can also be used to detect glitches in the timestreams using wavelet-based local regularity analysis. This assumes that these features have a shape similar to a Dirac-delta function, but the algorithm is also able to handle clipped glitches that have different shapes. The method, based on a continuous wavelet transform with a Mexican-hat wavelet is described in detail in Ordenovic et al. (2005, 2008).

## 2.2.2 Electrical filter response correction

During the readout process, AC bolometer signals are lock-in amplified at the bias frequency, a process that consists of a band-pass filter, a switch and a low-pass filter applied to the switched signal. The low-pass filter imposes a time delay on the detector signals, and thus a delay between the detector signals and the signals recording telescope pointing information. This delay can be as long as 74 ms, which causes a 2.2'' difference in position for nominal scan mode and 4.4'' shift in fast scan mode. A low-pass filter response correction is needed to correct for this effect. The correction happens in Fourier space by multiplying the timeline with a complex function whose parameters are stored in a calibration file and are based on the low-pass filter transfer function.

Usually a similar correction is applied to adjust for the time response of individual

bolometers. This delay is also determined from the calibration file but this correction step is usually carried out after the data have been converted from voltage values to flux densities.

### 2.2.3 Flux Calibration

Before map-making the detector timelines need to be converted from units of voltage to in-beam flux density. The detailed flux calibration for SPIRE is described in Bendo et al. (2013) and Griffin et al. (2013).

The spectral in-beam flux density of a source with surface brightness  $I_\nu(\theta, \phi)$  is

$$S(\nu) = \int_0^{2\pi} d\phi \int_0^\pi B(\theta, \phi) I_\nu(\theta, \phi) \sin \theta d\theta, \quad (2.6)$$

where  $B(\theta, \phi)$  is the normalized beam profile. As noted in Bendo et al. (2013) and Griffin et al. (2013) the bolometers measure the spectral response function (SRF) weighted flux density, which is proportional to the power that the bolometers absorbed. If  $F(\nu)$  is the spectral response function of the detector and  $\eta(\nu)$  is the aperture efficiency then this weighted flux density can be calculated as

$$\bar{S}_{\text{meas}} = \frac{\int_\nu S(\nu) F(\nu) \eta(\nu) d\nu}{\int_\nu F(\nu) \eta(\nu) d\nu}, \quad (2.7)$$

where we integrate over the passband frequencies. Bendo et al. (2013) find that the relation between small changes in  $\bar{S}_{\text{meas}}$  and the voltage change across the bolometer can be described by the function

$$\frac{d\bar{S}_{\text{meas}}}{dV} = f(V) = K_1 + \frac{K_2}{V - K_3}, \quad (2.8)$$

where  $K_1$ ,  $K_2$  and  $K_3$  are constants and are derived empirically based on internal calibration sources. The conversion from measured voltage to  $\bar{S}_{\text{meas}}$  happens by integrating this value between the operating voltage  $V_0$  of the bolometer and the measured  $V_m$  voltage after photon absorption from sources,

$$\bar{S}_{\text{meas}} = \int_{V_0}^{V_m} \left( K_1 + \frac{K_2}{V - K_3} \right) dV. \quad (2.9)$$

To convert the data units from the SRF-weighted flux density to monochromatic spectral flux density we usually assume that the source spectrum is a power law and can

be written as

$$S(\nu) = S(\nu_0) \left( \frac{\nu}{\nu_0} \right)^\alpha, \quad (2.10)$$

where  $\nu_0$  is the central frequency of the SPIRE bands corresponding to 250  $\mu\text{m}$ , 350  $\mu\text{m}$  and 500  $\mu\text{m}$  wavelengths. A power-law index of  $\alpha = -1$  is chosen in the SPIRE data reduction process in order to obtain a flat  $\nu S_\nu$  spectrum across the band. Combining Equations 2.10 and 2.7 we get

$$S(\nu) = \bar{S}_{meas} \left[ \frac{\nu_0^\alpha \int_\nu F(\nu) \eta(\nu) d\nu}{\int_\nu \nu^\alpha F(\nu) \eta(\nu) d\nu} \right] = K_4 \bar{S}_{meas}. \quad (2.11)$$

The main calibrator for SPIRE is the bright and almost point like source Neptune, with a well known spectral flux density and an absolute photometric uncertainty of  $\sim 4\%$  (Moreno, 1998; Bendo et al., 2013). The measured flux densities of Neptune are compared to the expected model values and the differences are corrected. These final pre-processed timelines will serve as the input for different map-making software packages.

## 2.3 Map-makers

Several map-making software packages are capable of working with time-ordered data pre-processed by the standard SPIRE pipeline. Some of these have been developed directly for SPIRE and others were adapted from different instruments. Early versions of the HIPE pipeline included the Naïve Mapper, which has been replaced by the Destriper. Other mappers include Scanamorphos, Unimap, HiRes and SUPREME. The description and a detailed comparison of the performance of these map-makers is presented in Xu et al. (2014).

Maps in the HerMES survey are usually created with the SPIRE-HerMES Iterative Mapper (SHIM, Levenson et al., 2010, Viero et al., 2013), which is part of the SMAP processing pipeline. For the largest maps in HerMES and also for the map observed in the HeRS survey we use SANEPIC (Signal And Noise Estimation Procedure Including Correlations, Patanchon et al., 2008), a maximum-likelihood map-maker that was originally developed for BLAST (Balloon-borne Large Aperture Submillimeter Telescope, Devlin et al., 2004), a telescope built effectively as a pathfinder for SPIRE. This map-maker uses the cross-correlation of noise between detector timestreams to remove correlated noise without removing the largest scale astronomical signal from the datasets. SANEPIC was developed at the University of British Columbia, and UBC also had a large involvement in the development of SHIM. In the following we focus on the SHIM and SANEPIC

map-makers, with emphasis on the optimization of SANEPIC to work with SPIRE data.

### 2.3.1 SANEPIC

SANEPIC (Signal And Noise Estimation Procedure Including Correlations, Patanchon et al., 2008) is a maximum likelihood map-maker developed for BLAST (Devlin et al., 2004), a balloon-borne experiment using similar detectors as the bolometers in SPIRE. SANEPIC can preserve large-scale signals in the sky by removing correlated noise from the timelines based on the cross-correlation of the timestreams of different detectors.

The timestream of a bolometer indexed by  $i$  can be modeled as

$$\vec{d}_i(t) = \sum_p \mathbf{A}_i(t, p) \vec{s}(p) + \vec{n}_i(t), \quad (2.12)$$

where  $t$  is the sample time,  $s$  is the signal in pixel  $p$  of the final map of the sky and  $A_i(t, p)$  is the pointing matrix, which gives the weight of the contribution of the signal in pixel  $p$  to the timestream of bolometer  $i$  at time  $t$ . If our map has  $n_p$  pixels and the TOD has  $n_s$  time-samples, then  $\mathbf{A}_i(t, p)$  is a matrix of size  $n_s \times n_p$ . The SPIRE beams are approximately symmetric, so we can treat  $\vec{s}$  as the beam-convolved sky, in which case the pointing matrix contains only zeros and ones and it simply tells us the pixel position where bolometer  $i$  points on the sky at time  $t$ .

If many closely-packed detectors observe the same area of the sky, then they can all feel similar biasing effects from their environment. The noise term  $n_i(t)$  can be modelled as the sum of an uncorrelated noise component  $\tilde{n}_i(t)$ , and a common-mode signal  $c(t)$ , which is the same for all detectors, apart from a detector-dependent multiplicative factor  $\alpha_i$ :

$$n_i(t) = \tilde{n}_i(t) + \alpha_i c(t). \quad (2.13)$$

If we assume that the noise is Gaussian and stationary, satisfying  $\langle n_i(t) \rangle = 0$ , then we can construct the time-domain noise covariance matrix for detectors  $i$  and  $j$  as

$$\mathbf{N}_{ij}(t, t') = \langle n_i(t) n_j(t') \rangle. \quad (2.14)$$

For timestreams containing  $n_s$  samples, this will be a matrix of size  $n_s \times n_s$  that will have non zero off-diagonal elements if there is correlated noise between detector  $i$  and  $j$ . We note that if we have multiple bolometers  $n_b$ , then in this notation  $\vec{d}$  and  $\vec{n}$  correspond to  $(n_s \cdot n_b)$  element column-vectors with all the detector timestreams stitched together, and the  $\mathbf{N}$  matrix of size  $(n_s \cdot n_b) \times (n_s \cdot n_b)$  is built up of  $n_s \times n_s$  sized blocks of  $\mathbf{N}_{ij}$ :

$$\vec{d} = \begin{pmatrix} \vec{d}_1(t) \\ \vec{d}_2(t) \\ \vdots \\ \vec{d}_{n_b}(t) \end{pmatrix}, \quad \vec{n} = \begin{pmatrix} \vec{n}_1(t) \\ \vec{n}_2(t) \\ \vdots \\ \vec{n}_{n_b}(t) \end{pmatrix}, \quad \mathbf{N} = \begin{pmatrix} \mathbf{N}_{11} & \mathbf{N}_{12} & \dots & \mathbf{N}_{1n_b} \\ \mathbf{N}_{21} & \mathbf{N}_{22} & \dots & \mathbf{N}_{2n_b} \\ \vdots & \vdots & \ddots & \vdots \\ \mathbf{N}_{n_b1} & \mathbf{N}_{n_b2} & \dots & \mathbf{N}_{n_bn_b} \end{pmatrix}. \quad (2.15)$$

The sky signal can be estimated from the detector TODs using maximum likelihood methods. The log-likelihood of the data is

$$\log L(\vec{d}|\vec{s}) = -\frac{1}{2}(\vec{d} - \mathbf{A}\vec{s})^T \mathbf{N}^{-1}(\vec{d} - \mathbf{A}\vec{s}). \quad (2.16)$$

and the maximum likelihood solution is given by

$$\vec{s} = (\mathbf{A}^T \mathbf{N}^{-1} \mathbf{A})^{-1} \mathbf{A}^T \mathbf{N}^{-1} \vec{d}. \quad (2.17)$$

The SPIRE instrument samples the sky at 18.6 Hz, which means that we have time samples 0.053 s apart, and many scans last for over 10 hours, creating TOD vectors that contain  $> 10^6$  elements. For datasets this large an explicit inversion of the time-domain covariance matrix  $\mathbf{N}$  would be too time-intensive. Instead SANEPIC assumes that the TODs have no gaps and are circulant, meaning that the observations end at the same place where they started. If this is true, then the covariance matrix is circulant too, and its values only depend on the time separation between samples as

$$\mathbf{N}(t, t') = f(|t - t'|). \quad (2.18)$$

The Fourier transform of a circulant matrix is diagonal and it can be constructed from the power spectrum of the timestreams. So if we know the power spectrum of the detector TODs then the inverse of the time-domain covariance matrix can be calculated as

$$\mathbf{N}^{-1} = \mathcal{F}^{-1}[\mathbf{P}(\omega)^{-1}], \quad (2.19)$$

where  $\mathcal{F}^{-1}$  represents an inverse Fourier-transform and  $\mathbf{P}(\omega)$  is a matrix constructed from the auto- and cross-power spectra of the TODs, containing information about the common-mode noise between bolometers in addition to the uncorrelated noise terms.  $\mathbf{P}(\omega)$  contains diagonal blocks of  $\mathbf{P}_{ij}$  sub-matrices that can be expressed as the bin-averaged power spectrum between bolometers. If we divide the frequency range into

$q$  bins with bin sizes  $dq$ , each bin containing  $n_q$  samples, then the bin-averaged power spectrum can be written as

$$\mathbf{P}_{ij}(\omega_q) = \frac{1}{n_q} \sum_{\omega_q-dq/2}^{\omega_q+dq/2} \tilde{d}_i^*(\omega) \tilde{d}_j(\omega), \quad (2.20)$$

where  $\tilde{d}_i(\omega)$  represents the Fourier-transformed TOD for bolometer  $i$ . We can also express the power spectrum in terms of the common-mode and uncorrelated noise components as

$$\mathbf{P}_{ij}(\omega) = \left[ \alpha_i \alpha_j \langle \tilde{c}^*(\omega) \tilde{c}(\omega) \rangle + \delta_{ij} \langle \tilde{n}_i^*(\omega) \tilde{n}_j(\omega) \rangle \right]. \quad (2.21)$$

In practice the latter equation is used in the SANEPIC algorithm and the parameters are determined by a blind component separation method similar to the one described in Delabrouille et al. (2003). The noise power spectra matrix of the timestreams is determined from the data during an iterative process. In the first iteration the algorithm assumes that the TODs contain only noise and a first realization of the sky map is created. In the subsequent iterations the current map needs to be reprojected into time-ordered data and subtracted from the data timestreams to remove the astronomical signal. An example comparison of an auto- and cross-power spectrum of a bolometer TOD is shown in Figure 2.1. It can be seen that the uncorrelated white noise at high frequencies dominantly comes from a single bolometer and the correlated noise that dominates at low frequencies is a component that both bolometers can see. The operation  $N^{-1}d$  corresponds to dividing the Fourier-transformed data with the noise power spectrum, and this step removes the large-scale correlated noise from the timestreams.

The inverse of the pixel-pixel noise covariance matrix,  $\mathbf{N}_{pp'}^{-1} = (\mathbf{A}^T \mathbf{N}^{-1} \mathbf{A})^{-1}$  is not calculated explicitly in the map-making process. Instead the map-maker uses an iterative algorithm based on the conjugate gradient method with preconditioner to find the maximum likelihood solution for the map. The method works by minimizing

$$\Psi = r^T \mathbf{N}_{pp'}^{-1} r, \quad (2.22)$$

where  $r$  is defined as

$$r = (A^T N^{-1} A \hat{s}_k - A^T N^{-1} d) = (A^T N^{-1} d_k - A^T N^{-1} d). \quad (2.23)$$

Here  $s_k$  is the map estimate at iteration  $k$  and  $d_k = A s_k$  is this map projected into a timestream.

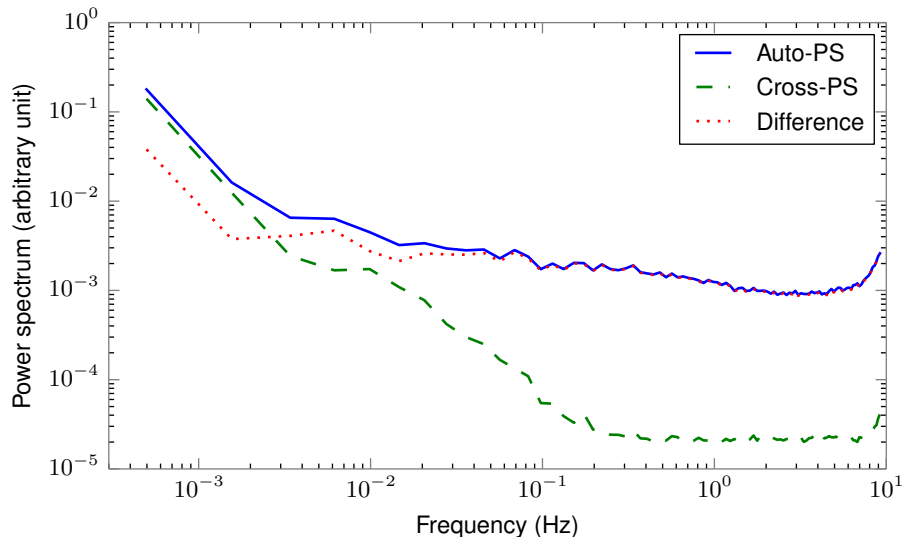


Figure 2.1: Diagonal values of two sub-matrices from the power spectrum matrix  $\mathbf{P}(\omega)$ . The solid line shows the diagonal values of an auto-power spectrum matrix  $\mathbf{P}_{ii}(\omega)$  calculated from the TOD of bolometer  $i$ , the dashed line shows the diagonal values of the cross-power spectrum matrix  $\mathbf{P}_{ij}(\omega)$  between two different bolometers  $i$  and  $j$  and the dotted line is the difference of the two plots. The correlated noise is seen by both bolometers and this information is used to de-weight the correlated noise in the timestreams.

Usually a few hundred iterations are needed to reach convergence. SANEPIC also creates an error map as an extension to the output products. This map gives an estimate of the variance of the noise in each pixel of the final map. Obtaining this error term correctly would require calculating the explicit pixel-pixel noise covariance matrix, but that operation is too computationally intensive and is never carried out during the iterative map-making. The error map SANEPIC creates is a first-order estimate of this noise, computed by neglecting the off-diagonal terms in the inverse pixel-pixel noise covariance matrix, assuming that the final map only contains white noise. We note, that this method can result in an over-estimation of the real residual noise values in the maps, but the error map can still be used to assign weights to each pixel in our final map.

### 2.3.2 SHIM

The SPIRE-HerMES Iterative Mapper (SHIM, Levenson et al., 2010, Viero et al., 2013) formalism is based on an iterative baseline removal algorithm. After a median subtraction the time-ordered data  $d(t)$  for a given detector in a given scan are passed to the map-maker where they are modelled as

$$\vec{d}(t) = g \sum_p \mathbf{A}(t, p) \vec{s}(p) + \vec{b}^m(t) + \vec{n}(t). \quad (2.24)$$

Like in Eq. 2.12,  $\sum_p \mathbf{A}(t, p) \vec{s}(p)$  represents the reprojected signal from the sky-map  $\vec{s}$  into a bolometer timestream, and  $\vec{n}(t)$  is the uncorrelated noise component. The baseline drift responsible for the low frequency  $1/f$  noise is modelled as an  $m$ th-order polynomial  $\vec{b}^m(t)$ , and  $g$  is the relative detector gain, which can be changed if we assume that the beam shapes of the individual bolometers are not exactly the same. As a first iteration the gain is set to unity and the timestream is simply rebinned into a map. In the following iteration steps the  $g$  value is first fixed to be the result from the previous iteration and the  $\vec{b}^m(t)$  polynomial is fit to the timestream residual  $R_k(t)$ , which is calculated at iteration  $k$  by subtracting the map calculated in the previous iteration from the timelines,

$$\vec{R}_k(t) = \vec{d}(t) - \left[ g_k \sum_p \mathbf{A}(t, p) \vec{s}_{k-1}(p) \right]. \quad (2.25)$$

After finding the optimal baseline, the  $g$  value can also be fitted to the data by minimizing  $R_k(t)$  while keeping the polynomial term fixed. The absolute detector gains for SPIRE have been determined from observations of calibration sources and these values are applied to the timestream during the HIPE pre-processing steps. In practice, the relative gain described here will not differ significantly from unity, and the  $g$  value is often kept constant during map-making. At the end of each iteration the inverse variance of the residual timestream is assigned as a weight to the bolometer TOD as

$$w_k = \left[ \frac{1}{N} \sum_t R_k(t)^2 \right]^{-1}. \quad (2.26)$$

This whole process is repeated for all detector timestreams in all of the individual scans of the observation and a new map is constructed by creating a weighted mean of all of the samples that fall into the same pixels,

$$s_k(p) = \frac{\sum_{\in p} w_k (d(t) - b_k^m) / g_k}{\sum_{\in p} w_k}, \quad (2.27)$$

where the sum runs over all samples in all bolometer timelines and all scans that map onto pixel  $p$ . The noise map is calculated from the weights as

$$\sigma_k(p) = \left[ \sum_{\epsilon p} w_k \right]^{-1/2}. \quad (2.28)$$

Unlike SANEPIC, SHIM deals with the low frequency noise component individually for each bolometer timestream, ignoring correlations between detectors. As a result, SHIM will not be as efficient in reconstructing the largest angular scales in a sky map as SANEPIC. We will compare the performance of SANEPIC and SHIM in Section 2.4.4.

## 2.4 Using SANEPIC with SPIRE data

The *Herschel* Multi-tiered Extragalactic Survey (HerMES, Oliver et al., 2012) is a “wedding cake” type survey containing small and deep maps and larger shallower observations of different fields. The area of these fields varies between  $0.005 \text{ deg}^2$  and  $19 \text{ deg}^2$ . In the HerMES project the native map-maker used to create the final data products is SHIM. SHIM maps are optimal for point-source detection and they also recover signals at larger angular scales than the size of the point-spread function, but the largest angular scales are filtered out in the map-making process. The recent addition of the  $280 \text{ deg}^2$  HeLMS field and the adjacent  $80 \text{ deg}^2$  HeRS field – which was observed in a close collaboration with HerMES – raised the need to improve the map-making process in order to fully exploit the large area of these maps by preserving the large scale sky signal as much as possible.

In the following we describe the HeLMS and HeRS surveys and the application of the SANEPIC map-maker to these two datasets. We compare the resulting maps to data products created with SHIM, investigate the noise properties and the transfer function, and discuss future uses of these large area maps.

### 2.4.1 The HeLMS and HerS surveys

The HerMES Large Mode Survey (HeLMS, Oliver et al., 2012) consists of a large area shallow observation of an equatorial field at wavelengths of 250, 350 and  $500 \mu\text{m}$ , obtained using SPIRE. HeLMS covers  $280 \text{ deg}^2$  of the sky, making it the largest area observed in the HerMES survey. The HeLMS field spans  $23^{\text{h}}14^{\text{m}} < \text{RA} < 1^{\text{h}}16^{\text{m}}$  and  $-9^\circ < \text{Dec} < +9^\circ$ , an equatorial region with low contamination from heated dust clouds in

the Milky Way (Galactic cirrus). It is designed to have a large overlap with the Sloan Digital Sky Survey’s Stripe 82 field, one of the most highly observed areas of the sky, with extensive multi-wavelength ancillary data coverage. The equatorial area has the advantage that it can be observed from almost any ground-based telescope site in the world. The HeLMS field was observed with the telescope operating in fast-scan mode ( $60 \text{ arcsec s}^{-1}$  scan-speed) and the observations were repeated in two nearly orthogonal scan-directions in order to obtain cross-linked data. The dataset consists of 11 individual scans, out of which six cover the full HeLMS area in one scan direction and five in the other. The coverage map is shown in Figure 2.2. Since the scans corresponding to the same scan-direction are designed to be adjacent to each other with minimal overlap, the coverage of the map is nearly uniform. Having only two scans at each part of the map gives shallower coverage than the deepest SPIRE maps. However, the noise is still only a few times higher than the confusion level, and the large area of the survey compensates for this loss in depth.

The *Herschel* Stripe 82 Survey (HerS, Viero et al., 2014) is a field adjacent to HeLMS and although this survey is not a part of HerMES, the two analysis teams work in a close collaboration with each other and have a substantial overlap in personnel. HerS covers  $79 \text{ deg}^2$  of the sky between  $0^{\text{h}}54^{\text{m}} < \text{RA} < 2^{\text{h}}24^{\text{m}}$  and  $-2^\circ < \text{Dec} < +2^\circ$ . The span in declination is smaller than that of the HeLMS field, but together HeLMS and HerS cover the whole Stripe 82 region in RA. The observing strategy for HerS was similar to that of HeLMS. This observation is made up of 21 individual scan-lines, but unlike in HeLMS, here the adjacent scans have some overlap with each other, creating areas in the map with deeper coverage. The HerS coverage map is shown in Figure 2.3.

Due to the equatorial position and the full overlap with the SDSS Stripe 82 field, the HeLMS and HerS surveys have a very rich ancillary data coverage. These datasets include the SDSS-III’s Baryon Oscillation Spectroscopic Survey (BOSS; Eisenstein et al., 2011), the Hobby-Eberly Telescope Dark Energy Experiment (HETDEX; Hill et al., 2008), the *Spitzer*-HETDEX Exploratory Large Area Survey (SHELA; Papovich et al., 2012), the *Spitzer*-IRAC Equatorial Survey (SpIES; Richards et al., 2012), the VLA-Stripe82 (Hodge et al., 2011), VISTA-VIKING (Emerson et al., 2004), and the Hyper Suprime-Cam (HSC; Miyazaki et al., 2012) surveys, among others. In addition, HeLMS and HerS overlap with a survey of the cosmic microwave background (CMB) conducted by the Atacama Cosmology Telescope (ACT; Swetz et al., 2011) in Stripe 82. There is a collaboration between HerMES, HerS and ACT to conduct studies that involve both the *Herschel* and ACT datasets. Part of this map-making project is to create data products that facilitate cross-correlation studies between the ACT and *Herschel* datasets.

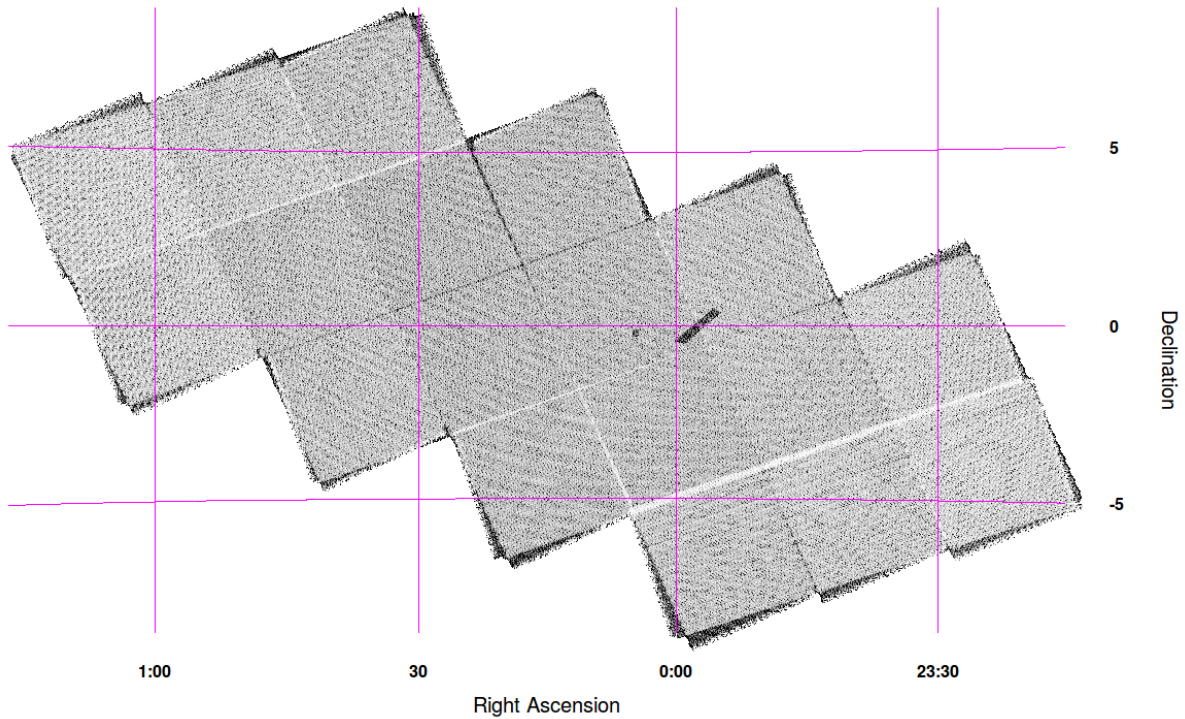


Figure 2.2: Coverage map of the HeLMS dataset. Dark areas have the lowest coverage, meaning that the number of detector time-samples projecting onto the map-pixel in question is low. The observation consists of 11 individual scans, five of which with similar scan directions span most of the RA range of the survey and the other six orthogonal scans span the total range in declination. The scans having similar detector orientation are adjacent to each other with minimal overlap, and the final map has a nearly uniform coverage.

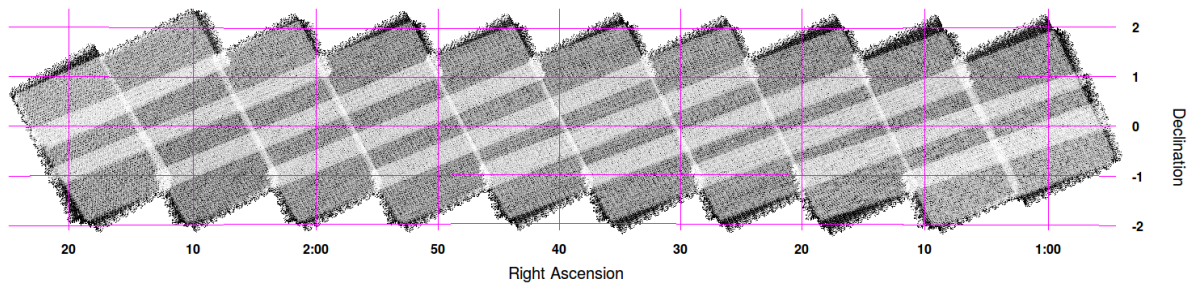


Figure 2.3: Coverage map of the HerS dataset. HerS consists of 21 individual scans, and while the adjacent observations spanning the declination range are designed to have minimal overlap, the scan-lines in the orthogonal scan direction overlap with each other to some extent, creating areas with better coverage than the rest of the map. Those areas that have been observed three times are clearly visible as light stripes in the coverage map. The pixel-noise in these areas is smaller than the noise in the rest of the map.

## 2.4.2 Additional timeline processing

The initial processing of the SPIRE time-ordered data segments is carried out in HIPE, as discussed in Section 2.2. Different map-makers might need to apply extra processing steps to these timelines, depending on the data properties and the assumptions made about the data by the mapping algorithm.

Before passing the data to either SHIM or SANEPIC, the TODs are read in by the SMAP pipeline. As discussed in 2.2.1, deglitching happens during the initial data pre-processing of the timelines in HIPE. In some cases, however, this first-level deglitching fails, and the anomalous signal propagates into the maps. The SHIM map-maker applies an iterative second-level glitch detection algorithm, using the fact that each pixel on the sky is sampled multiple times. Based on the large number of samples projecting onto the same sky pixels, the expected flux density in that pixel can be predicted and any samples that are more than  $10\sigma$  away from this value are flagged and not included in the map-making process. This deglitching information is saved and can be re-used later. We use this information created from initial SHIM-processing of the HeLMS and HerS data to remove residual glitches from the timestreams before passing the TODs to either SHIM or SANEPIC.

An astrometry correction step is also carried out in SMAP before map-making to test the reliability of the pointing information and to correct for any shifts in position. This is usually done by stacking initial maps for each observation on the positions of Spitzer-MIPS (Rieke et al., 2004)  $24\ \mu\text{m}$  sources. For the HeLMS and the HerS regions MIPS catalogs are not available and the correction is based on positions of sources in the WISE survey (Wright et al., 2010). Both of the MIPS and WISE catalogs have positional accuracies better than  $0.5''$ . After stacking the SPIRE maps on these positions the source profile is fitted to determine the measured position and the offsets (usually in the range of a few arcseconds) are applied as a correction in any later map-making process. After these processing steps the timelines are exported into FITS files that correspond to the SANEPIC input file format.

The largest component of the low frequency correlated noise between different detectors is the result of temperature fluctuations in the  $^3\text{He}$  cooler. As discussed in Section 2.1 all bolometers in the same focal-plane are cooled to the same temperature and the cooler is recycled periodically. Although the temperature is very stable for the most part of the cooler-cycle, slow temperature drifts will cause the signal of the bolometers to change over time. These changes are usually gradual and create a baseline well represented by a low-order polynomial.

Each detector array contains two thermistors that monitor the same temperature

changes that the bolometers experience. SMAP has a temperature-drift correction module nominally used before SHIM map-making, which removes the temperature-drifts from the detector timelines using the information from the thermistors. The thermistor timelines are smoothed to remove noise on small scales and these smoothed timelines are then fitted to the bolometer timelines and the fitted shape is subtracted. In this process the mean is also subtracted from each scan.

Before SANEPIC map-making the temperature-drift correction module in SMAP is turned off, since SANEPIC can handle the correlated noise in its own way. First a low-order polynomial is fit to each timeline and the result is subtracted. This step is needed because large gradients from variations on timescales longer than the timestream itself are not well represented by Fourier-modes and they can cause leakage during Fourier-transformation, which introduces striping and other artifacts in our maps. An example TOD before and after the baseline removal is shown on Figure 2.4.

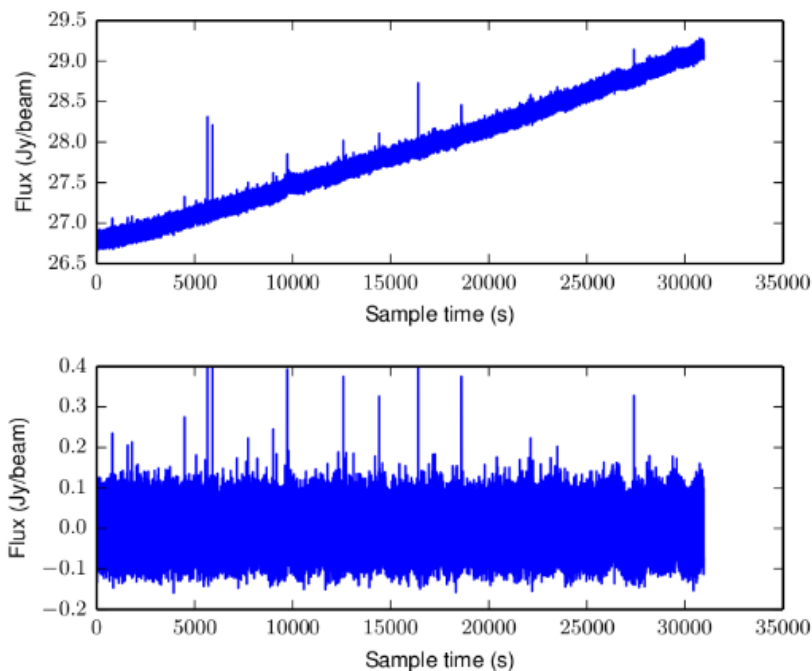


Figure 2.4: The effect of gradual temperature drifts in the cooler on the detector timelines. The changing temperature has a similar effect as absorbed power from photons, so the timestreams will have a non-zero baseline. This long variation needs to be subtracted from the timelines before map-making, since gradients can cause ringing during Fourier-transforms and the final maps would contain stripes. The bottom figure shows the same TOD after the baseline has been subtracted.

The order of the polynomial can be set manually and the shape of the timestreams needs to be investigated by eye before applying this setting. For the shorter HerS time-

lines this method works well, since the baseline is well fitted with a linear shape, but we have to be careful because some observations are carried out shortly after a cooler-recycle process when the temperature increases abnormally. The baseline caused by these “cooler-burps” cannot be fitted by a single polynomial. This effect is frequently seen in the very long ( $>11$  hours) HeLMS TODs. An example of a cooler-burp is shown on Figure 2.5. To remove this effect without using a harsh high-pass filter on the data we need to deal with the affected scans individually. These long timelines are broken up into parts where the TOD can be fit by a simple polynomial. Some of the largest scales might be removed due to the subtraction of the polynomials, but these scales can be recovered from the cross-scans during map-making.

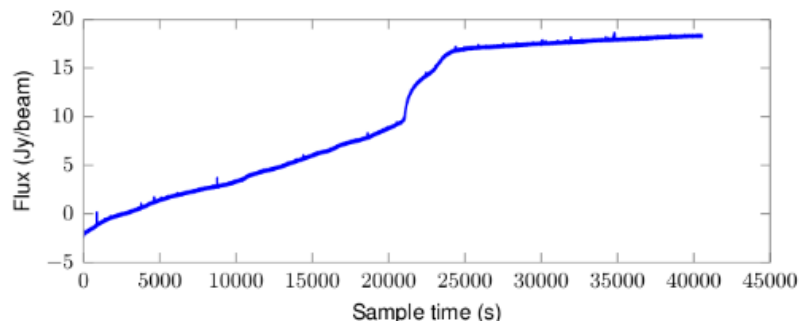


Figure 2.5: The effect of cooler-burps on the detector timestreams. During the recycling of the refrigerator the temperature changes abruptly and the detector baseline cannot be removed by a simple polynomial fit.

Since SANEPIC assumes that each data segment is circulant, and the start and end of the observation is strongly correlated, we apodize the data segments at the edges over 100 samples. The samples we remove this way are usually in a telescope turnaround region at the edges of the maps, where the coverage is sparse. These regions are usually masked out in any science analysis, so this process does not affect our data quality. After these processing steps the data segments are ready to be passed to the map-makers.

### 2.4.3 SANEPIC maps

Two sets of maps at 250, 350, and 500  $\mu\text{m}$  were made in order to accommodate different science goals. For the first set, we used a gnomonic or tangent-plane (TAN) projection with pixel sizes of 6'', 8.333'' and 12'' for the 250, 350, and 500  $\mu\text{m}$  maps, respectively. These values are typical for SPIRE maps, chosen to correspond to roughly one-third of the size of the SPIRE beams. Since the HeLMS and HerS fields overlap with the equatorial stripe observed by the Atacama Cosmology Telescope (ACT), we also made maps using

the nominal ACT map projection, to be used for cross-analysis of the two data sets. The motivation for matching pixels is that it avoids the reprojecting/regridding of maps that would be necessary to perform map-based operations, which could potentially introduce systematic uncertainties. These maps were made using a cylindrical equal-area (CEA) projection with pixel sizes of  $29.7''$  in all three bands, corresponding to the nominal ACT pixel size.

#### 2.4.4 Comparison of SANEPIC and SHIM maps

To test whether SANEPIC is indeed a better choice than SHIM to create maps from the largest observations, we compare two sets of maps made with each of these map-makers. We select a  $300 \times 300$  arcminute area from the HeLMS region, which is about the largest square area that can be selected. First we compute the 2-dimensional power spectrum, which is the square of the absolute value of the Fourier-transform of the maps, and contains information about the power in the maps at different angular frequencies. We show the 2D power spectrum of the  $350 \mu\text{m}$  SHIM and SANEPIC maps in Figure 2.6. If the original map has dimensions of  $n_{\text{pix}} \times n_{\text{pix}}$  with each pixel having a size of  $\theta_{\text{pix}}$  arcminutes, and the full size of the map in arcminutes is  $\theta_{\text{map}} \times \theta_{\text{map}}$ , where  $\theta_{\text{map}} = n_{\text{pix}} \times \theta_{\text{pix}}$ , then the dimension of the 2D power spectrum image is still  $n_{\text{pix}} \times n_{\text{pix}}$ , but the reciprocal-space pixel sizes are  $dk = 1/\theta_{\text{map}}$ , and the axes run from  $(-n_{\text{pix}}/2) \times dk$  to  $(n_{\text{pix}}/2) \times dk$ . The nearly isotropic power in the middle of both power spectra represents the largest scale signal in the maps. The main visible difference is extra power in the SHIM maps in symmetric patches at angular frequencies of  $k \sim 1.5$  and  $k \sim 3 \text{ arcmin}^{-1}$ , corresponding to an angular sizes of  $\sim 40''$  and  $\sim 20''$ , which is comparable to the beam size of  $25''$  at  $350 \mu\text{m}$ . The origin of this noise is as yet unknown, but these patches disappear in the SANEPIC maps.

We also calculate the azimuthally averaged power spectrum by averaging all modes in the 2D spectrum that are at a certain  $k$  radius away from the center. The results are plotted on Figure 2.7. Here it is clearly seen, that while both map-makers retain similar power at frequencies above  $k \sim 10^{-2} \text{ arcmin}^{-1}$ , the power at frequencies below this limit is attenuated in the SHIM maps. This corresponds to physical scales larger than  $\sim 100$  arcminutes. This filtering in SHIM probably comes from the mean-subtraction that is needed to apply the temperature drift correction. While both map-makers can produce similar quality data products for small-area observations, SANEPIC is clearly a better option to use when making very large maps.

The filtering effect of the SHIM map-maker is clearly visible for very large-scale bright

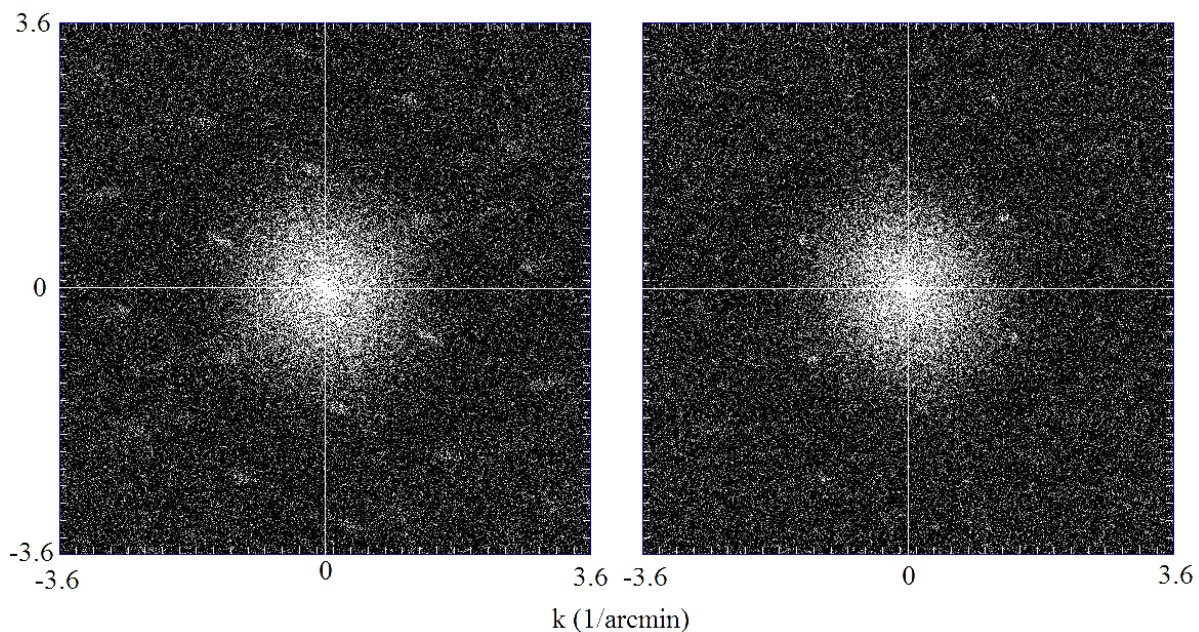


Figure 2.6: 2-dimensional power spectrum of a  $300 \times 300$  arcminute area selected from the HeLMS  $350 \mu\text{m}$  map. The left figure shows a power spectrum created from a map made with SHIM, and the right image shows the resulting power in the SANEPIC map.

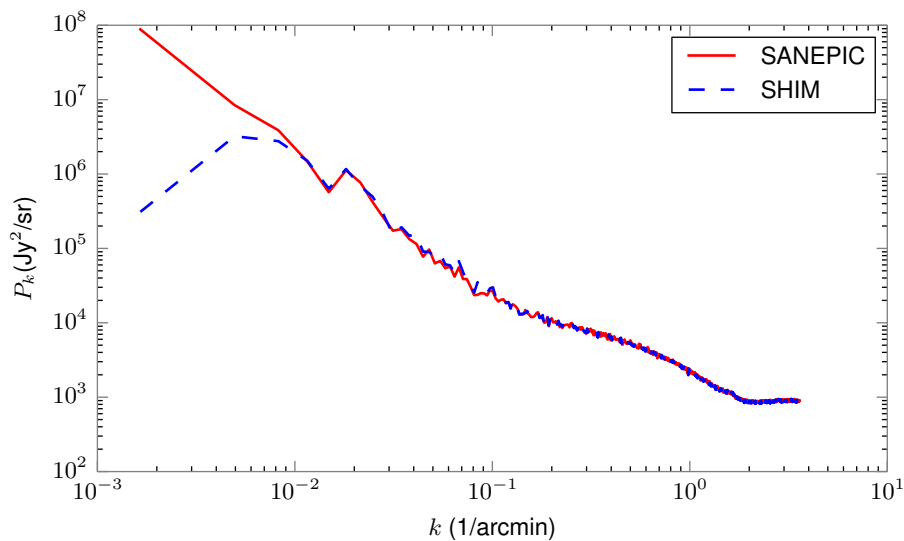


Figure 2.7: Azimuthally averaged power spectra for the HeLMS  $350 \mu\text{m}$  map created with SANEPIC and SHIM. SHIM attenuates angular frequencies below  $10^{-2} \text{ arcmin}^{-1}$ , corresponding to scales larger than 100 arcminutes on the sky, while SANEPIC is able to recover these larger scales.

Galactic cirrus structures in the maps. Figure 2.8 shows an area of the HerS map with a very bright patch of cirrus spanning more than  $150'$  on the sky. The dark patches around the bright structures in the SHIM map are the result of the filtering effect visible on the plot in Figure 2.7.

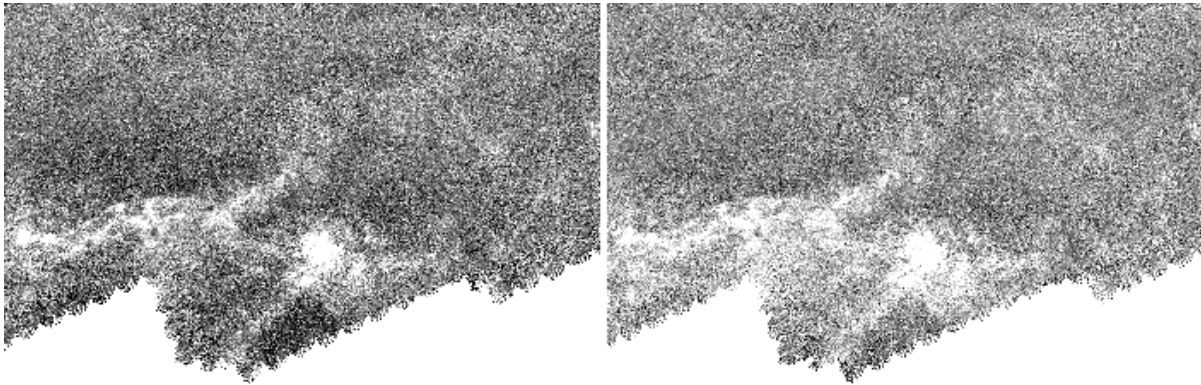


Figure 2.8: A strong Galactic cirrus patch spanning  $\sim 150$  arcminutes in HerS. The left image shows the SHIM reconstruction and the right image shows the SANEPIC maps. The dark patches around the bright regions in the SHIM map show the filtering effect for scales larger than 100 arcminutes. The large-scale structure is visibly better recovered with SANEPIC.

### 2.4.5 Noise properties

To examine the properties of the residual noise in our maps, we create so-called “jackknife” difference maps by splitting the timestream data into two halves and making a separate map for each half. The difference map is then made by multiplying one of the jackknives by minus one and then averaging the two maps. This process removes the astronomical signal but retains the noise, so the jackknife difference map contains the same instrumental noise properties as the co-added sky map.

There are in principle several different ways to split the data in half, some more effective than others, but the shallow depth of the HeLMS and HerS observations limit our options. If the map area is observed several times in the same manner, the data can be split by observation time. Since our fields are only scanned once in each orthogonal direction, this option is not available for these surveys. We could split the datasets based on the different scan directions, but we find that the resulting maps have very strong residual correlated noise along the scan directions due to the lack of cross-linking. A third way to split the data is to divide up the detector focal planes, and only use every second bolometer to make our maps. Even though this method gives the best coverage, at the

nominal pixel sizes, the resulting maps are still quite sparse, especially at  $500\ \mu\text{m}$  where the sampling density is the lowest. This problem is not present in the maps made in the ACT mapping configuration, since the pixel sizes are much larger and more time-samples are projected onto the same pixels.

In Figure 2.9 we plot the HerS pixel-histograms of the coadded (or sky) and differenced jackknife maps, showing both the standard (TAN) and ACT (CEA) projections. The coadded jackknife maps contain both instrumental and confusion noise (the latter illustrated as vertical dotted lines), and are thus wider than the differenced jackknife maps. While the instrumental noise is the dominant contribution in the TAN maps, the instrumental noise in the ACT-CEA maps is lower, due to their pixels being 24.5, 12.7, 6.1 times larger (by area) at 250, 350, and  $500\ \mu\text{m}$ , respectively, such that they have approximately equal contributions from instrument and confusion noise. We find that the noise is well described by a Gaussian distribution.

Having two independent maps from only half of the data also allows us to compare the pure signal and noise power spectrum of the maps. In Section 2.4.4 we investigated the auto-power spectrum of the map. If we instead compute the cross power-spectrum between the two half maps, then the uncorrelated noise is removed and the resulting power spectrum represents the astronomical signal that is visible in both of the half maps. In Figure 2.10 we show the auto-power spectrum of the total map and the jackknife noise map, and we also show the cross-power spectrum representing the sky-signal calculated from the two half-maps. We can see that the noise is not completely white; there is some excess correlated noise on larger scales in the maps but it is about 100 times smaller than the signal power at those scales. The signal spectrum reaches the white noise level on the high frequency side due to the smoothing effect of the pixelization of the maps.

## 2.4.6 Transfer function

To investigate how reliable SANEPIC is in reconstructing sky signal on different angular scales we determine the map-maker’s transfer function through simulations. This assessment is made by creating simulated pure-signal maps, which are then reprojected into detector TODs and fed back into our map-maker similarly to the real data timestreams. The transfer function is the ratio of the the azimuthally-averaged Fourier transforms of the reconstructed map and the pure-signal input map. In the ideal case the ratio should be unity at all spatial scales. If the map-maker introduces false signal into our maps, or removes existing power, then the transfer function deviates from unity at the corresponding angular scales.

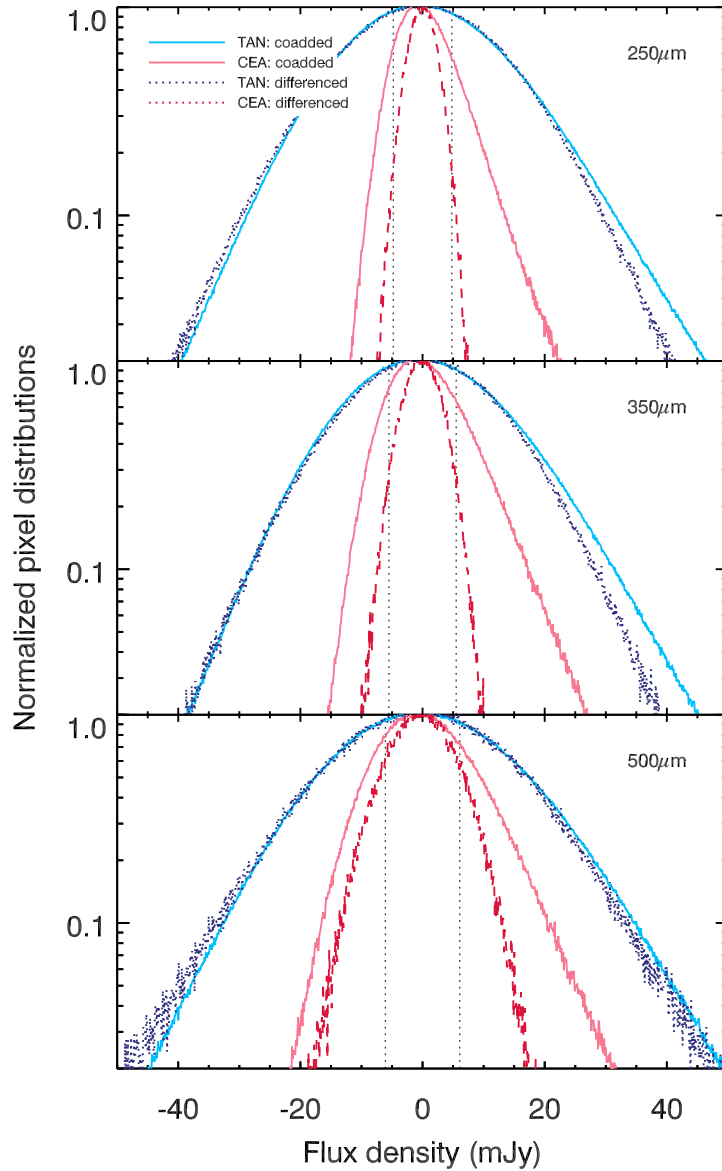


Figure 2.9: Pixel flux histogram of the HerS maps in both TAN and CEA projection, determined from jackknife tests. Solid lines show the sum of two jackknife maps made from each half of the data. This sum represents the total map, including sky signal and detector noise. Dotted lines represent the histogram of the maps made by taking the difference of the two jackknife maps. Taking the difference cancels out the sky contribution, so these maps can be used to investigate the properties of the residual noise. The noise can be well fitted by a Gaussian. The instrumental noise compared to the confusion noise is more dominant in the TAN projection maps, where the pixel sizes are smaller and thus contain fewer data samples per pixel. The excess tail in the coadded total maps arises due to the log-normal nature of the confusion noise distribution. From Viero et al. (2014)

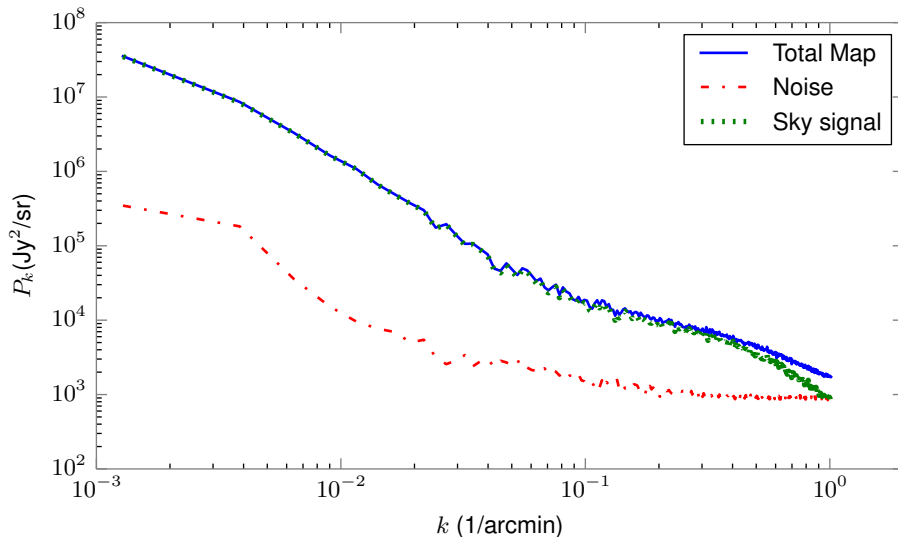


Figure 2.10: Azimuthally averaged auto-power spectra calculated from the difference of the jackknife maps showing the noise (dash-dotted red line), the full map that is a sum of both halves of the data (solid blue line), and a cross power spectrum of the two half jackknife maps (dotted green line), which shows the astronomical signal in the maps. The signal clearly dominates over the noise even on the largest scales where the noise is not completely white. The signal spectrum reaches the white noise level on the high frequency side due to the pixelization effects. This plot was made from the HerS CEA maps at  $350 \mu\text{m}$ .

We constructed 100 pure signal maps with a Monte Carlo simulation using a power-law power spectrum resembling that of the cosmic infrared background without the Galactic cirrus. Figure 2.11 shows the resulting transfer function for the HerS maps at  $500 \mu\text{m}$ . The simulated and reconstructed maps were made with the same pixel size, so the pixel window function does not have any effect here, and the transfer function remains unity on small scales. The transfer function only starts to drop at  $k \sim 0.01$  (or  $\ell \sim 200$  in the multipole notation usually used in power spectrum studies, where  $\ell \equiv 2\pi/\lambda[\text{rad}] = 21600 \times k_\theta[\text{arcmin}^{-1}]$ ) corresponding to a scale of 100 arcmin. In studies analyzing the power spectrum of the sky this function can be used to correct any deviations that are less than  $\sim 15\%$  from unity. Here this corresponds to  $k \sim 0.003$ , or scales smaller than 300 arcmin. For larger deviations the reconstruction of large scales is not reliable. The smallest extent of the HeRS survey is about this size, so most of the available scales are reconstructed by the map-maker.

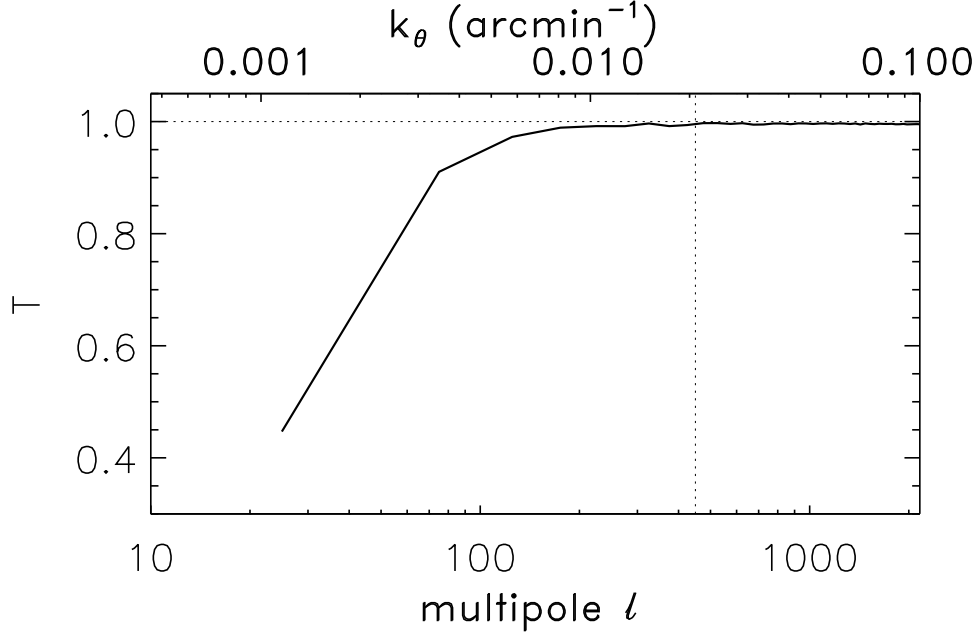


Figure 2.11: Transfer function,  $T$ , of the SANEPIC map-maker at  $500 \mu\text{m}$ , estimated with a Monte Carlo simulation as described in Section 2.4.6. The lower axis indicates the multipole scale usually used in CMB studies and is defined by  $\ell \equiv 2\pi/\lambda[\text{rad}] = 21600 \times k_\theta[\text{arcmin}^{-1}]$ .  $T$  is found to be approximately unity down to  $\ell \sim 200$  ( $\sim 100$  arcmin angular scales), dropping to 0.5 at  $\ell \sim 30$  ( $\sim 720$  arcmin). The vertical dashed line represents the largest accessible scale in the HeRS survey, showing that effectively all scales available in the HeRS map are reconstructed. From Viero et al. (2014)

### 2.4.7 Applications

We showed that while the SHIM and SANEPIC map-makers work similarly well on relatively small angular scales, SANEPIC clearly shows a better performance in reconstructing the largest structures in wide surveys. We constructed SANEPIC maps for the HeLMS and HerS surveys in both the nominal SPIRE projection and pixelization and also created maps that match the ACT equatorial maps in both projection and pixel size to help cross-correlation studies.

A very wide range of past, current and future projects are based on the analysis of the HeLMS and HerS maps. As an example, Gralla et al. (2014) investigate the thermal Sunyaev-Zel’dovich (SZ) effect (see Chapter 5) in 1.4 GHz selected radio AGNs by stacking their position on the ACT maps. They use the HeLMS and HerS maps in their analysis to show that there is no significant contamination from dusty galaxies in the SZ signal.

Wang et al. (2015) use the HeLMS and HerS maps to cross-correlate a sample of Type 1 quasars from the SDSS with the cosmic infrared background fluctuations. They detect

the submillimeter emission in the quasars and find that their star formation activity is stronger than the star formation in satellite galaxies in the outskirts of the halos that host these quasars.

An auto- and cross-frequency correlation analysis between the 250, 350 and  $500\mu\text{m}$  maps of HeLMS and HerS and also between these *Herschel* maps and the ACT 218 and 148 GHz maps is also underway. This study is similar to the analysis described in Hajian et al. (2012) and Viero et al. (2013), and the aim is to determine the correlation between the cosmic infrared background and the cosmic microwave background, and to detect the clustering signal of dusty star forming galaxies. These studies benefit the most from the better large-scale signal recovery properties of the SANEPIC map-maker, since this clustering signal extends to low spatial frequencies. The CIB can also act as a foreground for CMB measurements and these cross-correlation studies can also help in removing the bias from dusty galaxies on these very low SNR measurements.

Cross-correlations with other catalogs and maps will also be possible, including the BOSS QSO sample, optical SDSS cluster catalogs, the HETDEX LAE catalog, the Planck maps that have full sky coverage and also future instruments like ACTPol or ALMA.

In the following chapters of this thesis we will also describe two specific projects using the HeLMS and HerS observations. In Chapter 3 we describe a project to find a large sample of rare high-redshift dusty star forming galaxies in the HeLMS region, and in Chapter 5 we investigate the star formation activity in Sunyaev-Zel'dovich-selected galaxy clusters from the ACT equatorial maps that are found in the area overlapping with HeLMS and HerS.

# Chapter 3

## A search for high redshift dusty galaxies in the HerMES Large Mode Survey

As we discussed in Section 1.5, our knowledge about the evolution of the cosmic star formation rate density at  $z > 4$  is still uncertain due to the lack of statistically significant samples of high-redshift dust obscured star-forming galaxies, and the uncertainty of the extinction-correction of the available UV luminosity functions. At lower  $z$  the redshift distribution of the observed samples is usually determined by calculating photometric redshifts based on available multi-wavelength datasets. However, as of now only a small set of observed fields have sufficient ancillary data coverage, limiting the samples available with known redshift distribution. Additionally, dusty galaxies at  $z > 4$  are often undetectable at shorter wavelengths; thus the determination of the photometric redshifts becomes uncertain. To study the contribution of the high redshift dusty galaxies to the star formation rate density we need a way to select  $z > 4$  objects based on their properties in the available far-infrared/submillimeter datasets alone.

Dowell et al. (2014) constructed a catalog of potentially high- $z$  galaxies selected from 21 deg<sup>2</sup> of data from the *Herschel* Multi-tiered Extragalactic Survey (HerMES, Oliver et al., 2012) at wavelengths of 250, 350 and 500  $\mu\text{m}$ . They used a map-based search method to find sources with rising flux densities towards longer wavelengths ( $S_{500} > S_{350} > S_{250}$ ), since at  $z \gtrsim 4$  the redshifted spectrum of dusty galaxies is expected to peak at  $\lambda \gtrsim 500 \mu\text{m}$  (see Figure 1.1). Follow-up observations of a subsample of these sources showed that most of these galaxies are indeed at  $z > 4$ , and this analysis resulted in the detection of the  $z = 6.34$  source HFLS3 (Riechers et al., 2013), the highest redshift dusty starburst galaxy found to date, forming stars at a rate of several thousand solar masses

per year. Dowell et al. (2014) found an excess of these “500 micron riser” or “red” objects compared to available galaxy evolution model predictions, and if the current  $\sim 10$  red sources with spectroscopically confirmed high redshifts are representative of the whole population, then the number density of such galaxies poses a challenge to our current knowledge about galaxy evolution, indicating that dusty star formation had a larger role in the early universe than we predicted before. However, the Dowell et al. (2014) sample is still relatively small and insufficient to investigate the shape of the number counts.

In this chapter we describe a continuation of the program started by Dowell et al. (2014). We use a similar map-based search technique to create a large sample of potentially high redshift galaxies by analyzing the 280 deg<sup>2</sup> HeLMS field (see Section 2.4.1). The instrumental noise in this map is higher than the noise in any of the previously studied HerMES fields, so we will not be sensitive to the faintest objects close to the confusion limit. However, since the observed area is much larger than before, we expect to find a statistically significant sample of brighter objects, including some very rare, strongly lensed galaxies with flux densities above  $S_{500} = 100$  mJy as described by Negrello et al. (2010), Paciga et al. (2009) and others. With a sufficiently large catalog the differential number counts of high redshift galaxies can be investigated, and as we discussed before, the shape of the counts could hint to the evolution of the observed population. In the following we will describe the catalog creation, the observed number counts and simulations used to infer the corrected counts. We then discuss spectral energy distribution fits and follow-up observations.

### 3.1 Catalog creation

We use a technique similar to the map-based search method described in Dowell et al. (2014) to find red sources in the HeLMS field. This area of the sky lacks *Spitzer*-MIPS 24  $\mu$ m data that are often used in *Herschel* observations as a prior to deblend sources (see e.g. Roseboom et al., 2010). Note however, that these catalogs would not be very useful anyway to find high-redshift sources, since  $z > 4$  sources are often too faint at 24  $\mu$ m to be detected in these wide area surveys. Catalogs of *Herschel*-SPIRE objects are also often constructed by using the sources found in the higher resolution 250  $\mu$ m or 350  $\mu$ m maps as priors, but these datasets would not be optimal for finding our typical red sources, since we expect these 500  $\mu$ m-riser galaxies to have low signal-to-noise ratio in the 250  $\mu$ m or 350  $\mu$ m maps, and hence many of them would probably be undetected in such a catalog. As in Dowell et al. (2014), instead of matching sources found independently at each wavelength, we combine our observations at different wavelengths and use the

information in the maps directly. However, as a modification to the method we use a point source-matched filter instead of a Gaussian kernel to reduce the confusion noise in the smoothed maps.

### 3.1.1 Maps

We use the SHIM mapmaker described in Section 2.3.2 to create our maps. We note that SANEPIC maps were not yet available at the time when we carried out this analysis, however, as we showed before, SHIM has a performance similar to SANEPIC on small angular scales, so the SHIM maps are just as optimal for point source detection as the SANEPIC data products. The nominal pixel sizes at 250, 350 and 500  $\mu\text{m}$  are 6", 8.333" and 12", respectively, to match one third of the full-width half-maximum (FWHM) of the beam in each band (18", 25", 36"). Since we want to combine our observations, we create all three of our maps with matching pixel sizes of 6" instead. We also make sure that our maps are aligned, so that the same pixels correspond to the same coordinates.

We discard the edges of the map where the telescope turned around between scans and the data are not cross-linked. This area is too noisy and the coverage is too sparse to reliably estimate the fluxes of our objects. Similarly, we discard a smaller region in the middle of the map, where part of one of the overlapping scans had to be removed due to stray light in the telescope. The large-scale cirrus background is subtracted during the source-finding method, but there is a "seagull-shaped" area in the middle of the maps, where the cirrus is too strong to be easily removed and the flux estimations are biased high, so we mask this region manually (see Figure 3.1). The total remaining area that we use in our analysis is 273.9 deg<sup>2</sup>.

### 3.1.2 Matched filter

The convolution of a map with its point-spread function yields a map of the likelihood of point sources if the noise in the original map is uniform and uncorrelated and the signal consists of isolated sources (see e.g. Stetson, 1987). However, our maps already have significant confusion noise at their nominal resolution, and extra smoothing will further increase this highly correlated noise component. Although the  $1\sigma$  instrumental noise levels in the raw maps (12.8, 12.5 and 15.0 mJy at 250, 350 and 500  $\mu\text{m}$ , respectively) are larger than the nominal confusion levels in SPIRE (5.8, 6.3 and 6.8 mJy, Nguyen et al. 2010), after we smooth the maps to the same resolution the confusion noise in the smoothed maps will dominate over the instrumental noise. Dowell et al. (2014) smoothed the 500  $\mu\text{m}$  map using a Gaussian kernel with a full-width half-maximum of 35.3" (the

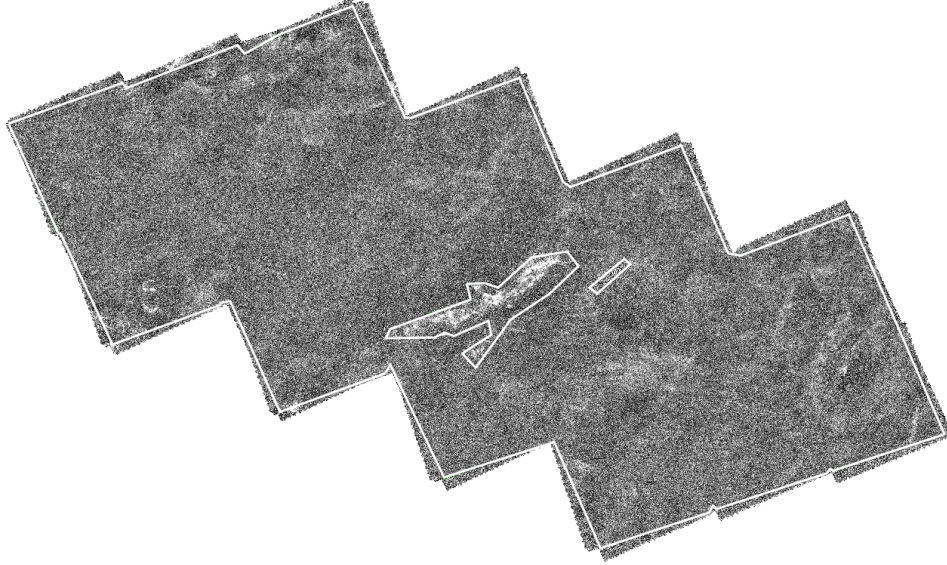


Figure 3.1: Grayscale image of the HeLMS 250  $\mu\text{m}$  map with solid lines showing the area we use in our analysis. We discard the edges of the maps, where the data lack overlapping scans, and we also discard a smaller region in the middle where part of the scan had to be removed and our coverage is sparse. We additionally mask out a “seagull-shaped” region of strong Galactic cirrus emission. The cirrus in this structure cannot be easily removed and biases our flux estimation of sources. The total area of the remaining dataset after applying the mask is 273.9  $\text{deg}^2$

beam size in this band). This resulted in a final resolution of 49.8" FWHM, and the 250 and 350  $\mu\text{m}$  maps were smoothed with a kernel so that their final resolution matched this value. We decided to apply a different filter to our maps, which reduces confusion and does not degrade our resolution as much as a Gaussian filter would.

We use an optimal filter that maximizes the signal-to-noise ratio in a map with non-negligible confusion noise. This filter is described in detail in Chapin et al. (2011). The signal-to-noise ratio in Fourier space after we cross-correlate our signal  $S$  with our filter  $F$  is

$$\text{SNR} = \frac{\sum_k \hat{F}_k^T \hat{S}_k}{\left(\sum_k |\hat{F}_k^T \hat{N}_k|^2\right)^{1/2}}. \quad (3.1)$$

Here  $N$  is the noise, the hats denote the discrete Fourier transforms of our variables, the T superscript refers to a transpose of our filter, and the index  $k$  corresponds to components

in the spatial frequency domain. We can derive the optimal filter by finding  $F$  for which

$$\frac{\partial(\text{SNR})}{\partial \hat{F}_j^T} = 0. \quad (3.2)$$

The resulting filter is

$$\hat{F}_j^T = \frac{\hat{S}_j}{|\hat{N}_j|^2} \left( \frac{\sum_k |\hat{F}_k^T \hat{N}_k|^2}{\sum_k \hat{F}_k^T \hat{S}_k} \right), \quad (3.3)$$

where  $N_j$  represents the total noise at each frequency component  $j$ . While the instrumental noise is white and its value is constant at all frequencies, the power spectrum of the confusion noise will have a shape similar to the point spread function, since confusion arises from point sources in the same beam. The shape of our matched filter can be seen in Figure 3.2, compared to the  $500 \mu\text{m}$  beam shape and the final source profile after applying the filter to our maps. Due to the smaller width of our filter, our final resolution will be closer to the original resolution of the  $500 \mu\text{m}$  map than in Dowell et al. (2014), and this can help reduce source blending effects for nearby objects (see an example in Figure 3.3).

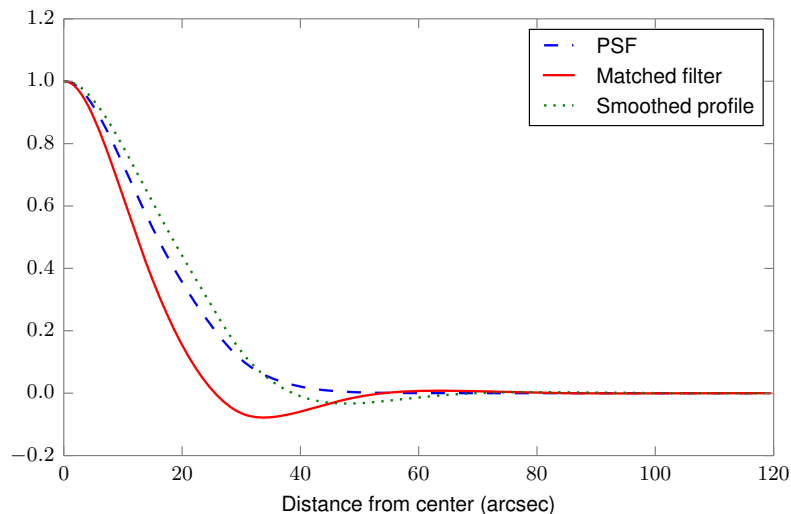


Figure 3.2: Shape of the matched filter at  $500 \mu\text{m}$ , compared to the Gaussian point spread function (PSF) and the final source profile in the smoothed maps. The filter used for smoothing our maps has a smaller full-width half-maximum than the beam, so the resolution of our maps after smoothing is close to the unsmoothed resolution.

After finding the optimal matched filter for the  $500 \mu\text{m}$  map, we need to construct the smoothing kernels  $K_{250,350}$  that create the same effective source shape at 250 and  $350 \mu\text{m}$

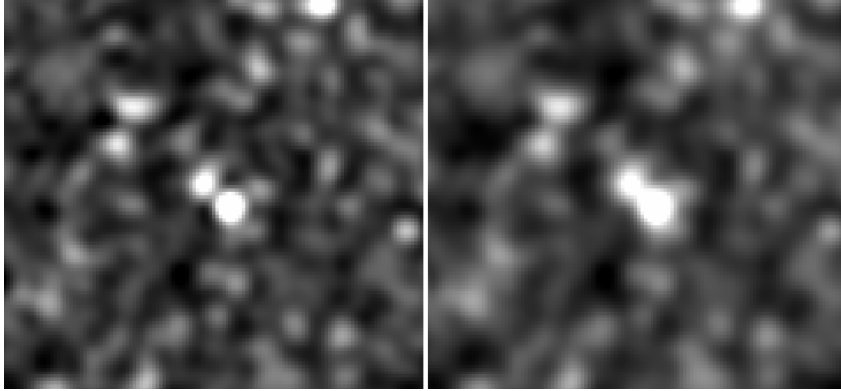


Figure 3.3: Comparison of the final resolution in our maps when using different smoothing kernels. On the left, we smoothed our map with the matched filter described in Sec. 3.1.2, while on the right we used a Gaussian filter. In addition to reducing the confusion noise from unresolved faint sources in our telescope beam, the matched filter also reduces blending effects between neighbouring bright sources.

that we measure in the smoothed  $500\ \mu\text{m}$  map. First we convolve the  $500\ \mu\text{m}$  beam (a Gaussian with  $35.3''$  FWHM) with the matched filter to find the final source shape in our smoothed maps. If  $P_{250,350}$  denote the nominal beam shapes at 250 and  $350\ \mu\text{m}$  and  $P_{\text{mf}500}$  is the matched-filtered source-shape at  $500\ \mu\text{m}$ , then we can find  $K_{250,350}$  from the convolution

$$P_{250,350} \otimes K_{250,350} = P_{\text{mf}500}. \quad (3.4)$$

Thus the smoothing kernels are determined by taking the inverse Fourier transformation of the Fourier-space ratio of the final and initial beam shapes.

Before filtering the maps, we subtract a local background to remove any large-scale fluctuation from Galactic cirrus (radiation from heated dust clouds in our Galaxy), which might otherwise affect our flux estimation. The background removal algorithm first breaks up the image into  $3' \times 3'$  blocks and calculates the median value in each block while iteratively removing sources by discarding pixels that are more than three standard deviation away from the median of the current image. Then, the image containing these  $3' \times 3'$  blocks with constant values is smoothed with a moving box with a size twice the subimage size. The resulting background map is subtracted from our original maps. We have tested that this method removes large scale cirrus fluctuations (see e.g Figure 3.4) but does not have a significant biasing effect on point source flux density estimation.

After background removal we filter our data with the matching kernels using inverse-variance weighting based on the error extension of our maps, which is an output of the mapmaker and gives us the noise values in each pixel. Since the mapmaking pipeline

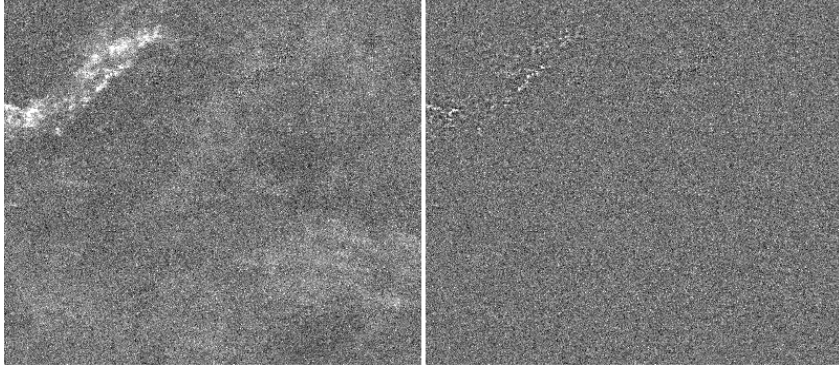


Figure 3.4: A patch of the HeLMS image containing extended cirrus emission, before (left) and after (right) background subtraction.

does not correct for the effects of pixelization, we create our filters on an oversampled grid, and then rebin them to our final pixel-size. We also apply our filters to our error maps to find the typical instrumental noise values in our pixels after smoothing. We test this filtering method by injecting fake sources with known flux density values into our raw maps, and find no significant bias in the recovered flux distribution after subtracting the background and applying our filter.

### 3.1.3 Difference map

Because the sources responsible for the confusion noise in the maps emit at all three SPIRE wavelengths, one can produce a difference map that has a substantially reduced confusion limit. It will be much more effective to search for bright  $500\ \mu\text{m}$  sources in such a difference map ( $D$ ) than in the raw  $500\ \mu\text{m}$  maps ( $M_{500}$ ). Dowell et al. (2014) have found that the difference

$$D = \sqrt{1 - k^2} M_{500} - k M_{250} \quad (3.5)$$

reduces confusion, while red sources remain bright in the  $D$  map. By carrying out extensive simulations using different coefficients, they demonstrated that the value  $k = 0.392$  works well empirically to maximize  $D/\sigma_{\text{conf}}$  in the maps. They also experimented with creating linear combinations using all three maps, but they have found that including a  $350\ \mu\text{m}$  term does not improve the efficiency of the source selection. We find that this same choice of coefficients also works well for our HeLMS maps.

Our final difference map is constructed as  $D = 0.920 M_{500} - 0.392 M_{250}$ . We also combine the error maps and measure the resulting instrumental noise levels. After measuring

the total variance of our map we calculate the confusion noise in our final map as

$$\sigma_{\text{conf}} = \sqrt{\sigma_{\text{total}}^2 - \sigma_{\text{instr}}^2}. \quad (3.6)$$

The noise levels in our smoothed maps and the difference map are listed in Table 3.1.

	$\sigma_{\text{tot}}$ (mJy)	$\sigma_{\text{inst}}$ (mJy)	$\sigma_{\text{conf}}$ (mJy)
250 $\mu\text{m}$	15.61	7.56	13.66
350 $\mu\text{m}$	12.88	6.33	11.21
500 $\mu\text{m}$	10.45	7.77	6.98
$D$	8.54	7.75	3.5

Table 3.1:  $1\sigma$  noise levels in our smoothed 250, 350 and 500  $\mu\text{m}$  maps and in the difference map.

### 3.1.4 Source extraction

To find red sources in our maps we first search for the brightest peaks in our difference map and then we select the 500  $\mu\text{m}$  riser objects from the resulting list. We apply a local-maxima search algorithm to our  $D$  map, which finds the positions of the pixels that have greater values than their eight adjacent pixels. We create a list of these peaks with a cutoff at  $4\sigma_{\text{total}}$  which corresponds to  $D = 34$  mJy in the difference map.

To select red sources from this list we simply require that  $S_{500} > S_{350} > S_{250}$ . However, to evaluate this we need to extract the actual flux densities from our single wavelength maps at these  $D$ -peak positions. It is not trivial to determine if it is optimal to use our smoothed maps to measure these values or to go back to the nominal resolution maps and find the sources there. Due to a typical positional uncertainty of  $\sim 6''$  between bands, extracting the fluxes at the precise  $D$  position biases our flux estimation at 250 and 350  $\mu\text{m}$ . To address this we could re-fit our peaks in each of the smoothed maps to find the actual peak position in each band and extract the fluxes there. However, a typical red source has an  $S_{500}/S_{350}$  flux density ratio that is close to 1, and hence adjacent sources often boost our 350  $\mu\text{m}$  flux density above  $S_{500}$ , even if in the nominal maps we clearly detect our source as a red source. This is an important issue at the bright end, where the source counts decrease rapidly, and even in our very large area field we expect only to find a handful of such objects.

After careful consideration, we decided that for this last step it is better to measure the fluxes from the less confused nominal resolution maps, but instead of doing photometry at the measured  $D$ -position, we find the best-fit source after taking into account our positional uncertainty. To achieve this we move around our  $D$ -peak position in sub-pixel steps, allowing the search radius to change corresponding to our typical uncertainty, and we calculate the Pearson correlation coefficient  $r$  between our data  $d$  and the beam shape  $P$  at each position by

$$r = \frac{\sum_{i=1}^{N_{\text{pixels}}} (d_i - \bar{d})(P_i - \bar{P})}{\left[ \sum_{i=1}^{N_{\text{pixels}}} (d_i - \bar{d})^2 \right]^{1/2} \left[ \sum_{i=1}^{N_{\text{pixels}}} (P_i - \bar{P})^2 \right]^{1/2}}. \quad (3.7)$$

We pick the position where the correlation is the largest, and we extract the flux density at this position using inverse variance weighting:

$$S = \frac{\sum_{i=1}^{N_{\text{pixels}}} d_i P_i / \sigma_i^2}{\sum_{i=1}^{N_{\text{pixels}}} P_i^2 / \sigma_i^2}. \quad (3.8)$$

We test the validity of this method by injecting artificial sources on a grid with known flux densities in the raw maps, and we run our source extraction pipeline on these maps. We inject 66 874 objects into the map, using the same mask as we used for source finding. These artificial sources are spaced 37.586 pixel away from each other, corresponding to 225.516'' angular separation. This spacing is deliberately not an exact multiple of the 6'' pixel size, so the source centres will not always coincide with the pixel centres, similarly to our real sources. We generate an oversampled Gaussian point spread function accounting for the corresponding sub-pixel shifts, then we re-bin this PSF to have 6'' pixels. This way we can generate sources with their peaks not always located the centre of the pixel. Then we run our detection pipeline and we compare the injected and measured flux densities. In Figure 3.5 we show an example of the distribution of measured flux densities after we inject sources into our three maps with flux densities  $S_{500} = 80$  mJy,  $S_{350} = 70$  mJy and  $S_{250} = 50$  mJy. Since we smooth our maps to match the resolution at 500  $\mu\text{m}$ , in this band all three methods give similar results. In the other two bands, however, fixing the peak position to the  $D$ -peak clearly under predicts the real flux densities. Finding the peaks in

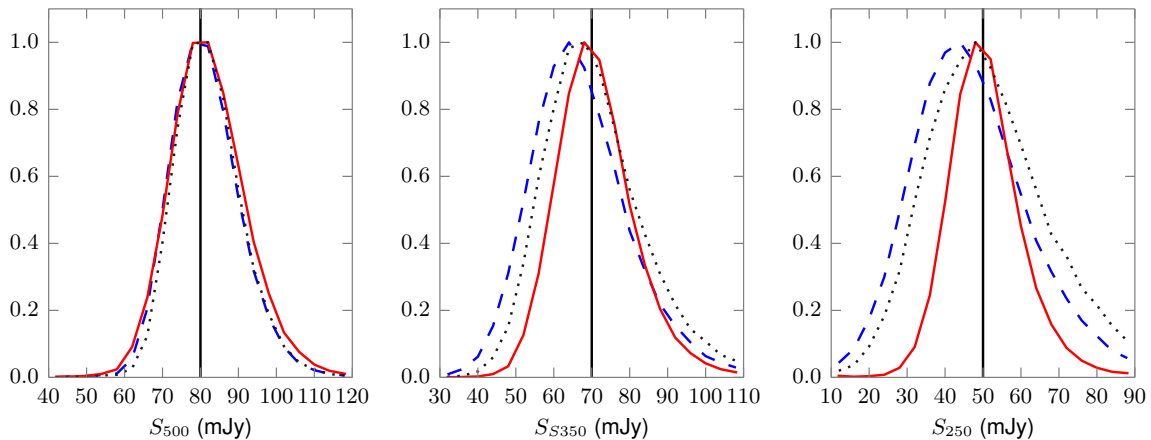


Figure 3.5: Histogram of the measured flux densities for injected sources with  $S_{500} = 80$  mJy,  $S_{350} = 70$  mJy,  $S_{250} = 50$  mJy. The blue dashed line shows the distribution of flux densities measured in the smoothed maps at the fixed  $D$ -peak position, the dotted black line is the distribution of flux densities measured in the smoothed maps after re-fitting the peak positions in each band, and the red solid line represents the recovered flux densities in the nominal resolution maps using the positions in each band where the correlation with the PSF is the largest.

each band and measuring the smoothed map flux densities at these peak positions does a better job in recovering the actual flux densities, but a small bias still exists, and due to the larger confusion noise in the smoothed maps, the recovered distribution is wider than what we measure in the nominal resolution maps, reducing the efficiency of finding sources that have flux densities close to our selection limits. Measuring the flux densities from the nominal resolution maps is clearly the best choice, and we conclude that the method described above reduces the bias due to positional uncertainties.

### 3.1.5 Final catalog

Before finalizing our high- $z$  catalog we need to address the radio source contamination of our sample. Flat spectrum radio quasars can have colors similar to those of our high-redshift dusty galaxy candidates, but these objects can be easily identified from available radio surveys. We compare our catalog to the 21 cm radio catalogs from the NRAO VLA Sky Survey (NVSS, Condon et al., 1998) and the FIRST survey (Becker et al., 1995) and we flag 17 of our sources that show up in these catalogs with a radio flux density brighter than 1 mJy. We do not use these sources in any further analysis.

Our catalogs could be contaminated by cosmic ray hits or other spikes in the detector

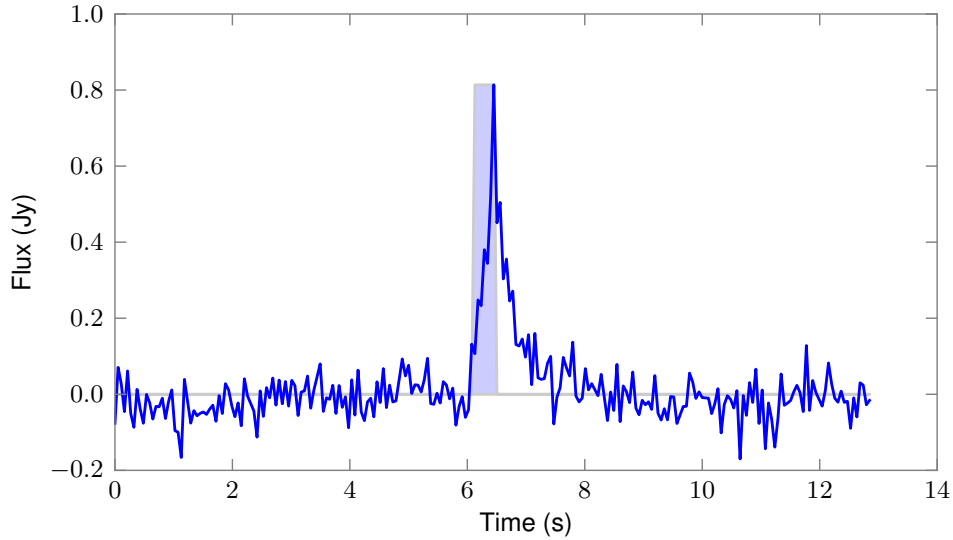


Figure 3.6: Example of incorrect glitch detection in the detector timestreams. The shaded area shows the part of the data that is masked out and not used in further processing. In this case, the large spike, usually caused by a cosmic ray hitting the detector array, is only partially masked out, and the long tail of the fluctuation is not removed.

timestreams that are not properly removed by the initial deglitching process described in Section 2.2.1. Figure 3.6 shows an example of a very large spike in the time-ordered data, where incorrectly only half of the feature is masked out during data pre-processing, and the long tail of the glitch is included in the further map-making steps. A spike left in the  $500\ \mu\text{m}$  array data would mimic a  $250$  and  $350\ \mu\text{m}$  dropout source. During the iterative mapmaking process for ordinary SPIRE data, isolated spikes are recognized as outliers among the samples associated with a given pixel, and are removed from the data as described in Section 2.4.2. However, the HeLMS maps are sparsely sampled and there may be too few samples near a given pixel for this recognition procedure to be reliable. The result is a “hot” pixel or a stripe of a few very bright pixels in the map from one array, while the neighbouring pixels show values consistent with the instrumental noise and no spike is present in the other arrays. After smoothing the map with our matched filters, these corrupted pixels appear like bright sources in the  $500\ \mu\text{m}$  map. An example of such a spurious source can be seen on Figure 3.7.

A common method to detect these objects is to create two maps, each from one half of the data. The false sources only show up in one of the maps. However, due to the very shallow depth of our observation these half-maps are sparsely sampled, and they contain new artifacts due to the lack of cross-linking. In the case of the HeLMS

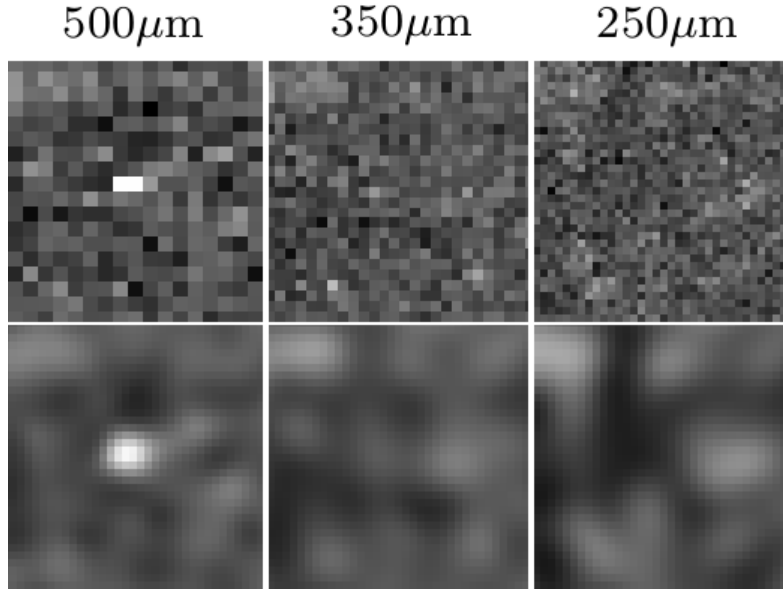


Figure 3.7: Example image of an undetected cosmic ray hit in our maps. The top row shows the raw images, with a stripe of very bright pixels showing up in the  $500\ \mu\text{m}$  map, while the other two maps show only noise. The bottom row shows the smoothed map, where the cosmic ray is detected as a very bright source at  $500\ \mu\text{m}$ , that has no counterparts in the shorter wavelength maps.

observations this method does not reliably remove cosmic rays from the maps. Instead we turn to a different approach. We compare the raw and smoothed maps in a  $5 \times 5$  pixel region around each source, and discard all candidates if any pixel shows a large difference,  $(S_{\text{raw}} - S_{\text{smooth}}) > 5\sigma_{\text{raw}}$ . Most cosmic rays produce outlier pixels almost  $10\sigma$  away from the smoothed values, and this method works well to discard these false sources. Nonetheless, we still use the images from each half of our data as a consistency check when there were no obvious artifacts in those maps, and we find that we correctly discard the bright outlier pixels caused by cosmic rays. In our final catalog we adopt a  $5\sigma$  cut of  $S_{500} > 52\ \text{mJy}$  to protect from fainter cosmic rays that this technique may not have recognized. After discarding these cosmic rays and the radio sources, the final number of objects in our catalog with  $S_{500} > 52\ \text{mJy}$ ,  $D > 34\ \text{mJy}$ , and red colors, is 477.

## 3.2 Number counts

We measure the raw  $500\ \mu\text{m}$  differential number counts of the red sources in our final catalog in nine logarithmic bins between  $52\ \text{mJy}$  and  $195\ \text{mJy}$ . The uncorrected numbers are listed in Table 3.2 and plotted on Figure 3.8. In practice, raw number counts need to be corrected for completeness and flux-boosting effects, and the expected number of false

$S_{\min}$	$S_{\max}$	$S_{\text{mean}}$	$N_{\text{bin}}$	$dN/dS$
(mJy)	(mJy)	(mJy)		( $\times 10^{-4}$ mJy $^{-1}$ deg $^{-2}$ )
52.0	60.2	56.1	225	$998.6 \pm 66.6$
60.2	69.8	65.0	154	$590.1 \pm 47.5$
69.8	80.8	75.3	55	$181.9 \pm 24.5$
80.8	93.6	87.2	27	$77.1 \pm 14.8$
93.6	108.4	101.0	9	$22.2 \pm 7.4$
108.4	125.5	117.0	4	$8.5 \pm 4.3$
125.5	145.4	135.4	1	$1.84^{+8.41}_{-1.79}$
145.4	168.4	156.9	1	$1.58^{+7.26}_{-1.55}$
168.4	195.0	181.7	1	$1.37^{+6.27}_{-1.33}$

Table 3.2: Raw 500  $\mu\text{m}$  number counts.

detections needs to be subtracted from the binned data in order to examine the underlying true source distribution. When measuring number counts at a single wavelength these corrections usually only depend on the flux density and signal-to-noise ratio, and they are relatively easy to simulate when we are investigating sources with flux densities far above the confusion limit. Our catalog, however, has a more complicated selection function, and the correction factors will also depend on the colors of our sources, with these colors having a very large scatter due to the low signal-to-noise ratio at our shorter wavelengths. Additionally, these corrections require us to assume an intrinsic shape for our number counts based on model predictions and previous observations, but due to the small sample sizes the slope of the red source counts has not been measured before. Here we do not explicitly correct our estimated counts for these biases, but instead, in the next subsection, we describe a simulation where we attempt to predict the most likely shape of our intrinsic source counts.

### 3.2.1 Intrinsic number counts

The raw source counts can provide a biased estimator of the intrinsic source distribution through a number of effects. In the following we describe the biases that change the shape of the observed distribution, and we describe a self-consistent simulation where we attempt to determine the shape of the intrinsic counts accounting for all these biases.

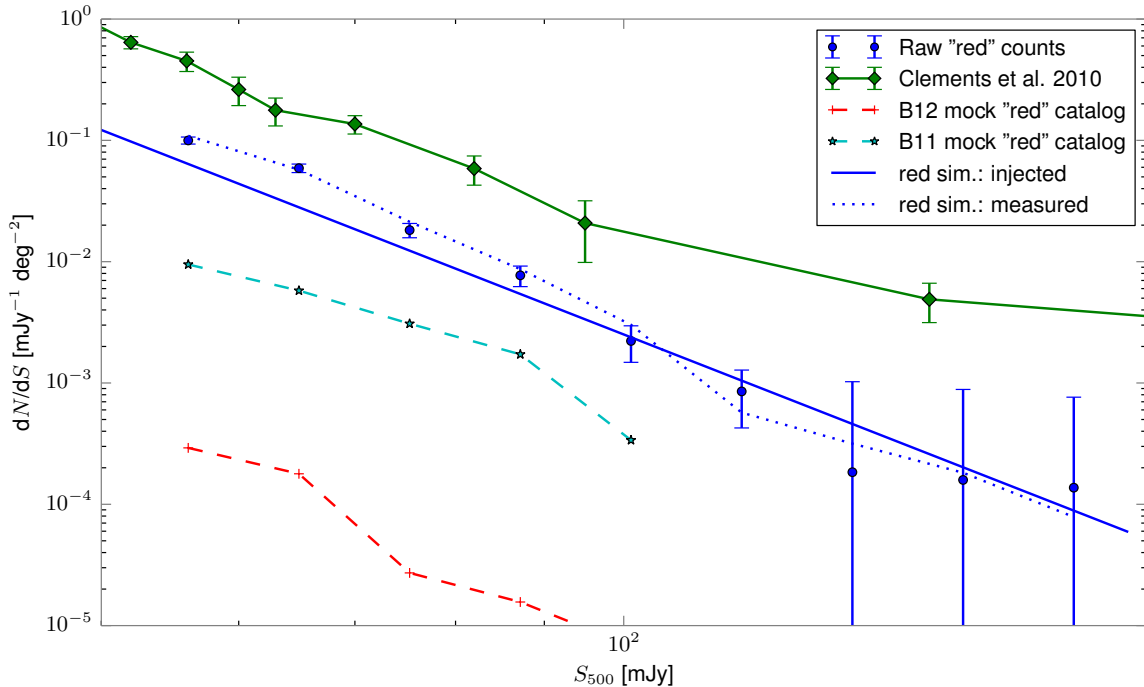


Figure 3.8: Raw 500  $\mu\text{m}$  differential number counts of our sample of “red” sources. Filled blue circles represent the raw counts with  $1\sigma$  Poisson error bars, except for the highest three flux density bins, where due to the very small number of objects we plot the 95% upper confidence limits. The green diamonds shows the total *Herschel* 500  $\mu\text{m}$  number counts measured by Clements et al. (2010). The dotted blue line represents the expected observed counts from an intrinsic distribution shown by the solid blue line. These two lines are derived from the simulations described in Section 3.2.1 which account for blending, Eddington bias, false detections and completeness. The cyan stars connected with a dashed line are binned data from creating a simulated catalog based on the earlier Béthermin et al. (2011) model, and selecting objects with the same criteria as we do for our catalog. The red crosses connected with a dashed line show the same with a catalog drawn from Béthermin et al. (2012a) model. The model comparisons are discussed in Section 3.2.2.

### 3.2.1.1 Blending

There may be a bias in our counts that arises from the variation of our angular resolution with wavelength. There will be closely adjacent sources that appear blended into one object at 500  $\mu\text{m}$  and resolved into several at 350 or 250  $\mu\text{m}$ . If one of these sources is very red, but not bright enough for catalog inclusion, and the other(s) neither very bright nor very red, the sum may well appear both bright enough and red enough for inclusion. This results in a fairly red but slightly faint object in the catalog. Examples of sources that appear to be a single object in the 500  $\mu\text{m}$  map and in the difference map are shown

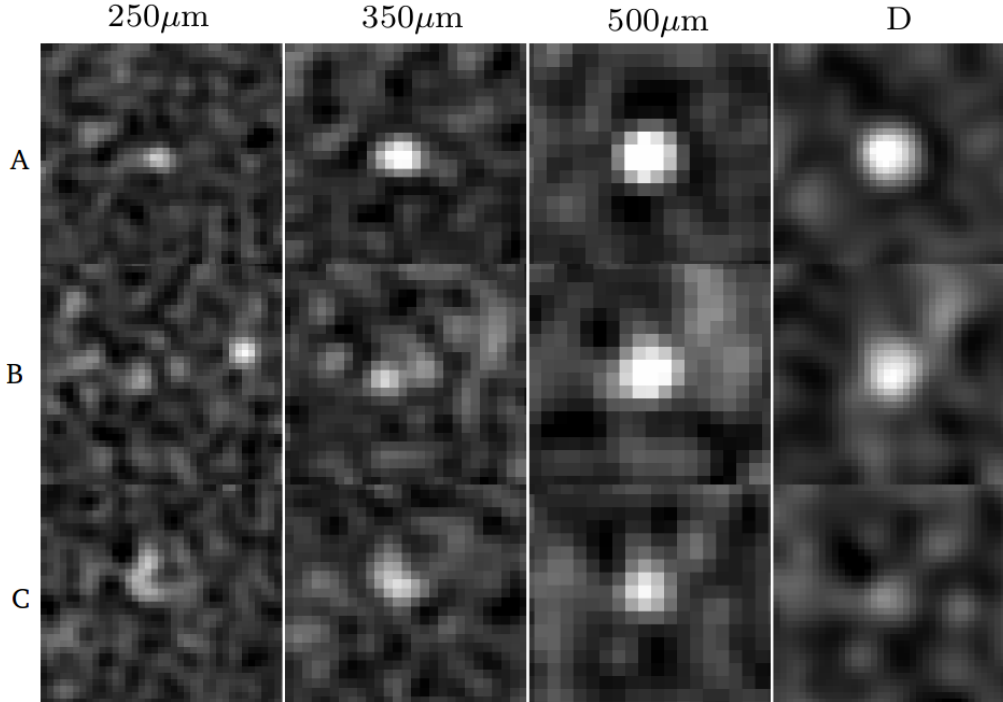


Figure 3.9: Postage-stamp images of three sources detected in our catalog that appear to be a single object in the  $500\ \mu\text{m}$  map and in  $D$ . From left to right we show the nominal resolution  $250\ \mu\text{m}$ ,  $350\ \mu\text{m}$  and  $500\ \mu\text{m}$  map, and the difference map, respectively. Example A shows a source that is isolated and has a clear counterpart in each band. Example B shows an object that clearly breaks up into two sources in the  $250\ \mu\text{m}$  and  $350\ \mu\text{m}$  maps, but is blended at  $500\ \mu\text{m}$ . Example C shows a complex blend with no clearly identifiable counterparts that could be used for deblending.

in Figure 3.9. During source selection we only require that our objects are detected as a point source at the  $500\ \mu\text{m}$  resolution, and appear red in the maps, but we do not require a detection at  $250$  and  $350\ \mu\text{m}$ , because that could bias our selection against the reddest objects. We note that the photometry method we described in Section 3.1.4 will bias our flux density estimation at these shorter wavelengths if our sources clearly break up into multiple component in these bands. In some cases the components of the blend are clearly identifiable in the  $250$  and  $350\ \mu\text{m}$  maps and their positions can in principle be used to deblend the  $500\ \mu\text{m}$  flux density, but most of the time we only see a very confused region with low signal-to-noise ratio and no clear detectable peak positions, so we cannot extract individual flux densities for these faint objects. We examined our objects by eye in the higher flux density bins, and determined that about 33% of our detected sources in each bin have an unreliable photometry due to blending or nearby sources. We still include these sources in our analysis, because simply discarding these objects by eye is highly subjective. We include the correlation values in our catalog to show how reliable

our flux estimation is in each band. We note that the simulation we describe in the following takes the effects of blending into account.

### 3.2.1.2 Detection efficiency

In an ideal case we would be able to determine the true flux densities of our sources without measurement errors, thus we would detect every source with a flux density above a given catalog cut with 100% efficiency. In practice, however, the measured flux densities can be scattered below this cutoff by noise. If we want to investigate the statistics of our catalog, we need to account for the sources that we potentially miss during source extraction. The completeness of a catalog at a given flux density is the ratio of the number of sources recovered with the source detection pipeline to the real number of objects with that intrinsic flux density in the map. The measured raw number counts are usually divided by the mean completeness in each flux density bin to account for sources that are missed during source extraction. Calculating the completeness in a catalog of sources selected at a single wavelength is straightforward, since the detection efficiency only depends on the signal-to-noise ratio of these sources. Having an extra color-constraint leads to a very large variation in the completeness at each  $500\ \mu\text{m}$  flux density bin, since even at high  $500\ \mu\text{m}$  signal-to-noise ratio the measured colors of sources with  $S_{500} \gtrsim S_{350}$  or  $S_{350} \gtrsim S_{250}$  are often not red due to the noise scattering.

To investigate how the detection efficiency changes with color, we create a 3-dimensional grid of flux density triplets, we determine the detection efficiencies at each grid-point, then we determine the efficiency of finding a source with a particular color using cubic interpolation between these grid points. To do this we inject sources into our raw maps as described in Section 3.1.4. In all three bands we create a separate map for injected flux densities ranging from 10 mJy to 200 mJy in 10 mJy steps. Then we combine the three maps of our different bands in all possible variations to calculate the efficiencies for all the flux density triplets corresponding to our grid points. We find, that if we fix the flux densities in any two bands, the detection efficiency of the source will be a smoothly changing function of the third flux density value, thus we can estimate the efficiencies from our three dimensional grid using axis-wise cubic interpolation. On Figure 3.10 we illustrate the smooth change in efficiency with the flux density at one particular SPIRE wavelength, while fixing the flux density values in the other two bands. It is clearly seen, that even sources detected with high signal-to-noise ratio in the  $500\ \mu\text{m}$  map can have a low detection efficiency if the  $350\ \mu\text{m}$  flux density is close to  $S_{500}$  or  $S_{250}$ , so unless we know the exact color distribution in our bins, we cannot correct our  $500\ \mu\text{m}$  number counts with an average completeness value.

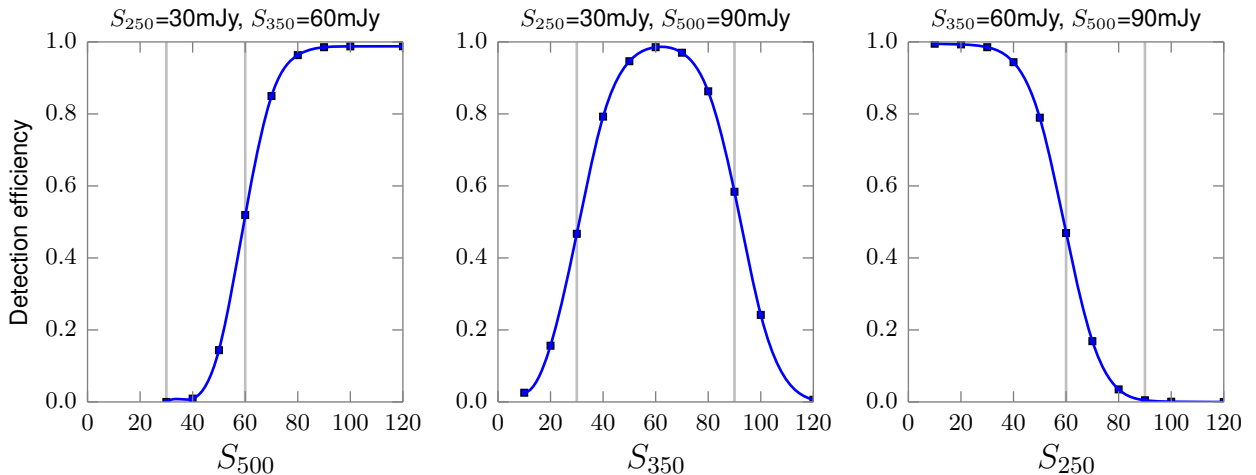


Figure 3.10: Detection efficiency as a function of flux density at a particular wavelength while the flux densities at the other two SPIRE wavelength are fixed. These fixed values are illustrated with vertical grey lines. The smooth change allows us to find the efficiency values between the grid points using axis-wise cubic interpolation. For a source with a fixed  $500\ \mu\text{m}$  flux density the detection efficiency drops to  $\sim 50\%$  if  $S_{500} \approx S_{350}$  or  $S_{350} \approx S_{250}$ , thus the completeness in a given  $500\ \mu\text{m}$  bin is not constant.

This effect is also illustrated on Figure 3.11, where we plot what the detection efficiency of each of our catalog sources would be if the measured flux density values corresponded to their true flux densities. In each  $500\ \mu\text{m}$  bin there is a large scatter in actual detection efficiencies. Dowell et al. (2014) calculated these efficiency values for each catalog source and used these values as a correction factor in the number counts measurement, but due to the large uncertainties of the flux density measurements of these sources this method is not optimal.

### 3.2.1.3 False detections and Eddington bias

On Figure 3.10 it can be seen that sources that have flux densities where the  $S_{500} > S_{350} > S_{250}$  relation does not apply can still have nonzero detection efficiencies due to the noise in the flux density measurements. To correctly determine the number of such falsely detected non-red sources, a correct model describing the population with almost red colors is needed, but current models are trained to describe the monochromatic number counts, not the color distribution of the SPIRE sources.

If the intrinsic source counts are a steep function of source brightness, or the flux uncertainties are large, a larger number of faint sources may accidentally appear to satisfy our catalog selection criteria than the number of acceptable sources that accidentally

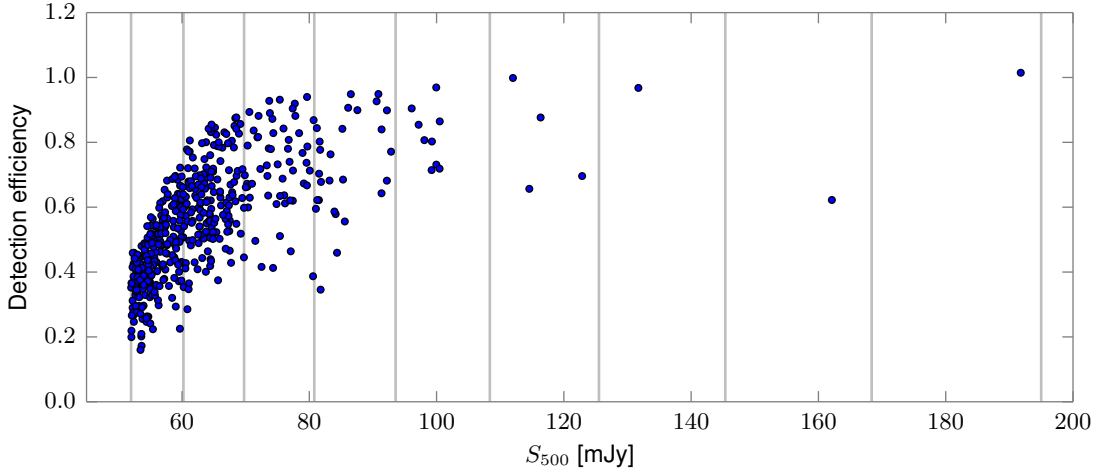


Figure 3.11: Detection efficiency calculated for each of our catalog sources, assuming that their measured flux density corresponds to their true flux density. The detection efficiency is not constant in our 500  $\mu\text{m}$  bins; the actual values also depend on the 250 and 350  $\mu\text{m}$  flux density values for each source.

appear not to. This so-called “Eddington bias” (Eddington, 1913) may be present at the cuts where we require  $S_{500} > 52 \text{ mJy}$ ,  $D > 34 \text{ mJy}$ ,  $S_{500} > S_{350}$  and  $S_{350} > S_{250}$ , and this will affect the observed slope of the number counts. In order to calculate the expected correction for this effect, we would need to know the shape of the intrinsic red source counts, but as we mentioned before, this has not been measured yet.

### 3.2.1.4 Simulations

The shape of our final measured number counts is a complex combination of the above mentioned effects, so instead of correcting for them separately, we take a self-consistent approach that incorporates all of these biases. We use the Béthermin et al. (2012a) model to create simulated maps at all three wavelengths that contain no red sources, then we add the measured instrumental noise to these maps and we inject artificial red sources into this dataset drawn from a parametric power-law distribution, and by using Monte Carlo simulations we fine-tune the parameters of this distribution until the measured counts in these simulated maps look similar to our real measured red source counts.

The Béthermin et al. (2012a) model is an empirical model that extrapolates locally known correlations of different galaxy properties to high redshift, without using physical information about the modelled population. The model’s predictions agree well with the observed monochromatic SPIRE number counts, so we draw sources from this model to create our simulated sky maps. The model is based on the evolution of main-sequence and

starburst galaxies and uses a simple SED template where the dust gets slightly warmer with increasing redshift. The first ingredient of the model is the stellar mass function of star-forming galaxies that evolves with redshift and can be described by a Schechter function as

$$\Phi_{M_*} = \frac{dN}{d\log(M_*)dV} = \Phi_b(z) \times \left(\frac{M_*}{M_b}\right)^{-0.3} \times \exp\left(-\frac{M_*}{M_b}\right) \times \ln(10), \quad (3.9)$$

where  $M_*$  is the stellar mass of the galaxy,  $M_b = 10^{11.2} M_\odot$  is the characteristic mass, and the characteristic density  $\Phi_b(z)$  is constant for  $z < 1$  ( $\Phi_{b,z<1} = 10^{-3.02} \text{ Mpc}^{-3}$ , Sargent et al. 2012), and decreases at  $z > 1$  as

$$\log(\Phi_b(z)) = \log(\Phi_{b,z<1}) + 0.4 \times (1 - z). \quad (3.10)$$

We can calculate the co-moving volume element  $dV$  as

$$dV = D_H \times \frac{D_L^2}{(1+z)^2 \sqrt{\Omega_m(1+z)^3 + 1 - \Omega_m}} dz d\Omega, \quad (3.11)$$

where  $D_H = c/H_0$  is the Hubble distance,  $c$  is the speed of light,  $D_L$  is the luminosity distance, and the cosmology parameters used are  $H_0 = 70 \text{ km s}^{-1} \text{ Mpc}^{-1}$ ,  $\Omega_m = 0.27$ ,  $\Omega_k = 0$ . Combining this relation with the mass function we can get an expression for the number of galaxies in intervals of redshift and logarithmic stellar mass per unit solid angle as

$$\frac{dN}{d\log(M_*)dzd\Omega} = \Phi_{M_*} \times \frac{dV}{dzd\Omega}. \quad (3.12)$$

We draw  $(z, M_*)$  value pairs from this distribution, finding the total number of sources per unit solid angle by integrating Equation 3.12 with respect to our whole  $z$  and  $\log(M_*)$  range.

The main sequence (MS) specific star formation rate for each source can be determined as

$$\text{sSFR}_{\text{MS}}(z, M_*) = \text{sSFR}_{\text{MS},0} \times \left(\frac{M_*}{10^{11} M_\odot}\right)^{-0.2} \times (1 + \min(z, z_{\text{evo}}))^3 \quad (3.13)$$

where  $\text{sSFR}_{\text{MS},0} = 10^{-10.2} \text{ yr}^{-1}$  is the specific star formation rate for an  $M_* = 10^{11} M_\odot$  galaxy at  $z = 0$ , and  $z_{\text{evo}} = 2.5$  represents the redshift where  $\text{sSFR}_{\text{MS}}$  stops to evolve. The actual specific star formation rate for galaxies will scatter around  $\text{sSFR}_{\text{MS}}$ , and starburst (SB) galaxies will have highly elevated  $\text{sSFR}$  values compared to the main sequence. The probability for a galaxy with known redshift  $z$ , stellar mass  $M_*$  and corresponding  $\text{sSFR}_{\text{MS}}$  value to have a certain  $\text{sSFR}$  specific star formation rate can be described by a

double log-normal distribution (Sargent et al., 2012) as

$$\begin{aligned}
p(\log(\text{sSFR}) | M_*, z) &\propto \exp\left(-\frac{(\log(\text{sSFR}) - \log(\text{sSFR}_{\text{MS}}))^2}{2\sigma_{\text{MS}}^2}\right) + \\
&+ r_{\text{SB}}(z) \times \exp\left(-\frac{(\log(\text{sSFR}) - \log(\text{sSFR}_{\text{MS}}) - B_{\text{SB}})^2}{2\sigma_{\text{SB}}^2}\right) \propto p_{\text{MS}} + p_{\text{SB}},
\end{aligned}
\tag{3.14}$$

where  $\sigma_{\text{MS}} = 0.15$  dex,  $\sigma_{\text{SB}} = 0.2$  dex (Salmi et al., 2012) are the standard deviation of the log-normal MS and SB distributions,  $B_{\text{SB}} = 0.6$  dex describes the boost in sSFR for starbursts compared to main sequence galaxies, and the redshift evolution up to  $z_{\text{SB}} = 1$  is coded in

$$r_{\text{SB}}(z) = 0.012 \times (1 + \min(z, z_{\text{SB}})). \tag{3.15}$$

We first assign an MS or SB type for each of our drawn galaxies based on the  $p_{\text{MS}}/(p_{\text{MS}} + p_{\text{SB}})$  and  $p_{\text{SB}}/(p_{\text{MS}} + p_{\text{SB}})$  probability ratios, then we draw an sSFR value from the double log-normal probability distribution centered on  $\text{sSFR}_{\text{MS}}$  for our main sequence objects or on  $\text{sSFR}_{\text{MS}} + B_{\text{SB}}$  for the starbursts.

Having drawn values of stellar mass and specific star formation rate for each of our sources, we can calculate the total star formation rate as  $\text{SFR} = \text{sSFR} \times M_*$ . The infrared star formation rate can be converted to infrared luminosity  $L_{\text{IR}}$  based on Kennicutt (1998) as

$$\frac{\text{SFR}_{\text{IR}}}{L_{\text{IR}}} = 1.7 \times 10^{-10} \text{M}_{\odot} \text{yr}^{-1} \text{L}_{\odot}^{-1}. \tag{3.16}$$

In lower mass dusty galaxies not all of the star formation is obscured by dust, and the total SFR is the sum of the infrared and UV star formation rates, with the mean ratio of these components depending on the stellar mass as

$$r = 2.5 \log\left(\frac{\text{SFR}_{\text{IR}}}{\text{SFR}_{\text{UV}}}\right) = 4.07 \times \log\left(\frac{M_*}{\text{M}_{\odot}}\right) - 39.32, \tag{3.17}$$

adopting the relation in Pannella et al. (2009). Combining equations 3.16 and 3.17 and using  $\text{SFR} = \text{SFR}_{\text{IR}} + \text{SFR}_{\text{UV}}$  we can convert our generated SFR values to infrared luminosity as

$$L_{\text{IR}} = \frac{\text{SFR}}{1.7 \times 10^{-10} \text{M}_{\odot} \text{yr}^{-1} \text{L}_{\odot}^{-1}} \times \frac{10^{0.4r}}{1 + 10^{0.4r}}. \tag{3.18}$$

With a redshift and  $L_{\text{IR}}$  value in hand for each simulated source, we determine the flux densities of these objects at the three SPIRE wavelengths using the infrared SED templates from Magdis et al. (2012).

After we determine the 250, 350 and 500  $\mu\text{m}$  flux densities of our generated sources,

we inject these sources into an empty map at random positions, then we add instrumental noise that resembles the noise measured in our real maps. We discard any sources that have red SPIRE colors in this simulated dataset, then we inject artificial red sources into our newly created sky maps. To do this we first draw  $500\ \mu\text{m}$  fluxes from a power-law distribution of the shape  $dN/dS = N_0 \times S^{-\alpha}$ , then we fix the color ratios of our injected objects to the median of the color ratios measured in our catalog,  $S_{500}/S_{250} = 1.55$  and  $S_{500}/S_{350} = 1.12$ . We note that the actual colors of our objects are not constant, but due to the large uncertainties in the color measurements it is not straightforward to determine the underlying color distribution. In Figure 3.12 we plot the measured color distribution in our  $500\ \mu\text{m}$  bins. The largest scatter is in the lowest two bins, where many of the objects with high color ratios are either blends or have very low signal-to-noise ratio counterparts at  $250$  and  $350\ \mu\text{m}$ . After injecting our artificial red sources we run our detection pipeline in the same way as we do for our real maps and we compare the measured counts from this simulated data with our raw numbers. In an iterative process we change the input parameters  $N_0$  and  $\alpha$  until the output counts resemble the measured raw number counts in our real data. In Figure 3.8 we show the result of a simulation with an area of  $1500\ \text{deg}^2$ . The blue solid line represents a power law  $dN/dS = N_0 \times S^\alpha$  with  $\alpha = -5.6$  and  $\log N_0 = 8.6$ , while the dotted blue line shows the measured number counts for simulated objects with  $500\ \mu\text{m}$  flux densities drawn from this distribution and with fixed color ratios. The simulations are in good agreement with our observed counts, suggesting that assuming a power-law model without a break is adequate for our purposes.

### 3.2.2 Comparison to models

We compare our observed number counts to mock “red” catalogs created from the Béthermin et al. (2011, B11) and the Béthermin et al. (2012a, B12) models. We generate  $1000\ \text{deg}^2$  simulations from both of these catalogs, and then select sources the same way as we do for our observed sample ( $S_{500} > 52\ \text{mJy}$ ,  $D > 34\ \text{mJy}$ , and red  $S_{500} > S_{350} > S_{250}$  colors). These two models predict the total *Herschel* number counts very well, but as Dowell et al. (2014) already showed, they both under-predict the number of red sources in the HerMES fields. The resulting counts from these simulations are plotted on Figure 3.8. We can see that B11 predicts more red sources; however, they are mostly at  $z < 3$ , and since all of our red objects with measured redshift are at  $z > 3$  we know that this model’s predictions are not correct. The B12 model predicts even fewer red sources than the B11 model, but in this sample all of the objects lie above  $z = 3$ , agreeing with

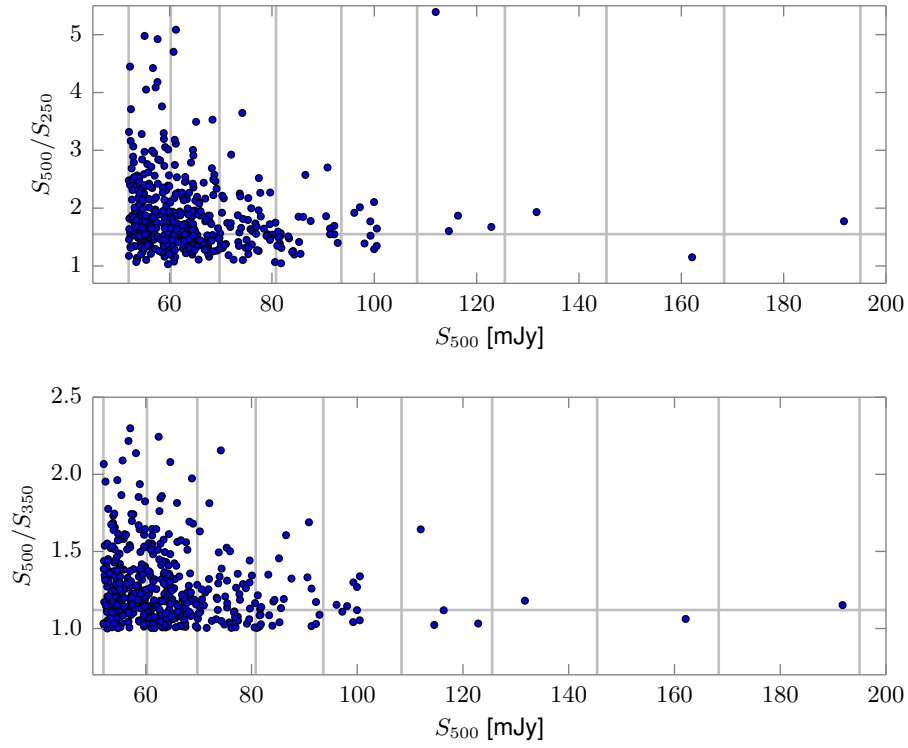


Figure 3.12: Measured SPIRE colors of red sources in our catalog as a function of the  $500\ \mu\text{m}$  flux density. The vertical lines show the edges of the flux density bins we used to measure the differential number counts. The horizontal lines at  $S_{500}/S_{250} = 1.55$  and  $S_{500}/S_{350} = 1.12$  show the median colors of our sample. The sources with anomalously large colors are mostly blends or objects without clear  $250$  and  $350\ \mu\text{m}$  detections.

our follow-up results. We note that both of these models are empirical and are based on extrapolation of the properties of lower redshift starburst galaxies, such as the luminosity function (B11) or the stellar mass function (B12), instead of the actual physics of these galaxies; however, at present none of the physically-motivated models have been fine-tuned to properly describe the observed *Herschel* number counts.

In Fig. 3.8 we also show the total SPIRE 500  $\mu\text{m}$  counts measured by Clements et al. (2010), which is in good agreement with other SPIRE total number counts measurements (Oliver et al., 2010; Glenn et al., 2010; Béthermin et al., 2012b). We can see that the inferred corrected slope of our counts is very steep, suggesting a strong evolution of our population of red sources. Negrello et al. (2010) predicted that the number counts of unlensed galaxies at 500  $\mu\text{m}$  are rapidly decreasing and reach zero at  $S_{500} \sim 100$  mJy. Every bright object with flux densities above this value is expected to be strongly lensed, and the number counts are expected to have a bright tail due to this lensed population. We have found several red objects with bright 500  $\mu\text{m}$  flux densities, but their low numbers in our flux density bins do not allow us to see an actual departure from the steep power-law shape of red sources at lower flux densities.

Our inferred number counts do not show any significant differences compared with the Dowell et al. (2014) findings, although we now have much better statistics. The Dowell et al. (2014) sample consists of red sources with  $S_{500} > 30$  mJy and  $D > 24$  mJy, and they found the total corrected cumulative counts to be  $3.3 \pm 0.8$  sources per  $\text{deg}^2$ . If we assume that the shape of our distribution can be described by the power law, that we found in Section 3.2.1, and that it does not have a break between 30 mJy and 52 mJy, then integrating this power law above 30 mJy gives us a total number of more than 10 red sources per  $\text{deg}^2$ . However, this comparison is not straightforward, since many of these objects at lower 500  $\mu\text{m}$  flux densities would be discarded by the  $D$  cut used in the Dowell et al. (2014) analysis. Integrating our power law for  $S_{500} > 40$  mJy (where the two samples have a larger overlap) results in 2.8 objects per  $\text{deg}^2$ , which is closer to the Dowell et al. (2014) result.

### 3.3 Colors and SED fits

The interpretation of our red color-selection as leading to a catalog rich in high- $z$  galaxies relies on the assumption that galaxies with rising flux densities towards longer wavelengths are at high redshifts. Although some observations suggest that the temperature of starburst galaxies could be rising slightly towards high  $z$ , it does not rise as fast as  $(1+z)$ , and the observed temperature  $T_{\text{obs}} = T_{\text{d}}/(1+z)$  drops with redshift. This behavior

is evident in the catalog of 25 strongly-lensed galaxies selected at 1.4 mm with the South Pole Telescope (Weiß et al., 2013; Vieira et al., 2013), where the apparent temperature is fit by  $T_{\text{obs}} = [11.1 - 0.8(1 + z)]$  K. This pattern is consistent with examining the spectral energy distributions (SEDs) of several known lower redshift dusty starburst galaxies, and measuring their expected flux-ratios at the SPIRE wavelengths for different redshifts.

In Figure 3.13 we present the color-color plot for our objects with  $S_{500} > 60$  mJy. As a comparison we also show the redshift tracks for two starburst galaxies, as well as the colors of our two red sources that have ALMA spectroscopic redshift measurements and four spectroscopically confirmed  $z > 4$  galaxies from the Dowell et al. (2014) sample. We have examined the SPIRE images of our  $S_{500} > 60$  mJy sources by eye and flagged objects that look blended at higher resolution. As discussed before, we include possible blends in our catalog, since although we are not able to deblend the flux densities of the components, we assume that at least one component is a red source. We included this effect in the number counts simulation, but when we are investigating the colors of individual objects, we need to note that blending effects can result in boosted flux densities that are not well fitted by a modified blackbody SED. We plot the positions of these confused sources in our color-color space with a different symbol on Figure 3.13 to illustrate how the anomalous colors that are very distant from the typical redshift tracks are often the result of blending.

In Section 1.3 we discussed that the spectral energy distribution of submillimeter galaxies is often modelled as an optically thin modified blackbody. Dowell et al. (2014) show that most of the red sources in their sample are better fit with an optically thick model described as

$$S_{\nu} = (1 - e^{-\tau_{\nu}})B_{\nu}(T_{\text{d}})\Omega_s, \quad (3.19)$$

where  $B_{\nu}(T_{\text{d}})$  is the Planck function,  $\Omega_s$  is the solid angle of the source, and

$$\tau_{\nu} = (\nu/\nu_0)^{\beta} \quad (3.20)$$

is the optical depth term. Here  $\beta$  is the dust grain spectral emissivity index as discussed before ( $\beta \sim 1-2$ ) and  $\nu_0$  defines the frequency at which the optical depth equals unity. At frequencies larger than  $\nu_0$ , where  $\tau_{\nu} > 1$ , the dust cloud becomes optically thick. This usually corresponds to rest-frame frequencies of  $\nu_0 \sim 1.5-3$  THz or wavelengths of  $\lambda \sim 100-200 \mu\text{m}$  (Draine, 2006; Conley et al., 2011). Dowell et al. (2014) applied an optically thick model to fit the SED of several dusty galaxies with well-sampled spectra, including three sources from their red sample, and they have found that the rest frame wavelengths where the dust cloud becomes optically thick are in the range

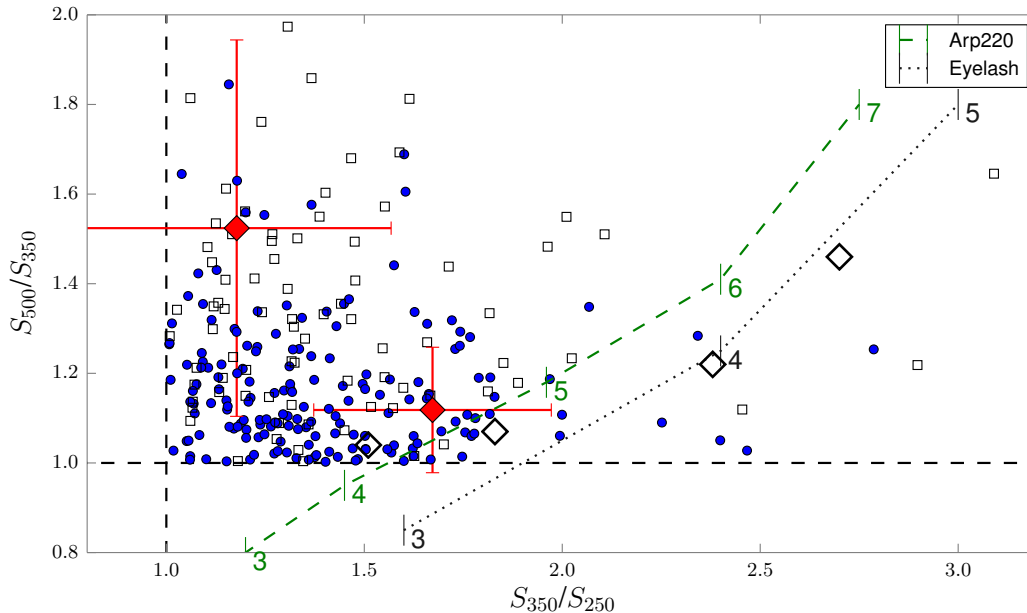


Figure 3.13: Color-color plot of our red sources with  $S_{500} > 60$  mJy. Blue filled circles represent the objects that look isolated in the nominal resolution maps, while open black squares show the more confused sources that we have flagged by eye to illustrate that anomalous colors are usually the result of blending. The green dashed line represents the redshift-track for the starburst galaxy Arp220 and the dotted black line for SMMJ21352–102 (Cosmic Eyelash, Swinbank et al. 2010b), with the labels on these curves showing the redshifts. Red filled diamonds show two sources from the catalog discussed in our paper that have ALMA spectroscopic redshift measurements. From left to right: HeLMS65 with  $z = 4.997$  (or  $z = 3.798$ , see discussion in Section 3.4); and HeLMS34 with  $z = 5.162$ . For these two sources we show the typical errors in their color measurements. The black open diamond symbols represent four sources from the Dowell et al. (2014) red source sample that have spectroscopic redshift measurements. From left to right: FLS1 ( $z = 4.3$ ); FLS5 ( $z = 4.4$ ); LSW102 ( $z = 5.3$ ); and FLS3 ( $z = 6.3$ ).

$190 \mu\text{m} < \lambda_0 < 270 \mu\text{m}$ .

We use the affine invariant Marcov chain Monte Carlo (MCMC) code described in Dowell et al. (2014) to fit an optically thick modified blackbody to our SPIRE flux densities. When fitting the redshifted SED in the observed frame, the fitted parameters become  $T_{\text{obs}} = T_{\text{d}}/(1+z)$  and  $\lambda_{0,\text{obs}} = \lambda_0(1+z)$ . Since we only have three data points, and four parameters to fit ( $T_{\text{obs}}$ ,  $\beta$ ,  $\lambda_{0,\text{obs}}$  and an amplitude), we apply a broad Gaussian prior to the parameters that are not well constrained by our SPIRE data alone. Following Dowell et al. (2014) these constraints are  $\beta = 1.8 \pm 0.3$  and  $\lambda_{0,\text{obs}} = (1100 \pm 400) \mu\text{m}$  (assuming a typical redshift of  $z \sim 4.5$  for red sources). An example of the parameter distribution of the MCMC samples for one of our sources (HELMS34) is shown in Fig-

ure 3.14. As shown on the marginal histograms, although  $\beta$  and  $\lambda_{0,\text{obs}}$  are not fixed, they are narrowed down and are only allowed to vary between the Gaussian limits given above. Figure 3.15 shows the observed temperature parameter distribution of the MCMC chains for the case when we do not apply a prior on  $\lambda_{0,\text{obs}}$ . The very large and small  $\lambda_{0,\text{obs}}$  values correspond to a long tail of the fitted temperature distribution, corresponding to values with low probability, thus applying the prior will not bias our results significantly.

The resulting observed temperature distribution for our isolated sources is plotted in Figure 3.16. We also show the distribution of  $\lambda_{\text{max}}$ , the observed wavelength where the SED peaks. The mean observed temperature is  $(11.03 \pm 1.91)$  K. This is cooler than  $T_{\text{obs}}$  for SPIRE-selected galaxies in general (e.g. Amblard et al., 2010; Casey et al., 2012). At the same time, this is warmer than the  $(8 \pm 2)$  K mean apparent temperature seen for galaxies in the 1.4-mm selected SPT sample. Since only a small fraction of our sample has very bright  $500 \mu\text{m}$  flux densities ( $S_{500} > 100 \text{ mJy}$ ), the majority of our sources are not expected to be strongly magnified by gravitational lensing and are thus intrinsically very luminous. Heating from intense star formation can explain these warmer dust temperatures. The SPT sample, however, contains very strongly lensed galaxies and we can assume that they select intrinsically fainter and colder objects than the typical red sources we find. This can explain the difference in the apparent temperature distributions. We have to be very careful however, when comparing temperature values quoted in the literature. Applying an optically thin model, where  $\lambda_0 \rightarrow 0$ , the fitted  $T_{\text{obs}}$  values can decrease by  $\sim 15\%$ , so the observed temperatures can have a different meaning depending on the SED model applied. Using the same parameters as Dowell et al. (2014), our observed temperature distribution is similar to their measurements, showing that we select a similar population of sources in our maps. Red sources with known redshifts have a very warm inferred intrinsic dust temperature. The three sources with spectroscopic redshift estimations listed in Dowell et al. (2014), FLS1 ( $z = 4.29$ ), FLS5 ( $z = 4.44$ ) and LSW20 ( $z = 3.36$ ) have dust temperatures of 63 K, 59 K and 48 K, respectively, and Riechers et al. (2013) quote  $T_d = 56$  K for the  $z = 6.3$  source HFLS3. The observed SED peak wavelength  $\lambda_{\text{max}}$  is more directly constrained by the data than  $T_{\text{obs}}$ . For a similar  $\lambda_{\text{max}}$  distribution as the one we measure, Dowell et al. (2014) estimates a mean photometric redshift of  $z = 4.7$  by determining priors of the rest-frame peak wavelength based on different comparison samples. While we did not carry out a similar analysis, based on the similar selection function and measured  $\lambda_{\text{max}}$  and  $T_{\text{obs}}$  distribution of our sample, we can assume that our catalog also consists of mostly high-redshift objects.

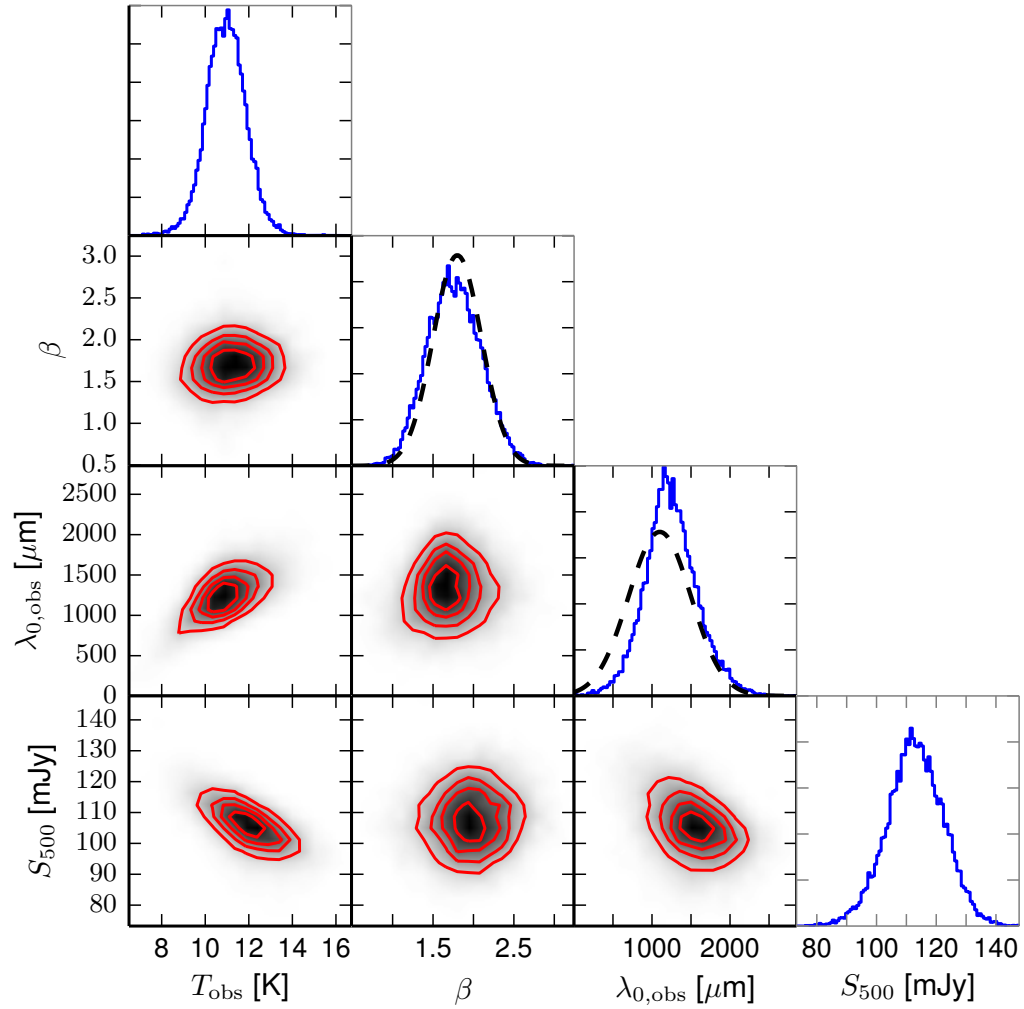


Figure 3.14: Parameter distributions for MCMC samples. We show joint distributions of two different variables, with arbitrary density contours, and also show marginal histograms of the given parameter. The black dashed line in the  $\beta$  and  $\lambda_{0,\text{obs}}$  histograms shows the Gaussian prior applied to these parameters.

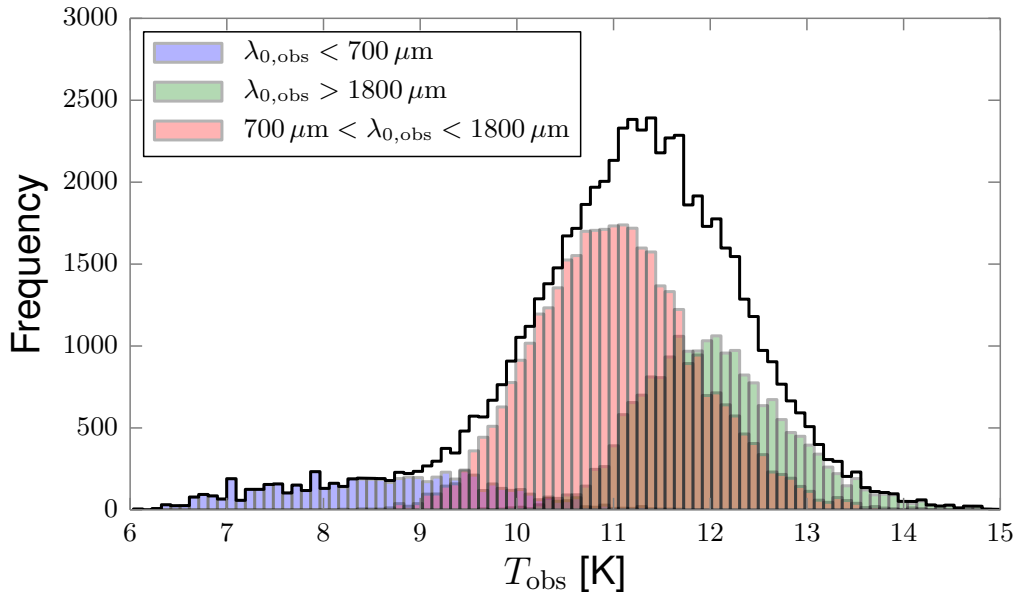


Figure 3.15: Histogram of the posterior temperatures from the MCMC chain when there is no prior applied to  $\lambda_{0,\text{obs}}$ . The black line shows the total distribution. Small and large  $\lambda_{0,\text{obs}}$  values contribute to low probability tails of the temperature distribution, showing that applying a prior on  $\lambda_{0,\text{obs}}$  will not change the fitted results significantly.

### 3.4 ALMA spectroscopy

Follow-up observations of red sources have already shown that we can indeed successfully select high-redshift dusty galaxies based on their red SPIRE colors. To further increase our sample of sources with confirmed spectroscopic redshift estimations we observed two of our red sources (HeLMS34 and HeLMS65) using the Atacama Large Millimeter/submillimeter Array (ALMA) during the Cycle 2 operational phase. These sources were selected based on their very red colors and we already have photometric redshift estimates for these two sources,  $z_{\text{phot}} = 5.15 \pm 0.12$  and  $z_{\text{phot}} = 5.24 \pm 0.27$ , respectively (Asboth et al. in prep.). The observations were carried out in Band 3, covering frequencies between 84 and 116 GHz, which contains the redshifted CO rotational lines typically below the  $J = 6 - 5$  transition.

The observed spectra are shown in Figure 3.17. In the spectrum of HeLMS34 we detect two lines, unambiguously identified as the CO(5 - 4) and CO(6 - 5) transitions. These correspond to a redshift of  $z = 5.162$  that is in very good agreement with the photo- $z$  estimate of 5.15.

Only a single strong line is seen in the spectrum of HeLMS65. There are several

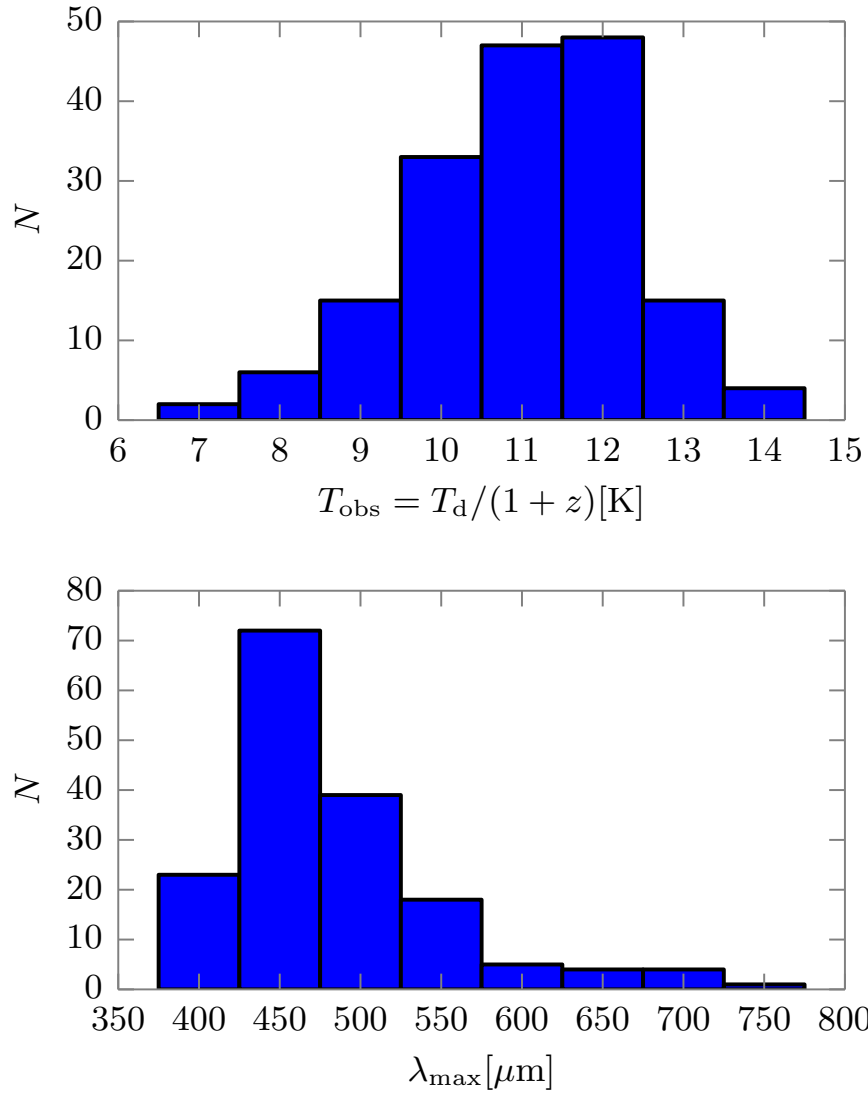


Figure 3.16: Distribution of the observed temperature  $T_d/(1+z)$ , and the observed SED peak wavelength  $\lambda_{\text{max}}$  of our red sources, measured by fitting an optically thick modified blackbody spectrum to our SPIRE flux densities, as described in Section 3.3.

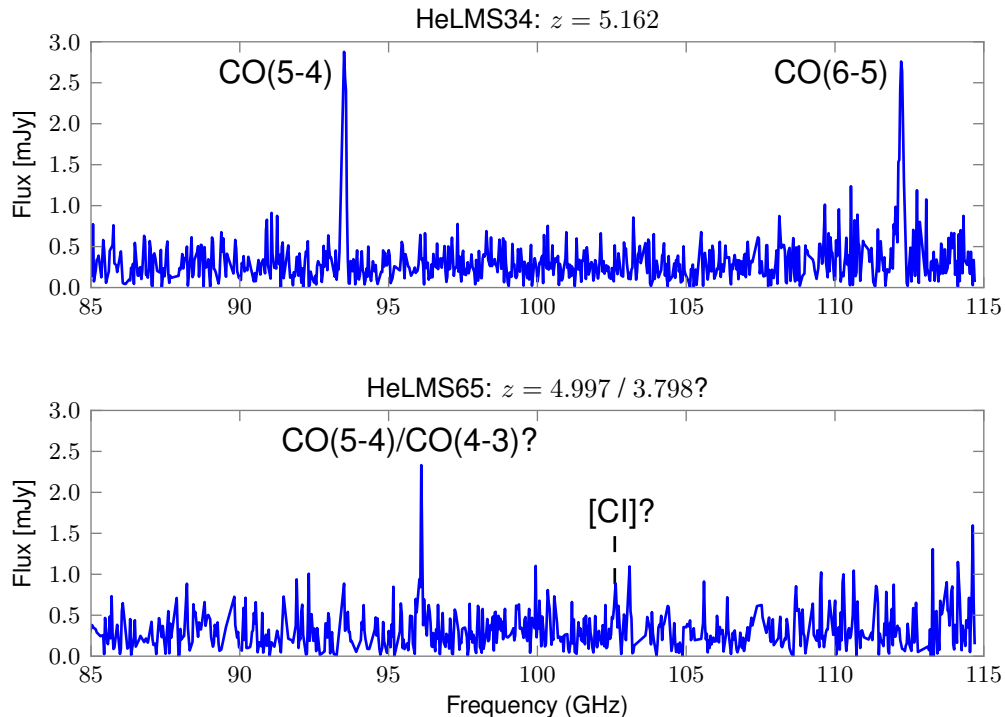


Figure 3.17: ALMA spectrum for two red sources in our catalog. In the spectrum of HeLMS34 we detect two CO lines and their observed frequencies correspond to redshift  $z = 5.162$ . HeLMS65 has only one high signal-to-noise line in its spectrum and the redshift can be either  $z = 4.997$  or  $z = 3.798$ , depending on whether the low signal-to-noise ratio spectral feature at 102.6 GHz is only a noise fluctuation or a faint [CI] spectral line. See the discussion in Section 3.4 for details.

spectral lines that could fall into this region. We can discard the possibility that the observed line is CO(6 – 5) or a higher transition, since then we would always detect other CO rotational lines in the observed spectrum. If we identify the detected line as the CO(5 – 4) transition, then the redshift of this source is  $z = 4.997$  and we would not see any other lines in the observed spectral range; this is consistent with the photo- $z$  estimate. If, on the other hand, the detected line corresponds to the CO(4 – 3) transition then the redshift is  $z = 3.798$  and we should be able to detect a [CI] line at 102.6 GHz. There is a possible low signal-to-noise peak near to this frequency, but the spectral feature in question is not larger than a dozen other spikes in the observed spectrum, and hence the identification is not definite. We note that we have seen cases where the photo- $z$  estimate is not consistent with later spectroscopic data, and so from this measurement alone we cannot determine the redshift unambiguously. Additional follow-up observations are planned to determine the actual redshift of this source.

Together with follow-up observation results of sources from the Dowell et al. (2014) sample we now have more than ten red sources with spectroscopically confirmed high-redshift, with the majority being at  $z > 4$ , and the rest at  $z > 3$ , strengthening the initial assumption that our search method selects high-redshift dusty galaxies.

### 3.5 Red sources in the ACT maps

Since red sources have increasing flux densities towards longer wavelengths, with their SED peaking close to  $500 \mu\text{m}$ , we expect that these galaxies should also be detected at millimeter wavelengths. As we discussed in Section 2.4.1, there is an overlap between the HeLMS region and equatorial observations made by the Atacama Cosmology Telescope (ACT; Swetz et al., 2011). ACT is a 6-m off-axis Gregorian telescope located in the Atacama Desert. It observes the sky in three frequency bands, at 148 GHz, 218 GHz and 277 GHz corresponding to wavelengths of  $2000 \mu\text{m}$ ,  $1400 \mu\text{m}$  and  $1100 \mu\text{m}$ , respectively. The ACT beams at these frequencies have a FWHM of  $84''$  ( $2000 \mu\text{m}$ ),  $60''$  ( $1400 \mu\text{m}$ ) and  $54''$  ( $1100 \mu\text{m}$ ). These beams are much larger than the SPIRE beams, so the ACT data cannot be used to refine the positions of our sources, but detecting millimeter emission towards these red galaxies would confirm their thermal nature.

We use the available  $1400 \mu\text{m}$  and  $2000 \mu\text{m}$  equatorial maps (Dünner et al., 2013) to find our red sources in the overlapping region. To improve point-source detectability, the maps are matched filtered with the ACT beams (Hasselfield et al., 2013b) as described in Marsden et al. (2014). The resulting maps have typical uncertainties of 3.3 and 2.2 mJy at  $1400 \mu\text{m}$  and  $2000 \mu\text{m}$ , respectively.

We find that only a small fraction of our sources are detected in the ACT maps with a signal-to-noise ratio larger than three, so instead of measuring the individual source flux densities, we define 10 mJy wide intervals of  $500 \mu\text{m}$  flux density values, and we stack the ACT maps at the positions of all of our sources in the overlapping area with  $S_{500}$  falling into the given interval. This method increases the signal-to-noise ratio in the ACT dataset and we are able to detect the average flux densities of the sources that are too faint to be detected individually. The stacked images are shown on Figure 3.18 and the average SPIRE and ACT flux density values for the sources falling into the different  $500 \mu\text{m}$  flux density bins are listed in Table 3.3. The errors are determined by dividing the standard deviation of the pixel values in the individual images at the position of the stacked peak by the square root of the number of objects that belong to the stack.

It is encouraging to find that all the stacked images (except for the  $2000 \mu\text{m}$  stack corresponding to  $90 \text{ mJy} > S_{500} > 80 \text{ mJy}$ ) show a clear point source at the position of

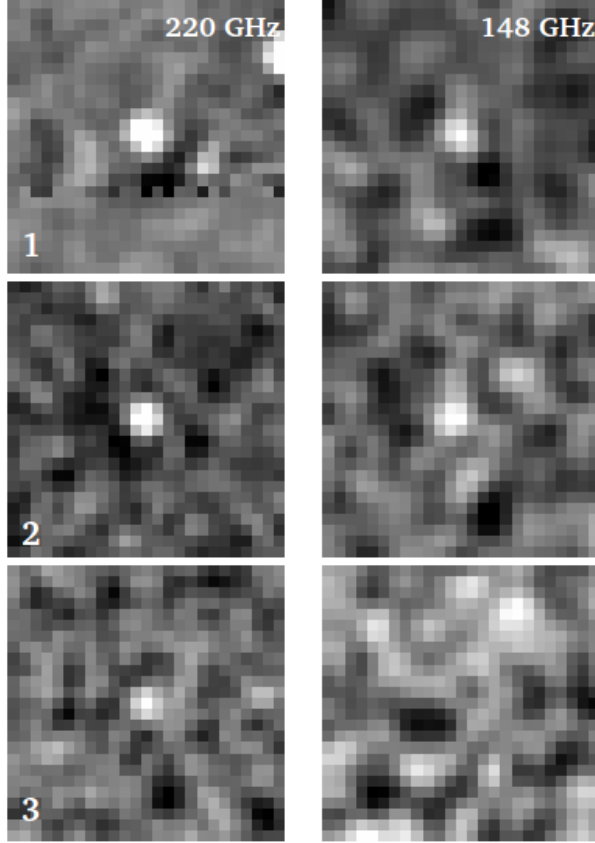


Figure 3.18: (a.) ACT stacks using the red source positions in different  $500\ \mu\text{m}$  flux density bins (bin 1:  $S_{500} > 100\ \text{mJy}$ , bin 2:  $90\text{--}100\ \text{mJy}$ , bin 3:  $80\text{--}90\ \text{mJy}$ ).

$S_{500}$ range (mJy)	$\langle S_{250} \rangle$ (mJy)	$\langle S_{350} \rangle$ (mJy)	$\langle S_{500} \rangle$ (mJy)	$\langle S_{1400} \rangle$ (mJy)	$\langle S_{2000} \rangle$ (mJy)
1 > 100	$86.69 \pm 11.75$	$118.76 \pm 13.01$	$132.34 \pm 13.74$	$19.13 \pm 2.41$	$5.55 \pm 1.53$
2 90–100	$56.10 \pm 4.33$	$80.16 \pm 4.65$	$94.27 \pm 1.28$	$8.66 \pm 2.64$	$3.55 \pm 0.41$
3 80–90	$57.82 \pm 1.81$	$72.90 \pm 1.68$	$82.92 \pm 0.47$	$3.30 \pm 0.99$	$0.29 \pm 0.72$
4 70–80	$46.49 \pm 1.89$	$64.01 \pm 1.62$	$74.84 \pm 0.52$	$5.24 \pm 1.16$	$1.66 \pm 0.41$
5 60–70	$38.80 \pm 0.97$	$52.83 \pm 0.82$	$64.58 \pm 0.25$	$2.20 \pm 0.44$	$0.85 \pm 0.33$
6 52–60	$30.79 \pm 0.72$	$44.06 \pm 0.60$	$55.80 \pm 0.19$	$2.51 \pm 0.33$	$0.95 \pm 0.24$

Table 3.3: Average  $250\ \mu\text{m}$ ,  $350\ \mu\text{m}$ ,  $500\ \mu\text{m}$ ,  $1400\ \mu\text{m}$  and  $2000\ \mu\text{m}$  flux densities of the sources falling into different  $500\ \mu\text{m}$  flux density bins.

our red sources. The average colors of our brightest sources with ACT detections are  $S_{500}/S_{1400} = 7.1$  and  $S_{500}/S_{2000} = 21.5$ . The average flux densities we detect in the stacked maps are lower than what we would expect from the  $S_{500}$  values. However, the

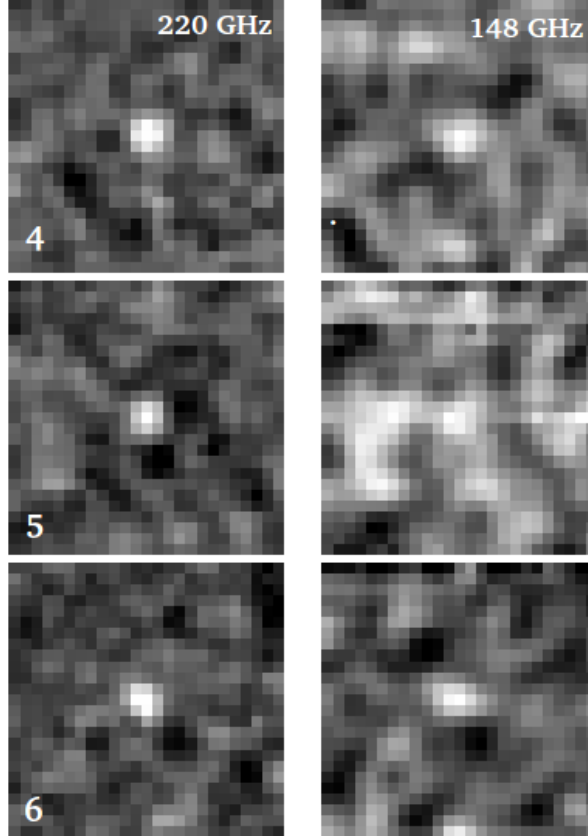


Figure 3.18: (b.) ACT stacks using the red source positions in different  $500\ \mu\text{m}$  flux density bins (bin 4: 70–80 mJy, bin 5: 60–70 mJy, bin 6: 52–60 mJy).

ratios mentioned above are typical for isolated sources, and as we discussed before, source blending is a significant biasing effect in our catalog, and it is possible, that a fraction of red sources in each of these stacks have a lower  $S_{500}$  flux density than what we measure. If the other component of the blend is a non-red source, then this component will probably be too faint to be detected in ACT, and it is possible that the millimeter emission we see is from the fainter, but red component of the blend. Additionally, we only detect the brightest sources in ACT individually, and these rare sources might be lensed but less luminous sources with different SED properties, than the majority of our sources in the catalog.

In Figure 3.19 we plot the average SED of the sources belonging to our different  $S_{500}$  bins. Except for Bin 3 all average SEDs follow a similar shape, showing that the sources in different bins have very similar properties. Our bin corresponding to  $90\ \text{mJy} > S_{500} > 80\ \text{mJy}$  shows higher  $250\ \mu\text{m}$  and lower longer wavelength flux densities than what we would expect based on the average SED in the other bins. To test whether this anomalous

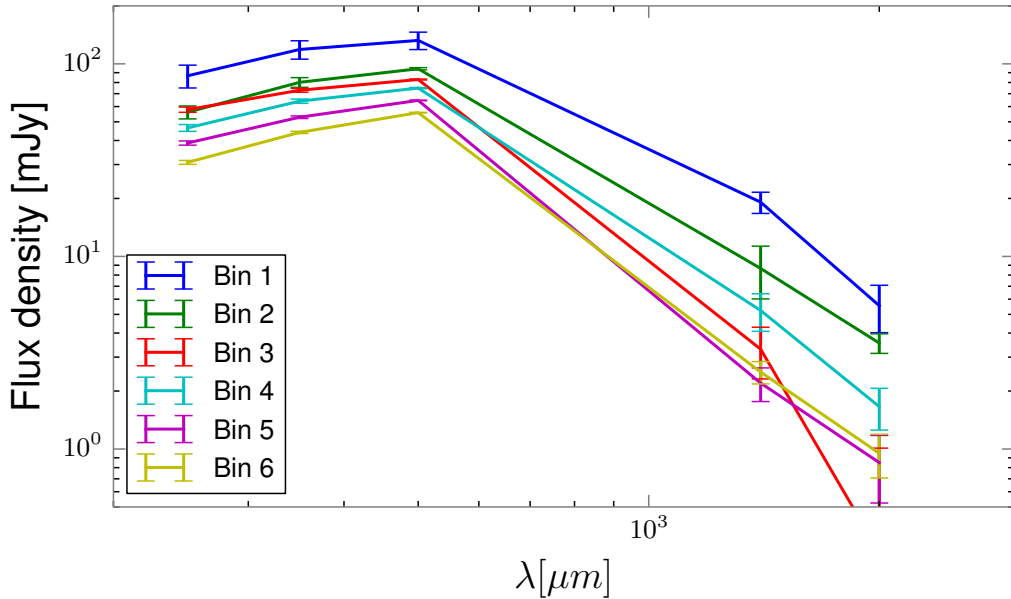


Figure 3.19: Average spectra of the sources falling into the different  $S_{500}$  bins listed in Table 3.3.

behavior is caused by some extreme outliers, or by sources with different SED properties than the rest of our red sources, we will need to investigate the sources belonging in this bin individually. We note, that due to the very steep  $500 \mu\text{m}$  source counts, the bins corresponding to higher  $S_{500}$  values contain significantly fewer galaxies than the lower flux density bins, thus these bins can be more biased by outliers. The successful detection of our sources in the ACT bands indicates that it is worth pursuing high-resolution interferometric follow-up observations of these sources at millimeter wavelengths. These follow-up observations would help us in several ways. Interferometric observations give a much more accurate position for our sources, which is crucial for spectroscopic redshift observations. Additionally the higher resolution and better sensitivity would allow us to investigate in more detail the biasing effects of blending on our number counts.

### 3.6 Summary

We used a map-based detection method similar to Dowell et al. (2014) to search for “red” ( $S_{500} > S_{350} > S_{250}$ ), potentially  $z > 4$  dusty star-forming galaxies in the HeLMS field. The HeLMS survey has a significantly larger area than the HerMES fields studied before, and this allowed us to assemble a catalog of red sources 15 times larger than the

catalog we had before. Spectral energy distribution fits to the SPIRE flux densities of the HeLMS red sources resulted in observed dust temperature and SED peak-wavelength distribution similar to what we measured in the Dowell et al. (2014) sample, showing that we were able to detect a similar population of sources in the HeLMS map. The total number of detected HeLMS red sources confirms previous findings, that there is an excess of luminous dusty star-forming galaxies at high redshifts compared to model predictions. Our large sample, however, also allowed us to investigate the functional form of the differential number counts of these high- $z$  galaxy candidates for the first time. The very steep slope of the  $500\ \mu\text{m}$  differential counts of our sources suggests that the properties of these galaxies are strongly evolving, and they possibly have a significant role in the stellar mass build-up of massive galaxies in the distant Universe. The very high redshift of two of our sources was confirmed by ALMA spectroscopic follow-up observations. So far, all red sources selected for follow-up observations either from the Dowell et al. (2014) sample, or the new HeLMS red galaxy sample described in this thesis, were proven to be indeed at high- $z$ , the majority of them at  $z > 4 - 5$ , and the lowest redshift source is still very distant ( $z > 3$ ). The detection of millimeter-wave emission from our sources in the ACT maps also shows that long-wavelength interferometric follow-up observations of red sources are worth pursuing. In the future, we will extend our spectroscopically confirmed subsample of high- $z$  red sources, and multi-wavelength photometric follow-up observations will allow us to determine the photometric redshift distribution of our population. This will help in the construction of the  $z > 4$  infrared luminosity function, and thus we will be able to determine the contribution of these luminous dusty galaxies to the high- $z$  cosmic star formation history.

# Chapter 4

## Observing SPIRE-selected “red” sources with SCUBA-2

We observed a sample of HerMES-selected “red” ( $S_{500} > S_{350} > S_{250}$ , as discussed in Chapter 3) sources with the SCUBA-2 instrument (Submillimetre Common-User Bolometer Array-2; Holland et al., 2013) on the James Clerk Maxwell Telescope (JCMT) operating at the summit of Mauna Kea in Hawaii. SCUBA-2 is a bolometer camera containing 10,000 detectors and it observes the sky simultaneously in two atmospheric windows at 450 and 850  $\mu\text{m}$ . Due to the telescope’s large 15-m diameter dish, the images observed with SCUBA-2 have significantly better resolution than the SPIRE images obtained by using the 3.5-m diameter *Herschel* mirror. The SCUBA-2 beams have a full-width half maximum of 7.5” and 14.5” at 450 and 850  $\mu\text{m}$ , respectively.

There are several advantages of observing our sources with SCUBA-2. First, obtaining submillimeter flux densities at 850  $\mu\text{m}$  – the long-wavelength side of the peak of the dusty spectral energy distribution – can confirm the thermal nature of the emission and thus can constrain the dust temperature, infrared luminosity, star formation rate and other physical properties of the sources. SCUBA-2 images have larger resolution and lower confusion limits than the SPIRE maps, which allows us to potentially detect overdensities of faint galaxies around these bright red objects. Detecting such overdensities would strengthen the idea that distant dusty starburst galaxies possibly reside in proto-cluster environments (see discussion in Section 1.6).

Our observational campaign had two tiers. First we observed a relatively large sample of red sources at 850  $\mu\text{m}$  to a depth of 4 mJy RMS, well above the confusion limit ( $\sigma_{\text{conf}} < 1$  mJy). Then we selected four of our reddest galaxies, and we mapped a large area field down to 2 mJy RMS around these sources in order to examine their environments. Although the telescope observes the sky simultaneously at both 450  $\mu\text{m}$  and 850  $\mu\text{m}$

wavelengths, the transmission of the atmosphere at  $450\ \mu\text{m}$  is only about half the  $850\ \mu\text{m}$  value; thus in order to obtain high signal-to-noise ratio data at  $450\ \mu\text{m}$  excellent weather quality and very long integration times are needed. Due to the limited telescope time available, we decided to design our observing proposal with the goal to reach the required depth at  $850\ \mu\text{m}$ , and due to the shorter integration times the  $450\ \mu\text{m}$  data we obtained were too noisy to be used in any further analysis.

In this chapter we describe our sample selection, the observations and the data reduction, and we summarize the early results of this observing campaign.

## 4.1 Sample selection

Our sample of red sources was selected from three HerMES fields (Lockman-SWIRE, Bootes and ELAIS-N1), which were visible from the JCMT during the observing semester. The location of these fields and their SPIRE detector noise levels are listed in Table 4.1.

We selected a total of 54 red sources from these fields detected with the map-based search method described in Section 3.1. We required that they look like point-sources at the  $500\ \mu\text{m}$  resolution, and that their SPIRE flux densities follow the relation  $S_{500} > S_{350} > S_{250}$ . We also required that their flux density at  $500\ \mu\text{m}$  should be greater than  $5 \times \sigma_{500}$  but at the same time less than 100 mJy. Above  $S_{500} = 100\ \text{mJy}$  the relative likelihood that a source is strongly lensed, rather than intrinsically luminous, increases dramatically (Negrello et al., 2010). The focus of our study is to find sources with the most intense star formation activity, while finding the bright, lensed ordinary sources is part of a separate program. Since the instrumental noise levels in these HerMES observations are lower than in the HeLMS maps, many of the selected sources are fainter at  $500\ \mu\text{m}$  than 52 mJy (the flux density cutoff in our HeLMS catalog), with the faintest sources having flux densities of  $S_{500} \sim 30\ \text{mJy}$ , but due to the thermal shape of the spectral energy distribution we expect to measure  $850\ \mu\text{m}$  flux densities in the range of 0.3 to  $1.0 \times S_{500}$ , so they should be visible in these SCUBA-2 maps with flux densities at a level of  $> 3\sigma$ .

In the second part of this observational campaign we observed four sources named LSW28, LSW102, XMM30 and XMM26. We required that these sources are “ultra-red”, meaning that their flux densities obey the  $S_{500}/S_{250} > 1.5$  criterion in the smoothed maps. The SPIRE flux densities of the observed sources are listed in Section 4.4 along with the SCUBA-2 flux density measurements.

Field	RA (deg)	Dec (deg)	Area (deg <sup>2</sup> )	$\sigma_{250}$ (mJy)	$\sigma_{350}$ (mJy)	$\sigma_{500}$ (mJy)
Lockman-SWIRE	162.20	58.16	16.1	9.1 (4.9)	8.9 (4.9)	10.8 (5.7)
Bootes	218.15	34.17	10.6	5.3 (3.4)	5.1 (3.4)	6.1 (4.2)
ELAIS-N1	242.55	54.33	3.3	3.4 (2.7)	3.2 (2.8)	3.9 (3.2)

Table 4.1: Location, area and  $1\sigma$  SPIRE detector noise values for the HerMES fields included in the red source sample selection. The noise values are measured in maps created with the nominal SPIRE pixel sizes of  $6''$ ,  $8.333''$  and  $12''$  at 250, 350 and 500  $\mu\text{m}$ , respectively, and the values in parentheses denote the noise values in point-source filtered maps.

## 4.2 Observations

The observations were carried out in April and December 2012. In the first part of the project in order to quickly obtain 850  $\mu\text{m}$  flux densities we observed our sources using a constant velocity “daisy” pattern (Holland et al., 2013). In this observing mode the telescope moves in a precessing ellipsoidal pattern around the observed source, giving a deep coverage in the central 3 arcminute region of the  $\sim 12$  arcminute wide image (see left panel in Fig. 4.1). In the second part of the project we used the rotating “pong-900” pattern (Holland et al., 2013) to obtain large and deep maps with uniform coverage. This observing mode results in a uniformly mapped area with a diameter of  $15'$  around the source (see right on Fig. 4.1).

The optimal integration time for each source depends on the requested depth, the size of the fields, the scanning pattern used and the weather quality at the time of the observation. The integration time to reach a given  $1-\sigma_{850}$  [mJy] depth is calculated as

$$t_{\text{integr}} = \frac{1}{f} \left[ \left( \frac{a}{T_{850}} - b \right) \frac{1}{\sigma_{850}} \right]^2, \quad (4.1)$$

where  $T_{850}$  is a weather-dependent atmospheric transmission factor,  $f$  is a sampling factor,  $(a, b) = (189, 48)$  for the “daisy” observations and  $(a, b) = (407, 104)$  for the “pong-900” pattern.

SCUBA-2 is a ground-based detector, so any signal with intensity  $I_0$  needs to travel through a volume of air; thus the measured intensity  $I_m$  will be attenuated compared to  $I_0$ .  $T_{850}$  describes the atmospheric transmission and it is calculated as the ratio of the

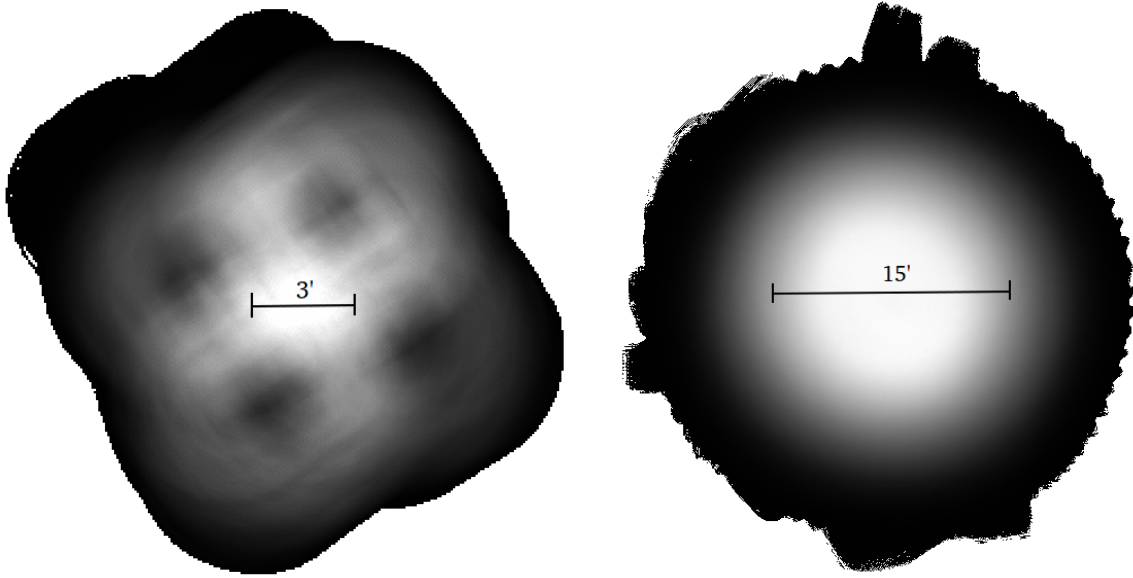


Figure 4.1: Coverage map of the “daisy” (left) and “pong-900” (right) scanning patterns of the JCMT. Bright colors correspond to areas with deep coverage.

measured and incident intensities,

$$T_{850} = \frac{I_m}{I_0} = e^{-\tau_{850}A}, \quad (4.2)$$

where  $A$  is the airmass (the optical path length through Earth’s atmosphere for light from a source on the sky) and  $\tau_{850}$  is the extinction coefficient or opacity at  $850 \mu\text{m}$ . The airmass  $A$  for a source at declination  $\delta$  during transit can be expressed as

$$A = \frac{1}{0.9 \cos \left[ \frac{\pi}{180} (\delta - 19.823) \right]}. \quad (4.3)$$

As described in Dempsey et al. (2013), the opacity is determined based on the amount of precipitable water vapor (PWV, in units of mm) in the atmosphere as

$$\tau_{850} = 0.179 \left[ \text{PWV} / (1\text{mm}) + 0.337 \right]. \quad (4.4)$$

The PWV values are measured with the JCMT’s water vapor monitor (WVM) at 183 GHz along the line-of-sight of the telescope. The neighbouring Caltech Submillimeter Observatory (CSO) has a radiometer that measures the zenith opacity at 225 GHz. Although the WVM has better time resolution than the CSO radiometer, and in general gives a better measurement of the opacity even when the atmosphere is unstable, during stable

Weather Grade	PWV	$\tau_{225}$
Grade 1	<0.83 mm	<0.05
Grade 2	0.83–1.58 mm	0.05–0.08
Grade 3	1.58–2.58 mm	0.08–0.12
Grade 4	2.58–4.58 mm	0.12–0.20
Grade 5	>4.58 mm	>0.20

Table 4.2: Weather grades defined at the JCMT. PWV means the amount of precipitable water vapor in the atmosphere in units of mm, and  $\tau_{225}$  is the opacity measured at 225 GHz at the Caltech Submillimeter Observatory (CSO).

weather conditions the 225 GHz opacity determined from PWV values measured at the zenith with the WVM as  $\tau_{225} = 0.04\text{PWV}_{\text{zen}} + 0.017$  are in excellent agreement with the CSO  $\tau_{225}$  measurements (Dempsey et al., 2013). In practice, the quality (or “grade”) of the weather during JCMT observations is defined based on the CSO  $\tau_{225}$  values. The corresponding PWV and opacity values are listed in Table 4.2.

The  $f$  value in Equation 4.1 is a sampling factor corresponding to the map-making options for SCUBA-2 data. The nominal pixel size of SCUBA-2 maps at  $850\ \mu\text{m}$  is  $4''$ , and the noise in each pixel depends on the number of samples that are projected onto the given pixel. If we know in advance that we want to use pixel sizes different from the nominal size, the final pixel noise will change, and we need to take this into account in the integration time calculation by applying a correction factor  $f$ , determined as

$$f = (\text{used pixel size/default pixel size})^2. \quad (4.5)$$

Additionally, if we are planning to use a point source matched filter during the analysis of the maps, which increases the signal-to-noise ratio in the final products, then the required integration time to reach a given sensitivity will decrease by a factor of  $f = 5$  at  $850\ \mu\text{m}$ .

To carry out the shallower “daisy” observations we applied for telescope time with Grade 3 weather conditions, and we intended our observations to reach an RMS of  $\sigma_{850} = 4\ \text{mJy}$ . This is well above the confusion limit, but since most of our objects are brighter than  $30\ \text{mJy}$  at  $500\ \mu\text{m}$ , we expect to detect these objects at a level of at least  $3\sigma$  in the  $850\ \mu\text{m}$  SCUBA-2 maps if their spectral energy distribution is indeed dominated by thermal dust emission. Using the matched-beam factors, we calculated observing times of 12–15 minutes per source depending on the declination of the target. The deeper “pong” observations were carried out during Grade 2 weather conditions, and we needed 2.5–3 hours of integration time per source to reach  $2\ \text{mJy}$  RMS ( $> 3\sigma$  above the confusion limit) with the matched-beam factors.

The success of any observational campaign depends on the weather conditions during the allocated observation periods, and due to bad weather not all of the proposed sources were observed. In the first part of the project we obtained data for 28 out of 54 sources, and out of the four deep maps XMM30 was only observed for a fraction of the proposed time, so that particular observation did not reach the required RMS.

### 4.3 Data reduction

The SCUBA-2 data reduction pipeline uses components of the Starlink Software Environment (Warren-Smith and Wallace, 1993; Jenness et al., 2009). There are two ways to reduce the raw telescope data. The ORAC-DR data reduction pipeline (Cavanagh et al., 2008) creates maps quickly with the most optimal settings for the given observation type. Additionally, one can use a combination of SMURF (Sub-Millimetre User Reduction Facility; Chapin et al., 2013) and KAPPA (Kernel Application Package; Currie and Berry, 2013) commands directly for more advanced customization options. Post-processing of the maps happens in PICARD (Pipeline for Combining and Analyzing Reduced Data; Gibb et al., 2012).

The maps are constructed with the Dynamic Iterative Map-Maker (DIMM, Chapin et al., 2013), which is part of the SMURF package. We use a configuration file that is optimized to reduce observations of blank fields containing only faint sources. In this configuration the map-maker applies a harsh high-pass filter to the detector timelines at the beginning of data processing to remove fluctuations on spatial scales larger than  $200''$ . Since we are not interested in recovering any large scale structure in these maps, this recipe applies a noise-removal method to each bolometer time stream independently, ignoring any possible correlations between detectors. An extinction correction is also applied during map-making to correct for the signal attenuation caused by the atmosphere. In this step a time varying scaling factor is applied to the data based on PWV measurements with the JCMT waver vapor monitor.

DIMM and the associated pipeline produces a map in units of pW (pikowatt). Orac-DR automatically uses the standard flux conversion factors (FCFs) to convert the maps to units of Jy. These FCFs are determined based on observations of bright calibrator sources with known flux densities (e.g. Uranus). The standard value at  $850\ \mu\text{m}$  is  $\text{FCF}_{850} = 537 \pm 24$  ( $\text{Jy pW}^{-1}$ ), as measured in Dempsey et al. (2013). During the actual observations, calibrator sources close to the target have been observed to make sure that the calibration falls within 5% of the standard value.

Our final maps have pixel sizes of  $4''$ . Very long observations are always split into

shorter timelines. Maps are made from these smaller datasets separately, and in PICARD we can co-add these images using inverse noise-weighting. The most important post-processing step is the application of a point-source matched filter. In this step the algorithm first smooths the image with a broad Gaussian kernel with a FWHM of  $30''$ , and subtracts this map from the original image to remove any large-scale background from the maps. The  $850\ \mu\text{m}$  beam is also smoothed with the same Gaussian, and a weighted convolution is carried out with this modified beam in order to increase the point-source detectability. For a raw map  $M(x, y)$  and an error map  $\sigma(x, y)$  the convolution with the beam  $P(x, y)$  is calculated as

$$M_{\text{filt}}(x, y) = \frac{[M_{\text{raw}}(x, y)/\sigma^2(x, y)] \otimes P(x, y)}{[1/\sigma^2(x, y)] \otimes [P^2(x, y)]}, \quad (4.6)$$

and after filtering the variance map becomes

$$\sigma_{\text{filt}}^2(x, y) = \frac{1}{[1/\sigma^2(x, y)] \otimes [P^2(x, y)]}. \quad (4.7)$$

In the resulting filtered maps the flux density of the detected sources is determined by their peak pixel values.

## 4.4 Results and discussion

Here we present the results of our two observing campaigns and our early findings, while a more detailed analysis of this dataset will be part of future projects, that also include follow-up data from several other telescopes at different wavelengths.

### 4.4.1 Daisy observations

The SPIRE 250, 350 and  $500\ \mu\text{m}$  flux densities, and the SCUBA-2  $850\ \mu\text{m}$  flux density values of our observed sources are listed in Table 4.3, and postage-stamp images of these objects are shown on Figure 4.2 (a,b,c,d). The SPIRE flux densities are measured from the nominal resolution matched-filtered maps, except for the sources that appear to be blends of several sources in the 250 and/or  $350\ \mu\text{m}$  maps. These sources are flagged with a star symbol in Table 4.3, and the quoted SPIRE flux densities of these objects correspond to the values in the maps that are smoothed to the  $500\ \mu\text{m}$  resolution. We did not discard any blends from our initial sample, since we expect that even blended objects should contain at least one red source if they appear to be red in the smoothed maps. We

note, that the observed sample was selected in the early stages of the red source search project, when we categorized sources as being red based on their smoothed flux densities. As we discussed in Section 3.1.4, the flux densities measured in the nominal resolution maps are less biased by the positional uncertainties, so whenever possible, we quote the latter values here. This is the reason why some of the sources listed in Table 4.3 have a maximum flux density at  $350\ \mu\text{m}$ .

To check whether the measured  $850\ \mu\text{m}$  flux densities of these sources are in agreement with the values predicted from the SPIRE fluxes alone, we fit a modified blackbody spectrum to the measured SPIRE and SCUBA-2 flux densities. As in Section 3.3, we use an optically thick SED model,

$$S_\nu = (1 - e^{-\tau_\nu})B_\nu(T_d)\Omega_s, \quad (4.8)$$

where  $B_\nu(T_d)$  is the Planck function,  $\Omega_s$  is the solid angle of the source,  $\tau_\nu = (\nu/\nu_0)^\beta$  is the optical depth,  $\beta$  is the dust grain spectral emissivity index, and  $\nu_0$  is the frequency where  $\tau_\nu = 1$  and the dust becomes optically thick. As we discussed in detail in Section 3.3 we marginalize over the Gaussian priors  $\beta = 1.8 \pm 0.3$  and  $\lambda_0(1+z) = (1100 \pm 400)\ \mu\text{m}$ . The fitted curves are shown on Figure 4.3 (a, b, c, d, e).

From Figure 4.2 and Table 4.3 it is clearly seen that most of our sources with a  $> 3\sigma$  detection in SCUBA-2 (LSW20, 28, 31, 36, BOOTES17, 23, 24, 28, 29, 33, 50, ELAIS-N11) have bright and isolated counterparts in the SPIRE maps. Figure 4.3 shows that the measured SCUBA-2 fluxes of these sources are in good agreement with the SPIRE flux density values, thus we can confirm that the luminosity of these sources is dominated by thermal dust emission and their SED is best fitted with an optically thick modified blackbody curve, similarly to the red sources selected in the HeLMS maps. We note, that many of these isolated sources have slightly higher  $500\ \mu\text{m}$  flux densities than our fitted values. Since we only select sources with  $S_{500} > S_{350}$ , we are introducing a bias because we are more likely to find objects with their  $500\ \mu\text{m}$  flux densities scattered higher than the real value. The number counts simulations we describe in Section 3.2.1 take this effect into account.

Our sources that look blended in the SPIRE maps typically show anomalously high  $500\ \mu\text{m}$  flux densities compared to the measured SCUBA-2 flux. Our reason to include these sources in the catalog is that we expect that at least one of the components of the blend should be red in order to produce red colors in the smoothed maps. The measured  $500\ \mu\text{m}$  flux density of such a source will be the co-added flux density of all components of the blend. If we assume that red sources are rare enough that they

Name	$S_{250}$ (mJy)	$S_{350}$ (mJy)	$S_{500}$ (mJy)	$S_{850}$ (mJy)	$\text{SNR}_{850}$
LSW19*	$27.4 \pm 7.6$	$42.3 \pm 6.9$	$41.9 \pm 6.5$	$10.6 \pm 3.9$	2.7
LSW20	$17.6 \pm 4.4$	$36.6 \pm 4.8$	$43.9 \pm 5.5$	$30.0 \pm 4.0$	7.5
LSW22*	$22.2 \pm 5.4$	$36.8 \pm 5.2$	$43.4 \pm 6.3$	$9.1 \pm 4.0$	2.3
LSW28	$33.4 \pm 5.2$	$55.9 \pm 4.7$	$60.0 \pm 5.1$	$40.5 \pm 4.0$	10.1
LSW31	$43.3 \pm 4.7$	$58.6 \pm 5.2$	$52.3 \pm 5.3$	$26.1 \pm 4.0$	6.5
LSW36	$55.3 \pm 6.2$	$63.6 \pm 6.8$	$62.5 \pm 7.0$	$21.8 \pm 3.5$	6.2
LSW37*	$26.9 \pm 5.0$	$45.3 \pm 4.6$	$48.7 \pm 6.2$	$8.2 \pm 3.9$	2.1
LSW38*	$25.3 \pm 7.8$	$37.9 \pm 7.1$	$47.2 \pm 7.6$	$0.6 \pm 3.7$	0.2
LSW40*	$49.0 \pm 6.8$	$51.0 \pm 5.8$	$53.7 \pm 7.5$	$-0.1 \pm 3.7$	0.0
LSW41	$26.9 \pm 8.6$	$28.8 \pm 6.3$	$45.2 \pm 9.2$	$11.7 \pm 4.1$	2.9
LSW42	$19.1 \pm 5.2$	$43.3 \pm 4.8$	$44.4 \pm 6.1$	$11.3 \pm 4.0$	2.9
LSW43*	$35.7 \pm 4.7$	$45.9 \pm 4.7$	$49.8 \pm 6.2$	$4.8 \pm 3.6$	1.3
LSW44	$28.6 \pm 5.4$	$36.7 \pm 5.3$	$45.2 \pm 5.9$	$11.7 \pm 4.2$	2.8
BOOTES17	$25.8 \pm 4.9$	$38.1 \pm 5.1$	$43.8 \pm 5.9$	$14.5 \pm 3.6$	4.0
BOOTES21*	$12.8 \pm 4.1$	$36.2 \pm 4.4$	$49.5 \pm 4.6$	$15.4 \pm 3.7$	4.2
BOOTES23	$33.9 \pm 5.1$	$51.2 \pm 5.0$	$52.5 \pm 6.0$	$21.7 \pm 3.6$	6.0
BOOTES24	$28.7 \pm 4.9$	$49.6 \pm 5.0$	$55.8 \pm 5.9$	$15.8 \pm 3.8$	4.2
BOOTES25*	$18.3 \pm 4.8$	$36.2 \pm 5.1$	$44.1 \pm 6.2$	$11.9 \pm 4.1$	2.9
BOOTES27	$24.6 \pm 5.2$	$30.0 \pm 5.6$	$36.9 \pm 5.5$	$4.2 \pm 3.8$	1.1
BOOTES28	$64.1 \pm 4.9$	$87.4 \pm 5.0$	$75.4 \pm 5.7$	$15.4 \pm 3.6$	4.3
BOOTES29	$64.0 \pm 5.3$	$74.5 \pm 5.1$	$64.8 \pm 5.5$	$17.6 \pm 4.3$	4.1
BOOTES33	$53.9 \pm 2.7$	$57.6 \pm 2.7$	$47.4 \pm 3.0$	$12.5 \pm 3.7$	3.4
BOOTES34	$23.6 \pm 5.2$	$34.7 \pm 5.2$	$37.2 \pm 6.3$	$6.8 \pm 3.7$	1.8
BOOTES37	$24.3 \pm 5.2$	$27.2 \pm 5.0$	$43.3 \pm 5.9$	$11.3 \pm 4.0$	2.8
BOOTES39	$15.3 \pm 5.0$	$29.6 \pm 5.1$	$28.3 \pm 5.5$	$6.1 \pm 3.7$	1.7
BOOTES42	$32.7 \pm 3.9$	$46.1 \pm 4.3$	$35.4 \pm 4.8$	$9.7 \pm 3.4$	2.9
BOOTES50	$16.9 \pm 5.3$	$28.1 \pm 5.3$	$36.9 \pm 6.1$	$14.4 \pm 3.7$	3.9
ELAISN11	$19.2 \pm 2.9$	$24.3 \pm 2.9$	$27.6 \pm 3.4$	$11.1 \pm 3.3$	3.3

Table 4.3: SPIRE 250, 350 and 500  $\mu\text{m}$  and SCUBA-2 850  $\mu\text{m}$  flux densities and the 850  $\mu\text{m}$  signal-to-noise ratio of our observed sources. The SPIRE flux densities are measured from the nominal resolution maps, except for the sources marked with a star symbol, where the flux densities could not be determined due to blending effects. Here we quote the flux density values we measured from maps smoothed to the same resolution.

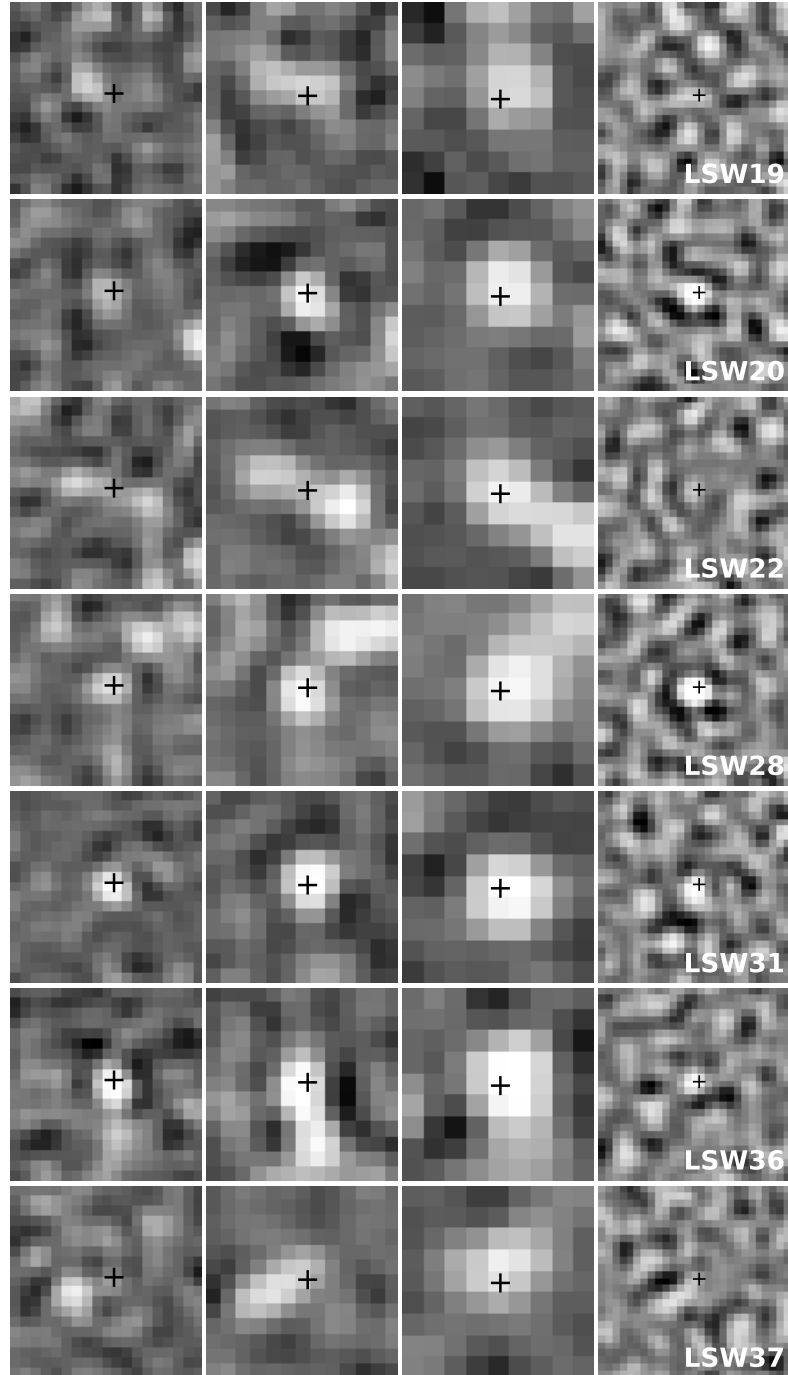


Figure 4.2: (a.) Postage-stamp images showing  $1.8' \times 1.8'$  area around our sources observed with “daisy” scans. From left to right we show the SPIRE 250, 350 and  $500 \mu\text{m}$  images and the SCUBA-2  $850 \mu\text{m}$  image, respectively. The SPIRE images are scaled between  $-5\sigma$  and  $+10\sigma$ , and the SCUBA-2 images are scaled between  $-3\sigma$  and  $+4\sigma$  for better visibility.

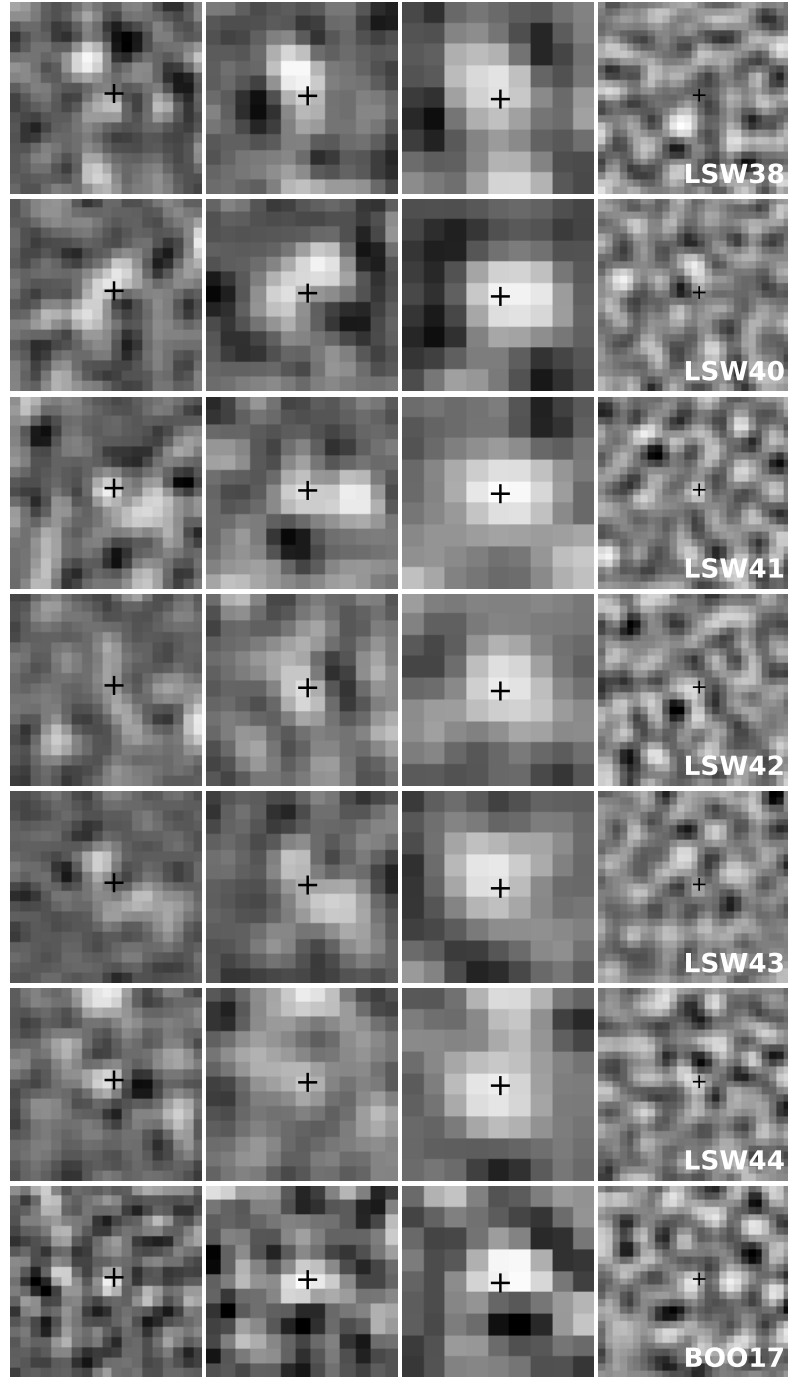


Figure 4.2: (b.) Postage-stamp images showing  $1.8' \times 1.8'$  area around our sources observed with “daisy” scans. From left to right we show the SPIRE 250, 350 and 500  $\mu\text{m}$  images and the SCUBA-2 850  $\mu\text{m}$  image, respectively. The SPIRE images are scaled between  $-5\sigma$  and  $+10\sigma$ , and the SCUBA-2 images are scaled between  $-3\sigma$  and  $+4\sigma$  for better visibility.

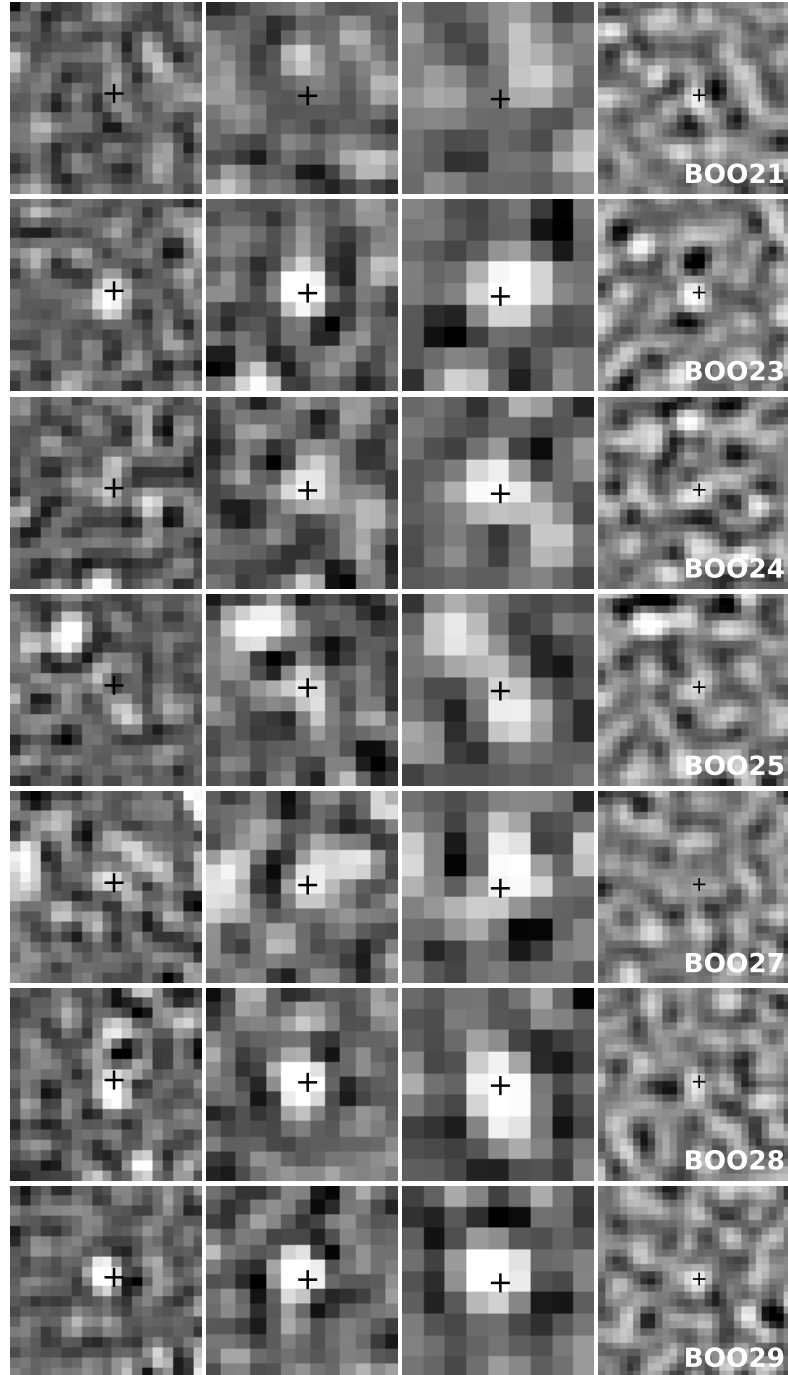


Figure 4.2: (c.) Postage-stamp images showing  $1.8' \times 1.8'$  area around our sources observed with “daisy” scans. From left to right we show the SPIRE 250, 350 and  $500 \mu\text{m}$  images and the SCUBA-2  $850 \mu\text{m}$  image, respectively. The SPIRE images are scaled between  $-5\sigma$  and  $+10\sigma$ , and the SCUBA-2 images are scaled between  $-3\sigma$  and  $+4\sigma$  for better visibility.

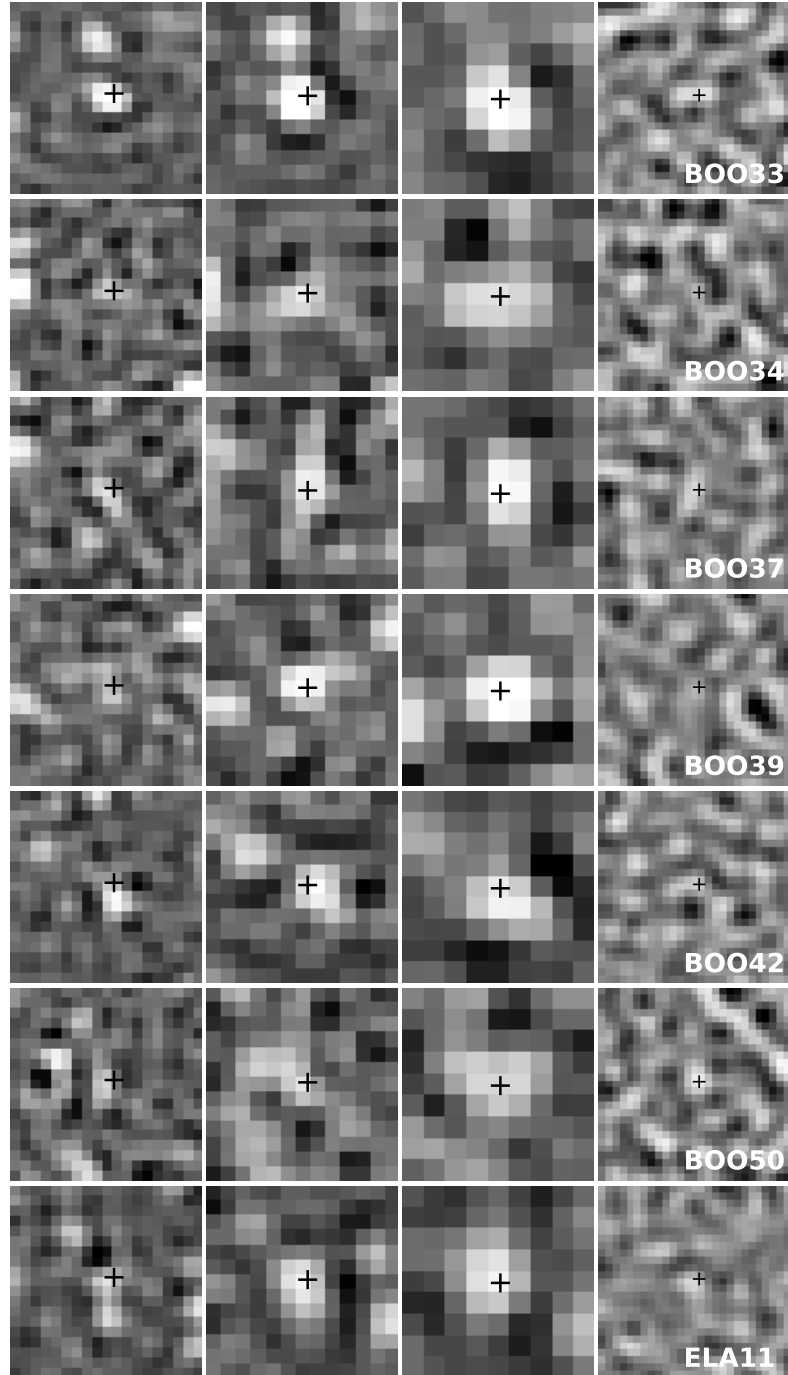


Figure 4.2: (d.) Postage-stamp images showing  $1.8' \times 1.8'$  area around our sources observed with “daisy” scans. From left to right we show the SPIRE 250, 350 and  $500 \mu\text{m}$  images and the SCUBA-2  $850 \mu\text{m}$  image, respectively. The SPIRE images are scaled between  $-5\sigma$  and  $+10\sigma$ , and the SCUBA-2 images are scaled between  $-3\sigma$  and  $+4\sigma$  for better visibility.

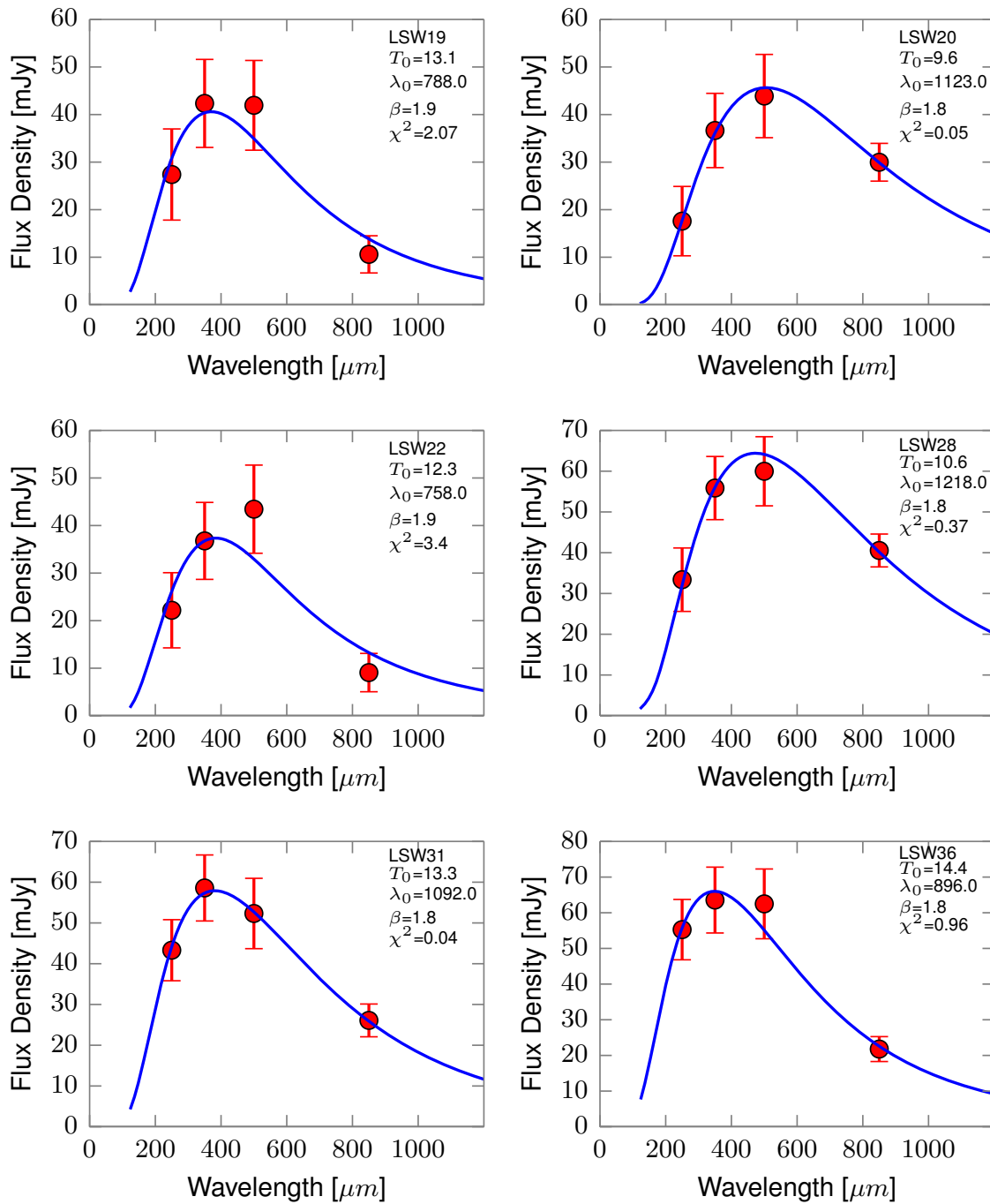


Figure 4.3: (a.) Modified blackbody SED fits to the SPIRE 250, 350 and 500  $\mu\text{m}$  and SCUBA-2 850  $\mu\text{m}$  flux densities.

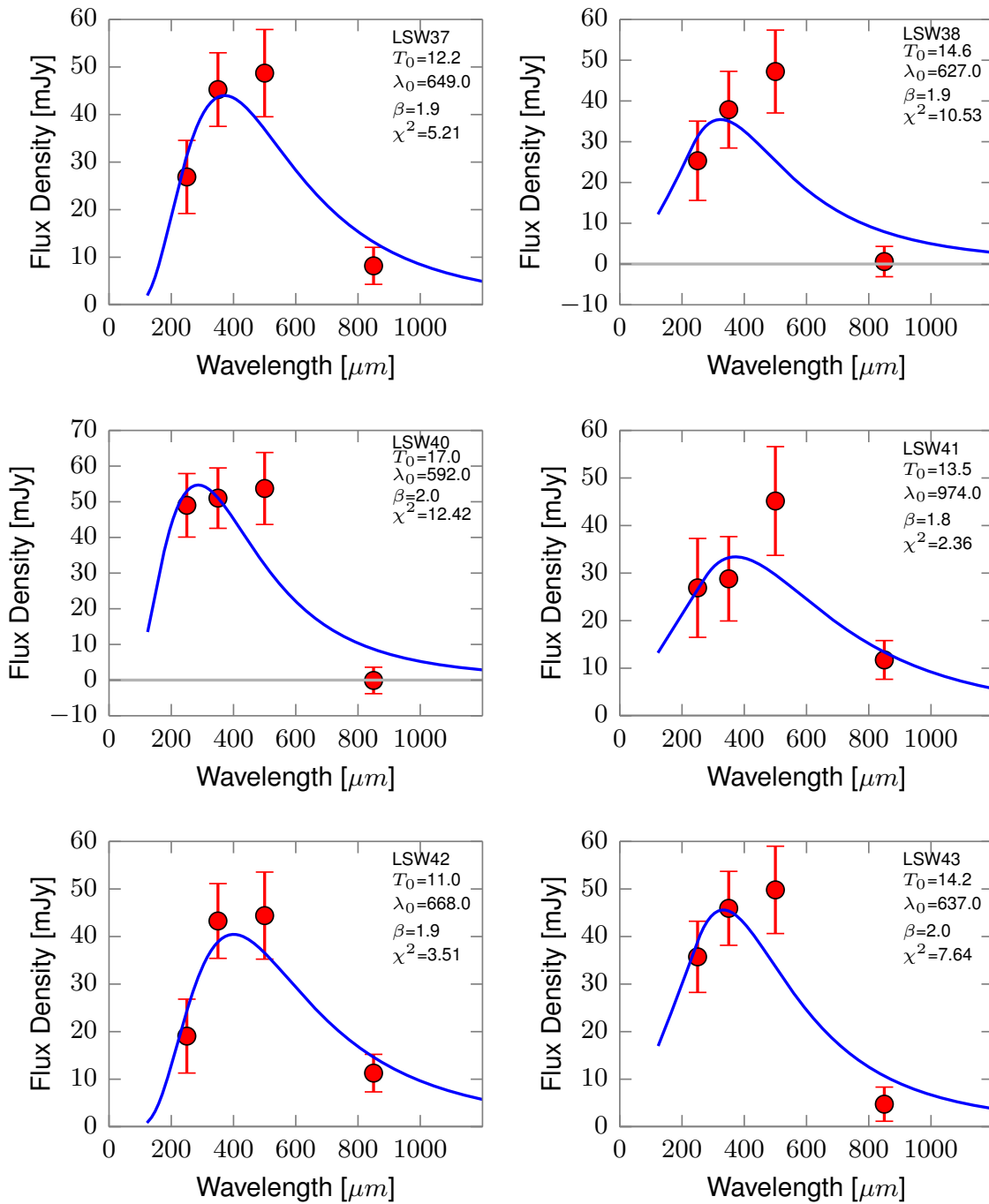


Figure 4.3: (b.) Modified blackbody SED fits to the SPIRE 250, 350 and 500  $\mu\text{m}$  and SCUBA-2 850  $\mu\text{m}$  flux densities.

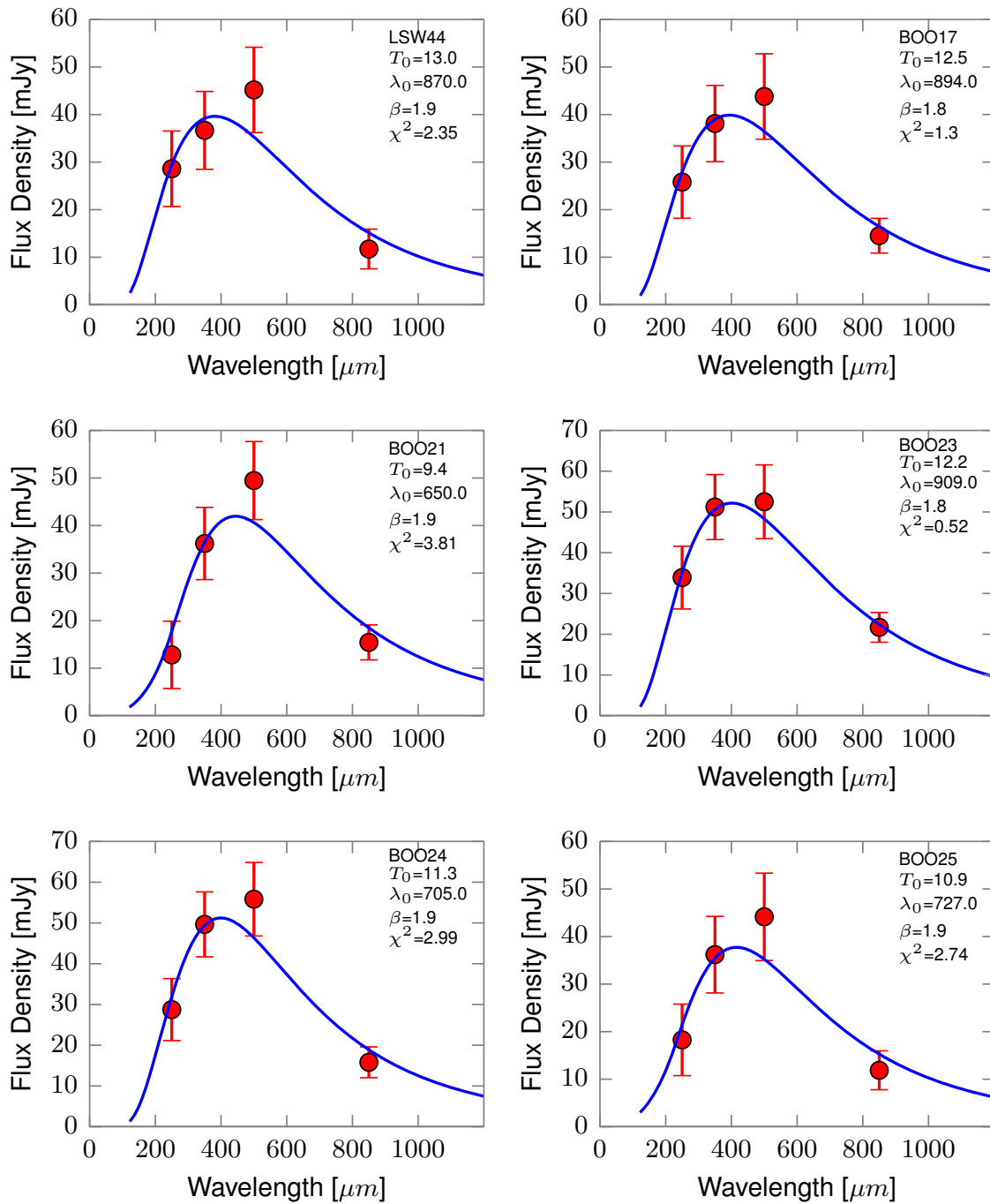


Figure 4.3: (c.) Modified blackbody SED fits to the SPIRE 250, 350 and 500  $\mu\text{m}$  and SCUBA-2 850  $\mu\text{m}$  flux densities.

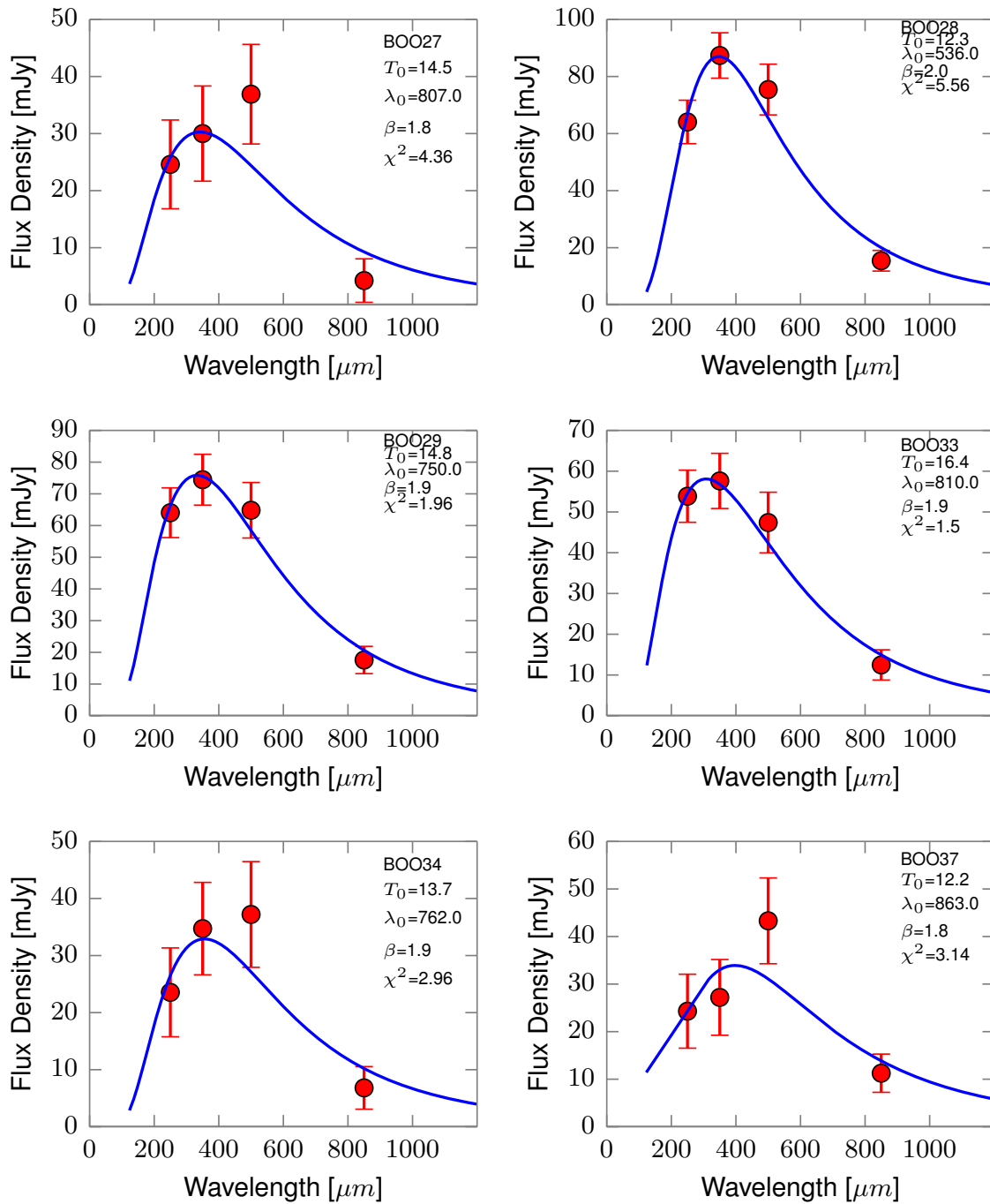


Figure 4.3: (d.) Modified blackbody SED fits to the SPIRE 250, 350 and 500  $\mu\text{m}$  and SCUBA-2 850  $\mu\text{m}$  flux densities.

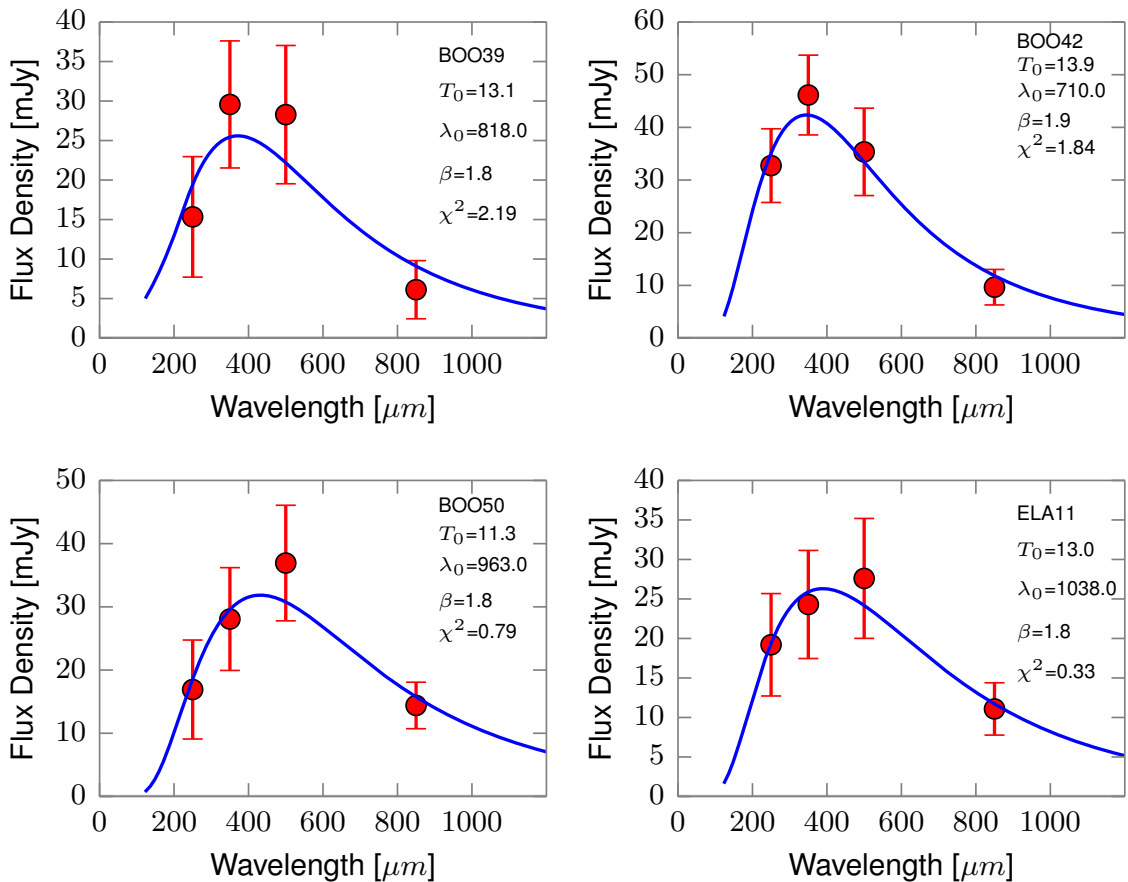


Figure 4.3: (e.) Modified blackbody SED fits to the SPIRE 250, 350 and 500  $\mu\text{m}$  and SCUBA-2 850  $\mu\text{m}$  flux densities.

are most likely to be blended with a non-red source, then it is possible that at longer wavelengths the contribution from this non-red object will become negligible, and the measured emission from the red source will be fainter than what the biased 500  $\mu\text{m}$  flux density would suggest. The fact that we often see a 2–3 $\sigma$  source in the SCUBA-2 images at the positions of these confused objects seems to support this scenario, and while the measured SPIRE flux densities are biased high, we cannot simply discard these objects as spurious detections. This result agrees with our findings in Section 3.5, where we show that even if we include the possible blends in our stacks we still detect a source at millimeter wavelengths. To examine the detailed properties of blended galaxies higher resolution images are needed, but both our SCUBA-2 and ACT measurements suggest

that these blends indeed contain at least one red source.

#### 4.4.2 Pong observations

The matched-filtered “pong” maps of LSW28, LSW102, XMM26 and XMM30 are shown on Figure 4.4. Each map has a diameter of  $15'$  (a 1 arcmin angular scale corresponds to a  $\sim 0.39$  Mpc physical scale at  $z \sim 5$ ), so they cover an area of  $177 \text{ arcmin}^2$  around the central bright red source. These pong maps are typically created from five observations of the same field, each  $\sim 40$  minutes long, and these scans are co-added in PICARD using inverse-variance weighting. Since the weather conditions are not always stable during long observations, and since the separate scans of the same field are often observed on different days, the final noise values will be different in each of these observed fields. Additionally, XMM30 was only observed two times, so the noise in that map is much higher than in the other three fields. The noise levels in the central region of the matched-filtered maps are  $\sigma_{\text{LSW28}} = 2.1 \text{ mJy}$ ,  $\sigma_{\text{LSW102}} = 2.5 \text{ mJy}$ ,  $\sigma_{\text{XMM26}} = 2.3 \text{ mJy}$  and  $\sigma_{\text{XMM30}} = 3.3 \text{ mJy}$ . As expected, our central sources are detected in each of these maps with a very high signal-to-noise ratio:  $S_{\text{LSW28}} = 34.8 \text{ mJy}$  ( $17\sigma$ ),  $S_{\text{LSW102}} = 72.8 \text{ mJy}$  ( $29\sigma$ ),  $S_{\text{XMM26}} = 18.5 \text{ mJy}$  ( $8\sigma$ ) and  $S_{\text{XMM30}} = 32.8 \text{ mJy}$  ( $10\sigma$ ).

To investigate whether there are over-densities of fainter sources around these galaxies, we create a signal-to-noise ratio map from our observations, and we search for peaks with  $\text{SNR} > 3.75$  in these maps. This SNR cut is needed in order to reduce the chance of false detections (e.g. Geach et al., 2013; Casey et al., 2013; Chen et al., 2013). The detected sources are highlighted with white circles on Figure 4.4, and their measured SCUBA-2 flux densities along with their separation from the central red source are listed in Table 4.4. We also list the SPIRE flux densities for the sources that are visible in the *Herschel* maps. We check the possibility of false detections by creating two separate maps for each field from only half of the data, and we examine the positions of the detected sources in these maps. All of our sources are visible in both halves of the data, thus we conclude that they are not noise peaks. Note, that the  $\text{SNR} > 3.75$  cut corresponds to different flux density limits in the four maps. We detect eight sources around LSW28 with flux densities  $S_{850} \gtrsim 7.8 \text{ mJy}$ , six sources around LSW102 with  $S_{850} \gtrsim 9.4 \text{ mJy}$ , seven sources around XMM26 with  $S_{850} \gtrsim 8.6 \text{ mJy}$ , and one source around XMM30 with  $S_{850} \gtrsim 12.3 \text{ mJy}$ .

To improve our statistics, we combine the results for our three fields with similar noise levels (LSW28, LSW102 and XMM26), and we investigate the average number of submillimeter-detected galaxies around these red sources. On Figure 4.5 we plot the

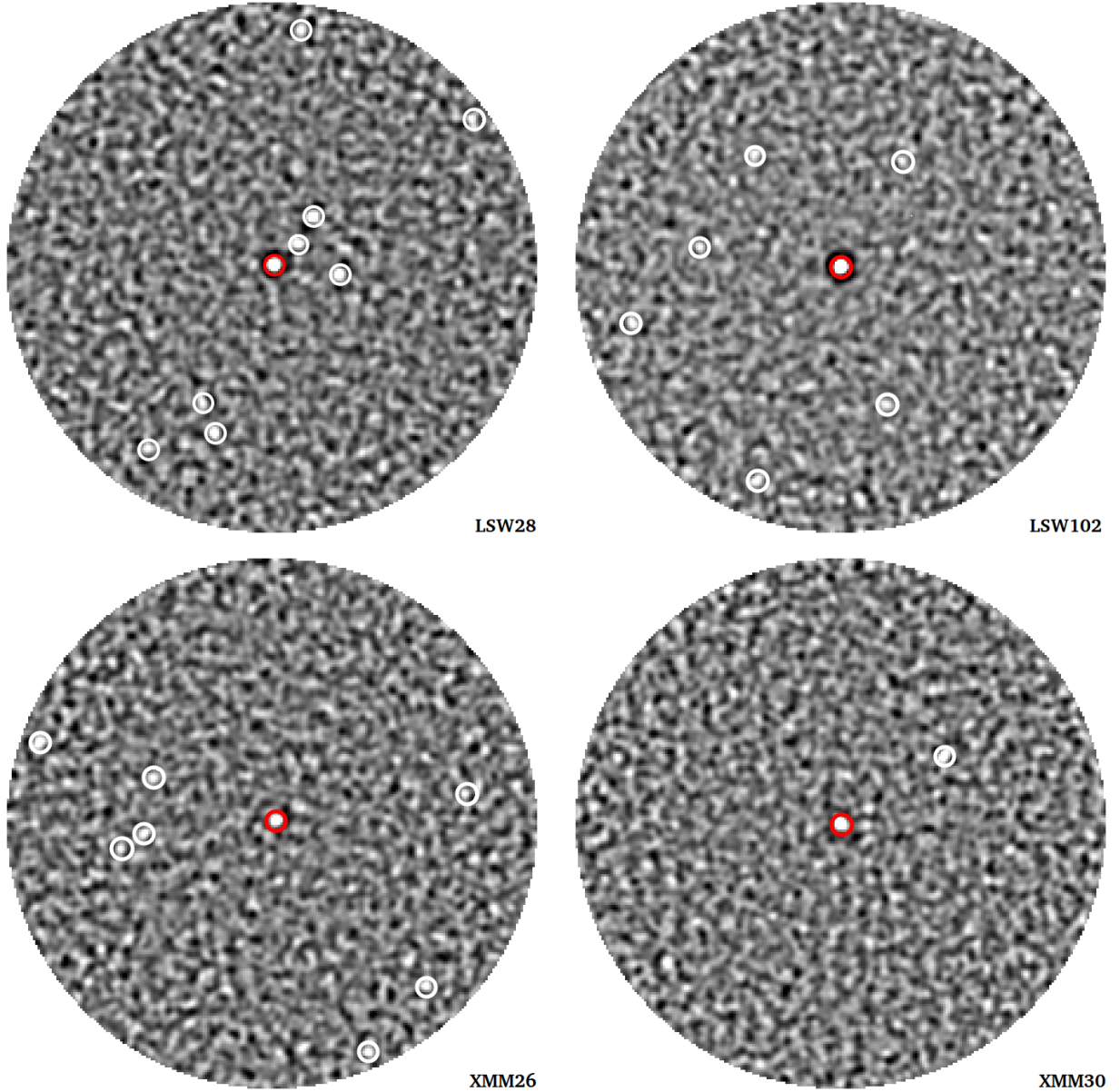


Figure 4.4:  $850\ \mu\text{m}$  “pong” observations of our sources LSW28, LSW102, XMM26, XMM30 (highlighted with red square symbols). The maps are matched-filtered, and the sources detected around our targets with flux densities above  $3.75\sigma$  are highlighted with white circles.

cumulative number counts of the combined fields and we compare our results to the Coppin et al. (2006) source densities measured in a blank field survey. The resulting number counts shows no obvious evidence for an over-density of faint galaxies around our red sources. Additionally, we can also see from Table 4.4 that the observed colors of the sources that have a counterpart in the SPIRE maps are usually not red, which

ID	$S_{850}$ (mJy)	SNR <sub>850</sub>	Distance (arcmin)	$S_{250}$ (mJy)	$S_{350}$ (mJy)	$S_{500}$ (mJy)
LSW28						
0	$34.8 \pm 2.06$	16.92	0.0	33.38	55.86	59.98
1	$15.69 \pm 2.05$	7.65	1.7	64.52	73.43	46.27
2	$13.49 \pm 2.05$	6.58	1.8	28.10	38.86	26.60
3	$12.39 \pm 2.10$	5.90	5.0	45.49	57.56	55.38
4	$11.49 \pm 2.05$	5.61	0.9	30.22	43.14	35.25
5	$8.4 \pm 2.07$	4.06	4.4	-	-	-
6	$8.53 \pm 2.26$	3.77	6.3	30.79	18.79	14.26
7	$9.25 \pm 2.46$	3.75	6.7	20.53	14.42	-
8	$9.48 \pm 2.53$	3.75	7.0	10.55	12.87	21.54
LSW102						
0	$72.80 \pm 2.51$	29.04	0.0	49.71	118.14	140.40
1	$11.43 \pm 2.82$	4.05	6.4	-	-	-
2	$10.86 \pm 2.72$	3.99	6.1	-	-	-
3	$9.83 \pm 2.53$	3.88	4.0	-	-	-
4	$9.79 \pm 2.53$	3.87	3.5	-	-	-
5	$9.56 \pm 2.51$	3.81	4.1	-	-	-
6	$9.48 \pm 2.53$	3.75	4.0	-	-	-
XMM26						
0	$18.48 \pm 2.31$	8.01	0.0	38.09	58.89	69.71
1	$10.48 \pm 2.30$	4.56	3.8	36.99	39.72	35.67
2	$11.02 \pm 2.69$	4.10	7.1	29.62	22.62	12.63
3	$9.58 \pm 2.37$	4.04	5.4	10.14	7.97	13.51
4	$9.17 \pm 2.28$	4.01	3.7	-	-	-
5	$9.19 \pm 2.32$	3.97	4.5	-	-	-
6	$10.7 \pm 2.71$	3.94	7.0	16.78	20.16	-
7	$9.61 \pm 2.51$	3.83	6.3	-	-	-
XMM30						
0	$32.79 \pm 3.41$	9.61	0.0	23.77	39.11	55.59
1	$20.58 \pm 3.35$	6.15	3.5	35.40	54.35	55.32

Table 4.4: Sources detected with  $S_{850} > 3.75\sigma$  around LSW28, LSW102, XMM26 and XMM30. ID = 0 refers to the central red source in all cases. See also Figure 4.4

might suggest that they are at a different redshift and are not physically associated with the central source. The one really bright source we find 3.5' away from XMM30 has red colors similarly to the central source, which could suggest that these two sources might be

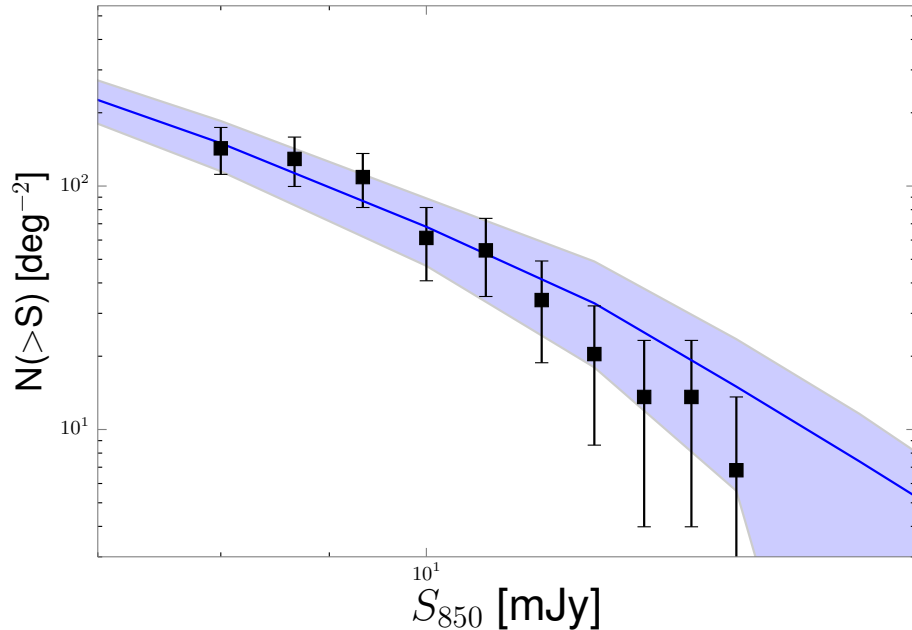


Figure 4.5: Cumulative 850  $\mu\text{m}$  number counts of the three combined 177 arcmin<sup>2</sup> fields mapped around our sources LSW28, LSW102 and XMM26. The black symbols represent our raw counts with Poisson errorbars. The blue solid line shows the Coppin et al. (2006) blank-field number counts with the shaded region corresponding to  $\pm 1\sigma$  uncertainties of these counts.

physically related to each other. Unfortunately the signal-to-noise ratio of the XMM30 map is too low to find a larger number of faint sources, so this one detection alone is not a strong indicator of an over-density; however, the close proximity of another bright red source makes this galaxy an ideal target for future follow-up observations.

On Figure 4.6 we plot the cumulative number of sources detected within different radii of the central red source, and we compare this to the distribution we would expect to observe if our sources were distributed in an unclustered fashion within the observed area. We do not see any strong deviation from the expected shape that would suggest angular clustering of the detected sources.

Several high redshift dusty starburst galaxies are known to reside in over-dense regions (e.g. Chapman et al., 2001; Daddi et al., 2009; Capak et al., 2011), and it was expected, that the red sources we select could also trace proto-clusters. The lack of observed over-density around our red sources is similar to the result described in Robson et al. (2014), who mapped the region around HFLS3 (Riechers et al., 2013), the  $z = 6.34$  red source found with our map-based search method during our analysis of the FLS field. One

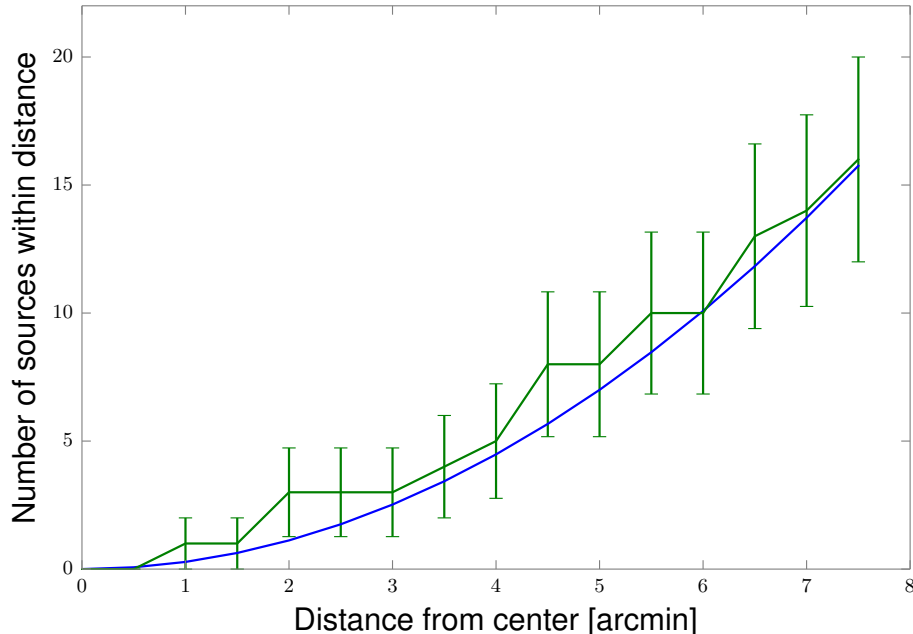


Figure 4.6: Cumulative number of sources within different radii of the central red source for the combined fields around LSW28, LSW102 and XMM26. The solid blue line shows the expected distribution from an unclustered source distribution.

might argue, that the possible companion galaxies might be even fainter than our current flux limits, or that they contain smaller amount of dust than expected. Laporte et al. (2015) carried out an analysis to search for Lyman-break galaxies (an unobscured high- $z$  galaxy population) in the vicinity of HFLS3, but they also came to the conclusion that the environment of HFLS3 shows no evidence of an over-density of similar redshift star forming galaxies. Robson et al. (2014) show that current large-scale structure simulations would predict that we should find an over-density around such a luminous source. But, on the other hand, our current observations of three red sources suggest, that it is not uncommon to find distant starburst galaxies without a clear over-density around them. This shows how important it is to obtain more observational constraints when modelling the evolution of star formation in the large-scale structures in the Universe.

## 4.5 Summary

We described a follow-up observational campaign for SPIRE-selected “red” ( $S_{500} > S_{350} > S_{250}$ ) galaxies with the SCUBA-2 instrument at  $850\ \mu\text{m}$ . We found that the observed  $850\ \mu\text{m}$  flux densities of sources that appear isolated in all three SPIRE wavelengths are

consistent with the values we would predict by fitting a thermal modified blackbody SED to the SPIRE flux densities alone. Together with other multi-wavelength follow-up observations in the future these additional photometry points will allow us to determine the photometric redshifts and constrain some physical properties of these sources (e.g.  $L_{\text{IR}}$ , dustmass, star formation rate). The observation of sources that appear to be a single object at the  $500\ \mu\text{m}$  resolution, but break up into multiple components in the higher resolution SPIRE maps resulted in lower signal-to-noise ratio  $850\ \mu\text{m}$  detections than we would have expected based on the  $500\ \mu\text{m}$  flux densities alone. At the position of most of these blends we still see a faint SCUBA-2 source; this suggests that at least one of the galaxies in the blend is a red source, although its  $500\ \mu\text{m}$  flux density is boosted high. This result shows that the higher-resolution of the SCUBA-2 instrument can help us assess the biasing effect of blending on our  $500\ \mu\text{m}$  number counts of red sources described in Chapter 3. We also examined the environment of four of our red sources. On average, we cannot see an over-density of fainter submillimeter galaxies around these sources that could suggest that these galaxies reside in a proto-cluster environment. This can suggest that environment has a smaller role in triggering extreme star formation events than previously predicted, or that these high-redshift dusty galaxies do not always reside in a proto-cluster environment, as previously thought.

# Chapter 5

## Average dusty star-formation activity in Sunyaev-Zel'dovich-selected galaxy clusters

Studying the star formation history of galaxy clusters – the largest gravitationally bound structures in the Universe – can help us assess whether the environment in which galaxies reside plays a role in triggering or quenching star formation activity. As we discussed in Section 1.1, in the local Universe there is no observational evidence for significant star formation activity in the cores of massive virialized structures; only galaxies in the outskirts of these clusters form new stars at a moderate rate. There is an ongoing debate whether this locally observed morphology-density relation universally holds at all redshifts, or whether there is a reversal in this relation in the high- $z$  Universe. There is observational evidence both for and against the theory that at higher redshifts star formation happens in denser environments.

Galaxy clusters can contain hundreds to thousands of individual galaxies, but the dominant baryonic component of these structures is the intra-cluster gas, having a mass larger by a factor of ten, than the total mass of the cluster-member galaxies (e.g. Kravtsov and Borgani, 2012). This hot, ionized gas is in hydrostatic equilibrium in the deep potential well of the cluster, and it is heated to a temperature of  $10^7$ – $10^8$  K. Due to the very hot temperature, the gas emits X-rays in the form of thermal bremsstrahlung radiation. Apart from identifying clusters by their optical richness (e.g. Abell, 1958; Gunn et al., 1986), the detection of this X-ray luminosity is one of the most widely used methods to find clusters of galaxies. The biggest limitation of this technique is, however,

the decrease of the intensity of the X-ray radiation with increasing distance, limiting the range of redshifts where these large clusters can be detected.

A redshift-independent way of finding massive galaxy clusters is based on the detection of the Sunyaev-Zel'dovich effect (Sunyaev and Zel'dovich 1972, and see reviews e.g. in Birkinshaw 1999; Carlstrom et al. 2002) in cosmic microwave background (CMB) measurements. The cosmic microwave background radiation originates from the epoch of recombination, when photons decoupled from the matter in the Universe and started to propagate freely. This background radiation has a remarkably uniform temperature of 2.725 K. Very small fluctuations of this temperature trace the primordial matter density perturbations, but secondary anisotropies can also emerge due to the CMB photons propagating through structures along the line of sight. As the CMB photons pass through the hot intra-cluster gas in the core of massive galaxy clusters, the hot electrons in the gas can scatter these photons through inverse Compton scattering. As a result, the temperature and thus the energy of the CMB photons increases, and the blackbody spectrum of the cosmic microwave background becomes distorted, since photons are scattered from the long wavelength Rayleigh-Jeans side of the peak of the spectrum to the shorter wavelength Wien side. This distortion is called the Sunyaev-Zel'dovich (SZ) effect, and in practice it is observed as a relative change in the CMB temperature as

$$\frac{\Delta T_{\text{SZ}}}{T_{\text{CMB}}} = f_{\text{SZ}}(x) y = f_{\text{SZ}}(x) \int n_e \frac{k_{\text{B}} T_e}{m_e c^2} \sigma_{\text{T}} d\ell, \quad (5.1)$$

where  $x = h\nu/(k_{\text{B}}T_{\text{CMB}})$  is a dimensionless frequency,  $y$  is called the Compton  $y$ -parameter,  $n_e$  is the electron number density,  $\sigma_{\text{T}}$  is the Thomson scattering cross-section,  $T_e$  is the temperature of the electrons in the hot gas,  $k_{\text{B}}$  is the Boltzmann constant and  $d\ell$  represents the the line of sight extent of the cluster. The frequency dependence of the distortion is given by the function  $f_{\text{SZ}}(x)$  as

$$f_{\text{SZ}}(x) = \left( x \frac{e^x + 1}{e^x - 1} - 4 \right) (1 + \delta_{\text{SZ}}(x, T_e)). \quad (5.2)$$

Here  $\delta_{\text{SZ}}(x, T_e)$  is a relativistic correction that cannot be ignored when we are looking for massive clusters containing very hot gas. The result of this frequency dependence is an observed decrement in the CMB temperatures below frequencies  $\nu \sim 220$  GHz (corresponding to wavelengths greater than  $\lambda \sim 1.3$  mm), and an increment for larger frequencies (shorter wavelengths). A similar relation can be applied to the observed intensity of the background radiation, where the change in the intensity is also proportional to the Compton  $y$ -parameter ( $\Delta I_0 \propto y I_0$ ).

The amplitude of the thermal distortion is independent of redshift, but it depends on the line of sight extent of the cluster; thus SZ surveys are limited by the cluster mass and are usually able to select only the most massive structures. Apart from the thermal Sunyaev-Zel'dovich effect, a distortion in the CMB temperature can also occur due to bulk motion of the electrons in the hot gas, but the amplitude of this so-called “kinetic SZ-effect” (Sunyaev and Zeldovich, 1980) is much smaller than the distortion caused by the inverse Compton scattering of CMB photons. The thermal distortion is already very small ( $< 1$  mK), so the kinetic SZ effect can be essentially ignored in cluster surveys.

Recently, large cluster samples have been assembled using the Sunyaev-Zel'dovich detection technique by the Atacama Cosmology Telescope (Marriage et al., 2011; Hasselfield et al., 2013a), the South Pole Telescope (Vanderlinde et al., 2010; Reichardt et al., 2013) and the *Planck* satellite (Planck Collaboration et al., 2011, 2014b). The ACT and SPT telescopes operate at millimeter wavelengths, where a cluster can be detected as a decrement in the intensity of the cosmic microwave background. At far-infrared and submillimeter wavelengths the thermal SZ effect causes an increment in the observed background intensity, which has been detected at 350 and 500  $\mu\text{m}$  with *Herschel* (Zemcov et al., 2010) and at 850  $\mu\text{m}$  with SCUBA (Zemcov et al., 2003), as well as with Planck. In this wavelength range sources behind the cluster that are magnified by gravitational lensing can also contribute to the excess measured FIR/submillimeter flux density towards these clusters, as well as dusty star-forming galaxies that reside inside the observed cluster. While these point sources are treated as contaminants in the Sunyaev-Zel'dovich effect measurements, these objects are a focus of several different studies. Exploiting the lensing magnification allows us to study dusty galaxies with flux densities below our detection limits, and investigating the rare star-forming galaxies inside clusters can help us understand the interaction between environment and star formation activity.

In this chapter we exploit the large overlap of our HeLMS and HerS regions with an equatorial field observed by the Atacama Cosmology Telescope. We investigate dusty galaxy emission towards massive Sunyaev-Zel'dovich-selected galaxy clusters found with ACT. Due to the low resolution available with the large SPIRE beams, as well as the shallow depth of our HeLMS and HerS maps, we do not attempt to investigate the far infrared emission towards each of these clusters individually and we do not focus on the cluster member galaxies. Instead we stack the *Herschel* maps on the positions of the centers of the clusters determined from the Sunyaev-Zel'dovich effect to increase our signal-to-noise ratio, and we investigate the average far-infrared emission towards these massive galaxy clusters.

## 5.1 The ACT equatorial cluster sample

The ACT Sunyaev-Zel’dovich-selected equatorial cluster sample (Hasselfield et al., 2013a) consists of 68 galaxy clusters detected at 148 GHz with a signal-to-noise ratio  $\text{SNR} > 5.1$ . All of the cluster candidates have been confirmed to be actual clusters based on optical or infrared data (Menanteau et al., 2013). As a first step in this confirmation process the brightest cluster galaxy (BCG) is identified in each candidate cluster using mainly Sloan Digital Sky Survey (SDSS) data. The BCGs are usually the most massive cluster-member galaxies and reside in the centers of the clusters. The next step is to find the so-called red sequence around this central galaxy. The red sequence consists of elliptical and lenticular (“early-type”) galaxies that have a very tight color-magnitude relation with the redder galaxies being brighter. This population can be found in all galaxy clusters and the identification of this red sequence is often used as optical cluster-detection technique (Gladders and Yee, 2000). A candidate is confirmed as a cluster if it contains more than 15 galaxies within a projected 1 Mpc area of the center of the cluster. The redshifts of these clusters are determined from follow-up observations, or – if available – from already existing SDSS spectroscopy data of cluster-member galaxies.

The clusters were selected from a  $504 \text{ deg}^2$  field along the celestial equator spanning  $20^{\text{h}}16^{\text{m}}00^{\text{s}} < \text{RA} < 3^{\text{h}}52^{\text{m}}24^{\text{s}}$  and  $-2^{\circ}07' < \text{Dec} < 2^{\circ}18'$ . This area has  $\sim 100 \text{ deg}^2$  overlap with our HeLMS field, and contains the full HerS region (see Section 2.4.1). In our analysis we select all clusters from the Hasselfield et al. (2013a) sample that fall into our HeLMS and HerS fields. We find 15 ACT SZ clusters in HeLMS and 11 clusters in our HerS region. The redshift range of these clusters is  $0.21 < z < 1.11$  and their typical masses are  $\sim 5 \times 10^{14} M_{\odot}$ . The ACT IDs, locations and redshifts of these clusters are summarized in Table 5.1 for HeLMS and in Table 5.2 for HerS.

## 5.2 Data analysis

Our goal is to investigate the mean far-infrared emission measured towards galaxy clusters as a function of the distance from their centers determined by the Sunyaev-Zel’dovich effect. This can be done by stacking our SPIRE maps on the ACT cluster positions, and investigating the radially-averaged flux density distribution. A simple co-addition of our maps, however, does not take into account the changing angular extent of these clusters at different redshifts.

We can define the characteristic physical radius of a cluster to be 1 Mpc (e.g. Koester et al., 2007; Hasselfield et al., 2013a; Menanteau et al., 2013). Here we adopt similar

ACT ID	RA (deg)	Dec (deg)	$z$	$D_A$ (Mpc)	$\theta_{1\text{Mpc}}$ (arcmin)
ACT-CL J0022.2-0036	5.5553	-0.6050	0.805	1576.4	2.2
ACT-CL J0059.1-0049	14.7855	-0.8326	0.786	1563.0	2.2
ACT-CL J2337.6+0016	354.4156	0.2690	0.275	869.5	4.0
ACT-CL J0014.9-0057	3.7276	-0.9502	0.533	1316.3	2.6
ACT-CL J0044.4+0113	11.1076	1.2221	1.110	1721.9	2.0
ACT-CL J0058.0+0030	14.5189	0.5106	0.760	1543.8	2.2
ACT-CL J2351.7+0009	357.9349	0.1538	0.990	1678.0	2.0
ACT-CL J0018.2-0022	4.5623	-0.3795	0.750	1536.1	2.2
ACT-CL J0104.8+0002	16.2195	0.0495	0.277	874.0	3.9
ACT-CL J0017.6-0051	4.4138	-0.8580	0.211	712.9	4.8
ACT-CL J0051.1+0055	12.7875	0.9323	0.690	1485.8	2.3
ACT-CL J2327.4-0204	351.8660	-2.0777	0.705	1499.1	2.3
ACT-CL J0045.2-0152	11.3051	-1.8827	0.545	1331.5	2.6
ACT-CL J0026.2+0120	6.5699	1.3367	0.650	1448.2	2.4
ACT-CL J0008.1+0201	2.0418	2.0204	0.360	1045.7	3.3

Table 5.1: ACT Sunyaev-Zel’dovich-selected clusters in the HeLMS region. Based on the redshift, we calculate the angular diameter distance  $D_A$  and the corresponding observed angular size  $\theta_{1\text{Mpc}}$  of a cluster with a physical size of 1 Mpc.

ACT ID	RA (deg)	Dec (deg)	$z$	$D_A$ (Mpc)	$\theta_{1\text{Mpc}}$ (arcmin)
ACT-CL J0206.2-0114	31.5567	-1.2428	0.676	1473.0	2.3
ACT-CL J0218.2-0041	34.5626	-0.6883	0.672	1469.3	2.3
ACT-CL J0215.4+0030	33.8699	0.5091	0.865	1614.6	2.1
ACT-CL J0127.2+0020	21.8227	0.3468	0.379	1080.8	3.2
ACT-CL J0119.9+0055	19.9971	0.9193	0.720	1511.8	2.3
ACT-CL J0058.0+0030	14.5189	0.5106	0.760	1543.8	2.2
ACT-CL J0219.8+0022	34.9533	0.3755	0.537	1321.4	2.6
ACT-CL J0139.3-0128	24.8407	-1.4769	0.700	1494.7	2.3
ACT-CL J0104.8+0002	16.2195	0.0495	0.277	874.0	3.9
ACT-CL J0152.7+0100	28.1764	1.0059	0.230	761.8	4.5
ACT-CL J0156.4-0123	29.1008	-1.3879	0.450	1199.4	2.9

Table 5.2: ACT Sunyaev-Zel’dovich-selected clusters in the HerS region. Based on the redshift, we calculate the angular diameter distance  $D_A$  and the corresponding observed angular size  $\theta_{1\text{Mpc}}$  of a cluster with a physical size of 1 Mpc.

standard flat cosmology parameters as used in Hasselfield et al. (2013a), with  $\Omega_m = 0.27$ ,  $\Omega_\lambda = 0.73$  and  $H_0 = 70 \text{ km s}^{-1}\text{Mpc}^{-1}$ . If we know the physical size  $x$  of an object at redshift  $z$ , the observed angular size  $\theta$  can be determined from the angular size-redshift relation for small angles as

$$\theta = \frac{x}{D_A(z)}, \quad (5.3)$$

where  $D_A(z)$  is the angular diameter distance, a commonly used distance measure in astronomy. In a flat ( $\Omega_k = 0$ ) universe  $D_A(z)$  can be expressed as

$$D_A(z) = \frac{c}{H_0(1+z)} \int_0^z \frac{dz'}{\sqrt{\Omega_m(1+z')^3 + 1 - \Omega_m}}. \quad (5.4)$$

This relates to the quantity  $D_L$  used in Chapter 3 as  $D_A = D_L/(1+z)^2$  (see e.g. Hogg, 1999). Using these relations we calculate  $D_A(z)$  and  $\theta_{1\text{Mpc}}$  values for each cluster. These values are listed in Table 5.1 and 5.2. It can be seen that there is a large variation in the angular size of our clusters, since a 1 Mpc physical size corresponds to an angular size of  $\theta_{1\text{Mpc}} \sim 5'$  at  $z \sim 0.2$  and  $\theta_{1\text{Mpc}} \sim 2'$  at  $z \sim 1.1$ . If our sample was larger, these clusters could be binned based on their angular size, and stacks could be created in each of these bins in order to investigate the star formation activity on a physical scale. Instead, due to the relatively small number of clusters in our sample we create a single stacked image from all of our 26 clusters, while we resize our individual images so that the pixel sizes in the SPIRE images corresponds to similar physical extent. We choose to scale all of our images to match an image where  $2'$  corresponds to a 1 Mpc physical scale. Our nominal SPIRE pixel sizes at 250, 350 and 500  $\mu\text{m}$  are  $6''$ ,  $8.333''$  and  $12''$ , respectively, so  $2'$  corresponds to 20.0, 14.4 and 10.0 pixels in each band. In practice as a first step in each SPIRE band we create  $50' \times 50'$  postage-stamp images centered on the position of each SZ cluster. After we convert our  $\theta_{1\text{Mpc}}$  values in Tables 5.1 and 5.2 from units of arcminutes to pixels in the corresponding band ( $\theta_{250}, \theta_{350}, \theta_{500}$ ), the re-binning factors for each of our postage-stamp images are calculated as  $20.0/\theta_{250}$ ,  $14.4/\theta_{350}$  and  $10.0/\theta_{500}$ . After this step we trim the edges of each image so that all of our postage-stamp images have the same dimensions. As a result, our final cut-out images have pixel sizes corresponding to 50 kpc (250  $\mu\text{m}$ ), 69 kpc (350  $\mu\text{m}$ ) and 100 kpc (500  $\mu\text{m}$ ) (see Figure 5.1). Due to the negative  $k$ -correction at FIR/submm wavelengths we do not expect a significant decrease in flux density for objects at higher redshifts, so the observed flux densities are not rescaled during this analysis.

We create a stack from all the postage-stamp images in HeLMS and HerS by calculating their weighted mean. After re-binning the noise-per-pixel values will change

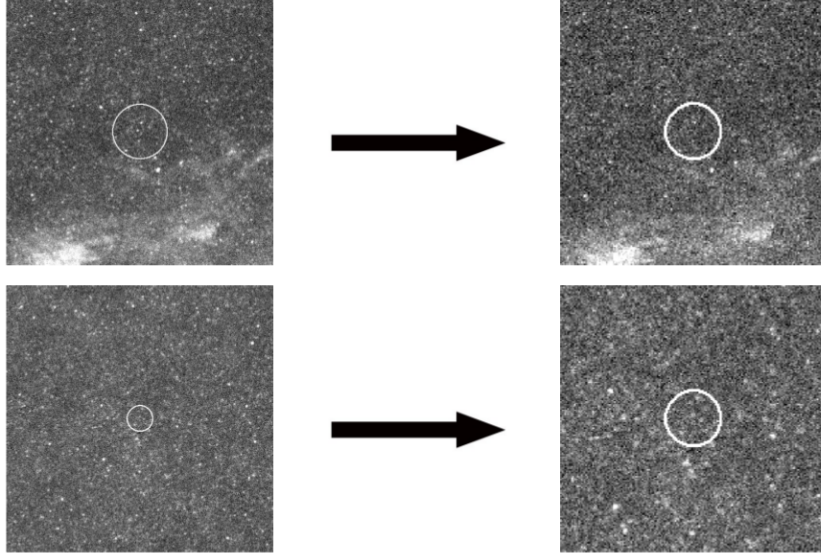


Figure 5.1: Result of re-binning the SPIRE images of ACT clusters at different redshifts. A physical radius of 1 Mpc corresponds to an angular scale of  $\theta \sim 5'$  at  $z \sim 0.2$  and  $\theta \sim 2'$  at  $z \sim 1.3$ , as shown with white circles. Before re-binning, the pixel sizes correspond to  $6''$  ( $250 \mu\text{m}$ ),  $8.333''$  ( $350 \mu\text{m}$ ) and  $12''$  ( $500 \mu\text{m}$ ) angular size. After re-binning, the new pixel sizes correspond to a physical extent of 50 kpc ( $250 \mu\text{m}$ ), 69 kpc ( $350 \mu\text{m}$ ) and 100 kpc ( $500 \mu\text{m}$ ).

in our images and we re-scale our noise values based on the ratio of the noise in the re-binned maps to the original cutouts. The final stack of all 26 cluster images is shown in Figure 5.2, with white circles illustrating the characteristic 1 Mpc cluster radius.

### 5.3 Results and discussion

We calculate the radial averages of our stacked images in 100 kpc bins in each band. The results are plotted in Figure 5.3. Since some of the 26 clusters contain bright objects that we did not remove, we have to investigate how these outliers affect the mean we observe. We re-calculate the mean and standard deviation using a bootstrap method. First we randomly select 20 clusters from our sample of clusters, and we calculate the radial average of the stacked image created from these 20 clusters. We then repeat this procedure 1000 times, always selecting a different random set of 20 clusters. We calculate the mean and standard deviation of the resulting curves of all these different realizations, and these results are also plotted on Figure 5.3. We can see that the full sample of 26 sources appears to contain some outliers, but the resulting radial average curve is still less than  $2\sigma$  away from the mean calculated by the bootstrap method. We also investigate

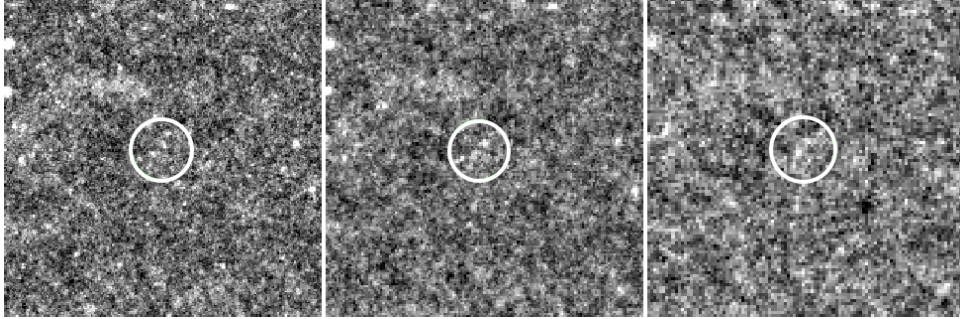


Figure 5.2: Stacked image of the 26 ACT Sunyaev-Zel'dovich selected cluster positions in HeLMS and HerS at 250, 350 and 500  $\mu\text{m}$  (left to right). The white circles correspond to a physical radius of 1 Mpc.

stacks made from random positions in the map that do not correspond to cluster centres. Figure 5.4 shows the result of the mean and standard deviation of 1000 realizations of picking 26 random positions in our maps and calculating the radial average similarly to the red curve on Figure 5.3.

Our results show that excess far-infrared emission is seen in Fig. 5.3 in all three bands towards the centers of the clusters compared to the results obtained from stacking random positions in the maps. This excess is visible up to a distance of  $\sim 1.5$  Mpc from the center of the clusters. As we discussed before, an excess of FIR/submm emission towards clusters could be a result of the SZ increment, or it can be a contribution from dusty star-forming galaxies inside the cluster, and distant, lensed galaxies behind the cluster.

Zemcov et al. (2010) measured a Sunyaev-Zel'dovich increment of  $\Delta I_0 = 0.268 \text{ MJy sr}^{-1}$  in the 500  $\mu\text{m}$  surface brightness. The amplitude of the increment depends on the line-of-sight extent of the clusters that the CMB photons need to travel through, and this is encoded in the Compton- $y$  parameter (Eq. 5.1). Zemcov et al. (2010) quote an average of  $y = 3.46 \times 10^{-4}$  for their observed clusters. From Hasselfield et al. (2013a) we determine that our sample has an average  $y \simeq 0.95 \times 10^{-4}$ , and since  $\Delta I_0 \propto y$ , we expect to find an increment of  $\Delta I_0 \approx 0.073 \text{ MJy sr}^{-1}$  in the 500  $\mu\text{m}$  surface brightness, which corresponds to flux densities of  $\Delta S_{500} \approx 2.5 \text{ mJy beam}^{-1}$ . The SZ increment in the 250  $\mu\text{m}$  and 350  $\mu\text{m}$  is expected to be below our detection limits, thus the excess we see in these bands should be the result of dusty galaxy emission along the line of sight to the clusters. Typical dusty galaxies are brightest in the 250  $\mu\text{m}$  or 350  $\mu\text{m}$  SPIRE bands and faintest at 500  $\mu\text{m}$ . Our observed flux densities in Figure 5.3 are at a similar level in all three bands. This result is consistent with detecting dusty galaxy emission in the line of sight of the cluster, while the measured 500  $\mu\text{m}$  flux densities are boosted high by

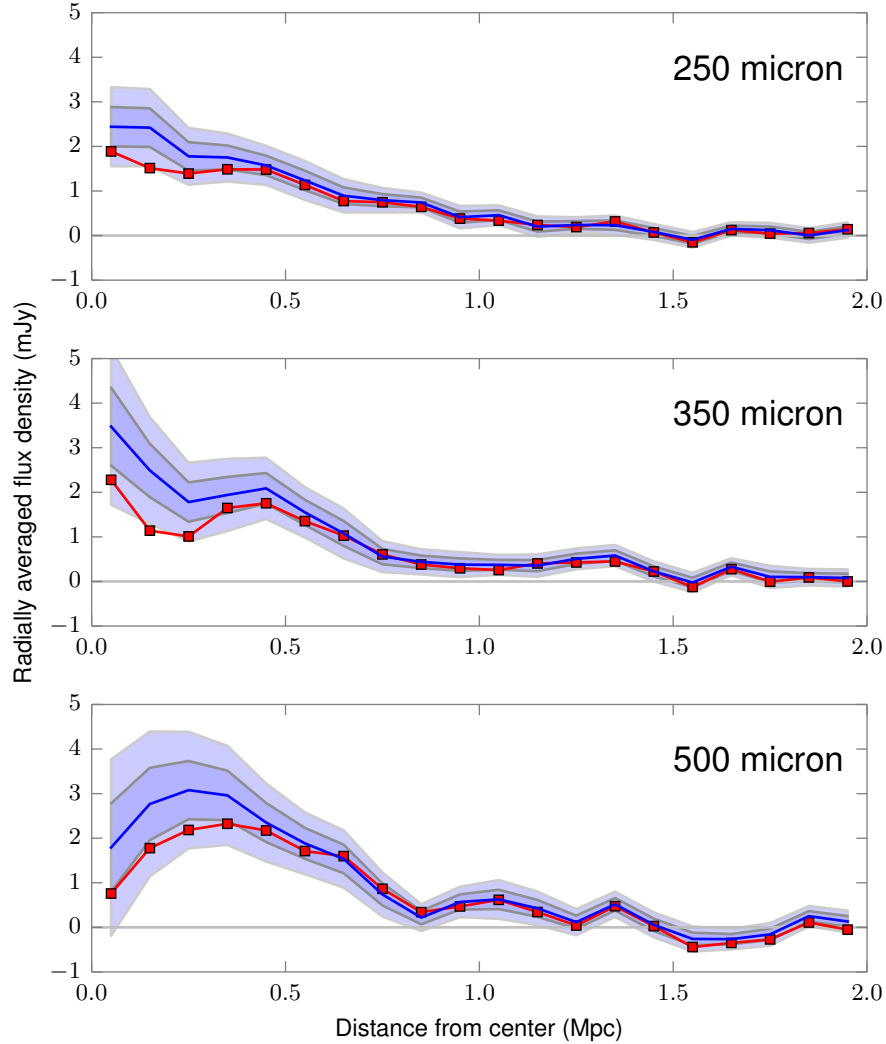


Figure 5.3: Radial average of SPIRE images stacked at ACT cluster positions. The radial average of the stacked image containing all 26 clusters is shown with a red line. The central blue line corresponds to the mean radial profile calculated from a bootstrap method, by averaging 1000 realizations of radial profiles created from stacking 20 random cluster positions from our full sample of 26 clusters. The blue contours correspond to the  $\pm 1\sigma$  and  $\pm 2\sigma$  errors determined from the bootstrap method.

the SZ increment. A similar effect is shown in Gralla et al. (2014, Fig. 2.) where the stacked flux densities of radio AGN would normally decrease towards  $500 \mu\text{m}$  but the SZ increment increases the measured  $S_{500}$  flux density.

As discussed in Zemcov et al. (2007) and Zemcov et al. (2013), lensing magnification

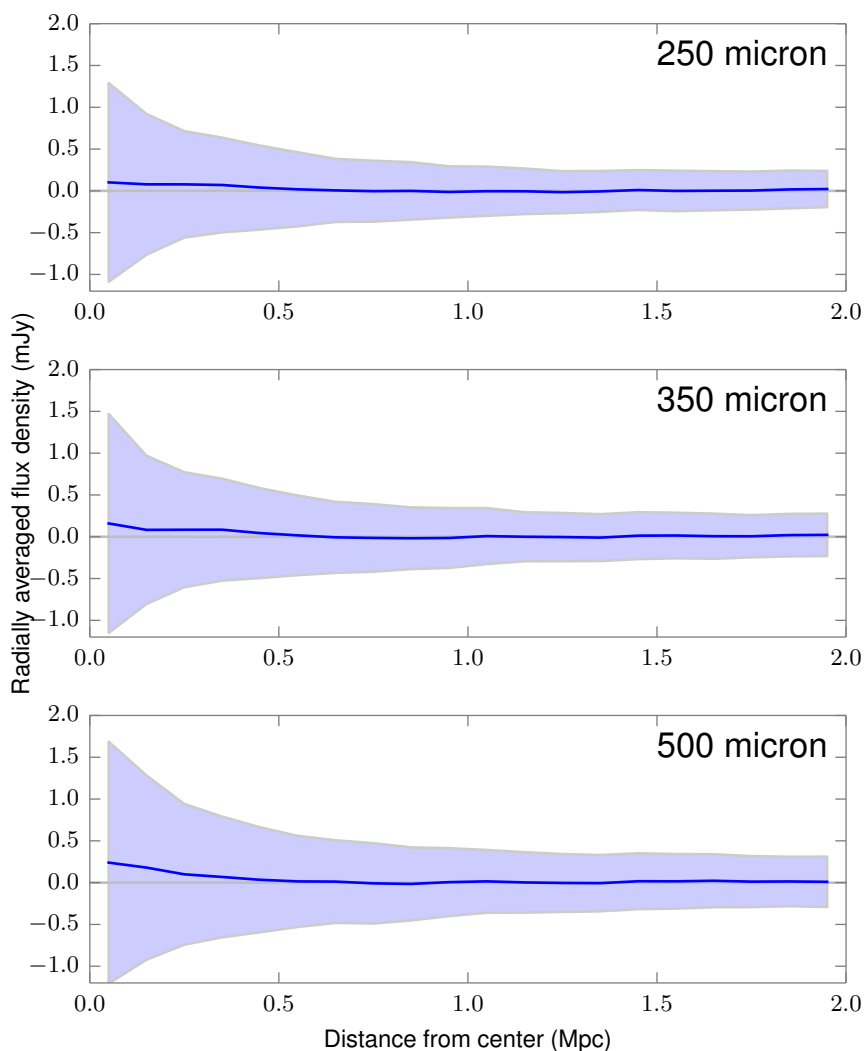


Figure 5.4: Radial average of SPIRE images stacked at random map positions. The blue curves and the contours represent the mean and  $\pm 1\sigma$  standard deviation of 1000 realizations of radial profiles created by stacking 26 randomly-selected positions in the map that do not correspond to cluster centers.

of sources is more likely to happen at some distance from the geometrical center of the clusters, since sources that fall directly behind the center of the lensing mass are distorted into an Einstein ring and the flux at their centers should decrease. Thus towards the centers of massive clusters a deficit is expected in the cosmic infrared background surface brightness, which has been detected in Zemcov et al. (2013). The flux in our stacked

images consistently increases all the way to the center of the clusters in our  $250\ \mu\text{m}$  and  $350\ \mu\text{m}$  bands, so it is likely that lensed galaxies only contribute partially to the excess flux density, and that we see dust emission from cluster member galaxies, possibly even from the brightest cluster galaxies at the centers of these massive structures.

To determine whether these point sources are star-forming galaxies falling into the cluster, or lensed dusty galaxies behind the clusters, more detailed analysis is needed. High signal-to-noise measurements with large resolution instruments can help resolve the individual galaxies that contribute to this emission. Determining the redshifts of these sources will unambiguously confirm whether these galaxies are part of the cluster or not. Additionally, stacking the maps on cluster members identified in optical surveys can tell us how much dusty star formation exists in these clusters.

Regardless of whether our excess FIR emission emerges from cluster member galaxies or lensed sources, our results show that the contribution of dusty star-formation towards these SZ selected galaxy clusters cannot be ignored. Any survey based on the detection of the SZ distortion needs to take the contribution of these dusty sources into account. These galaxies could be faint enough at millimeter-wavelengths, that they are not detected individually, but their flux densities can partially fill in the SZ decrement, thus biasing SZ cluster surveys against finding galaxy clusters containing dusty star-forming galaxies. The clusters already identified can have an even deeper decrement, thus a larger mass than predicted without identifying the contamination from such dusty sources. This shows the importance of cross-frequency studies in cluster detection surveys and the need to correctly model and disentangle all components that act as contaminants in these surveys. As we mentioned before, a much smaller amplitude distortion in the background intensities can arise due to the relative motion of the galaxy clusters compared to the uniform Hubble flow. Measuring this kinetic SZ effect (Sunyaev and Zeldovich, 1980) is an important part of understanding the velocity field of our Universe, and these measurements are also very sensitive to contamination from dusty sources. While in the above mentioned studies of the CMB the dusty galaxies act as a source of contamination, we can also learn important insights from cross-correlation studies of the far-infrared emission and the CMB temperature. Currently we are not able to directly detect the first galaxies that contributed to the reionization of the early Universe, but we can still learn about these objects by investigating the temperature changes of the CMB photons that pass through the gas that these first galaxies ionized with their radiation. Thus CIB-CMB cross correlation studies can help us learn more about the timing of the reionization of the Universe (e.g. Atrio-Barandela and Kashlinsky, 2014).

# Chapter 6

## Conclusions

In this thesis we investigated the role of dusty star formation at different redshifts and in different environments. Studying the evolution of the cosmic star formation history and the role of the galaxy environment in triggering and quenching star-forming processes is crucial in order to understand the evolution of large-scale structures in the Universe. It has been known that dusty star-forming galaxies play a significant role in the stellar mass build-up at high redshifts, but the currently available samples are limited by observed sky area and accurate redshift measurements; thus their contribution to the cosmic star formation rate density at  $z > 4$  is still unknown.

Our main datasets analyzed in this thesis included two recent large area surveys, the HerMES Large Mode Survey (HeLMS) and the Herschel Stripe 82 Survey (HerS) observed at far-infrared wavelengths by the SPIRE instrument aboard the *Herschel Space Observatory*. To fully exploit the spatial extent of these observations it is important to create maps that provide an unbiased estimate of the brightness variations in the sky on all angular scales. We created maps for both the HeLMS and HerS field with two mapmaker software packages, SHIM and SANEPIC. SANEPIC was designed to work with BLAST data, a pathfinder instrument for SPIRE. After we adapted the SANEPIC mapmaker to work with SPIRE data, we carried out an analysis to compare the performance of the two algorithms. We concluded that at small angular scales both mapmakers perform similarly well, but the largest angular scales are better recovered by SANEPIC. Our final data products have been and will be the base of many multi-wavelength studies. The large areas of these surveys allow for the detection of statistically significant numbers of the galaxies that constitute the cosmic infrared background, including the rarest objects on the sky. The power spectrum of the background emission from unresolved faint galaxies also contains critical information about the underlying galaxy populations, and cross-correlation studies with other maps at different wavelengths can provide important

constraints on the evolution of the large-scale structure of the Universe.

The main result of our work is the creation of a large catalog of candidate  $z > 4$  luminous dusty star-forming galaxies detected in the HeLMS survey. We used a map-based search method to locate galaxies with increasing flux densities towards longer SPIRE wavelengths. This method has been shown to select high-redshift actively star-forming objects. In a previous analysis of smaller area HerMES maps we have found an excess of these “red” galaxies, but the small samples only allowed us to measure the total number of sources above some flux density limit. In this work we applied our search method to the HeLMS field and we created a catalog of 477 red sources. This catalog is large enough that for the first time we were able to infer the shape of the differential number counts of these high-redshift galaxy candidates. After carefully investigating the different biasing effects, we determined the differential number counts of our sources at  $500 \mu\text{m}$ . While the total number of sources confirmed the excess we have seen before, the very steep slope we found for our number counts suggests that this population is strongly evolving and that massive luminous dusty galaxies were more important in the past than popular galaxy evolution models predict. Current simulations are not able to reproduce the massive gas reservoirs at such early times, which are needed to fuel the very active star formation.

We determined the spectroscopic redshift for two of our reddest sources with ALMA. These redshifts are  $z = 5.126$  and  $z = 4.994$  (or  $z = 3.798$ ). Including these results we now have more than ten red sources with a confirmed  $z > 4$  redshift, and the lowest redshift red source we have found so far was still at  $z > 3$ . In the future the sample of sources with confirmed redshift will be extended, and knowing the exact redshift distribution of these sources will allow us to construct the infrared luminosity functions at  $z > 4$  and to infer the evolution of the star formation rate density at these high redshifts. Our current knowledge of the evolution of the star formation history at these epochs comes from high- $z$  UV data sets that measure unobscured star formation rates, and are in need of significant and yet quite uncertain corrections due to dust extinction. The addition of our high redshift far-infrared sample will play a crucial role in understanding the stellar mass build-up at  $z > 4$ .

We designed a follow-up project to measure the  $850 \mu\text{m}$  flux densities of a sample of red sources with the SCUBA-2 instrument. Based on the SPIRE flux densities alone, the spectrum of the red sources is usually better fit with an “optical-depth-modified” blackbody curve than an optically thin model. In this case the dust becomes optically thick for rest frame wavelengths  $\lambda < 200 \mu\text{m}$ . Our measured SCUBA-2  $850 \mu\text{m}$  flux densities of sources that are isolated in all three SPIRE bands confirm this trend. Due

to the large beamsize in our  $500\ \mu\text{m}$  SPIRE band some of the red sources we find break up into several components in the higher resolution  $250\ \mu\text{m}$  and  $350\ \mu\text{m}$  maps. Our assumption was that at least one component of these blends should still be a red source, although with its measured  $500\ \mu\text{m}$  flux density statistically biased high. Our observed SCUBA-2 sample contained such blended sources, and we have found that many of these blends are still detected with SCUBA-2, although with an anomalously high  $S_{500}/S_{850}$  ratio. This suggest that our initial assumption, that these blends contain a red source is correct, and while the non-red component of the blend becomes undetectable, the fainter red source still shows emission at these longer wavelengths.

In a different analysis we stacked the positions of our HeLMS selected red sources on maps obtained by the Atacama Cosmology Telescope at wavelengths of  $1400\ \mu\text{m}$  and  $2000\ \mu\text{m}$ . We created stacks of sources with  $500\ \mu\text{m}$  flux densities belonging to different bins, and in almost all of our bins we have detected a source in the stacked ACT maps. The average flux density of these sources is lower than we would expect based on their average  $500\ \mu\text{m}$  flux densities, but all of our stacks contained blended objects too, which have been shown to have anomalous colors. The successful detection of isolated sources with SCUBA-2 and the fact that we can see emission at long wavelengths at the position of blended objects shows the importance of future follow-up campaigns with better resolution millimeter-wave interferometric instruments. We were also successful in getting telescope time to observe all of our sources in the HeLMS catalog with SCUBA-2. The HeLMS sources all have  $S_{500} > 50\ \text{mJy}$  flux densities, so we expect a large detection fraction at  $850\ \mu\text{m}$ . This new dataset will help us reduce the bias in the number counts caused by blending effects and it will help to better constrain the spectral energy distributions of the red sources.

We also mapped a larger area around four red sources with SCUBA-2 to investigate their environments. Our goal was to search for over-densities of fainter star-forming submillimeter galaxies near these starbursts, similar to what was observed for several well-studied high redshift dusty galaxies. Such an over-density might indicate that these galaxies reside in a proto-cluster environment. Our measurements show no obvious over-density in the vicinity of our red sources. We cannot rule out that the other proto-cluster members are simply too faint to be detected in our survey, perhaps because they contain smaller amount of dust than the central red source and are less luminous. Nevertheless, our results are consistent with environmental studies of the highest redshift dusty starburst galaxy, the  $z = 6.34$  red source HFLS3, where studies have found no over-density of either submillimeter emitting or optical Lyman-break galaxies. This suggests that there are different physical processes triggering extreme star formation apart from

environmental effects, but in order to create better constraints on the current evolution models, more observations will be needed.

To exploit the large overlap between the equatorial field mapped by the Atacama Cosmology Telescope and our HeLMS and HerS surveys, we investigated the average dusty galaxy emission in the line of sight of moderate redshift massive galaxy clusters detected by ACT, based on the decrement in surface brightness caused by the Sunyaev-Zel'dovich effect. We stacked our SPIRE maps at the positions of the 26 clusters that are found in the overlapping area, and we detected excess submillimeter emission in all three SPIRE bands. The observed amplitudes of this excess are similar in all three bands, and this suggests that the excess emission comes from dusty galaxies inside the clusters or lensing magnified clusters that are located behind the cluster, and since the flux density of these sources should decrease towards  $500\ \mu\text{m}$ , the flux we see at  $500\ \mu\text{m}$  is a possible detection of the expected SZ increment. While the current signal-to-noise ratio and the available resolution are not sufficient to investigate this excess in detail, this result suggests that there might be more dust-obscured star formation happening in massive virialized clusters at higher  $z$  than in local clusters. These dusty galaxies also bias the detection of both the kinetic and thermal SZ signals in cosmic microwave background experiments, so cross correlation of the datasets will be an important part of reducing this bias.

In summary, we showed the importance of mapping large area fields and detecting the average properties of high-redshift galaxy populations. In the future, extensive multi-wavelength studies of our sources will be carried out to investigate the co-evolution of different populations, to determine the redshift distribution and the contribution to the total star formation history. Extragalactic astronomers will continue to exploit the significantly better resolution of interferometric instruments like ALMA, which will help us to learn about the structure, the dust properties and the environment of individual galaxies in the star-forming population.

# Bibliography

Abell, G. O. (1958). The Distribution of Rich Clusters of Galaxies. *ApJS*, 3:211.

Amblard, A., Cooray, A., Serra, P., Altieri, B., Arumugam, V., Aussel, H., Blain, A., Bock, J., Boselli, A., Buat, V., Castro-Rodríguez, N., Cava, A., Chanical, P., Chapin, E., Clements, D. L., Conley, A., Conversi, L., Dowell, C. D., Dwek, E., Eales, S., Elbaz, D., Farrah, D., Franceschini, A., Gear, W., Glenn, J., Griffin, M., Halpern, M., Hatziminaoglou, E., Ibar, E., Isaak, K., Ivison, R. J., Khostovan, A. A., Lagache, G., Levenson, L., Lu, N., Madden, S., Maffei, B., Mainetti, G., Marchetti, L., Marsden, G., Mitchell-Wynne, K., Nguyen, H. T., O'Halloran, B., Oliver, S. J., Omont, A., Page, M. J., Panuzzo, P., Papageorgiou, A., Pearson, C. P., Pérez-Fournon, I., Pohlen, M., Rangwala, N., Roseboom, I. G., Rowan-Robinson, M., Portal, M. S., Schulz, B., Scott, D., Seymour, N., Shupe, D. L., Smith, A. J., Stevens, J. A., Symeonidis, M., Trichas, M., Tugwell, K., Vaccari, M., Valiante, E., Valtchanov, I., Vieira, J. D., Vigroux, L., Wang, L., Ward, R., Wright, G., Xu, C. K., and Zemcov, M. (2011). Submillimetre galaxies reside in dark matter haloes with masses greater than  $3 \times 10^{11}$  solar masses. *Nature*, 470:510–512.

Amblard, A., Cooray, A., Serra, P., Temi, P., Barton, E., Negrello, M., Auld, R., Baes, M., Baldry, I. K., Bamford, S., Blain, A., Bock, J., Bonfield, D., Burgarella, D., Buttiglione, S., Cameron, E., Cava, A., Clements, D., Croom, S., Dariush, A., de Zotti, G., Driver, S., Dunlop, J., Dunne, L., Dye, S., Eales, S., Frayer, D., Fritz, J., Gardner, J. P., Gonzalez-Nuevo, J., Herranz, D., Hill, D., Hopkins, A., Hughes, D. H., Ibar, E., Ivison, R. J., Jarvis, M., Jones, D. H., Kelvin, L., Lagache, G., Leeuw, L., Liske, J., Lopez-Caniego, M., Loveday, J., Maddox, S., Michałowski, M., Norberg, P., Parkinson, H., Peacock, J. A., Pearson, C., Pascale, E., Pohlen, M., Popescu, C., Prescott, M., Robotham, A., Rigby, E., Rodighiero, G., Samui, S., Sansom, A., Scott, D., Serjeant, S., Sharp, R., Sibthorpe, B., Smith, D. J. B., Thompson, M. A., Tuffs, R., Valtchanov, I., van Kampen, E., van der Werf, P., Verma, A., Vieira, J., and Vlahakis,

- C. (2010). Herschel-ATLAS: Dust temperature and redshift distribution of SPIRE and PACS detected sources using submillimetre colours. *A&A*, 518:L9.
- Atrio-Barandela, F. and Kashlinsky, A. (2014). Probing the Epoch of Pre-reionization by Cross-correlating Cosmic Microwave and Infrared Background Anisotropies. *ApJL*, 797:L26.
- Austermann, J. E., Dunlop, J. S., Perera, T. A., Scott, K. S., Wilson, G. W., Aretxaga, I., Hughes, D. H., Almaini, O., Chapin, E. L., Chapman, S. C., Cirasuolo, M., Clements, D. L., Coppin, K. E. K., Dunne, L., Dye, S., Eales, S. A., Egami, E., Farrah, D., Ferrusca, D., Flynn, S., Haig, D., Halpern, M., Ibar, E., Ivison, R. J., van Kampen, E., Kang, Y., Kim, S., Lacey, C., Lowenthal, J. D., Maukopf, P. D., McLure, R. J., Mortier, A. M. J., Negrello, M., Oliver, S., Peacock, J. A., Pope, A., Rawlings, S., Rieke, G., Roseboom, I., Rowan-Robinson, M., Scott, D., Serjeant, S., Smail, I., Swinbank, A. M., Stevens, J. A., Velazquez, M., Wagg, J., and Yun, M. S. (2010). AzTEC half square degree survey of the SHADES fields - I. Maps, catalogues and source counts. *MNRAS*, 401:160–176.
- Barger, A. J., Cowie, L. L., and Sanders, D. B. (1999). Resolving the Submillimeter Background: The 850 Micron Galaxy Counts. *ApJL*, 518:L5–L8.
- Barger, A. J., Cowie, L. L., Sanders, D. B., Fulton, E., Taniguchi, Y., Sato, Y., Kawara, K., and Okuda, H. (1998). Submillimetre-wavelength detection of dusty star-forming galaxies at high redshift. *Nature*, 394:248–251.
- Barkana, R. and Loeb, A. (2001). In the beginning: the first sources of light and the reionization of the universe. *Physics Reports*, 349:125–238.
- Baugh, C. M., Lacey, C. G., Frenk, C. S., Granato, G. L., Silva, L., Bressan, A., Benson, A. J., and Cole, S. (2005). Can the faint submillimetre galaxies be explained in the  $\Lambda$  cold dark matter model? *MNRAS*, 356:1191–1200.
- Becker, R. H., White, R. L., and Helfand, D. J. (1995). The FIRST Survey: Faint Images of the Radio Sky at Twenty Centimeters. *ApJ*, 450:559.
- Bendo, G. J., Griffin, M. J., Bock, J. J., Conversi, L., Dowell, C. D., Lim, T., Lu, N., North, C. E., Papageorgiou, A., Pearson, C. P., Pohlen, M., Polehampton, E. T., Schulz, B., Shupe, D. L., Sibthorpe, B., Spencer, L. D., Swinyard, B. M., Valtchanov, I., and Xu, C. K. (2013). Flux calibration of the Herschel\*-SPIRE photometer. *MNRAS*, 433:3062–3078.

- Bennett, C. L., Larson, D., Weiland, J. L., Jarosik, N., Hinshaw, G., Odegard, N., Smith, K. M., Hill, R. S., Gold, B., Halpern, M., Komatsu, E., Nolte, M. R., Page, L., Spergel, D. N., Wollack, E., Dunkley, J., Kogut, A., Limon, M., Meyer, S. S., Tucker, G. S., and Wright, E. L. (2013). Nine-year Wilkinson Microwave Anisotropy Probe (WMAP) Observations: Final Maps and Results. *ApJS*, 208:20.
- B  thermin, M., Daddi, E., Magdis, G., Sargent, M. T., Hezaveh, Y., Elbaz, D., Le Borgne, D., Mullaney, J., Pannella, M., Buat, V., Charmandaris, V., Lagache, G., and Scott, D. (2012a). A Unified Empirical Model for Infrared Galaxy Counts Based on the Observed Physical Evolution of Distant Galaxies. *ApJL*, 757:L23.
- B  thermin, M., Dole, H., Lagache, G., Le Borgne, D., and Penin, A. (2011). Modeling the evolution of infrared galaxies: a parametric backward evolution model. *A&A*, 529:A4.
- B  thermin, M., Le Floc'h, E., Ilbert, O., Conley, A., Lagache, G., Amblard, A., Arumugam, V., Aussel, H., Berta, S., Bock, J., Boselli, A., Buat, V., Casey, C. M., Castro-Rodr  guez, N., Cava, A., Clements, D. L., Cooray, A., Dowell, C. D., Eales, S., Farrah, D., Franceschini, A., Glenn, J., Griffin, M., Hatziminaoglou, E., Heinis, S., Ibar, E., Ivison, R. J., Kartaltepe, J. S., Levenson, L., Magdis, G., Marchetti, L., Marsden, G., Nguyen, H. T., O'Halloran, B., Oliver, S. J., Omont, A., Page, M. J., Panuzzo, P., Papageorgiou, A., Pearson, C. P., P  rez-Fournon, I., Pohlen, M., Rigopoulou, D., Roseboom, I. G., Rowan-Robinson, M., Salvato, M., Schulz, B., Scott, D., Seymour, N., Shupe, D. L., Smith, A. J., Symeonidis, M., Trichas, M., Tugwell, K. E., Vaccari, M., Valtchanov, I., Vieira, J. D., Viero, M., Wang, L., Xu, C. K., and Zemcov, M. (2012b). HerMES: deep number counts at 250  $\mu\text{m}$ , 350  $\mu\text{m}$  and 500  $\mu\text{m}$  in the COSMOS and GOODS-N fields and the build-up of the cosmic infrared background. *A&A*, 542:A58.
- Birkinshaw, M. (1999). The Sunyaev-Zel'dovich effect. *PhR*, 310:97–195.
- Blain, A. W. (1996). Galaxy-galaxy gravitational lensing in the millimetre/submillimetre waveband. *MNRAS*, 283.
- Blain, A. W., Chapman, S. C., Smail, I., and Ivison, R. (2004). Accurate Spectral Energy Distributions and Selection Effects for High-Redshift Dusty Galaxies: A New Hot Population to Discover with the Spitzer Space Telescope? *ApJ*, 611:52–58.
- Blain, A. W., Kneib, J.-P., Ivison, R. J., and Smail, I. (1999). Deep Counts of Submillimeter Galaxies. *ApJL*, 512:L87–L90.

- Blain, A. W. and Longair, M. S. (1993). Submillimetre Cosmology. *MNRAS*, 264.
- Borys, C., Chapman, S., Halpern, M., and Scott, D. (2003). The Hubble Deep Field North SCUBA Super-map - I. Submillimetre maps, sources and number counts. *MNRAS*, 344:385–398.
- Brinchmann, J., Charlot, S., White, S. D. M., Tremonti, C., Kauffmann, G., Heckman, T., and Brinkmann, J. (2004). The physical properties of star-forming galaxies in the low-redshift Universe. *MNRAS*, 351:1151–1179.
- Buat, V., Giovannoli, E., Burgarella, D., Altieri, B., Amblard, A., Arumugam, V., Aus-sel, H., Babbedge, T., Blain, A., Bock, J., Boselli, A., Castro-Rodríguez, N., Cava, A., Chanial, P., Clements, D. L., Conley, A., Conversi, L., Cooray, A., Dowell, C. D., Dwek, E., Eales, S., Elbaz, D., Fox, M., Franceschini, A., Gear, W., Glenn, J., Griffin, M., Halpern, M., Hatziminaoglou, E., Heinis, S., Ibar, E., Isaak, K., Ivison, R. J., Lagache, G., Levenson, L., Lonsdale, C. J., Lu, N., Madden, S., Maffei, B., Magdis, G., Mainetti, G., Marchetti, L., Morrison, G. E., Nguyen, H. T., O’Halloran, B., Oliver, S. J., Omont, A., Owen, F. N., Page, M. J., Pannella, M., Panuzzo, P., Papageorgiou, A., Pearson, C. P., Pérez-Fournon, I., Pohlen, M., Rigopoulou, D., Rizzo, D., Roseboom, I. G., Rowan-Robinson, M., Sánchez Portal, M., Schulz, B., Seymour, N., Shupe, D. L., Smith, A. J., Stevens, J. A., Strazzullo, V., Symeonidis, M., Trichas, M., Tugwell, K. E., Vaccari, M., Valiante, E., Valtchanov, I., Vigroux, L., Wang, L., Ward, R., Wright, G., Xu, C. K., and Zemcov, M. (2010). Measures of star formation rates from infrared (Herschel) and UV (GALEX) emissions of galaxies in the HerMES fields. *MNRAS*, 409:L1–L6.
- Burgarella, D., Buat, V., Gruppioni, C., Cucciati, O., Heinis, S., Berta, S., Béthermin, M., Bock, J., Cooray, A., Dunlop, J. S., Farrah, D., Franceschini, A., Le Floc’h, E., Lutz, D., Magnelli, B., Nordon, R., Oliver, S. J., Page, M. J., Popesso, P., Pozzi, F., Riguccini, L., Vaccari, M., and Viero, M. (2013). Herschel PEP/HerMES: the redshift evolution ( $0 \leq z \leq 4$ ) of dust attenuation and of the total (UV+IR) star formation rate density. *A&A*, 554:A70.
- Bussmann, R. S., Pérez-Fournon, I., Amber, S., Calanog, J., Gurwell, M. A., Dannerbauer, H., De Bernardis, F., Fu, H., Harris, A. I., Krips, M., Lapi, A., Maiolino, R., Omont, A., Riechers, D., Wardlow, J., Baker, A. J., Birkinshaw, M., Bock, J., Bourne, N., Clements, D. L., Cooray, A., De Zotti, G., Dunne, L., Dye, S., Eales, S., Farrah, D., Gavazzi, R., González Nuevo, J., Hopwood, R., Ibar, E., Ivison, R. J.,

- Laporte, N., Maddox, S., Martínez-Navajas, P., Michalowski, M., Negrello, M., Oliver, S. J., Roseboom, I. G., Scott, D., Serjeant, S., Smith, A. J., Smith, M., Streblyanska, A., Valiante, E., van der Werf, P., Verma, A., Vieira, J. D., Wang, L., and Wilner, D. (2013). Gravitational Lens Models Based on Submillimeter Array Imaging of Herschel-selected Strongly Lensed Sub-millimeter Galaxies at  $z > 1.5$ . *ApJ*, 779:25.
- Butcher, H. and Oemler, Jr., A. (1978). The evolution of galaxies in clusters. I - ISIT photometry of C1 0024+1654 and 3C 295. *ApJ*, 219:18–30.
- Capak, P. L., Riechers, D., Scoville, N. Z., Carilli, C., Cox, P., Neri, R., Robertson, B., Salvato, M., Schinnerer, E., Yan, L., Wilson, G. W., Yun, M., Civano, F., Elvis, M., Karim, A., Mobasher, B., and Staguhn, J. G. (2011). A massive protocluster of galaxies at a redshift of  $z \sim 5.3$ . *Nature*, 470:233–235.
- Carlstrom, J. E., Holder, G. P., and Reese, E. D. (2002). Cosmology with the Sunyaev-Zel’dovich Effect. *ARA&A*, 40:643–680.
- Casey, C. M., Berta, S., Béthermin, M., Bock, J., Bridge, C., Budynkiewicz, J., Burgarella, D., Chapin, E., Chapman, S. C., Clements, D. L., Conley, A., Conselice, C. J., Cooray, A., Farrah, D., Hatziminaoglou, E., Ivison, R. J., le Floch, E., Lutz, D., Magdis, G., Magnelli, B., Oliver, S. J., Page, M. J., Pozzi, F., Rigopoulou, D., Riguccini, L., Roseboom, I. G., Sanders, D. B., Scott, D., Seymour, N., Valtchanov, I., Vieira, J. D., Viero, M., and Wardlow, J. (2012). A Redshift Survey of Herschel Far-infrared Selected Starbursts and Implications for Obscured Star Formation. *ApJ*, 761:140.
- Casey, C. M., Chen, C.-C., Cowie, L. L., Barger, A. J., Capak, P., Ilbert, O., Koss, M., Lee, N., Le Floch, E., Sanders, D. B., and Williams, J. P. (2013). Characterization of SCUBA-2 450  $\mu\text{m}$  and 850  $\mu\text{m}$  selected galaxies in the COSMOS field. *MNRAS*, 436:1919–1954.
- Cavanagh, B., Jenness, T., Economou, F., and Currie, M. J. (2008). The ORAC-DR data reduction pipeline. *Astronomische Nachrichten*, 329:295–297.
- Chapin, E. L., Berry, D. S., Gibb, A. G., Jenness, T., Scott, D., Tilanus, R. P. J., Economou, F., and Holland, W. S. (2013). SCUBA-2: iterative map-making with the Sub-Millimetre User Reduction Facility. *MNRAS*, 430:2545–2573.
- Chapin, E. L., Chapman, S. C., Coppin, K. E., Devlin, M. J., Dunlop, J. S., Greve, T. R., Halpern, M., Hasselfield, M. F., Hughes, D. H., Ivison, R. J., Marsden, G., Moncelsi,

- L., Netterfield, C. B., Pascale, E., Scott, D., Smail, I., Viero, M., Walter, F., Weiss, A., and van der Werf, P. (2011). A joint analysis of BLAST 250-500  $\mu\text{m}$  and LABOCA 870  $\mu\text{m}$  observations in the Extended Chandra Deep Field-South. *MNRAS*, 411:505–549.
- Chapman, S. C., Blain, A. W., Smail, I., and Ivison, R. J. (2005). A Redshift Survey of the Submillimeter Galaxy Population. *ApJ*, 622:772–796.
- Chapman, S. C., Lewis, G. F., Scott, D., Richards, E., Borys, C., Steidel, C. C., Adelberger, K. L., and Shapley, A. E. (2001). Submillimeter Imaging of a Protocluster Region at  $Z=3.09$ . *ApJL*, 548:L17–L21.
- Chapman, S. C., Windhorst, R., Odewahn, S., Yan, H., and Conselice, C. (2003). Hubble Space Telescope Images of Submillimeter Sources: Large Irregular Galaxies at High Redshift. *ApJ*, 599:92–104.
- Chen, C.-C., Cowie, L. L., Barger, A. J., Casey, C. M., Lee, N., Sanders, D. B., Wang, W.-H., and Williams, J. P. (2013). Resolving the Cosmic Far-infrared Background at 450 and 850  $\mu\text{m}$  with SCUBA-2. *ApJ*, 776:131.
- Cimatti, A., Daddi, E., Renzini, A., Cassata, P., Vanzella, E., Pozzetti, L., Cristiani, S., Fontana, A., Rodighiero, G., Mignoli, M., and Zamorani, G. (2004). Old galaxies in the young Universe. *Nature*, 430:184–187.
- Clements, D. L., Rigby, E., Maddox, S., Dunne, L., Mortier, A., Pearson, C., Amblard, A., Auld, R., Baes, M., Bonfield, D., Burgarella, D., Buttiglione, S., Cava, A., Cooray, A., Dariush, A., de Zotti, G., Dye, S., Eales, S., Frayer, D., Fritz, J., Gardner, J. P., Gonzalez-Nuevo, J., Herranz, D., Ibar, E., Ivison, R., Jarvis, M. J., Lagache, G., Leeuw, L., Lopez-Caniego, M., Negrello, M., Pascale, E., Pohlen, M., Rodighiero, G., Samui, S., Serjeant, S., Sibthorpe, B., Scott, D., Smith, D. J. B., Temi, P., Thompson, M., Valtchanov, I., van der Werf, P., and Verma, A. (2010). Herschel-ATLAS: Extragalactic number counts from 250 to 500 microns. *A&A*, 518:L8.
- Clements, D. L., Sutherland, W. J., McMahon, R. G., and Saunders, W. (1996). Optical imaging of ultraluminous IRAS galaxies: how many are mergers? *MNRAS*, 279:477–497.
- Collins, C. A., Stott, J. P., Hilton, M., Kay, S. T., Stanford, S. A., Davidson, M., Hosmer, M., Hoyle, B., Liddle, A., Lloyd-Davies, E., Mann, R. G., Mehrtens, N., Miller, C. J., Nichol, R. C., Romer, A. K., Sahlén, M., Viana, P. T. P., and West, M. J. (2009). Early assembly of the most massive galaxies. *Nature*, 458:603–606.

- Condon, J. J. (1974). Confusion and Flux-Density Error Distributions. *ApJ*, 188:279–286.
- Condon, J. J., Cotton, W. D., Greisen, E. W., Yin, Q. F., Perley, R. A., Taylor, G. B., and Broderick, J. J. (1998). The NRAO VLA Sky Survey. *AJ*, 115:1693–1716.
- Conley, A., Cooray, A., Vieira, J. D., González Solares, E. A., Kim, S., Aguirre, J. E., Amblard, A., Auld, R., Baker, A. J., Beelen, A., Blain, A., Blundell, R., Bock, J., Bradford, C. M., Bridge, C., Brisbin, D., Burgarella, D., Carpenter, J. M., Chanical, P., Chapin, E., Christopher, N., Clements, D. L., Cox, P., Djorgovski, S. G., Dowell, C. D., Eales, S., Earle, L., Ellsworth-Bowers, T. P., Farrah, D., Franceschini, A., Frayer, D., Fu, H., Gavazzi, R., Glenn, J., Griffin, M., Gurwell, M. A., Halpern, M., Ibar, E., Ivison, R. J., Jarvis, M., Kamenetzky, J., Krips, M., Levenson, L., Lupu, R., Mahabal, A., Maloney, P. D., Maraston, C., Marchetti, L., Marsden, G., Matsuhara, H., Mortier, A. M. J., Murphy, E., Naylor, B. J., Neri, R., Nguyen, H. T., Oliver, S. J., Omont, A., Page, M. J., Papageorgiou, A., Pearson, C. P., Pérez-Fournon, I., Pohlen, M., Rangwala, N., Rawlings, J. I., Raymond, G., Riechers, D., Rodighiero, G., Roseboom, I. G., Rowan-Robinson, M., Schulz, B., Scott, D., Scott, K., Serra, P., Seymour, N., Shupe, D. L., Smith, A. J., Symeonidis, M., Tugwell, K. E., Vaccari, M., Valiante, E., Valtchanov, I., Verma, A., Viero, M. P., Vigroux, L., Wang, L., Wiebe, D., Wright, G., Xu, C. K., Zeimann, G., Zemcov, M., and Zmuidzinas, J. (2011). Discovery of a Multiply Lensed Submillimeter Galaxy in Early HerMES Herschel/SPIRE Data. *ApJL*, 732:L35.
- Conselice, C. J., Chapman, S. C., and Windhorst, R. A. (2003). Evidence for a Major Merger Origin of High-Redshift Submillimeter Galaxies. *ApJL*, 596:L5–L8.
- Cooray, A. and Sheth, R. (2002). Halo models of large scale structure. *PhR*, 372:1–129.
- Coppin, K., Chapin, E. L., Mortier, A. M. J., Scott, S. E., Borys, C., Dunlop, J. S., Halpern, M., Hughes, D. H., Pope, A., Scott, D., Serjeant, S., Wagg, J., Alexander, D. M., Almaini, O., Aretxaga, I., Babbedge, T., Best, P. N., Blain, A., Chapman, S., Clements, D. L., Crawford, M., Dunne, L., Eales, S. A., Edge, A. C., Farrah, D., Gaztañaga, E., Gear, W. K., Granato, G. L., Greve, T. R., Fox, M., Ivison, R. J., Jarvis, M. J., Jenness, T., Lacey, C., Lepage, K., Mann, R. G., Marsden, G., Martinez-Sansigre, A., Oliver, S., Page, M. J., Peacock, J. A., Pearson, C. P., Percival, W. J., Priddey, R. S., Rawlings, S., Rowan-Robinson, M., Savage, R. S., Seigar, M., Sekiguchi, K., Silva, L., Simpson, C., Smail, I., Stevens, J. A., Takagi, T., Vaccari, M., van Kampen, E., and Willott, C. J. (2006). The SCUBA Half-Degree Extragalactic

Survey - II. Submillimetre maps, catalogue and number counts. *MNRAS*, 372:1621–1652.

Coppin, K. E. K., Smail, I., Alexander, D. M., Weiss, A., Walter, F., Swinbank, A. M., Greve, T. R., Kovacs, A., De Breuck, C., Dickinson, M., Ibar, E., Ivison, R. J., Reddy, N., Spinrad, H., Stern, D., Brandt, W. N., Chapman, S. C., Dannerbauer, H., van Dokkum, P., Dunlop, J. S., Frayer, D., Gawiser, E., Geach, J. E., Huynh, M., Knudsen, K. K., Koekemoer, A. M., Lehmer, B. D., Menten, K. M., Papovich, C., Rix, H.-W., Schinnerer, E., Wardlow, J. L., and van der Werf, P. P. (2009). A submillimetre galaxy at  $z = 4.76$  in the LABOCA survey of the Extended Chandra Deep Field-South. *MNRAS*, 395:1905–1914.

Cowie, L. L., Songaila, A., Hu, E. M., and Cohen, J. G. (1996). New Insight on Galaxy Formation and Evolution From Keck Spectroscopy of the Hawaii Deep Fields. *AJ*, 112:839.

Currie, M. J. and Berry, D. S. (2013). KAPPA - Kernel Application Package. *Starlink User Note 95*.

Daddi, E., Bournaud, F., Walter, F., Dannerbauer, H., Carilli, C. L., Dickinson, M., Elbaz, D., Morrison, G. E., Riechers, D., Onodera, M., Salmi, F., Krips, M., and Stern, D. (2010). Very High Gas Fractions and Extended Gas Reservoirs in  $z = 1.5$  Disk Galaxies. *ApJ*, 713:686–707.

Daddi, E., Dannerbauer, H., Elbaz, D., Dickinson, M., Morrison, G., Stern, D., and Ravindranath, S. (2008). Vigorous Star Formation with Low Efficiency in Massive Disk Galaxies at  $z = 1.5$ . *ApJL*, 673:L21–L24.

Daddi, E., Dannerbauer, H., Stern, D., Dickinson, M., Morrison, G., Elbaz, D., Gialisco, M., Mancini, C., Pope, A., and Spinrad, H. (2009). Two Bright Submillimetre Galaxies in a  $z = 4.05$  Protocluster in GOODS-North, and Accurate Radio-Infrared Photometric Redshifts. *ApJ*, 694:1517–1538.

Davé, R., Finlator, K., Oppenheimer, B. D., Fardal, M., Katz, N., Kereš, D., and Weinberg, D. H. (2010). The nature of submillimetre galaxies in cosmological hydrodynamic simulations. *MNRAS*, 404:1355–1368.

de Graauw, T., Helmich, F. P., Phillips, T. G., Stutzki, J., Caux, E., Whyborn, N. D., Dieleman, P., Roelfsema, P. R., Aarts, H., Assendorp, R., Bachiller, R., Baechtold, W., Barcia, A., Beintema, D. A., Belitsky, V., Benz, A. O., Bieber, R., Boogert,

A., Borys, C., Bumble, B., Caïs, P., Caris, M., Cerulli-Irelli, P., Chattopadhyay, G., Cherednichenko, S., Ciechanowicz, M., Coeur-Joly, O., Comito, C., Cros, A., de Jonge, A., de Lange, G., Delforges, B., Delorme, Y., den Boggende, T., Desbat, J.-M., Diez-González, C., di Giorgio, A. M., Dubbeldam, L., Edwards, K., Eggens, M., Erickson, N., Evers, J., Fich, M., Finn, T., Franke, B., Gaier, T., Gal, C., Gao, J. R., Gallego, J.-D., Gauffre, S., Gill, J. J., Glenz, S., Golstein, H., Goulooze, H., Gunsing, T., Güsten, R., Hartogh, P., Hatch, W. A., Higgins, R., Honingh, E. C., Huisman, R., Jackson, B. D., Jacobs, H., Jacobs, K., Jarchow, C., Javadi, H., Jellema, W., Justen, M., Karpov, A., Kasemann, C., Kawamura, J., Keizer, G., Kester, D., Klapwijk, T. M., Klein, T., Kollberg, E., Kooi, J., Kooiman, P.-P., Kopf, B., Krause, M., Krieg, J.-M., Kramer, C., Kruizenga, B., Kuhn, T., Laauwen, W., Lai, R., Larsson, B., Leduc, H. G., Leinz, C., Lin, R. H., Liseau, R., Liu, G. S., Loose, A., López-Fernandez, I., Lord, S., Luinge, W., Marston, A., Martín-Pintado, J., Maestrini, A., Maiwald, F. W., McCoey, C., Mehdi, I., Megej, A., Melchior, M., Meinsma, L., Merkel, H., Michalska, M., Monstein, C., Moratschke, D., Morris, P., Muller, H., Murphy, J. A., Naber, A., Natale, E., Nowosielski, W., Nuzzolo, F., Olberg, M., Olbrich, M., Orfei, R., Orleanski, P., Ossenkopf, V., Peacock, T., Pearson, J. C., Peron, I., Phillip-May, S., Piazzo, L., Planesas, P., Rataj, M., Ravera, L., Risacher, C., Salez, M., Samoska, L. A., Saraceno, P., Schieder, R., Schlecht, E., Schlöder, F., Schmölling, F., Schultz, M., Schuster, K., Siebertz, O., Smit, H., Szczerba, R., Shipman, R., Steinmetz, E., Stern, J. A., Stokroos, M., Teipen, R., Teyssier, D., Tils, T., Trappe, N., van Baaren, C., van Leeuwen, B.-J., van de Stadt, H., Visser, H., Wildeman, K. J., Wafelbakker, C. K., Ward, J. S., Wesselius, P., Wild, W., Wulff, S., Wunsch, H.-J., Tielens, X., Zaal, P., Zirath, H., Zmuidzinas, J., and Zwart, F. (2010). The Herschel-Heterodyne Instrument for the Far-Infrared (HIFI). *A&A*, 518:L6.

Dekel, A., Birnboim, Y., Engel, G., Freundlich, J., Goerdt, T., Mumcuoglu, M., Neistein, E., Pichon, C., Teyssier, R., and Zinger, E. (2009). Cold streams in early massive hot haloes as the main mode of galaxy formation. *Nature*, 457:451–454.

Delabrouille, J., Cardoso, J.-F., and Patanchon, G. (2003). Multidetector multicomponent spectral matching and applications for cosmic microwave background data analysis. *MNRAS*, 346:1089–1102.

Dempsey, J. T., Friberg, P., Jenness, T., Tilanus, R. P. J., Thomas, H. S., Holland, W. S., Bintley, D., Berry, D. S., Chapin, E. L., Chrysostomou, A., Davis, G. R., Gibb, A. G., Parsons, H., and Robson, E. I. (2013). SCUBA-2: on-sky calibration using submillimetre standard sources. *MNRAS*, 430:2534–2544.

- Devlin, M. J., Ade, P. A. R., Aretxaga, I., Bock, J. J., Chapin, E. L., Griffin, M., Gundersen, J. O., Halpern, M., Hargrave, P. C., Hughes, D. H., Klein, J., Marsden, G., Martin, P. G., Mauskopf, P., Moncelsi, L., Netterfield, C. B., Ngo, H., Olmi, L., Pascale, E., Patanchon, G., Rex, M., Scott, D., Semisch, C., Thomas, N., Truch, M. D. P., Tucker, C., Tucker, G. S., Viero, M. P., and Wiebe, D. V. (2009). Over half of the far-infrared background light comes from galaxies at  $z \geq 1.2$ . *Nature*, 458:737–739.
- Devlin, M. J., Ade, P. A. R., Aretxaga, I., Bock, J. J., Chung, J., Chapin, E., Dicker, S. R., Griffin, M., Gundersen, J., Halpern, M., Hargrave, P., Hughes, D., Klein, J., Marsden, G., Martin, P., Mauskopf, P. D., Netterfield, B., Olmi, L., Pascale, E., Rex, M., Scott, D., Semisch, C., Truch, M., Tucker, C., Tucker, G., Turner, A. D., and Weibe, D. (2004). The Balloon-borne Large Aperture Submillimeter Telescope (BLAST). In *Z-Spec: a broadband millimeter-wave grating spectrometer: design, construction, and first cryogenic measurements*, volume 5498, pages 42–54.
- Dole, H., Lagache, G., and Puget, J.-L. (2003). Predictions for Cosmological Infrared Surveys from Space with the Multiband Imaging Photometer for SIRTF. *ApJ*, 585:617–629.
- Dole, H., Lagache, G., Puget, J.-L., Caputi, K. I., Fernández-Conde, N., Le Floch, E., Papovich, C., Pérez-González, P. G., Rieke, G. H., and Blaylock, M. (2006). The cosmic infrared background resolved by Spitzer. Contributions of mid-infrared galaxies to the far-infrared background. *A&A*, 451:417–429.
- Dowell, C. D., Conley, A., Glenn, J., Arumugam, V., Asboth, V., Aussel, H., Bertoldi, F., Béthermin, M., Bock, J., Boselli, A., Bridge, C., Buat, V., Burgarella, D., Cabrera-Lavers, A., Casey, C. M., Chapman, S. C., Clements, D. L., Conversi, L., Cooray, A., Dannerbauer, H., De Bernardis, F., Ellsworth-Bowers, T. P., Farrah, D., Franceschini, A., Griffin, M., Gurwell, M. A., Halpern, M., Hatziminaoglou, E., Heinis, S., Ibar, E., Ivison, R. J., Laporte, N., Marchetti, L., Martínez-Navajas, P., Marsden, G., Morrison, G. E., Nguyen, H. T., O’Halloran, B., Oliver, S. J., Omont, A., Page, M. J., Papa-georgiou, A., Pearson, C. P., Petitpas, G., Pérez-Fournon, I., Pohlen, M., Riechers, D., Rigopoulou, D., Roseboom, I. G., Rowan-Robinson, M., Sayers, J., Schulz, B., Scott, D., Seymour, N., Shupe, D. L., Smith, A. J., Streblyanska, A., Symeonidis, M., Vaccari, M., Valtchanov, I., Vieira, J. D., Viero, M., Wang, L., Wardlow, J., Xu, C. K., and Zemcov, M. (2014). HerMES: Candidate High-redshift Galaxies Discovered with Herschel/SPIRE. *ApJ*, 780:75.

- Draine, B. T. (2006). On the Submillimeter Opacity of Protoplanetary Disks. *ApJ*, 636:1114–1120.
- Dressler, A. (1980). Galaxy morphology in rich clusters - Implications for the formation and evolution of galaxies. *ApJ*, 236:351–365.
- Duband, L. (1997). A He<sup>3</sup> adsorption cooler associated with a 2.5 K mechanical cooler. In *Sixth European Symposium on Space Environmental Control Systems*, volume 400, page 503.
- Dünner, R., Hasselfield, M., Marriage, T. A., Sievers, J., Acquaviva, V., Addison, G. E., Ade, P. A. R., Aguirre, P., Amiri, M., Appel, J. W., Barrientos, L. F., Battistelli, E. S., Bond, J. R., Brown, B., Burger, B., Calabrese, E., Chervenak, J., Das, S., Devlin, M. J., Dicker, S. R., Bertrand Doriese, W., Dunkley, J., Essinger-Hileman, T., Fisher, R. P., Gralla, M. B., Fowler, J. W., Hajian, A., Halpern, M., Hernández-Monteagudo, C., Hilton, G. C., Hilton, M., Hincks, A. D., Hlozek, R., Huffenberger, K. M., Hughes, D. H., Hughes, J. P., Infante, L., Irwin, K. D., Baptiste Juin, J., Kaul, M., Klein, J., Kosowsky, A., Lau, J. M., Limon, M., Lin, Y.-T., Louis, T., Lupton, R. H., Marsden, D., Martocci, K., Mauskopf, P., Menanteau, F., Moodley, K., Moseley, H., Netterfield, C. B., Niemack, M. D., Nolta, M. R., Page, L. A., Parker, L., Partridge, B., Quintana, H., Reid, B., Sehgal, N., Sherwin, B. D., Spergel, D. N., Staggs, S. T., Swetz, D. S., Switzer, E. R., Thornton, R., Trac, H., Tucker, C., Warne, R., Wilson, G., Wollack, E., and Zhao, Y. (2013). The Atacama Cosmology Telescope: Data Characterization and Mapmaking. *ApJ*, 762:10.
- Dwek, E., Arendt, R. G., Hauser, M. G., Fixsen, D., Kelsall, T., Leisawitz, D., Pei, Y. C., Wright, E. L., Mather, J. C., Moseley, S. H., Odegard, N., Shafer, R., Silverberg, R. F., and Weiland, J. L. (1998). The COBE Diffuse Infrared Background Experiment Search for the Cosmic Infrared Background. IV. Cosmological Implications. *ApJ*, 508:106–122.
- Eales, S., Lilly, S., Webb, T., Dunne, L., Gear, W., Clements, D., and Yun, M. (2000). The Canada-UK Deep Submillimeter Survey. IV. The Survey of the 14 Hour Field. *AJ*, 120:2244–2268.
- Eddington, A. S. (1913). On a formula for correcting statistics for the effects of a known error of observation. *MNRAS*, 73.
- Eisenstein, D. J., Weinberg, D. H., Agol, E., Aihara, H., Allende Prieto, C., Anderson, S. F., Arns, J. A., Aubourg, É., Bailey, S., Balbinot, E., and et al. (2011). SDSS-III:

- Massive Spectroscopic Surveys of the Distant Universe, the Milky Way, and Extra-Solar Planetary Systems. *AJ*, 142:72.
- Ellingson, E., Lin, H., Yee, H. K. C., and Carlberg, R. G. (2001). The Evolution of Population Gradients in Galaxy Clusters: The Butcher-Oemler Effect and Cluster Infall. *ApJ*, 547:609–622.
- Emerson, J. P., Sutherland, W. J., McPherson, A. M., Craig, S. C., Dalton, G. B., and Ward, A. K. (2004). The Visible & Infrared Survey Telescope for Astronomy. *The Messenger*, 117:27–32.
- Fixsen, D. J., Dwek, E., Mather, J. C., Bennett, C. L., and Shafer, R. A. (1998). The Spectrum of the Extragalactic Far-Infrared Background from the COBE FIRAS Observations. *ApJ*, 508:123–128.
- Franceschini, A., Toffolatti, L., Mazzei, P., Danese, L., and de Zotti, G. (1991). Galaxy counts and contributions to the background radiation from 1 micron to 1000 microns. *A&AS*, 89:285–310.
- Geach, J. E., Chapin, E. L., Coppin, K. E. K., Dunlop, J. S., Halpern, M., Smail, I., van der Werf, P., Serjeant, S., Farrah, D., Roseboom, I., Targett, T., Arumugam, V., Asboth, V., Blain, A., Chrysostomou, A., Clarke, C., Ivison, R. J., Jones, S. L., Karim, A., Mackenzie, T., Meijerink, R., Michałowski, M. J., Scott, D., Simpson, J. M., Swinbank, A. M., Alexander, D. M., Almaini, O., Aretxaga, I., Best, P., Chapman, S., Clements, D. L., Conselice, C., Danielson, A. L. R., Eales, S., Edge, A. C., Gibb, A. G., Hughes, D., Jenness, T., Knudsen, K. K., Lacey, C. G., Marsden, G., McMahon, R., Oliver, S. J., Page, M. J., Peacock, J. A., Rigopoulou, D., Robson, E. I., Spaans, M., Stevens, J., Webb, T. M. A., Willott, C., Wilson, C. D., and Zemcov, M. (2013). The SCUBA-2 Cosmology Legacy Survey: blank-field number counts of 450- $\mu$ m-selected galaxies and their contribution to the cosmic infrared background. *MNRAS*, 432:53–61.
- Geach, J. E., Smail, I., Moran, S. M., MacArthur, L. A., Lagos, C. d. P., and Edge, A. C. (2011). On the Evolution of the Molecular Gas Fraction of Star-Forming Galaxies. *ApJL*, 730:L19.
- Genzel, R., Tacconi, L. J., Gracia-Carpio, J., Sternberg, A., Cooper, M. C., Shapiro, K., Bolatto, A., Bouché, N., Bournaud, F., Burkert, A., Combes, F., Comerford, J., Cox, P., Davis, M., Schreiber, N. M. F., Garcia-Burillo, S., Lutz, D., Naab, T., Neri, R.,

- Omont, A., Shapley, A., and Weiner, B. (2010). A study of the gas-star formation relation over cosmic time. *MNRAS*, 407:2091–2108.
- Gibb, A. G., Jenness, T., and Economou, F. (2012). PICARD - A Pipeline for Combining and Analyzing Reduced Data. *Starlink User Note 265*.
- Gladders, M. D. and Yee, H. K. C. (2000). A New Method For Galaxy Cluster Detection. I. The Algorithm. *AJ*, 120:2148–2162.
- Glenn, J., Conley, A., Béthermin, M., Altieri, B., Amblard, A., Arumugam, V., Aussel, H., Babbedge, T., Blain, A., Bock, J., Boselli, A., Buat, V., Castro-Rodríguez, N., Cava, A., Chanical, P., Clements, D. L., Conversi, L., Cooray, A., Dowell, C. D., Dwek, E., Eales, S., Elbaz, D., Ellsworth-Bowers, T. P., Fox, M., Franceschini, A., Gear, W., Griffin, M., Halpern, M., Hatziminaoglou, E., Ibar, E., Isaak, K., Ivison, R. J., Lagache, G., Laurent, G., Levenson, L., Lu, N., Madden, S., Maffei, B., Mainetti, G., Marchetti, L., Marsden, G., Nguyen, H. T., O’Halloran, B., Oliver, S. J., Omont, A., Page, M. J., Panuzzo, P., Papageorgiou, A., Pearson, C. P., Pérez-Fournon, I., Pohlen, M., Rigopoulou, D., Rizzo, D., Roseboom, I. G., Rowan-Robinson, M., Portal, M. S., Schulz, B., Scott, D., Seymour, N., Shupe, D. L., Smith, A. J., Stevens, J. A., Symeonidis, M., Trichas, M., Tugwell, K. E., Vaccari, M., Valtchanov, I., Vieira, J. D., Vigroux, L., Wang, L., Ward, R., Wright, G., Xu, C. K., and Zemcov, M. (2010). HERMES: deep galaxy number counts from a P(D) fluctuation analysis of SPIRE Science Demonstration Phase observations. *MNRAS*, 409:109–121.
- Gobat, R., Daddi, E., Onodera, M., Finoguenov, A., Renzini, A., Arimoto, N., Bouwens, R., Brusa, M., Chary, R.-R., Cimatti, A., Dickinson, M., Kong, X., and Mignoli, M. (2011). A mature cluster with X-ray emission at  $z = 2.07$ . *A&A*, 526:A133.
- Gómez, P. L., Nichol, R. C., Miller, C. J., Balogh, M. L., Goto, T., Zabludoff, A. I., Romer, A. K., Bernardi, M., Sheth, R., Hopkins, A. M., Castander, F. J., Connolly, A. J., Schneider, D. P., Brinkmann, J., Lamb, D. Q., SubbaRao, M., and York, D. G. (2003). Galaxy Star Formation as a Function of Environment in the Early Data Release of the Sloan Digital Sky Survey. *ApJ*, 584:210–227.
- Gralla, M. B., Crichton, D., Marriage, T. A., Mo, W., Aguirre, P., Addison, G. E., Asboth, V., Battaglia, N., Bock, J., Bond, J. R., Devlin, M. J., Dünner, R., Hajian, A., Halpern, M., Hilton, M., Hincks, A. D., Hlozek, R. A., Huffenberger, K. M., Hughes, J. P., Ivison, R. J., Kosowsky, A., Lin, Y.-T., Marsden, D., Menanteau, F., Moodley, K., Morales, G., Niemack, M. D., Oliver, S., Page, L. A., Partridge, B., Reese, E. D.,

- Rojas, F., Sehgal, N., Sievers, J., Sifón, C., Spergel, D. N., Staggs, S. T., Switzer, E. R., Viero, M. P., Wollack, E. J., and Zemcov, M. B. (2014). A measurement of the millimetre emission and the Sunyaev-Zel'dovich effect associated with low-frequency radio sources. *MNRAS*, 445:460–478.
- Greve, T. R., Bertoldi, F., Smail, I., Neri, R., Chapman, S. C., Blain, A. W., Ivison, R. J., Genzel, R., Omont, A., Cox, P., Tacconi, L., and Kneib, J.-P. (2005). An interferometric CO survey of luminous submillimetre galaxies. *MNRAS*, 359:1165–1183.
- Griffin, M. J. (2009). The SPIRE Analogue Signal Chain and Photometer Detector Data Processing Pipeline. *Document Number: SPIRE-UCF-DOC-002890, Issue 7*.
- Griffin, M. J., Abergel, A., Abreu, A., Ade, P. A. R., André, P., Augueres, J.-L., Babbedge, T., Bae, Y., Baillie, T., Baluteau, J.-P., Barlow, M. J., Bendo, G., Benielli, D., Bock, J. J., Bonhomme, P., Brisbin, D., Brockley-Blatt, C., Caldwell, M., Cara, C., Castro-Rodriguez, N., Cerulli, R., Chanical, P., Chen, S., Clark, E., Clements, D. L., Clerc, L., Coker, J., Communal, D., Conversi, L., Cox, P., Crumb, D., Cunningham, C., Daly, F., Davis, G. R., de Antoni, P., Delderfield, J., Devin, N., di Giorgio, A., Didschuns, I., Dohlen, K., Donati, M., Dowell, A., Dowell, C. D., Duband, L., Dumaye, L., Emery, R. J., Ferlet, M., Ferrand, D., Fontignie, J., Fox, M., Franceschini, A., Frerking, M., Fulton, T., Garcia, J., Gastaud, R., Gear, W. K., Glenn, J., Goizel, A., Griffin, D. K., Grundy, T., Guest, S., Guillemet, L., Hargrave, P. C., Harwit, M., Hastings, P., Hatziminaoglou, E., Herman, M., Hinde, B., Hristov, V., Huang, M., Imhof, P., Isaak, K. J., Israelsson, U., Ivison, R. J., Jennings, D., Kiernan, B., King, K. J., Lange, A. E., Latter, W., Laurent, G., Laurent, P., Leeks, S. J., Lellouch, E., Levenson, L., Li, B., Li, J., Lilienthal, J., Lim, T., Liu, S. J., Lu, N., Madden, S., Mainetti, G., Marliani, P., McKay, D., Mercier, K., Molinari, S., Morris, H., Moseley, H., Mulder, J., Mur, M., Naylor, D. A., Nguyen, H., O'Halloran, B., Oliver, S., Olofsson, G., Olofsson, H.-G., Orfei, R., Page, M. J., Pain, I., Panuzzo, P., Papageorgiou, A., Parks, G., Parr-Burman, P., Pearce, A., Pearson, C., Pérez-Fournon, I., Pinsard, F., Pisano, G., Podosek, J., Pohlen, M., Polehampton, E. T., Pouliquen, D., Rigopoulou, D., Rizzo, D., Roseboom, I. G., Roussel, H., Rowan-Robinson, M., Rownd, B., Saraceno, P., Sauvage, M., Savage, R., Savini, G., Sawyer, E., Scharnberg, C., Schmitt, D., Schneider, N., Schulz, B., Schwartz, A., Shafer, R., Shupe, D. L., Sibthorpe, B., Sidher, S., Smith, A., Smith, A. J., Smith, D., Spencer, L., Stobie, B., Sudiwala, R., Sukhatme, K., Surace, C., Stevens, J. A., Swinyard, B. M., Trichas, M., Tourette, T., Triou, H., Tseng, S., Tucker, C., Turner, A., Vaccari, M., Valtchanov, I., Vigroux, L.,

- Virique, E., Voellmer, G., Walker, H., Ward, R., Waskett, T., Weilert, M., Wesson, R., White, G. J., Whitehouse, N., Wilson, C. D., Winter, B., Woodcraft, A. L., Wright, G. S., Xu, C. K., Zavagno, A., Zemcov, M., Zhang, L., and Zonca, E. (2010). The Herschel-SPIRE instrument and its in-flight performance. *A&A*, 518:L3.
- Griffin, M. J., North, C. E., Schulz, B., Amaral-Rogers, A., Bendo, G., Bock, J., Conversi, L., Conley, A., Dowell, C. D., Ferlet, M., Glenn, J., Lim, T., Pearson, C., Pohlen, M., Sibthorpe, B., Spencer, L., Swinyard, B., and Valtchanov, I. (2013). Flux calibration of broad-band far-infrared and submillimetre photometric instruments: theory and application to Herschel-SPIRE. *MNRAS*, 434:992–1004.
- Gruppioni, C., Pozzi, F., Rodighiero, G., Delvecchio, I., Berta, S., Pozzetti, L., Zamorani, G., Andreani, P., Cimatti, A., Ilbert, O., Le Floc’h, E., Lutz, D., Magnelli, B., Marchetti, L., Monaco, P., Nordon, R., Oliver, S., Popesso, P., Riguccini, L., Roseboom, I., Rosario, D. J., Sargent, M., Vaccari, M., Altieri, B., Aussel, H., Bongiovanni, A., Cepa, J., Daddi, E., Domínguez-Sánchez, H., Elbaz, D., Förster Schreiber, N., Genzel, R., Iribarrem, A., Magliocchetti, M., Maiolino, R., Poglitsch, A., Pérez García, A., Sanchez-Portal, M., Sturm, E., Tacconi, L., Valtchanov, I., Amblard, A., Arumugam, V., Bethermin, M., Bock, J., Boselli, A., Buat, V., Burgarella, D., Castro-Rodríguez, N., Cava, A., Chanical, P., Clements, D. L., Conley, A., Cooray, A., Dowell, C. D., Dwek, E., Eales, S., Franceschini, A., Glenn, J., Griffin, M., Hatziminaoglou, E., Ibar, E., Isaak, K., Ivison, R. J., Lagache, G., Levenson, L., Lu, N., Madden, S., Maffei, B., Mainetti, G., Nguyen, H. T., O’Halloran, B., Page, M. J., Panuzzo, P., Papageorgiou, A., Pearson, C. P., Pérez-Fournon, I., Pohlen, M., Rigopoulou, D., Rowan-Robinson, M., Schulz, B., Scott, D., Seymour, N., Shupe, D. L., Smith, A. J., Stevens, J. A., Symeonidis, M., Trichas, M., Tugwell, K. E., Vigroux, L., Wang, L., Wright, G., Xu, C. K., Zemcov, M., Bardelli, S., Carollo, M., Contini, T., Le Fèvre, O., Lilly, S., Mainieri, V., Renzini, A., Scodreggio, M., and Zucca, E. (2013). The Herschel PEP/HerMES luminosity function - I. Probing the evolution of PACS selected Galaxies to  $z \simeq 4$ . *MNRAS*, 432:23–52.
- Gunn, J. E. and Gott, III, J. R. (1972). On the Infall of Matter Into Clusters of Galaxies and Some Effects on Their Evolution. *ApJ*, 176:1.
- Gunn, J. E., Hoessel, J. G., and Oke, J. B. (1986). A systematic survey for distant galaxy clusters. *ApJ*, 306:30–37.

- Haines, C. P., Smith, G. P., Egami, E., Ellis, R. S., Moran, S. M., Sanderson, A. J. R., Merluzzi, P., Busarello, G., and Smith, R. J. (2009). LOCUSS: The Mid-Infrared Butcher-Oemler Effect. *ApJ*, 704:126–136.
- Hajian, A., Viero, M. P., Addison, G., Aguirre, P., Appel, J. W., Battaglia, N., Bock, J. J., Bond, J. R., Das, S., Devlin, M. J., Dicker, S. R., Dunkley, J., Dünner, R., Essinger-Hileman, T., Hughes, J. P., Fowler, J. W., Halpern, M., Hasselfield, M., Hilton, M., Hincks, A. D., Hlozek, R., Irwin, K. D., Klein, J., Kosowsky, A., Lin, Y.-T., Marriage, T. A., Marsden, D., Marsden, G., Menanteau, F., Moncelsi, L., Moodley, K., Netterfield, C. B., Niemack, M. D., Nolta, M. R., Page, L. A., Parker, L., Patanchon, G., Scott, D., Sehgal, N., Sievers, J., Spergel, D. N., Staggs, S. T., Swetz, D. S., Switzer, E. R., Thornton, R., and Wollack, E. (2012). Correlations in the (Sub)millimeter Background from ACT x BLAST. *ApJ*, 744:40.
- Hasselfield, M., Hilton, M., Marriage, T. A., Addison, G. E., Barrientos, L. F., Battaglia, N., Battistelli, E. S., Bond, J. R., Crichton, D., Das, S., Devlin, M. J., Dicker, S. R., Dunkley, J., Dünner, R., Fowler, J. W., Gralla, M. B., Hajian, A., Halpern, M., Hincks, A. D., Hlozek, R., Hughes, J. P., Infante, L., Irwin, K. D., Kosowsky, A., Marsden, D., Menanteau, F., Moodley, K., Niemack, M. D., Nolta, M. R., Page, L. A., Partridge, B., Reese, E. D., Schmitt, B. L., Sehgal, N., Sherwin, B. D., Sievers, J., Sifón, C., Spergel, D. N., Staggs, S. T., Swetz, D. S., Switzer, E. R., Thornton, R., Trac, H., and Wollack, E. J. (2013a). The Atacama Cosmology Telescope: Sunyaev-Zel’dovich selected galaxy clusters at 148 GHz from three seasons of data. *JCAP*, 7:8.
- Hasselfield, M., Moodley, K., Bond, J. R., Das, S., Devlin, M. J., Dunkley, J., Dünner, R., Fowler, J. W., Gallardo, P., Gralla, M. B., Hajian, A., Halpern, M., Hincks, A. D., Marriage, T. A., Marsden, D., Niemack, M. D., Nolta, M. R., Page, L. A., Partridge, B., Schmitt, B. L., Sehgal, N., Sievers, J., Staggs, S. T., Swetz, D. S., Switzer, E. R., and Wollack, E. J. (2013b). The Atacama Cosmology Telescope: Beam Measurements and the Microwave Brightness Temperatures of Uranus and Saturn. *ApJS*, 209:17.
- Hauser, M. G., Arendt, R. G., Kelsall, T., Dwek, E., Odegard, N., Weiland, J. L., Freudenreich, H. T., Reach, W. T., Silverberg, R. F., Moseley, S. H., Pei, Y. C., Lubin, P., Mather, J. C., Shafer, R. A., Smoot, G. F., Weiss, R., Wilkinson, D. T., and Wright, E. L. (1998). The COBE Diffuse Infrared Background Experiment Search for the Cosmic Infrared Background. I. Limits and Detections. *ApJ*, 508:25–43.

- Hayward, C. C., Narayanan, D., Kereš, D., Jonsson, P., Hopkins, P. F., Cox, T. J., and Hernquist, L. (2013). Submillimetre galaxies in a hierarchical universe: number counts, redshift distribution and implications for the IMF. *MNRAS*, 428:2529–2547.
- Hildebrand, R. H. (1983). The Determination of Cloud Masses and Dust Characteristics from Submillimetre Thermal Emission. *QJRAS*, 24.
- Hill, G. J., Gebhardt, K., Komatsu, E., Drory, N., MacQueen, P. J., Adams, J., Blanc, G. A., Koehler, R., Rafal, M., Roth, M. M., Kelz, A., Gronwall, C., Ciardullo, R., and Schneider, D. P. (2008). The Hobby-Eberly Telescope Dark Energy Experiment (HETDEX): Description and Early Pilot Survey Results. In *Panoramic Views of Galaxy Formation and Evolution*, volume 399 of *Astronomical Society of the Pacific Conference Series*, page 115.
- Hodge, J. A., Becker, R. H., White, R. L., Richards, G. T., and Zeimann, G. R. (2011). High-resolution Very Large Array Imaging of Sloan Digital Sky Survey Stripe 82 at 1.4 GHz. *AJ*, 142:3.
- Hogg, D. W. (1999). Distance measures in cosmology. *ArXiv Astrophysics e-prints*, arXiv:astro-ph/9905116.
- Holland, W. S., Bintley, D., Chapin, E. L., Chrysostomou, A., Davis, G. R., Dempsey, J. T., Duncan, W. D., Fich, M., Friberg, P., Halpern, M., Irwin, K. D., Jenness, T., Kelly, B. D., MacIntosh, M. J., Robson, E. I., Scott, D., Ade, P. A. R., Atad-Ettedgui, E., Berry, D. S., Craig, S. C., Gao, X., Gibb, A. G., Hilton, G. C., Hollister, M. I., Kycia, J. B., Lunney, D. W., McGregor, H., Montgomery, D., Parkes, W., Tilanus, R. P. J., Ullom, J. N., Walther, C. A., Walton, A. J., Woodcraft, A. L., Amiri, M., Atkinson, D., Burger, B., Chuter, T., Coulson, I. M., Doriese, W. B., Dunare, C., Economou, F., Niemack, M. D., Parsons, H. A. L., Reintsema, C. D., Sibthorpe, B., Smail, I., Sudiwala, R., and Thomas, H. S. (2013). SCUBA-2: the 10 000 pixel bolometer camera on the James Clerk Maxwell Telescope. *MNRAS*, 430:2513–2533.
- Holland, W. S., Robson, E. I., Gear, W. K., Cunningham, C. R., Lightfoot, J. F., Jenness, T., Ivison, R. J., Stevens, J. A., Ade, P. A. R., Griffin, M. J., Duncan, W. D., Murphy, J. A., and Naylor, D. A. (1999). SCUBA: a common-user submillimetre camera operating on the James Clerk Maxwell Telescope. *MNRAS*, 303:659–672.
- Hopkins, P. F., Hernquist, L., Cox, T. J., and Kereš, D. (2008). A Cosmological Framework for the Co-Evolution of Quasars, Supermassive Black Holes, and Elliptical Galaxies. I. Galaxy Mergers and Quasar Activity. *ApJS*, 175:356–389.

- Houck, J. R., Schneider, D. P., Danielson, G. E., Neugebauer, G., Soifer, B. T., Beichman, C. A., and Lonsdale, C. J. (1985). Unidentified IRAS sources - Ultrahigh-luminosity galaxies. *ApJL*, 290:L5–L8.
- Hughes, D. H., Serjeant, S., Dunlop, J., Rowan-Robinson, M., Blain, A., Mann, R. G., Ivison, R., Peacock, J., Efstathiou, A., Gear, W., Oliver, S., Lawrence, A., Longair, M., Goldschmidt, P., and Jenness, T. (1998). High-redshift star formation in the Hubble Deep Field revealed by a submillimetre-wavelength survey. *Nature*, 394:241–247.
- Jain, B. and Lima, M. (2011). Magnification effects on source counts and fluxes. *MNRAS*, 411:2113–2117.
- Jenness, T., Berry, D. S., Cavanagh, B., Currie, M. J., Draper, P. W., and Economou, F. (2009). Developments in the Starlink Software Collection. In *Astronomical Data Analysis Software and Systems XVIII*, volume 411, page 418.
- Kartaltepe, J. S., Dickinson, M., Alexander, D. M., Bell, E. F., Dahlen, T., Elbaz, D., Faber, S. M., Lotz, J., McIntosh, D. H., Wiklind, T., Altieri, B., Aussel, H., Bethermin, M., Bournaud, F., Charmandaris, V., Conselice, C. J., Cooray, A., Dannerbauer, H., Davé, R., Dunlop, J., Dekel, A., Ferguson, H. C., Grogin, N. A., Hwang, H. S., Ivison, R., Kocevski, D., Koekemoer, A., Koo, D. C., Lai, K., Leiton, R., Lucas, R. A., Lutz, D., Magdis, G., Magnelli, B., Morrison, G., Mozena, M., Mullaney, J., Newman, J. A., Pope, A., Popesso, P., van der Wel, A., Weiner, B., and Wuyts, S. (2012). GOODS-Herschel and CANDELS: The Morphologies of Ultraluminous Infrared Galaxies at  $z \sim 2$ . *ApJ*, 757:23.
- Kennicutt, Jr., R. C. (1998). The Global Schmidt Law in Star-forming Galaxies. *ApJ*, 498:541–552.
- Knudsen, K. K., van der Werf, P. P., and Kneib, J.-P. (2008). Probing the submillimetre number counts at  $f_{850\mu\text{m}} < 2\text{mJy}$ . *MNRAS*, 384:1611–1626.
- Koester, B. P., McKay, T. A., Annis, J., Wechsler, R. H., Evrard, A., Bleem, L., Becker, M., Johnston, D., Sheldon, E., Nichol, R., Miller, C., Scranton, R., Bahcall, N., Barrentine, J., Brewington, H., Brinkmann, J., Harvanek, M., Kleinman, S., Krzesinski, J., Long, D., Nitta, A., Schneider, D. P., Sneddin, S., Voges, W., and York, D. (2007). A MaxBCG Catalog of 13,823 Galaxy Clusters from the Sloan Digital Sky Survey. *ApJ*, 660:239–255.

- Kovács, A., Chapman, S. C., Dowell, C. D., Blain, A. W., Ivison, R. J., Smail, I., and Phillips, T. G. (2006). SHARC-2 350  $\mu\text{m}$  Observations of Distant Submillimeter-selected Galaxies. *ApJ*, 650:592–603.
- Kravtsov, A. V. and Borgani, S. (2012). Formation of Galaxy Clusters. *ARA&A*, 50:353–409.
- Laporte, N., Pérez-Fournon, I., Calanog, J. A., Cooray, A., Wardlow, J. L., Bock, J., Bridge, C., Burgarella, D., Bussmann, R. S., Cabrera-Lavers, A., Casey, C. M., Clements, D. L., Conley, A., Farrah, D., Fu, H., Gavazzi, R., González-Solares, E. A., Ivison, R. J., Lo Faro, B., Ma, B., Magdis, G., Marques-Chaves, R., Martínez-Navajas, P., Oliver, S. J., Osage, W. A., Riechers, D., Rigopoulou, D., Scott, D., Streblyanska, A., and Vieira, J. D. (2015). Environment of the submillimeter-bright massive starburst HFLS3 at  $z \sim 6.34$ .
- Larson, R. B., Tinsley, B. M., and Caldwell, C. N. (1980). The evolution of disk galaxies and the origin of S0 galaxies. *ApJ*, 237:692–707.
- Le Floch, E., Papovich, C., Dole, H., Bell, E. F., Lagache, G., Rieke, G. H., Egami, E., Pérez-González, P. G., Alonso-Herrero, A., Rieke, M. J., Blaylock, M., Engelbracht, C. W., Gordon, K. D., Hines, D. C., Misselt, K. A., Morrison, J. E., and Mould, J. (2005). Infrared Luminosity Functions from the Chandra Deep Field-South: The Spitzer View on the History of Dusty Star Formation at  $0 \lesssim z \lesssim 1$ . *ApJ*, 632:169–190.
- Levenson, L., Marsden, G., Zemcov, M., Amblard, A., Blain, A., Bock, J., Chapin, E., Conley, A., Cooray, A., Dowell, C. D., Ellsworth-Bowers, T. P., Franceschini, A., Glenn, J., Griffin, M., Halpern, M., Nguyen, H. T., Oliver, S. J., Page, M. J., Papageorgiou, A., Pérez-Fournon, I., Pohlen, M., Rangwala, N., Rowan-Robinson, M., Schulz, B., Scott, D., Serra, P., Shupe, D. L., Valiante, E., Vieira, J. D., Vigroux, L., Wiebe, D., Wright, G., and Xu, C. K. (2010). HerMES: SPIRE Science Demonstration Phase maps. *MNRAS*, 409:83–91.
- Li, Y., Hernquist, L., Robertson, B., Cox, T. J., Hopkins, P. F., Springel, V., Gao, L., Di Matteo, T., Zentner, A. R., Jenkins, A., and Yoshida, N. (2007). Formation of  $z \sim 6$  Quasars from Hierarchical Galaxy Mergers. *ApJ*, 665:187–208.
- Lilly, S. J., Eales, S. A., Gear, W. K. P., Hammer, F., Le Fèvre, O., Crampton, D., Bond, J. R., and Dunne, L. (1999). The Canada-United Kingdom Deep Submillimeter Survey. II. First Identifications, Redshifts, and Implications for Galaxy Evolution. *ApJ*, 518:641–655.

- Madau, P. and Dickinson, M. (2014). Cosmic Star-Formation History. *ARA&A*, 52:415–486.
- Magdis, G. E., Daddi, E., Béthermin, M., Sargent, M., Elbaz, D., Pannella, M., Dickinson, M., Dannerbauer, H., da Cunha, E., Walter, F., Rigopoulou, D., Charmandaris, V., Hwang, H. S., and Kartaltepe, J. (2012). The Evolving Interstellar Medium of Star-forming Galaxies since  $z = 2$  as Probed by Their Infrared Spectral Energy Distributions. *ApJ*, 760:6.
- Magnelli, B., Popesso, P., Berta, S., Pozzi, F., Elbaz, D., Lutz, D., Dickinson, M., Altieri, B., Andreani, P., Aussel, H., Béthermin, M., Bongiovanni, A., Cepa, J., Charmandaris, V., Chary, R.-R., Cimatti, A., Daddi, E., Förster Schreiber, N. M., Genzel, R., Gruppioni, C., Harwit, M., Hwang, H. S., Ivison, R. J., Magdis, G., Maiolino, R., Murphy, E., Nordon, R., Pannella, M., Pérez García, A., Poglitsch, A., Rosario, D., Sanchez-Portal, M., Santini, P., Scott, D., Sturm, E., Tacconi, L. J., and Valtchanov, I. (2013). The deepest Herschel-PACS far-infrared survey: number counts and infrared luminosity functions from combined PEP/GOODS-H observations. *A&A*, 553:A132.
- Marriage, T. A., Acquaviva, V., Ade, P. A. R., Aguirre, P., Amiri, M., Appel, J. W., Barrientos, L. F., Battistelli, E. S., Bond, J. R., Brown, B., Burger, B., Chervenak, J., Das, S., Devlin, M. J., Dicker, S. R., Bertrand Doriese, W., Dunkley, J., Dünner, R., Essinger-Hileman, T., Fisher, R. P., Fowler, J. W., Hajian, A., Halpern, M., Hasselfield, M., Hernández-Monteagudo, C., Hilton, G. C., Hilton, M., Hincks, A. D., Hlozek, R., Huffenberger, K. M., Handel Hughes, D., Hughes, J. P., Infante, L., Irwin, K. D., Baptiste Juin, J., Kaul, M., Klein, J., Kosowsky, A., Lau, J. M., Limon, M., Lin, Y.-T., Lupton, R. H., Marsden, D., Martocci, K., Mauskopf, P., Menanteau, F., Moodley, K., Moseley, H., Netterfield, C. B., Niemack, M. D., Nolta, M. R., Page, L. A., Parker, L., Partridge, B., Quintana, H., Reese, E. D., Reid, B., Sehgal, N., Sherwin, B. D., Sievers, J., Spergel, D. N., Staggs, S. T., Swetz, D. S., Switzer, E. R., Thornton, R., Trac, H., Tucker, C., Warne, R., Wilson, G., Wollack, E., and Zhao, Y. (2011). The Atacama Cosmology Telescope: Sunyaev-Zel’dovich-Selected Galaxy Clusters at 148 GHz in the 2008 Survey. *ApJ*, 737:61.
- Marsden, D., Gralla, M., Marriage, T. A., Switzer, E. R., Partridge, B., Massardi, M., Morales, G., Addison, G., Bond, J. R., Crichton, D., Das, S., Devlin, M., Dünner, R., Hajian, A., Hilton, M., Hincks, A., Hughes, J. P., Irwin, K., Kosowsky, A., Menanteau, F., Moodley, K., Niemack, M., Page, L., Reese, E. D., Schmitt, B., Sehgal, N., Sievers, J., Staggs, S., Swetz, D., Thornton, R., and Wollack, E. (2014). The Atacama Cosmol-

- ogy Telescope: dusty star-forming galaxies and active galactic nuclei in the Southern survey. *MNRAS*, 439:1556–1574.
- Marsden, G., Ade, P. A. R., Bock, J. J., Chapin, E. L., Devlin, M. J., Dicker, S. R., Griffin, M., Gundersen, J. O., Halpern, M., Hargrave, P. C., Hughes, D. H., Klein, J., Mauskopf, P., Magnelli, B., Moncelsi, L., Netterfield, C. B., Ngo, H., Olmi, L., Pascale, E., Patanchon, G., Rex, M., Scott, D., Semisch, C., Thomas, N., Truch, M. D. P., Tucker, C., Tucker, G. S., Viero, M. P., and Wiebe, D. V. (2009). BLAST: Resolving the Cosmic Submillimeter Background. *ApJ*, 707:1729–1739.
- Menanteau, F., Sifón, C., Barrientos, L. F., Battaglia, N., Bond, J. R., Crichton, D., Das, S., Devlin, M. J., Dicker, S., Dünner, R., Gralla, M., Hajian, A., Hasselfield, M., Hilton, M., Hincks, A. D., Hughes, J. P., Infante, L., Kosowsky, A., Marriage, T. A., Marsden, D., Moodley, K., Niemack, M. D., Nolta, M. R., Page, L. A., Partridge, B., Reese, E. D., Schmitt, B. L., Sievers, J., Spergel, D. N., Staggs, S. T., Switzer, E., and Wollack, E. J. (2013). The Atacama Cosmology Telescope: Physical Properties of Sunyaev-Zel’dovich Effect Clusters on the Celestial Equator. *ApJ*, 765:67.
- Miyazaki, S., Komiyama, Y., Nakaya, H., Kamata, Y., Doi, Y., Hamana, T., Karoji, H., Furusawa, H., Kawanomoto, S., Morokuma, T., Ishizuka, Y., Nariai, K., Tanaka, Y., Uruguchi, F., Utsumi, Y., Obuchi, Y., Okura, Y., Oguri, M., Takata, T., Tomono, D., Kurakami, T., Namikawa, K., Usuda, T., Yamanoi, H., Terai, T., Uekiyo, H., Yamada, Y., Koike, M., Aihara, H., Fujimori, Y., Mineo, S., Miyatake, H., Yasuda, N., Nishizawa, J., Saito, T., Tanaka, M., Uchida, T., Katayama, N., Wang, S.-Y., Chen, H.-Y., Lupton, R., Loomis, C., Bickerton, S., Price, P., Gunn, J., Suzuki, H., Miyazaki, Y., Muramatsu, M., Yamamoto, K., Endo, M., Ezaki, Y., Itoh, N., Miwa, Y., Yokota, H., Matsuda, T., Ebinuma, R., and Takeshi, K. (2012). Hyper Suprime-Cam. In *Society of Photo-Optical Instrumentation Engineers (SPIE) Conference Series*, volume 8446, page 0.
- Moore, B., Katz, N., Lake, G., Dressler, A., and Oemler, A. (1996). Galaxy harassment and the evolution of clusters of galaxies. *Nature*, 379:613–616.
- Moreno, R. (1998). Phd thesis. *Universite de Paris*.
- Murphy, Jr., T. W., Armus, L., Matthews, K., Soifer, B. T., Mazzarella, J. M., Shupe, D. L., Strauss, M. A., and Neugebauer, G. (1996). Visual and Near-Infrared Imaging of Ultraluminous Infrared Galaxies: The IRAS 2 Jy Sample. *AJ*, 111:1025.

Negrello, M., Hopwood, R., De Zotti, G., Cooray, A., Verma, A., Bock, J., Frayer, D. T., Gurwell, M. A., Omont, A., Neri, R., Dannerbauer, H., Leeuw, L. L., Barton, E., Cooke, J., Kim, S., da Cunha, E., Rodighiero, G., Cox, P., Bonfield, D. G., Jarvis, M. J., Serjeant, S., Ivison, R. J., Dye, S., Aretxaga, I., Hughes, D. H., Ibar, E., Bertoldi, F., Valtchanov, I., Eales, S., Dunne, L., Driver, S. P., Auld, R., Buttiglione, S., Cava, A., Grady, C. A., Clements, D. L., Dariush, A., Fritz, J., Hill, D., Hornbeck, J. B., Kelvin, L., Lagache, G., Lopez-Caniego, M., Gonzalez-Nuevo, J., Maddox, S., Pascale, E., Pohlen, M., Rigby, E. E., Robotham, A., Simpson, C., Smith, D. J. B., Temi, P., Thompson, M. A., Woodgate, B. E., York, D. G., Aguirre, J. E., Beelen, A., Blain, A., Baker, A. J., Birkinshaw, M., Blundell, R., Bradford, C. M., Burgarella, D., Danese, L., Dunlop, J. S., Fleuren, S., Glenn, J., Harris, A. I., Kamenetzky, J., Lupu, R. E., Maddalena, R. J., Madore, B. F., Maloney, P. R., Matsuhara, H., Michałowski, M. J., Murphy, E. J., Naylor, B. J., Nguyen, H., Popescu, C., Rawlings, S., Rigopoulou, D., Scott, D., Scott, K. S., Seibert, M., Smail, I., Tuffs, R. J., Vieira, J. D., van der Werf, P. P., and Zmuidzinas, J. (2010). The Detection of a Population of Submillimeter-Bright, Strongly Lensed Galaxies. *Science*, 330:800–.

Negrello, M., Perrotta, F., González-Nuevo, J., Silva, L., de Zotti, G., Granato, G. L., Baccigalupi, C., and Danese, L. (2007). Astrophysical and cosmological information from large-scale submillimetre surveys of extragalactic sources. *MNRAS*, 377:1557–1568.

Neugebauer, G., Habing, H. J., van Duinen, R., Aumann, H. H., Baud, B., Beichman, C. A., Beintema, D. A., Boggess, N., Clegg, P. E., de Jong, T., Emerson, J. P., Gautier, T. N., Gillett, F. C., Harris, S., Hauser, M. G., Houck, J. R., Jennings, R. E., Low, F. J., Marsden, P. L., Miley, G., Olon, F. M., Pottasch, S. R., Raimond, E., Rowan-Robinson, M., Soifer, B. T., Walker, R. G., Wesselius, P. R., and Young, E. (1984). The Infrared Astronomical Satellite (IRAS) mission. *ApJL*, 278:L1–L6.

Nguyen, H. T., Schulz, B., Levenson, L., Amblard, A., Arumugam, V., Aussel, H., Babbedge, T., Blain, A., Bock, J., Boselli, A., Buat, V., Castro-Rodriguez, N., Cava, A., Chanical, P., Chapin, E., Clements, D. L., Conley, A., Conversi, L., Cooray, A., Dowell, C. D., Dwek, E., Eales, S., Elbaz, D., Fox, M., Franceschini, A., Gear, W., Glenn, J., Griffin, M., Halpern, M., Hatziminaoglou, E., Ibar, E., Isaak, K., Ivison, R. J., Lagache, G., Lu, N., Madden, S., Maffei, B., Mainetti, G., Marchetti, L., Marsden, G., Marshall, J., O’Halloran, B., Oliver, S. J., Omont, A., Page, M. J., Panuzzo, P., Papageorgiou, A., Pearson, C. P., Perez Fournon, I., Pohlen, M., Rangwala, N.,

- Rigopoulou, D., Rizzo, D., Roseboom, I. G., Rowan-Robinson, M., Scott, D., Seymour, N., Shupe, D. L., Smith, A. J., Stevens, J. A., Symeonidis, M., Trichas, M., Tugwell, K. E., Vaccari, M., Valtchanov, I., Vigroux, L., Wang, L., Ward, R., Wiebe, D., Wright, G., Xu, C. K., and Zemcov, M. (2010). HerMES: The SPIRE confusion limit. *A&A*, 518:L5.
- Noeske, K. G., Weiner, B. J., Faber, S. M., Papovich, C., Koo, D. C., Somerville, R. S., Bundy, K., Conselice, C. J., Newman, J. A., Schiminovich, D., Le Floc’h, E., Coil, A. L., Rieke, G. H., Lotz, J. M., Primack, J. R., Barmby, P., Cooper, M. C., Davis, M., Ellis, R. S., Fazio, G. G., Guhathakurta, P., Huang, J., Kassin, S. A., Martin, D. C., Phillips, A. C., Rich, R. M., Small, T. A., Willmer, C. N. A., and Wilson, G. (2007). Star Formation in AEGIS Field Galaxies since  $z=1.1$ : The Dominance of Gradually Declining Star Formation, and the Main Sequence of Star-forming Galaxies. *ApJL*, 660:L43–L46.
- Oliver, S. J., Bock, J., Altieri, B., Amblard, A., Arumugam, V., Aussel, H., Babbedge, T., Beelen, A., Béthermin, M., Blain, A., Boselli, A., Bridge, C., Brisbin, D., Buat, V., Burgarella, D., Castro-Rodríguez, N., Cava, A., Chanical, P., Cirasuolo, M., Clements, D. L., Conley, A., Conversi, L., Cooray, A., Dowell, C. D., Dubois, E. N., Dwek, E., Dye, S., Eales, S., Elbaz, D., Farrah, D., Feltre, A., Ferrero, P., Fiolet, N., Fox, M., Franceschini, A., Gear, W., Giovannoli, E., Glenn, J., Gong, Y., González Solares, E. A., Griffin, M., Halpern, M., Harwit, M., Hatziminaoglou, E., Heinis, S., Hurley, P., Hwang, H. S., Hyde, A., Ibar, E., Ilbert, O., Isaak, K., Ivison, R. J., Lagache, G., Le Floc’h, E., Levenson, L., Faro, B. L., Lu, N., Madden, S., Maffei, B., Magdis, G., Mainetti, G., Marchetti, L., Marsden, G., Marshall, J., Mortier, A. M. J., Nguyen, H. T., O’Halloran, B., Omont, A., Page, M. J., Panuzzo, P., Papageorgiou, A., Patel, H., Pearson, C. P., Pérez-Fournon, I., Pohlen, M., Rawlings, J. I., Raymond, G., Rigopoulou, D., Riguccini, L., Rizzo, D., Rodighiero, G., Roseboom, I. G., Rowan-Robinson, M., Sánchez Portal, M., Schulz, B., Scott, D., Seymour, N., Shupe, D. L., Smith, A. J., Stevens, J. A., Symeonidis, M., Trichas, M., Tugwell, K. E., Vaccari, M., Valtchanov, I., Vieira, J. D., Viero, M., Vigroux, L., Wang, L., Ward, R., Wardlow, J., Wright, G., Xu, C. K., and Zemcov, M. (2012). The Herschel Multi-tiered Extragalactic Survey: HerMES. *MNRAS*, 424:1614–1635.
- Oliver, S. J., Wang, L., Smith, A. J., Altieri, B., Amblard, A., Arumugam, V., Auld, R., Aussel, H., Babbedge, T., Blain, A., Bock, J., Boselli, A., Buat, V., Burgarella, D., Castro-Rodríguez, N., Cava, A., Chanical, P., Clements, D. L., Conley, A., Conversi, L., Cooray, A., Dowell, C. D., Dwek, E., Eales, S., Elbaz, D., Fox, M., Franceschini,

- A., Gear, W., Glenn, J., Griffin, M., Halpern, M., Hatziminaoglou, E., Ibar, E., Isaak, K., Ivison, R. J., Lagache, G., Levenson, L., Lu, N., Madden, S., Maffei, B., Mainetti, G., Marchetti, L., Mitchell-Wynne, K., Mortier, A. M. J., Nguyen, H. T., O'Halloran, B., Omont, A., Page, M. J., Panuzzo, P., Papageorgiou, A., Pearson, C. P., Pérez-Fournon, I., Pohlen, M., Rawlings, J. I., Raymond, G., Rigopoulou, D., Rizzo, D., Roseboom, I. G., Rowan-Robinson, M., Sánchez Portal, M., Savage, R., Schulz, B., Scott, D., Seymour, N., Shupe, D. L., Stevens, J. A., Symeonidis, M., Trichas, M., Tugwell, K. E., Vaccari, M., Valiante, E., Valtchanov, I., Vieira, J. D., Vigroux, L., Ward, R., Wright, G., Xu, C. K., and Zemcov, M. (2010). HerMES: SPIRE galaxy number counts at 250, 350, and 500  $\mu\text{m}$ . *A&A*, 518:L21.
- Ordenovic, C., Surace, C., Torresani, B., and Llebaria, A. (2008). Detection of glitches and signal reconstruction using Hoelder and wavelet analysis. *Statistical Methodology*, 5:373–386.
- Ordenovic, C., Surace, C., Torresani, B., Llebaria, A., and Baluteau, J. P. (2005). Use of a local regularity analysis by a wavelet analysis for glitch detection. *SPIE*, 5909:556–567.
- Ott, S. (2010). The Herschel Data Processing System - HIPE and Pipelines - Up and Running Since the Start of the Mission. 434:139.
- Paciga, G., Scott, D., and Chapin, E. L. (2009). Strong lensing of submillimetre galaxies: a tracer of foreground structure? *MNRAS*, 395:1153–1162.
- Pannella, M., Carilli, C. L., Daddi, E., McCracken, H. J., Owen, F. N., Renzini, A., Strazzullo, V., Civano, F., Koekemoer, A. M., Schinnerer, E., Scoville, N., Smolčić, V., Taniguchi, Y., Aussel, H., Kneib, J. P., Ilbert, O., Mellier, Y., Salvato, M., Thompson, D., and Willott, C. J. (2009). Star Formation and Dust Obscuration at  $z \sim 2$ : Galaxies at the Dawn of Downsizing. *ApJL*, 698:L116–L120.
- Papovich, C., Dole, H., Egami, E., Le Floc'h, E., Pérez-González, P. G., Alonso-Herrero, A., Bai, L., Beichman, C. A., Blaylock, M., Engelbracht, C. W., Gordon, K. D., Hines, D. C., Misselt, K. A., Morrison, J. E., Mould, J., Muzerolle, J., Neugebauer, G., Richards, P. L., Rieke, G. H., Rieke, M. J., Rigby, J. R., Su, K. Y. L., and Young, E. T. (2004). The 24 Micron Source Counts in Deep Spitzer Space Telescope Surveys. *ApJS*, 154:70–74.
- Papovich, C. J., Gebhardt, K., Behroozi, P., Bender, R., Blanc, G. A., Ciardullo, R., DePoy, D., de Jong, R., Drory, N., Evans, N., Fabricius, M., Finkelstein, S., Gawiser,

- E., Greene, J., Gronwall, C., Hill, G., Hopp, U., Jogee, S., Lacy, M., Landriau, M., Marshall, J., Tuttle, S., Somerville, R., Steinmetz, M., Suntzeff, N., Tran, K., Wechsler, R., and Wisotzki, L. (2012). SHELA: The Spitzer-HETDEX Exploratory Large Area Survey. volume 219 of *American Astronomical Society Meeting Abstracts*, page 424.09.
- Partridge, R. B. and Peebles, P. J. E. (1967). Are Young Galaxies Visible? II. The Integrated Background. *ApJ*, 148:377.
- Pascale, E., Ade, P. A. R., Bock, J. J., Chapin, E. L., Devlin, M. J., Dye, S., Eales, S. A., Griffin, M., Gundersen, J. O., Halpern, M., Hargrave, P. C., Hughes, D. H., Klein, J., Marsden, G., Maukopf, P., Moncelsi, L., Ngo, H., Netterfield, C. B., Olmi, L., Patanchon, G., Rex, M., Scott, D., Semisch, C., Thomas, N., Truch, M. D. P., Tucker, C., Tucker, G. S., Viero, M. P., and Wiebe, D. V. (2009). BLAST: A Far-Infrared Measurement of the History of Star Formation. *ApJ*, 707:1740–1749.
- Patanchon, G., Ade, P. A. R., Bock, J. J., Chapin, E. L., Devlin, M. J., Dicker, S., Griffin, M., Gundersen, J. O., Halpern, M., Hargrave, P. C., Hughes, D. H., Klein, J., Marsden, G., Martin, P. G., Maukopf, P., Netterfield, C. B., Olmi, L., Pascale, E., Rex, M., Scott, D., Semisch, C., Truch, M. D. P., Tucker, C., Tucker, G. S., Viero, M. P., and Wiebe, D. V. (2008). SANEPIC: A Mapmaking Method for Time Stream Data from Large Arrays. *ApJ*, 681:708–725.
- Patanchon, G., Ade, P. A. R., Bock, J. J., Chapin, E. L., Devlin, M. J., Dicker, S. R., Griffin, M., Gundersen, J. O., Halpern, M., Hargrave, P. C., Hughes, D. H., Klein, J., Marsden, G., Maukopf, P., Moncelsi, L., Netterfield, C. B., Olmi, L., Pascale, E., Rex, M., Scott, D., Semisch, C., Thomas, N., Truch, M. D. P., Tucker, C., Tucker, G. S., Viero, M. P., and Wiebe, D. V. (2009). Submillimeter Number Counts from Statistical Analysis of BLAST Maps. *ApJ*, 707:1750–1765.
- Peng, Y.-j., Lilly, S. J., Kovač, K., Bolzonella, M., Pozzetti, L., Renzini, A., Zamorani, G., Ilbert, O., Knobel, C., Iovino, A., Maier, C., Cucciati, O., Tasca, L., Carollo, C. M., Silverman, J., Kampczyk, P., de Ravel, L., Sanders, D., Scoville, N., Contini, T., Mainieri, V., Scodreggio, M., Kneib, J.-P., Le Fèvre, O., Bardelli, S., Bongiorno, A., Caputi, K., Coppa, G., de la Torre, S., Franzetti, P., Garilli, B., Lamareille, F., Le Borgne, J.-F., Le Brun, V., Mignoli, M., Perez Montero, E., Pello, R., Ricciardelli, E., Tanaka, M., Tresse, L., Vergani, D., Welikala, N., Zucca, E., Oesch, P., Abbas, U., Barnes, L., Bordoloi, R., Bottini, D., Cappi, A., Cassata, P., Cimatti, A., Fumana, M., Hasinger, G., Koekemoer, A., Leauthaud, A., Maccagni, D., Marinoni, C., McCracken,

- H., Memeo, P., Meneux, B., Nair, P., Porciani, C., Presotto, V., and Scaramella, R. (2010). Mass and Environment as Drivers of Galaxy Evolution in SDSS and zCOSMOS and the Origin of the Schechter Function. *ApJ*, 721:193–221.
- Perera, T. A., Chapin, E. L., Austermann, J. E., Scott, K. S., Wilson, G. W., Halpern, M., Pope, A., Scott, D., Yun, M. S., Lowenthal, J. D., Morrison, G., Aretxaga, I., Bock, J. J., Coppin, K., Crowe, M., Frey, L., Hughes, D. H., Kang, Y., Kim, S., and Mauskopf, P. D. (2008). An AzTEC 1.1mm survey of the GOODS-N field - I. Maps, catalogue and source statistics. *MNRAS*, 391:1227–1238.
- Pilbratt, G. L., Riedinger, J. R., Passvogel, T., Crone, G., Doyle, D., Gageur, U., Heras, A. M., Jewell, C., Metcalfe, L., Ott, S., and Schmidt, M. (2010). Herschel Space Observatory. An ESA facility for far-infrared and submillimetre astronomy. *A&A*, 518:L1.
- Planck Collaboration, Ade, P. A. R., Aghanim, N., Alves, M. I. R., Armitage-Caplan, C., Arnaud, M., Ashdown, M., Atrio-Barandela, F., Aumont, J., Aussel, H., et al. (2014a). Planck 2013 results. I. Overview of products and scientific results. *A&A*, 571:A1.
- Planck Collaboration, Ade, P. A. R., Aghanim, N., Armitage-Caplan, C., Arnaud, M., Ashdown, M., Atrio-Barandela, F., Aumont, J., Aussel, H., Baccigalupi, C., and et al. (2014b). Planck 2013 results. XXIX. The Planck catalogue of Sunyaev-Zeldovich sources. *A&A*, 571:A29.
- Planck Collaboration, Ade, P. A. R., Aghanim, N., Arnaud, M., Ashdown, M., Aumont, J., Baccigalupi, C., Balbi, A., Banday, A. J., Barreiro, R. B., and et al. (2011). Planck early results. VIII. The all-sky early Sunyaev-Zeldovich cluster sample. *A&A*, 536:A8.
- Poglitsch, A., Waelkens, C., Geis, N., Feuchtgruber, H., Vandenbussche, B., Rodriguez, L., Krause, O., Renotte, E., van Hoof, C., Saraceno, P., Cepa, J., Kerschbaum, F., Agnèse, P., Ali, B., Altieri, B., Andreani, P., Augueres, J.-L., Balog, Z., Barl, L., Bauer, O. H., Belbachir, N., Benedettini, M., Billot, N., Boulade, O., Bischof, H., Blommaert, J., Callut, E., Cara, C., Cerulli, R., Cesarsky, D., Contursi, A., Creten, Y., De Meester, W., Doublier, V., Doumayrou, E., Duband, L., Exter, K., Genzel, R., Gillis, J.-M., Grözinger, U., Henning, T., Herreros, J., Huygen, R., Inguscio, M., Jakob, G., Jamar, C., Jean, C., de Jong, J., Katterloher, R., Kiss, C., Klaas, U., Lemke, D., Lutz, D., Madden, S., Marquet, B., Martignac, J., Mazy, A., Merken, P., Montfort, F., Morbidelli, L., Müller, T., Nielbock, M., Okumura, K., Orfei, R., Ottensamer, R., Pezzuto, S., Popesso, P., Putzeys, J., Regibo, S., Reveret, V., Royer,

- P., Sauvage, M., Schreiber, J., Stegmaier, J., Schmitt, D., Schubert, J., Sturm, E., Thiel, M., Tofani, G., Vavrek, R., Wetzstein, M., Wieprecht, E., and Wiezorrek, E. (2010). The Photodetector Array Camera and Spectrometer (PACS) on the Herschel Space Observatory. *A&A*, 518:L2.
- Pope, A., Borys, C., Scott, D., Conselice, C., Dickinson, M., and Mobasher, B. (2005). The Hubble Deep Field North SCUBA Super-map - III. Optical and near-infrared properties of submillimetre galaxies. *MNRAS*, 358:149–167.
- Press, W. H. and Schechter, P. (1974). Formation of Galaxies and Clusters of Galaxies by Self-Similar Gravitational Condensation. *ApJ*, 187:425–438.
- Puget, J.-L., Abergel, A., Bernard, J.-P., Boulanger, F., Burton, W. B., Desert, F.-X., and Hartmann, D. (1996). Tentative detection of a cosmic far-infrared background with COBE. *A&A*, 308:L5.
- Reichardt, C. L., Stalder, B., Bleem, L. E., Montroy, T. E., Aird, K. A., Andersson, K., Armstrong, R., Ashby, M. L. N., Bautz, M., Bayliss, M., Bazin, G., Benson, B. A., Brodwin, M., Carlstrom, J. E., Chang, C. L., Cho, H. M., Clocchiatti, A., Crawford, T. M., Crites, A. T., de Haan, T., Desai, S., Dobbs, M. A., Dudley, J. P., Foley, R. J., Forman, W. R., George, E. M., Gladders, M. D., Gonzalez, A. H., Halverson, N. W., Harrington, N. L., High, F. W., Holder, G. P., Holzappel, W. L., Hoover, S., Hrubes, J. D., Jones, C., Joy, M., Keisler, R., Knox, L., Lee, A. T., Leitch, E. M., Liu, J., Lueker, M., Luong-Van, D., Mantz, A., Marrone, D. P., McDonald, M., McMahon, J. J., Mehl, J., Meyer, S. S., Mocanu, L., Mohr, J. J., Murray, S. S., Natoli, T., Padin, S., Plagge, T., Pryke, C., Rest, A., Ruel, J., Ruhl, J. E., Saliwanchik, B. R., Saro, A., Sayre, J. T., Schaffer, K. K., Shaw, L., Shirokoff, E., Song, J., Spieler, H. G., Staniszewski, Z., Stark, A. A., Story, K., Stubbs, C. W., Šuhada, R., van Engelen, A., Vanderlinde, K., Vieira, J. D., Vikhlinin, A., Williamson, R., Zahn, O., and Zenteno, A. (2013). Galaxy Clusters Discovered via the Sunyaev-Zel’dovich Effect in the First 720 Square Degrees of the South Pole Telescope Survey. *ApJ*, 763:127.
- Richards, G., Lacy, M., Strauss, M., Spergel, D., Anderson, S., Bauer, F., Bochanski, J., Brandt, N., Cushing, M., Fan, X., Gallagher, S., Glikman, E., Haggard, D., Hewett, P., Hodge, J., Hopkins, P., Hughes, J., Jiang, L., Knapp, G., Kneib, J.-P., Lin, Y.-T., Lupton, R., Makler, M., McGehee, P., McMahon, R., Menanteau, F., Myers, A., Nichol, R., Ross, N., Ryan, E., Schneider, D., Szalay, A., Urry, C. M., Viero, M., Warren, S., and Zakamska, N. (2012). SpIES: The Spitzer-IRAC Equatorial Survey. Spitzer Proposal.

- Riechers, D. A., Bradford, C. M., Clements, D. L., Dowell, C. D., Pérez-Fournon, I., Ivison, R. J., Bridge, C., Conley, A., Fu, H., Vieira, J. D., Wardlow, J., Calanog, J., Cooray, A., Hurley, P., Neri, R., Kamenetzky, J., Aguirre, J. E., Altieri, B., Arumugam, V., Benford, D. J., Béthermin, M., Bock, J., Burgarella, D., Cabrera-Lavers, A., Chapman, S. C., Cox, P., Dunlop, J. S., Earle, L., Farrah, D., Ferrero, P., Franceschini, A., Gavazzi, R., Glenn, J., Solares, E. A. G., Gurwell, M. A., Halpern, M., Hatziminaoglou, E., Hyde, A., Ibar, E., Kovács, A., Krips, M., Lupu, R. E., Maloney, P. R., Martinez-Navajas, P., Matsuhara, H., Murphy, E. J., Naylor, B. J., Nguyen, H. T., Oliver, S. J., Omont, A., Page, M. J., Petitpas, G., Rangwala, N., Roseboom, I. G., Scott, D., Smith, A. J., Staguhn, J. G., Streblyanska, A., Thomson, A. P., Valtchanov, I., Viero, M., Wang, L., Zemcov, M., and Zmuidzinas, J. (2013). A dust-obscured massive maximum-starburst galaxy at a redshift of 6.34. *Nature*, 496:329–333.
- Rieke, G. H., Young, E. T., Engelbracht, C. W., Kelly, D. M., Low, F. J., Haller, E. E., Beeman, J. W., Gordon, K. D., Stansberry, J. A., Misselt, K. A., Cadien, J., Morrison, J. E., Rivlis, G., Latter, W. B., Noriega-Crespo, A., Padgett, D. L., Stapelfeldt, K. R., Hines, D. C., Egami, E., Muzerolle, J., Alonso-Herrero, A., Blaylock, M., Dole, H., Hinz, J. L., Le Floch, E., Papovich, C., Pérez-González, P. G., Smith, P. S., Su, K. Y. L., Bennett, L., Frayer, D. T., Henderson, D., Lu, N., Masci, F., Pesenson, M., Rebull, L., Rho, J., Keene, J., Stolovy, S., Wachter, S., Wheaton, W., Werner, M. W., and Richards, P. L. (2004). The Multiband Imaging Photometer for Spitzer (MIPS). *ApJS*, 154:25–29.
- Robson, E. I., Ivison, R. J., Smail, I., Holland, W. S., Geach, J. E., Gibb, A. G., Riechers, D., Ade, P. A. R., Bintley, D., Bock, J., Chapin, E. L., Chapman, S. C., Clements, D. L., Conley, A., Cooray, A., Dunlop, J. S., Farrah, D., Fich, M., Fu, H., Jenness, T., Laporte, N., Oliver, S. J., Omont, A., Pérez-Fournon, I., Scott, D., Swinbank, A. M., and Wardlow, J. (2014). Imaging the Environment of a  $z = 6.3$  Submillimeter Galaxy with SCUBA-2. *ApJ*, 793:11.
- Rodighiero, G., Daddi, E., Baronchelli, I., Cimatti, A., Renzini, A., Aussel, H., Popesso, P., Lutz, D., Andreani, P., Berta, S., Cava, A., Elbaz, D., Feltre, A., Fontana, A., Förster Schreiber, N. M., Franceschini, A., Genzel, R., Grazian, A., Gruppioni, C., Ilbert, O., Le Floch, E., Magdis, G., Magliocchetti, M., Magnelli, B., Maiolino, R., McCracken, H., Nordon, R., Poglitsch, A., Santini, P., Pozzi, F., Riguccini, L., Tacconi, L. J., Wuyts, S., and Zamorani, G. (2011). The Lesser Role of Starbursts in Star Formation at  $z = 2$ . *ApJL*, 739:L40.

- Roseboom, I. G., Oliver, S. J., Kunz, M., Altieri, B., Amblard, A., Arumugam, V., Auld, R., Aussel, H., Babbedge, T., Béthermin, M., Blain, A., Bock, J., Boselli, A., Brisbin, D., Buat, V., Burgarella, D., Castro-Rodríguez, N., Cava, A., Chanical, P., Chapin, E., Clements, D. L., Conley, A., Conversi, L., Cooray, A., Dowell, C. D., Dwek, E., Dye, S., Eales, S., Elbaz, D., Farrah, D., Fox, M., Franceschini, A., Gear, W., Glenn, J., Solares, E. A. G., Griffin, M., Halpern, M., Harwit, M., Hatziminaoglou, E., Huang, J., Ibar, E., Isaak, K., Ivison, R. J., Lagache, G., Levenson, L., Lu, N., Madden, S., Maffei, B., Mainetti, G., Marchetti, L., Marsden, G., Mortier, A. M. J., Nguyen, H. T., O’Halloran, B., Omont, A., Page, M. J., Panuzzo, P., Papageorgiou, A., Patel, H., Pearson, C. P., Pérez-Fournon, I., Pohlen, M., Rawlings, J. I., Raymond, G., Rigopoulou, D., Rizzo, D., Rowan-Robinson, M., Portal, M. S., Schulz, B., Scott, D., Seymour, N., Shupe, D. L., Smith, A. J., Stevens, J. A., Symeonidis, M., Trichas, M., Tugwell, K. E., Vaccari, M., Valtchanov, I., Vieira, J. D., Vigroux, L., Wang, L., Ward, R., Wright, G., Xu, C. K., and Zemcov, M. (2010). The Herschel Multi-Tiered Extragalactic Survey: source extraction and cross-identifications in confusion-dominated SPIRE images. *MNRAS*, 409:48–65.
- Rownd, B., Bock, J. J., Chattopadhyay, G., Glenn, J., and Griffin, M. J. (2003). Design and performance of feedhorn-coupled bolometer arrays for SPIRE. In *Millimeter and Submillimeter Detectors for Astronomy*, volume 4855, pages 510–519.
- Saintonge, A., Tran, K.-V. H., and Holden, B. P. (2008). Spitzer/MIPS 24  $\mu\text{m}$  Observations of Galaxy Clusters: An Increasing Fraction of Obscured Star-forming Members from  $z = 0.02$  to  $z = 0.83$ . *ApJL*, 685:L113–L116.
- Salmi, F., Daddi, E., Elbaz, D., Sargent, M. T., Dickinson, M., Renzini, A., Béthermin, M., and Le Borgne, D. (2012). Dissecting the Stellar-mass-SFR Correlation in  $z = 1$  Star-forming Disk Galaxies. *ApJL*, 754:L14.
- Sanders, D. B. and Mirabel, I. F. (1996). Luminous Infrared Galaxies. *ARA&A*, 34:749.
- Sargent, M. T., Béthermin, M., Daddi, E., and Elbaz, D. (2012). The Contribution of Starbursts and Normal Galaxies to Infrared Luminosity Functions at  $z < 2$ . *ApJL*, 747:L31.
- Schmidt, M. (1968). Space Distribution and Luminosity Functions of Quasi-Stellar Radio Sources. *ApJ*, 151:393.
- Siringo, G., Kreysa, E., Kovács, A., Schuller, F., Weiß, A., Esch, W., Gemünd, H.-P., Jethava, N., Lundershausen, G., Colin, A., Güsten, R., Menten, K. M., Beelen, A.,

- Bertoldi, F., Beeman, J. W., and Haller, E. E. (2009). The Large APEX BOlometer CAmera LABOCA. *A&A*, 497:945–962.
- Smail, I., Chapman, S. C., Blain, A. W., and Ivison, R. J. (2004). The Rest-Frame Optical Properties of SCUBA Galaxies. *ApJ*, 616:71–85.
- Smail, I., Ivison, R. J., and Blain, A. W. (1997). A Deep Sub-millimeter Survey of Lensing Clusters: A New Window on Galaxy Formation and Evolution. *ApJL*, 490:L5–L8.
- Smail, I., Ivison, R. J., Owen, F. N., Blain, A. W., and Kneib, J.-P. (2000). Radio Constraints on the Identifications and Redshifts of Submillimeter Galaxies. *ApJ*, 528:612–616.
- Soifer, B. T. and Neugebauer, G. (1991). The properties of infrared galaxies in the local universe. *AJ*, 101:354–361.
- Soifer, B. T., Rowan-Robinson, M., Houck, J. R., de Jong, T., Neugebauer, G., Aumann, H. H., Beichman, C. A., Boggess, N., Clegg, P. E., Emerson, J. P., Gillett, F. C., Habing, H. J., Hauser, M. G., Low, F. J., Miley, G., and Young, E. (1984). Infrared galaxies in the IRAS minisurvey. *ApJL*, 278:L71–L74.
- Springel, V., White, S. D. M., Jenkins, A., Frenk, C. S., Yoshida, N., Gao, L., Navarro, J., Thacker, R., Croton, D., Helly, J., Peacock, J. A., Cole, S., Thomas, P., Couchman, H., Evrard, A., Colberg, J., and Pearce, F. (2005). Simulations of the formation, evolution and clustering of galaxies and quasars. *Nature*, 435:629–636.
- Stetson, P. B. (1987). DAOPHOT - A computer program for crowded-field stellar photometry. *PASP*, 99:191–222.
- Sunyaev, R. A. and Zeldovich, I. B. (1980). The velocity of clusters of galaxies relative to the microwave background - The possibility of its measurement. *MNRAS*, 190:413–420.
- Sunyaev, R. A. and Zel'dovich, Y. B. (1972). The Observations of Relic Radiation as a Test of the Nature of X-Ray Radiation from the Clusters of Galaxies. *Comments on Astrophysics and Space Physics*, 4:173.
- Swetz, D. S., Ade, P. A. R., Amiri, M., Appel, J. W., Battistelli, E. S., Burger, B., Chervenak, J., Devlin, M. J., Dicker, S. R., Doriese, W. B., Dünner, R., Essinger-Hileman, T., Fisher, R. P., Fowler, J. W., Halpern, M., Hasselfield, M., Hilton, G. C., Hincks, A. D., Irwin, K. D., Jarosik, N., Kaul, M., Klein, J., Lau, J. M., Limon, M., Marriage, T. A., Marsden, D., Martocci, K., Mauskopf, P., Moseley, H., Netterfield,

- C. B., Niemack, M. D., Nolta, M. R., Page, L. A., Parker, L., Staggs, S. T., Stryzak, O., Switzer, E. R., Thornton, R., Tucker, C., Wollack, E., and Zhao, Y. (2011). Overview of the Atacama Cosmology Telescope: Receiver, Instrumentation, and Telescope Systems. *ApJS*, 194:41.
- Swinbank, A. M., Chapman, S. C., Smail, I., Lindner, C., Borys, C., Blain, A. W., Ivison, R. J., and Lewis, G. F. (2006). The link between submillimetre galaxies and luminous ellipticals: near-infrared IFU spectroscopy of submillimetre galaxies. *MNRAS*, 371:465–476.
- Swinbank, A. M., Smail, I., Chapman, S. C., Borys, C., Alexander, D. M., Blain, A. W., Conselice, C. J., Hainline, L. J., and Ivison, R. J. (2010a). A Hubble Space Telescope NICMOS and ACS morphological study of  $z \sim 2$  submillimetre galaxies. *MNRAS*, 405:234–244.
- Swinbank, A. M., Smail, I., Longmore, S., Harris, A. I., Baker, A. J., De Breuck, C., Richard, J., Edge, A. C., Ivison, R. J., Blundell, R., Coppin, K. E. K., Cox, P., Gurwell, M., Hainline, L. J., Krips, M., Lundgren, A., Neri, R., Siana, B., Siringo, G., Stark, D. P., Wilner, D., and Younger, J. D. (2010b). Intense star formation within resolved compact regions in a galaxy at  $z = 2.3$ . *Nature*, 464:733–736.
- Tacconi, L. J., Genzel, R., Neri, R., Cox, P., Cooper, M. C., Shapiro, K., Bolatto, A., Bouché, N., Bournaud, F., Burkert, A., Combes, F., Comerford, J., Davis, M., Schreiber, N. M. F., Garcia-Burillo, S., Gracia-Carpio, J., Lutz, D., Naab, T., Omont, A., Shapley, A., Sternberg, A., and Weiner, B. (2010). High molecular gas fractions in normal massive star-forming galaxies in the young Universe. *Nature*, 463:781–784.
- Tacconi, L. J., Genzel, R., Smail, I., Neri, R., Chapman, S. C., Ivison, R. J., Blain, A., Cox, P., Omont, A., Bertoldi, F., Greve, T., Förster Schreiber, N. M., Genel, S., Lutz, D., Swinbank, A. M., Shapley, A. E., Erb, D. K., Cimatti, A., Daddi, E., and Baker, A. J. (2008). Submillimeter Galaxies at  $z \sim 2$ : Evidence for Major Mergers and Constraints on Lifetimes, IMF, and CO-H<sub>2</sub> Conversion Factor. *ApJ*, 680:246–262.
- Targett, T. A., Dunlop, J. S., Cirasuolo, M., McLure, R. J., Bruce, V. A., Fontana, A., Galametz, A., Paris, D., Davé, R., Dekel, A., Faber, S. M., Ferguson, H. C., Grogin, N. A., Kartaltepe, J. S., Kocevski, D. D., Koekemoer, A. M., Kurczynski, P., Lai, K., and Lotz, J. (2013). The properties of (sub-)millimetre-selected galaxies as revealed by CANDELS HST WFC3/IR imaging in GOODS-South. *MNRAS*, 432:2012–2042.

- Trumpler, R. J. (1930). Preliminary results on the distances, dimensions and space distribution of open star clusters. *Lick Observatory Bulletin*, 14:154–188.
- Turner, A. D., Bock, J. J., Beeman, J. W., Glenn, J., Hargrave, P. C., Hristov, V. V., Nguyen, H. T., Rahman, F., Sethuraman, S., and Woodcraft, A. L. (2001). Silicon nitride Micromesh Bolometer Array for Submillimeter Astrophysics. *Applied Optics*, 40:4921–4932.
- Valiante, E., Lutz, D., Sturm, E., Genzel, R., and Chapin, E. L. (2009). A Backward Evolution Model for Infrared Surveys: The Role of AGN- and Color- $L_{TIR}$  Distributions. *ApJ*, 701:1814–1838.
- Vanderlinde, K., Crawford, T. M., de Haan, T., Dudley, J. P., Shaw, L., Ade, P. A. R., Aird, K. A., Benson, B. A., Bleem, L. E., Brodwin, M., Carlstrom, J. E., Chang, C. L., Crites, A. T., Desai, S., Dobbs, M. A., Foley, R. J., George, E. M., Gladders, M. D., Hall, N. R., Halverson, N. W., High, F. W., Holder, G. P., Holzappel, W. L., Hrubes, J. D., Joy, M., Keisler, R., Knox, L., Lee, A. T., Leitch, E. M., Loehr, A., Lueker, M., Marrone, D. P., McMahon, J. J., Mehl, J., Meyer, S. S., Mohr, J. J., Montroy, T. E., Ngeow, C.-C., Padin, S., Plagge, T., Pryke, C., Reichardt, C. L., Rest, A., Ruel, J., Ruhl, J. E., Schaffer, K. K., Shirokoff, E., Song, J., Spieler, H. G., Stalder, B., Staniszewski, Z., Stark, A. A., Stubbs, C. W., van Engelen, A., Vieira, J. D., Williamson, R., Yang, Y., Zahn, O., and Zenteno, A. (2010). Galaxy Clusters Selected with the Sunyaev-Zel’dovich Effect from 2008 South Pole Telescope Observations. *ApJ*, 722:1180–1196.
- Vieira, J. D., Marrone, D. P., Chapman, S. C., De Breuck, C., Hezaveh, Y. D., Weiß, A., Aguirre, J. E., Aird, K. A., Aravena, M., Ashby, M. L. N., Bayliss, M., Benson, B. A., Biggs, A. D., Bleem, L. E., Bock, J. J., Bothwell, M., Bradford, C. M., Brodwin, M., Carlstrom, J. E., Chang, C. L., Crawford, T. M., Crites, A. T., de Haan, T., Dobbs, M. A., Fomalont, E. B., Fassnacht, C. D., George, E. M., Gladders, M. D., Gonzalez, A. H., Greve, T. R., Gullberg, B., Halverson, N. W., High, F. W., Holder, G. P., Holzappel, W. L., Hoover, S., Hrubes, J. D., Hunter, T. R., Keisler, R., Lee, A. T., Leitch, E. M., Lueker, M., Luong-van, D., Malkan, M., McIntyre, V., McMahon, J. J., Mehl, J., Menten, K. M., Meyer, S. S., Mocanu, L. M., Murphy, E. J., Natoli, T., Padin, S., Plagge, T., Reichardt, C. L., Rest, A., Ruel, J., Ruhl, J. E., Sharon, K., Schaffer, K. K., Shaw, L., Shirokoff, E., Spilker, J. S., Stalder, B., Staniszewski, Z., Stark, A. A., Story, K., Vanderlinde, K., Welikala, N., and Williamson, R. (2013).

Dusty starburst galaxies in the early Universe as revealed by gravitational lensing. *Nature*, 495:344–347.

Viero, M. P., Ade, P. A. R., Bock, J. J., Chapin, E. L., Devlin, M. J., Griffin, M., Gundersen, J. O., Halpern, M., Hargrave, P. C., Hughes, D. H., Klein, J., MacTavish, C. J., Marsden, G., Martin, P. G., Mauskopf, P., Moncelsi, L., Negrello, M., Netterfield, C. B., Olmi, L., Pascale, E., Patanchon, G., Rex, M., Scott, D., Semisch, C., Thomas, N., Truch, M. D. P., Tucker, C., Tucker, G. S., and Wiebe, D. V. (2009). BLAST: Correlations in the Cosmic Far-Infrared Background at 250, 350, and 500  $\mu\text{m}$  Reveal Clustering of Star-forming Galaxies. *ApJ*, 707:1766–1778.

Viero, M. P., Asboth, V., Roseboom, I. G., Moncelsi, L., Marsden, G., Mentuch Cooper, E., Zemcov, M., Addison, G., Baker, A. J., Beelen, A., Bock, J., Bridge, C., Conley, A., Devlin, M. J., Doré, O., Farrah, D., Finkelstein, S., Font-Ribera, A., Geach, J. E., Gebhardt, K., Gill, A., Glenn, J., Hajian, A., Halpern, M., Jogee, S., Kurczynski, P., Lapi, A., Negrello, M., Oliver, S. J., Papovich, C., Quadri, R., Ross, N., Scott, D., Schulz, B., Somerville, R., Spergel, D. N., Vieira, J. D., Wang, L., and Wechsler, R. (2014). The Herschel Stripe 82 Survey (HerS): Maps and Early Catalog. *ApJS*, 210:22.

Viero, M. P., Wang, L., Zemcov, M., Addison, G., Amblard, A., Arumugam, V., Aussel, H., Béthermin, M., Bock, J., Boselli, A., Buat, V., Burgarella, D., Casey, C. M., Clements, D. L., Conley, A., Conversi, L., Cooray, A., De Zotti, G., Dowell, C. D., Farrah, D., Franceschini, A., Glenn, J., Griffin, M., Hatziminaoglou, E., Heinis, S., Ibar, E., Ivison, R. J., Lagache, G., Levenson, L., Marchetti, L., Marsden, G., Nguyen, H. T., O’Halloran, B., Oliver, S. J., Omont, A., Page, M. J., Papageorgiou, A., Pearson, C. P., Pérez-Fournon, I., Pohlen, M., Rigopoulou, D., Roseboom, I. G., Rowan-Robinson, M., Schulz, B., Scott, D., Seymour, N., Shupe, D. L., Smith, A. J., Symeonidis, M., Vaccari, M., Valtchanov, I., Vieira, J. D., Wardlow, J., and Xu, C. K. (2013). HerMES: Cosmic Infrared Background Anisotropies and the Clustering of Dusty Star-forming Galaxies. *ApJ*, 772:77.

Wang, L., Viero, M., Ross, N. P., Asboth, V., Béthermin, M., Bock, J., Clements, D., Conley, A., Cooray, A., Farrah, D., Hajian, A., Han, J., Lagache, G., Marsden, G., Myers, A., Norberg, P., Oliver, S., Page, M., Symeonidis, M., Schulz, B., Wang, W., and Zemcov, M. (2015). Co-evolution of black hole growth and star formation from a cross-correlation analysis between quasars and the cosmic infrared background. *MNRAS*, 449:4476–4493.

Wardlow, J. L., Cooray, A., De Bernardis, F., Amblard, A., Arumugam, V., Aussel, H., Baker, A. J., Béthermin, M., Blundell, R., Bock, J., Boselli, A., Bridge, C., Buat, V., Burgarella, D., Bussmann, R. S., Cabrera-Lavers, A., Calanog, J., Carpenter, J. M., Casey, C. M., Castro-Rodríguez, N., Cava, A., Chanial, P., Chapin, E., Chapman, S. C., Clements, D. L., Conley, A., Cox, P., Dowell, C. D., Dye, S., Eales, S., Farrah, D., Ferrero, P., Franceschini, A., Frayer, D. T., Frazer, C., Fu, H., Gavazzi, R., Glenn, J., González Solares, E. A., Griffin, M., Gurwell, M. A., Harris, A. I., Hatziminaoglou, E., Hopwood, R., Hyde, A., Ibar, E., Ivison, R. J., Kim, S., Lagache, G., Levenson, L., Marchetti, L., Marsden, G., Martinez-Navajas, P., Negrello, M., Neri, R., Nguyen, H. T., O'Halloran, B., Oliver, S. J., Omont, A., Page, M. J., Panuzzo, P., Papageorgiou, A., Pearson, C. P., Pérez-Fournon, I., Pohlen, M., Riechers, D., Rigopoulou, D., Roseboom, I. G., Rowan-Robinson, M., Schulz, B., Scott, D., Scoville, N., Seymour, N., Shupe, D. L., Smith, A. J., Streblyanska, A., Strom, A., Symeonidis, M., Trichas, M., Vaccari, M., Vieira, J. D., Viero, M., Wang, L., Xu, C. K., Yan, L., and Zemcov, M. (2013). HerMES: Candidate Gravitationally Lensed Galaxies and Lensing Statistics at Submillimeter Wavelengths. *ApJ*, 762:59.

Warren-Smith, R. F. and Wallace, P. T. (1993). The STARLINK Software Collection. In *Astronomical Data Analysis Software and Systems II*, volume 52, page 229.

Weiß, A., De Breuck, C., Marrone, D. P., Vieira, J. D., Aguirre, J. E., Aird, K. A., Aravena, M., Ashby, M. L. N., Bayliss, M., Benson, B. A., Béthermin, M., Biggs, A. D., Bleem, L. E., Bock, J. J., Bothwell, M., Bradford, C. M., Brodwin, M., Carlstrom, J. E., Chang, C. L., Chapman, S. C., Crawford, T. M., Crites, A. T., de Haan, T., Dobbs, M. A., Downes, T. P., Fassnacht, C. D., George, E. M., Gladders, M. D., Gonzalez, A. H., Greve, T. R., Halverson, N. W., Hezaveh, Y. D., High, F. W., Holder, G. P., Holzzapfel, W. L., Hoover, S., Hrubes, J. D., Husband, K., Keisler, R., Lee, A. T., Leitch, E. M., Lueker, M., Luong-Van, D., Malkan, M., McIntyre, V., McMahan, J. J., Mehl, J., Menten, K. M., Meyer, S. S., Murphy, E. J., Padin, S., Plagge, T., Reichardt, C. L., Rest, A., Rosenman, M., Ruel, J., Ruhl, J. E., Schaffer, K. K., Shirokoff, E., Spilker, J. S., Stalder, B., Staniszewski, Z., Stark, A. A., Story, K., Vanderlinde, K., Welikala, N., and Williamson, R. (2013). ALMA Redshifts of Millimeter-selected Galaxies from the SPT Survey: The Redshift Distribution of Dusty Star-forming Galaxies. *ApJ*, 767:88.

White, S. D. M. and Rees, M. J. (1978). Core condensation in heavy halos - A two-stage theory for galaxy formation and clustering. *MNRAS*, 183:341–358.

- Wilson, G. W., Austermann, J. E., Perera, T. A., Scott, K. S., Ade, P. A. R., Bock, J. J., Glenn, J., Golwala, S. R., Kim, S., Kang, Y., Lydon, D., Mauskopf, P. D., Predmore, C. R., Roberts, C. M., Souccar, K., and Yun, M. S. (2008). The AzTEC mm-wavelength camera. *MNRAS*, 386:807–818.
- Wright, E. L., Eisenhardt, P. R. M., Mainzer, A. K., Ressler, M. E., Cutri, R. M., Jarrett, T., Kirkpatrick, J. D., Padgett, D., McMillan, R. S., Skrutskie, M., Stanford, S. A., Cohen, M., Walker, R. G., Mather, J. C., Leisawitz, D., Gautier, III, T. N., McLean, I., Benford, D., Lonsdale, C. J., Blain, A., Mendez, B., Irace, W. R., Duval, V., Liu, F., Royer, D., Heinrichsen, I., Howard, J., Shannon, M., Kendall, M., Walsh, A. L., Larsen, M., Cardon, J. G., Schick, S., Schwalm, M., Abid, M., Fabinsky, B., Naes, L., and Tsai, C.-W. (2010). The Wide-field Infrared Survey Explorer (WISE): Mission Description and Initial On-orbit Performance. *AJ*, 140:1868–1881.
- Xu, C. K., Ayasso, H., Beelen, A., Conversi, L., Konyves, V., Papageorgiou, A., Piazzo, L., Roussel, H., Schulz, B., and Shupe, D. (2014). Spire map-making test report. *ArXiv Astrophysics e-prints*, arXiv:1401.2109.
- Zemcov, M., Blain, A., Cooray, A., Béthermin, M., Bock, J., Clements, D. L., Conley, A., Conversi, L., Dowell, C. D., Farrah, D., Glenn, J., Griffin, M., Halpern, M., Jullo, E., Kneib, J.-P., Marsden, G., Nguyen, H. T., Oliver, S. J., Richard, J., Roseboom, I. G., Schulz, B., Scott, D., Shupe, D. L., Smith, A. J., Valtchanov, I., Viero, M., Wang, L., and Wardlow, J. (2013). HerMES: A Deficit in the Surface Brightness of the Cosmic Infrared Background due to Galaxy Cluster Gravitational Lensing. *ApJL*, 769:L31.
- Zemcov, M., Borys, C., Halpern, M., Mauskopf, P., and Scott, D. (2007). A study of the Sunyaev-Zel’dovich increment using archival SCUBA data. *MNRAS*, 376:1073–1098.
- Zemcov, M., Halpern, M., Borys, C., Chapman, S., Holland, W., Pierpaoli, E., and Scott, D. (2003). Measurement of the Sunyaev-Zel’dovich increment in massive galaxy clusters. *MNRAS*, 346:1179–1188.
- Zemcov, M., Rex, M., Rawle, T. D., Bock, J. J., Egami, E., Altieri, B., Blain, A. W., Boone, F., Bridge, C. R., Clement, B., Combes, F., Dowell, C. D., Dessauges-Zavadsky, M., Fadda, D., Ilbert, O., Ivison, R. J., Jauzac, M., Kneib, J.-P., Lutz, D., Pelló, R., Pereira, M. J., Pérez-González, P. G., Richard, J., Rieke, G. H., Rodighiero, G., Schaerer, D., Smith, G. P., Valtchanov, I., Walth, G. L., van der Werf, P., and Werner,

M. W. (2010). First detection of the Sunyaev Zel'dovich effect increment at  $\lambda < 650$   $\mu\text{m}$ . *A&A*, 518:L16.